UNIVERSITY OF Southampton

University of Southampton Research Repository
ePrints Soton

Copyright © and Moral Rights for this thesis are retained by the author and/or other copyright owners. A copy can be downloaded for personal non-commercial research or study, without prior permission or charge. This thesis cannot be reproduced or quoted extensively from without first obtaining permission in writing from the copyright holder/s. The content must not be changed in any way or sold commercially in any format or medium without the formal permission of the copyright holders.

When referring to this work, full bibliographic details including the author, title, awarding institution and date of the thesis must be given e.g.

AUTHOR (year of submission) "Full thesis title", University of Southampton, name of the University School or Department, PhD Thesis, pagination

http://eprints.soton.ac.uk

UNIVERSITY OF SOUTHAMPTON

FACULTY OF NATURAL AND ENVIRONMENTAL SCIENCES

School of Ocean and Earth Sciences

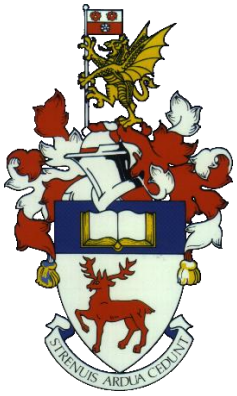

Characterisation of pH and pCO_2 optodes towards high resolution *in situ* ocean deployment

by

Jennifer Sarah Clarke

Thesis for the degree of Doctor of Philosophy

September 2015

UNIVERSITY OF SOUTHAMPTON

ABSTRACT

FACULTY OF NATURAL AND ENVIRONMENTAL SCIENCES

Ocean and Earth Sciences

Thesis for the degree of Doctor of Philosophy

CHARACTERISATION OF pH AND pCO_2 OPTODES TOWARDS HIGH RESOLUTION *IN SITU* OCEAN DEPLOYMENT

Jennifer Sarah Clarke

Anthropogenic emissions of carbon dioxide (CO_2) into the atmosphere results in climate change and perturbations of the oceanic carbonate system. Atmospheric CO_2 concentrations have increased from pre-industrial times from land use changes, fossil fuel combustion and increasing cement production. The ocean is currently a major sink for this anthropogenic CO_2, increasing pCO_2 and dissolved inorganic carbon concentrations and decreasing pH and carbonate ion concentrations. This has potential biogeochemical and ecosystem consequences. To monitor the ocean's uptake of CO_2, identify regions of enhanced carbonate system changes, and observe the effectiveness of CO_2 emission mitigation strategies, high quality pCO_2 and pH measurements with good temporal and spatial coverage are required. This thesis presents the characterisation of novel pH and pCO_2 sensing spots which use fluorescent detection techniques, and evaluates their potential for *in situ* seawater deployments.

The optode sensing spots were illuminated with low intensity light (0.2 mA, 0.72 mWatt), and the time-domain dual lifetime referencing analysis technique was applied to maximise the lifetime of the spot and reduce overall power consumption of the measurement (1.8 Watt). The same hardware was used for both the pH and pCO_2 spot interrogation, thereby demonstrating the versatility of the optode. After initial calibrations over typical seawater ranges for pH and pCO_2, (pH range 7.6 – 8.2 and pCO_2 range 280-1000 µatm) the temperature and salinity dependence of the spots was evaluated. The pH displayed both a temperature (-0.046 pH / °C from 5-25 °C) and salinity dependency (-0.01 pH /psu over 5-35), while the pCO_2 sensor showed only a temperature dependence (-39 µatm $°C^{-1}$). Precision of the repeated measurement of certified reference material was 0.0074 pH and 0.8 µatm for the pH and pCO_2 optodes, respectively. The optodes were deployed as shipboard autonomous underway systems in the North Atlantic and Southern Ocean, both important CO_2 sink regions. The successful pCO_2 data deployment produced good quality data that has been used to quantify the spatial controls on carbonate chemistry and air-sea CO_2 fluxes in the North Atlantic, and evaluate the effect of sampling rate and interpolation method on the determined flux. This thesis demonstrates the potential of these small sensors, with the ultimate aim to deploy them on ARGO floats and gliders.

Table of Contents

Table of Contents ..... **i**

List of Tables ..... **v**

List of Figures ..... **vii**

Declaration of Authorship ..... **ix**

Acknowledgements ..... **xi**

Definitions and Abbreviations ..... **xiii**

Chapter 1 : Introduction **1**

1.1 Motivation 1

1.2 Carbonate System 3

1.2.1 Ocean carbon distribution 6

1.2.2 Sea-Air fluxes 7

1.2.3 Determining the ocean carbon system 9

1.2.4 pH definitions 10

1.3 Measurement platforms 11

1.4 Techniques to determine pH in seawater 11

1.5 Techniques to determine pCO_2 in seawater 12

1.6 Immobilised sensor spots. 13

1.6.1 PreSens spot 16

1.7 Overarching aims of the thesis 17

1.8 Breakdown of Ph.D. Thesis. 18

Chapter 2 : Characterisation and deployment of an immobilised pH sensor spot towards surface ocean pH measurements. **19**

Abstract 19

2.1 Introduction 21

2.1.1 pH sensors for Oceanic waters 21

2.1.2 Sensing Spots 23

2.2 Materials & Methods 26

2.2.1 Materials & Methods 26

2.2.2 pH Buffer Solutions 26

2.2.3 pH optode hardware 27

2.2.4 Analytical protocols for pH measurements 29

2.2.5 Cruise deployment details 33

2.3 Results and Discussion 34

2.3.1 pH sensor spot characterisation 34

2.3.2 Temperature dependence 35
2.3.3 Salinity dependence 37
2.3.4 Chlorophyll influence 38
2.3.5 Metrology 39
2.3.6 Multi-linear regression 42
2.3.7 Cruise data 43
2.4 Current limitations and future directions 44
2.5 Conclusion 45

Chapter 3 : Developments in marine pCO_2 measurement technology. 47

Abstract 47
3.1 Introduction 48
3.2 Carbonate variables 49
3.3 Measurement platforms 50
3.4 Gas-based methods 53
3.4.1 Gas chromatography based pCO_2 measurements 54
3.4.2 NDIR spectrometry pCO_2 systems 54
3.4.3 Cavity ring-down spectroscopy for pCO_2 measurements 56
3.5 Electrochemical pCO_2 systems 57
3.5.1 ISFET pCO_2 58
3.6 Wet chemical spectrophotometric pCO_2 systems 58
3.7 Optodes for pCO_2 systems 59
3.7.1 Spot composition. 60
3.7.1.1 Membrane 61
3.7.1.2 Indicators 61
3.7.2 Hardware 62
3.7.2.1 Light Source 63
3.7.2.2 Photodetector 63
3.7.3 Analysis methods 63
3.7.3.1 Fluorescence intensity 64
3.7.3.2 FRET 64
3.7.3.3 *f*-DLR. 64
3.7.3.4 *t*-DLR 65
3.8 Optodes pCO_2 for ocean monitoring. 66
3.9 Summary and future directions 68

Chapter 4 : Characterisation of a pCO_2 sensor spot 71

Abstract 71
4.1 Introduction 72
4.2 pCO_2 sensor spot 73
4.3 Methods 75
4.3.1 Hardware 75
4.3.2 Artificial seawater solutions 75
4.3.3 Methods to alter levels of pCO_2 76
4.3.3.1 Sosna rig 76
4.3.3.2 Manual manipulation 78
4.3.4 Equipment and additional reference material 78
4.3.5 Salinity and temperature variations 79
4.3.6 Chlorophyll interference with the pCO_2 measurement 79
4.3.7 Metrology 80
4.4 Results and Discussion 81
4.4.1 Calibration 81
4.4.2 Temperature Variations. 84
4.4.3 Salinity 85
4.4.4 Combined temperature and salinity variations 88
4.4.5 Multi-linear regression 89
4.4.6 Chlorophyll 89
4.4.7 Drift 91
4.4.8 Metrology 94
4.5 Limitations and future work 96
4.5 Conclusions 97

Chapter 5 : Surface water variability in the high latitude North Atlantic 99

Abstract 99
5.1 Introduction 100
5.2 Methods 102
5.2.1 Cruise 102
5.2.1.1 Continuous underway measurements 103
5.2.1.1.1 pCO_2 optode 103
5.2.1.1.2 DIC measurements 104
5.2.1.2 Discrete sampling 104
5.2.2 Nutrient and Oxygen data 105
5.2.3 Calculation of carbonate parameters 105
5.2.4 Satellite data 106

5.2.5 Statistical Analysis 106
5.2.6 Flux calculations 107
5.3 Results and Discussion 109
5.3.1 Observed hydrography 109
5.3.2 Carbonate chemistry variability. 114
5.3.3 Continuous underway compared to discrete bottle samples 120
5.3.4 Air-sea flux 123
5.3.5 Controls on surface pCO_2 129
5.4 Summary and Conclusion 132

Chapter 6 : Conclusion and future directions 133

Abstract 133
6.1 Optodes 134
6.2 Sensor spots 134
6.3 Future developments for the system 136
6.4 Concluding remarks 138

Appendices 139

Appendix A 141

A.1 Satellite Chlorophyll Maps 141
A.2 Temperature and Salinity Plots 145
A.3 Underway DIC CRM measurements 146

List of References 147

List of Tables

Table 1.1 Estimated errors from calculated parameters of the carbonate system with different input combinations. 9

Table 2.1 Details of reported spot-based pH optodes 25

Table 3.1 A selection of commonly used ocean pCO_2 sensors 52

Table 3.2 pCO_2 optodes deployed in marine environments 66

Table 4.1 Coefficients of the polynomial fit in figure 4.4. 85

Table 4.2 Coefficients of the linear regressions in figure 4.4. 85

Table 4.3 Coefficients and standard error of the multi-linear regression 89

Table 5.1 Mean air-sea fluxes across the cruise 125

Table 5.2 Means and standard deviations of underway variables along the cruise 130

Table 6.1 Specifications of the pH and pCO_2 spots in this study. 135

List of Figures

Figure 1.1 Figure from the IPCC report comparing atmospheric pCO_2, seawater pCO_2 and seawater pH 3

Figure 1.2 Distribution of the carbon system in surface water 5

Figure 1.3 Graphical representation of t-DLR and *f*-DLR measurements 15

Figure 2.1 Schematic of the pH sensor for use as a shipboard autonomous underway system 28

Figure 2.2 Fluorescence intensity change with time caused by turning the LED on and off 30

Figure 2.3 Sigmoidal shaped fluorescence response from measurements of salinity 5 buffer solutions. 34

Figure 2.4 Response of the spot to temperature variations 36

Figure 2.5 Response of the spot to salinity variations 37

Figure 2.6 Results of the pH sensor reproducibility experiment 39

Figure 2.7 Comparison of the optode determined pH compared to a spectrophotometric sensor 40

Figure 2.8 pH sensor drift over 3 days 41

Figure 2.9 Plot of underway pH in the Southern Ocean 43

Figure 3.1 Platforms available to deploy sensors in the ocean. 50

Figure 3.2 Generalised pCO_2 spot composition 60

Figure 3.3 Schematic of optode setup 62

Figure 3.4 Results of the shipboard deployment of a pCO_2 optode spot in the North Atlantic 68

Figure 4.1 Schematic of the Sosna gas calibration rig 77

Figure 4.2 Manual manipulation of pCO_2 in artificial seawater 82

Figure 4.3 Initial calibration run with the Sosna rig in artificial seawater 83

Figure 4.4 Response of the pCO_2 spot to temperature variations 84

Figure 4.5 pCO_2 optodes in NaCl solutions and artificial seawater 87

Figure 4.6 Plot of salinity and temperature variations in artificial seawater 88

Figure 4.7 Chlorophyll influence on pCO_2 spot response 90

Figure 4.8 Stability of the pCO_2 spot over 3 days 91

Figure 4.9 Residuals from the stability test 92

Figure 4.10 Residuals for the post and pre-bleach experiments. 93

Figure 4.11 Comparison of optode CRM measurements and certified values over the North Atlantic cruise 94

Figure 4.12 Repeat measurement of certified reference materials (n=10) 95

Figure 5.1 Map of the JR302 cruise route 102

Figure 5.2 Map of the temperatures and currents on the cruise route 109

Figure 5.3 Measured total alkalinity plotted against salinity 110

Figure 5.4 Measured phosphate plotted against nitrate 111

Figure 5.5 Mixed layer depth along the cruise route and temperature-salinity plots for select stations 113

Figure 5.6 Water column dissolved inorganic carbon and total alkalinity sections. 115

Figure 5.7 Subplots of underway variables over time 116

Figure 5.8 Subplots of CTD variables with increasing CTD station numbers. 117

Figure 5.9 Maps of monthly sea-ice fraction 118

Figure 5.10 Top 100 m water column dissolved inorganic carbon and total alkalinity on transects towards Greenland 119

Figure 5.11 Underway pCO_2 compared to pCO_2 calculated underway discrete samples. . .121

Figure 5.12 Comparison of Apollo underway dissolved inorganic carbon samples, to optode pCO_2, and discrete underway and CTD samples. 122

Figure 5.13 Residuals in the flux from varying ($k \bullet K_0$) and keeping ($k \bullet K_0$) constant 124

Figure 5.14 Residuals in the flux calculated from the varying sampling rate at a wind speed of 5 m s^{-1} 126

Figure 5.15 Residuals in the flux calculated from the varying sampling rate at a wind speed of 10 m s^{-1} 127

Figure 5.16 Effect of wind speed on the flux calculation 128

Figure 5.16 Map of pCO_2 flux along the cruise route 129

DECLARATION OF AUTHORSHIP

I, ... [please print name]

declare that this thesis and the work presented in it are my own and has been generated by me as the result of my own original research.

Characterisation of pH and *p*CO_2 optodes towards highresolution in situ ocean deployment.

I confirm that:

1. This work was done wholly or mainly while in candidature for a research degree at this University;
2. Where any part of this thesis has previously been submitted for a degree or any other qualification at this University or any other institution, this has been clearly stated;
3. Where I have consulted the published work of others, this is always clearly attributed;
4. Where I have quoted from the work of others, the source is always given. With the exception of such quotations, this thesis is entirely my own work;
5. I have acknowledged all main sources of help;
6. Where the thesis is based on work done by myself jointly with others, I have made clear exactly what was done by others and what I have contributed myself;
7. Parts of this work have been published, as:
    a. Clarke, J. S., Achterberg, E. P., Rérolle, V. M. C., Bey, S. A. K., Floquet, C. F. A., Mowlem, M. C., (2015). "Characterisation and deployment of an immobilised pH sensor spot towards surface ocean pH measurements." Analytica Chimica Acta **897** : 69-80

Signed:.....

Date:.....

Acknowledgements

The past three and a half years could not have happened without the help and support of many people who I count myself lucky to have worked with. I would first like to thank my supervisors Prof's Eric Achterberg, Matt Mowlem, and Toby Tyrrell, for your constant support, encouragement and fruitful discussions on sensors and carbonate chemistry. A particular thank you to Eric, for pushing me to improve my scientific writing, and inspiring me when things did not go as 'fantastically' as planned. Thanks to Cedric Floquet, for giving me a good starting point for my PhD, and continued advice.

I am indebted to the NOC sensors group for all the help when things suddenly stop working, in particular to Chris Cardwell and Iain Ogilvie. Victoire Rérolle, thank you for your patience with a panicked first year at sea while you were writing up; I am eternally grateful for your willingness to let me repeatedly deploy (and break) your sensor, and for all the thought-provoking discussions. Thanks to Rosie, Lucie and Chris for providing me with coccolithophores and chlorophyll concentrations.

I would like to thank all the scientists I've had the pleasure of meeting and working with on cruises, in particular the carbonate teams: Eithne, Marianna, Becky, and Jan –Lukas and the PI's Colin Griffiths, Geraint Tarling and Brian King for letting me join your cruises. I am grateful to the NMF and BAS staff who have spent many hours helping me fix instruments: Martin, Mark, Seth and Simon amongst others. Thanks to Team Nuts on JR302, for the lab companionship and letting me use your data!

To all the many friends I have accumulated, I would not have been able to accomplish this without you all, and your seemingly endless support, advice and distractions. To all the proof –readers for helping make this thesis come together. To the SWAGGers: Alex, MPH, MPC and Claudia for the instructive and thought provoking meetings. To my original and new officemates: Sara, Tish, James, Mario, Fran and Matthew for making the office a habitable and productive place. To my housemates (past and present) for the endless cups of tea, and bringing home emergency chocolate when needed. To Carolyn for understanding my thought processes, being there every day, and being the other half of the Jen and Carolyn dream team! To Fran Graham for all the ski adventures and support through this degree and the last.

To Matt, for putting up with all my panics and stresses, making me laugh even when I was feeling grumpy, and always believing I could do whatever I set my mind to, even when I didn't.

Finally, to my family, for everything, and to whom this is dedicated.

Definitions and Abbreviations

CO_2	Carbon Dioxide
pCO_2	Partial pressure of carbon dioxide in a body of air
$[CO_3^{2-}]$	Carbonate ion concentration
$[HCO_3^-]$	Bicarbonate ion concentration
$[H^+]$	Hydrogen ion concentration
$[CO_2]$	Carbon dioxide concentration
Ω	Calcium carbonate saturation state
DIC	Total Dissolved Inorganic Carbon
TA	Total Alkalinity
γ	Activity Coefficient
mpH	milli- pH
HPTS	1-hydroxy-3, 6, 8 – pyrenetrisulfonic acid
pK_a	Isoelectric point of a weak acid or base (buffer)
pK_a'	Apparent isoelectric point of a weak acid or base (buffer), not corrected for the non-ideality of the solution
FRET	Fluorescence resonance energy transfer
t-DLR	Time domain dual lifetime referencing
f-DLR	Frequency domain dual lifetime referencing
LED	Light emitting diode
CRM	Certified reference material
T	Temperature
S	Salinity
CTD	Conductivity Temperature and Depth rosette cast
ISFET	Ion selective field effect transistor
PMT	Photon multiplier tube
NIST	National Institute of Standards and Technology
Tris	2-amino-2-hydroxymethyl-propane-1, 3-diol
R	Sensor output fluorescence ratio

Chl-a	Chlorophyll-a
t_{97}	Time the sensor takes to reach 97 % of the final response
t_{90}	Time the sensor takes to reach 90 % of the final response
t_{63}	Time the sensor takes to reach 63 % of the final response
df	Degrees of freedom
ppm	parts per million
GC	Gas Chromatography
NDIR	Non-dispersive Infrared spectroscopy
CRDS	Cavity ring down spectroscopy
TOA	Tetraoctyl ammonium
O_2	Oxygen
NAC	North Atlantic Current
SARCT	Sub-Arctic North Atlantic
ARCT	Arctic North Atlantic
NADR	North Atlantic Drift region
EGC	East Greenland Current
EEL	Extended Ellett line
Lab Sea	Labrador Sea
GL	Greenland
NO_3	Nitrate
PO_4	Phosphate
ENAW	Eastern North Atlantic Water
Ø	Diameter

Chapter 1:

Introduction

1.1 Motivation

Carbon dioxide (CO_2) is a potent greenhouse gas, with a radiative forcing of 1.68 Wm^{-2} (IPCC, 2013) and a long atmospheric lifetime of 300 years (Archer, 2005). Increasing atmospheric CO_2 concentrations (2 ppm yr^{-1} between 2002-2011, Ciais et al. (2013)) can be attributed to increasing anthropogenic inputs from fossil fuel burning, cement production and land-use changes (Ciais et al., 2013, Le Quéré et al., 2013). The increasing atmospheric CO_2 levels and consequent climate effects, such as global warming, are well documented (Solomon et al., 2009), however only 43-46 % of annual anthropogenic CO_2 emissions remain in the atmosphere (Raven and Falkowski, 1999, Knorr, 2009, Le Quéré et al., 2009). The ocean absorbs ca. 24 % of annually emitted CO_2 (Canadell et al., 2007, Le Quéré et al., 2009) and some of the CO_2-generated heat (Hansen et al., 1981), with the land biosphere taking up 27 % (Sabine et al., 2004). The ocean is therefore one of the largest reservoirs for CO_2 (Archer et al., 2009) and a major sink for atmospheric CO_2 in the global carbon cycle (Sabine et al., 2004, Khatiwala et al., 2013)

When CO_2 diffuses into the ocean across the air-sea interface, the surface ocean carbon equilibria shift, leading to decreasing pH, carbonate ion concentration ($[CO_3^{2-}]$) and saturation states of the calcium carbonate ($CaCO_3$) minerals calcite (Ω_c) and aragonite (Ω_a) (Orr et al., 2005). A surface ocean pH decrease of ~0.002 pH units per year has been observed (Byrne et al., 2010, Lauvset and Gruber, 2014, Lauvset et al., 2015), with an overall change from a pre-industrial pH of 8.25 to ca 8.10 today (Jacobson, 2005). The decrease in surface ocean pH has been observed at time series stations in both the North Atlantic and North Pacific Oceans (Bindoff et al., 2007), keeping pace with the increasing ocean pCO_2 levels. Ocean pCO_2 concentrations are following the increasing atmospheric pCO_2 levels (Figure 1.1, IPCC (2013)). The surface pH is projected to continue decreasing in proportion to the increase in atmospheric CO_2, with reductions of 0.3-0.5 pH by 2100 under the IPCC SRES pathways A1, A2, B1 and B2(Caldeira and Wickett, 2005), and further reductions of upto 0.7 pH by 2300 under the business as usual scenario (IPCC IS92a)(Caldeira and Wickett, 2003).

The under-saturation of aragonite that is likely to occur in high latitude regions in the next century (Orr et al., 2005) as a result of the decreasing [CO_3^{2-}] in surface waters will have physiological effects on calcifying organisms particularly in species that require aragonite to form their shells (Bednaršek et al., 2012). The current saturation horizon (the point at which the water changes from saturated to undersaturated with respect to calcium carbonate) is likely to rise causing the habitable area to shrink, and as organisms fall below the saturation horizon, they are expected experience increased shell dissolution (Orr et al., 2005). Aragonite saturation state has already decreased by ~16 % since pre-industrial times causing a declining growth rate in corals (De'ath et al., 2005) which use this form of $CaCO_3$ in their exo-skeletons. The increasing sea surface temperature from increasing atmospheric CO_2 may also be contributing to the decline of calcified organisms (Kleypas and Langdon, 2006). At higher CO_2 levels there is a higher likelihood the reefs will be more rapidly eroded due to less acclimatisation and loss of biodiversity, as the more thermally stable and rapidly colonizing corals will thrive, leading to a greater inability for the reef to break waves (Hoegh-Guldberg et al., 2007). However a consistent biological response to increasing CO_2 concentrations has not been found, with the ultimate fate of ocean biota unclear (Bach et al., 2015).

The ocean's ability to take up the increasing anthropogenic atmospheric CO_2 is controlled by the efficiency of physical and biological processes in the ocean which varies both with season and ocean region (Siegenthaler and Sarmiento, 1993). The spatial variability in the oceanic pH and pCO_2 distributions are discussed below in section 1.2.1.

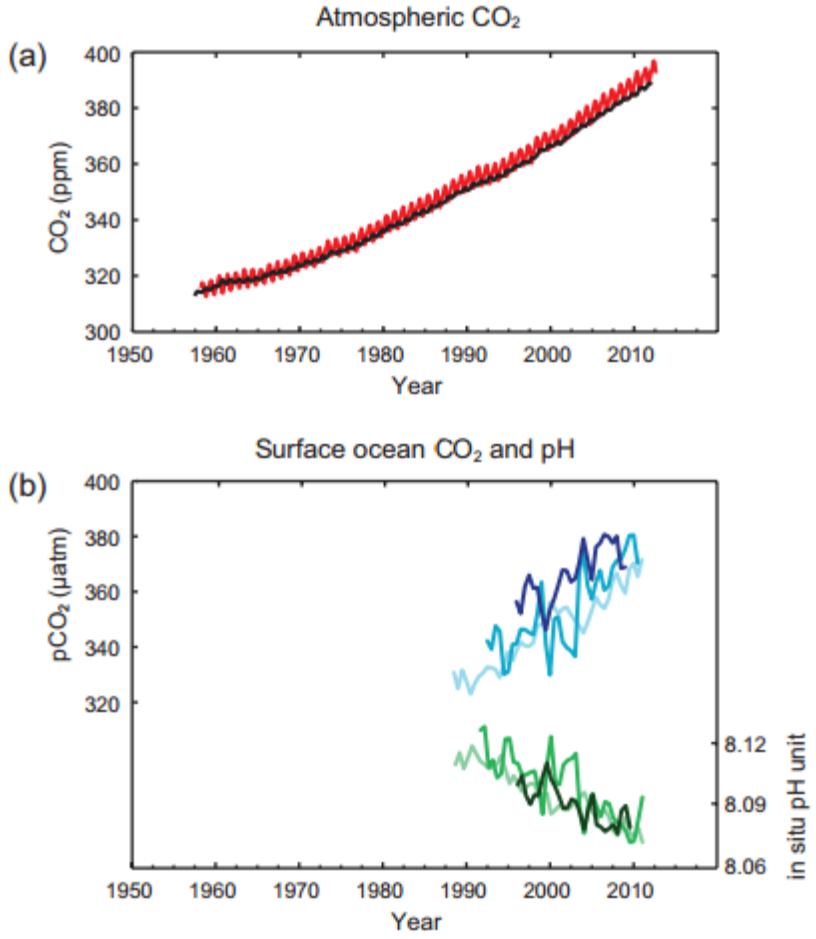

Figure 1.1. (a) Atmospheric pCO_2. Black line is measurements from the South Pole, and red is from the Mauna Loa Observatory Hawaii. (b) Surface ocean pH (green lines) and surface ocean pCO_2 (blue lines) at two Atlantic Ocean locations (dark lines- European Station for Time series in the Ocean (ESTOC, 29°10'N, 15°30'W), and pale lines Bermuda Atlantic Time Series (BATS, 31°40'N, 64°10'W)) and one Pacific location (medium lines Hawaii Ocean Time Series (HOTS, 22°45'N, 158°00'W)). Surface Ocean pCO_2 closely tracks the trend in atmospheric pCO_2, and pH shows the corresponding decrease to ocean pCO_2. Figure taken from IPCC 2013 Summary for Policy makers, SPM-04 (IPCC, 2013).

1.2 Carbonate System

Carbon dioxide in the atmosphere is constantly exchanging with the surface ocean, maintaining an overall global equilibrium (Takahashi et al., 2009). The exchange is controlled by the difference between atmospheric pCO_2 and the seawater pCO_2. The solubility of atmospheric pCO_2 in seawater can be understood through Henry's law, Equation 1.1.

Equation 1.1

$$[CO_{2(aq)}] = k_0^* \cdot pCO_2$$

where $[CO_{2(aq)}]$ is the concentration of dissolved CO_2 (mol kg^{-1}), pCO_2 is the partial pressure of CO_2 in a parcel of air (µatm), and k_0 is Henry's constant (solubility coefficient, sometimes

written as k_H). The star next to Henry's constant denotes the temperature, salinity and pressure dependence of the solubility coefficient, indicating the thermodynamic drivers of the equilibrium process. At lower temperatures, CO_2 is increasingly soluble and has a decreasing k_0. At high salinities, CO_2 is less soluble, through a process referred to as 'salting out', causing an increase in k_0.

Seawater pCO_2 is the partial pressure of CO_2 in theoretical air in equilibrium with the water sample of interest with a CO_2 concentration in mol kg^{-1}, while atmospheric pCO_2 is the partial pressure of CO_2 in the air. The concentration of CO_2 in seawater is directly proportional to the pCO_2. From here on, pCO_2 when used without further explanation refers to the seawater pCO_2, while 'atmospheric pCO_2' is explicitly stated.

Once in the water, the CO_2 behaves differently to other, inert atmospheric gases such as nitrogen and oxygen. CO_2 reacts to form carbonic acid, which rapidly dissociates to bicarbonate and carbonate ions. Carbonic acid (H_2CO_3) is present in such low concentrations (less than 1 % of dissolved inorganic carbon species) in seawater it can be considered as part of dissolved CO_2, and is included in the term $[CO_2]$ in Equation 1.3 and Equation 1.5. The formation of H_2CO_3 is negligible, so CO_2 is generally considered to form bicarbonate ions directly, Equation 1.2 (Zeebe and Wolf-Gladrow, 2005).

Equation 1.2

$$CO_{2(aq)} + H_2O \overset{k_1^*}{\rightleftharpoons} HCO_3^- + H^+ \overset{k_2^*}{\rightleftharpoons} CO_3^{2-} + H^+$$

Equation 1.3

$$k_1^* = \frac{[HCO_3^-][H^+]}{[CO_2]}$$

Equation 1.4

$$k_2^* = \frac{[CO_3^{2-}][H^+]}{[HCO_3^-]}$$

where Equation 1.3 and Equation 1.4 refer to the calculations of the rate constants (k_1* and k_2*) for the reactions indicated in Equation 1.2. Square brackets denote concentrations in mol kg^{-1} (moles per kilogram of seawater), and the star next to each rate constant again indicates dependence on temperature, salinity and pressure of the rate constant and therefore the equilibrium reactions themselves.

The distribution of the carbonate equilibria between the bicarbonate and carbonate ions is represented by the equilibrium constants (k_1 and k_2, Equation 1.3 and Equation 1.4 respectively). Bicarbonate ions are the most abundant species at surface seawater pH (~8.1), shown in Figure 1.2, making up ca. 90 % of the carbonate species, while carbonate ions are approximately 10 % and the combined dissolved CO_2 and H_2CO_3 are less than 1 %.

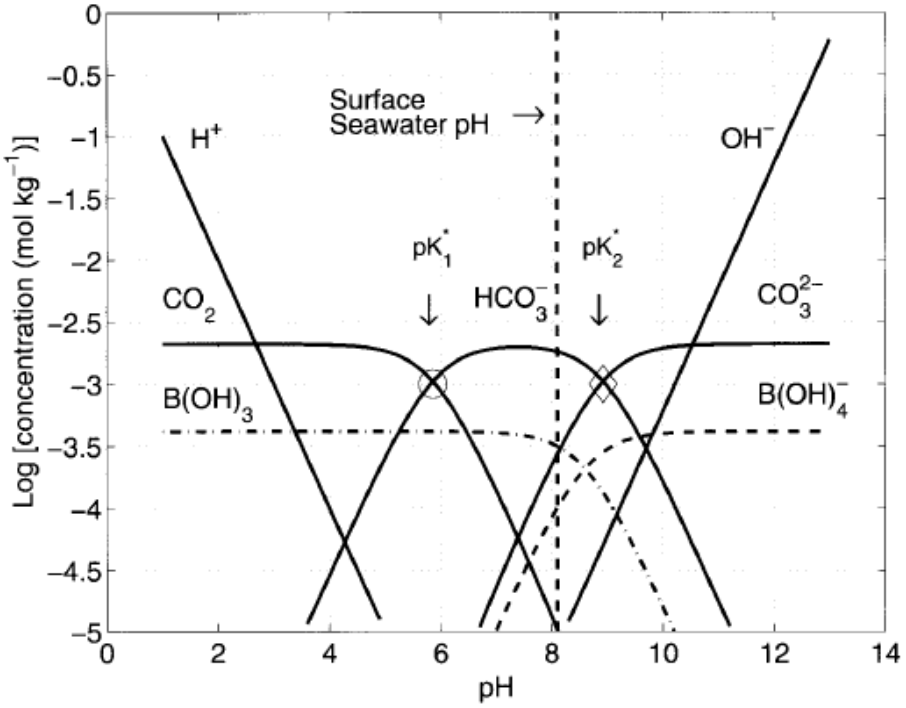

Figure 1.2 Equilibrium distribution of the carbon system in surface seawater conditions, where pK_1^* is equivalent to the negative logarithm of k_1^* from Equation 1.3, and the pK_2^* is equivalent to the negative logarithm of k_2^* from Equation 1.4. At surface seawater pH, the dominant species is bicarbonate (HCO_3^-), with small concentrations of carbonate (CO_3^{2-}) and CO_2. Note, the proportions of CO_2, HCO_3^- and CO_3^{2-} control pH. Figure is taken from Zeebe and Wolf-Gladrow (2005).

The sum of all the inorganic carbonate species present in water is denoted total dissolved inorganic carbon (DIC), shown in Equation 1.5 (Zeebe and Wolf-Gladrow, 2005). Other abbreviations commonly found in the literature include TC, C_T and TCO_2.

Equation 1.5. Dissolved inorganic carbon (DIC), from Zeebe and Wolf-Gladrow (2005)

$$\mathrm{DIC} \equiv \sum \mathrm{CO_2} = [\mathrm{CO_2}] + [\mathrm{HCO_3^-}] + [\mathrm{CO_3^{2-}}]$$

Where square brackets again denote concentrations in mol kg^{-1}, and $[CO_2]$ refers to the combined $CO_{2\,(aq)}$ and H_2CO_3.

The total alkalinity (TA) of seawater is defined as the "excess of proton acceptors over proton donors with respect to a certain zero level of protons" (Wolf-Gladrow et al., 2007) and can be

considered as the oceanic charge balance; the sum of the major conservative anions in seawater does not completely balance the sum of the major conservative cations (Dickson, 1981). This difference is made up through minor anions such as phosphoric acid, borate, and carbonate ions, explicitly written in Equation 1.6 (Wolf-Gladrow et al., 2007). Other abbreviations widely used for TA include Alk and A_T.

Equation 1.6 taken from Wolf-Gladrow et al. (2007)

$$\mathrm{TA} = [\mathrm{HCO_3^-}] + 2[\mathrm{CO_3^{2-}}] + [\mathrm{B(OH)_4^-}] + [\mathrm{OH^-}] + [\mathrm{HPO_4^{2-}}] + 2[\mathrm{PO_4^{3-}}] + [\mathrm{H_3SiO_4^-}] + [\mathrm{NH_3}] + [\mathrm{HS^-}] + \cdots - [\mathrm{H^+}] - [\mathrm{HSO_4^-}] - [\mathrm{HF}] - [\mathrm{H_3PO_4}] - [\mathrm{HNO_2}]$$

Where the ellipses stand for additional, as yet unidentified or poorly constrained acid-base pairs such as organic molecules (Kim et al., 2006, Muller and Bleie, 2008, Kim and Lee, 2009).

Both DIC and TA are conservative with respect to temperature, mixing and pressure. They can therefore useful in understanding the distribution of CO_2 in the ocean. The defining variables of the carbonate system are [HCO_3^-], [CO_3^{2-}], DIC, TA, pCO_2 and pH. The knowledge of any two of these variables (with temperature, salinity and nutrients) allows complete determination of the carbonate system (Zeebe and Wolf-Gladrow, 2005).

1.2.1 Ocean carbon distribution

The distribution of carbon through the ocean carbonate system is controlled by a series of mechanisms or "pumps" (Sarmiento and Gruber, 2006).

The physical pump, also termed the solubility pump, refers to the uptake of atmospheric CO_2 by the ocean and subsequent partition through the other species in the carbon species. It is the thermodynamically-driven control on the CO_2 solubility from the temperature, salinity and pressure dependent rate constants, k_0*, k_1*, and k_2* as discussed in section 1.2.

The other major control on the spatial and seasonal distribution of carbon in the ocean is biology. The biological pump can be broken down into the soft tissue pump and the carbonate pump. The soft-tissue pump begins with a photoautotroph's photosynthetic conversion of pCO_2 into organic matter. This locks away the carbon until the organism dies, as it sinks the particulate organic matter (POM), and particulate organic carbon (POC) is bacterially respired and DIC returned to the system. The formation of $CaCO_3$ as part of organism's shells is the start of the carbonate pump. This again locks away the DIC until the organism dies, and as it sinks, the $CaCO_3$ (particulate inorganic carbon, PIC) is remineralised and returned to the system as DIC. POM and POC have densities similar that of seawater, reducing the sinking rate, allowing them to be respired before reaching a significant depth. Export of POC (and POM) occurs either by organism migration, or ballasted with aggregates (Honjo et al., 2008).

The aggregate sinking particles are generally combinations of PIC and POC with silicate, PIC and dust comprising the majority of the mass allowing these to sink. There is much ongoing investigation into the "ballast effect" and its influence on the strength biological carbon pump (Sanders et al., 2010). The biological drawdown of CO_2 is strongest in the equatorial and sub-polar oceans (for example the sub-arctic North Atlantic and sub-arctic northwestern Pacific), the eastern equatorial Pacific, the upwelling area near Chile, and Antarctic coastal waters (Takahashi et al., 2002), due to the nutrient availability in these areas.

A combination of the physical and biological pumps controls carbon distribution in the ocean. For example, sequestration of CO_2 from the atmosphere occurs in the high latitude regions such as the Southern Ocean (Caldeira and Duffy, 2000, Blain et al., 2007), North Atlantic Ocean (Gruber et al., 2002) and the Arctic Ocean (Bates and Mathis, 2009) where there are low water temperatures and high biological productivity (Watson et al., 1991).

1.2.2 Sea-air fluxes

The calculation of sea-air fluxes allows us to determine regions of the ocean that are CO_2 sinks or sources of CO_2 to the atmosphere. The flux calculation is based on Fick's first law whereby the concentration gradient is linear and converted into partial pressure using Henry's equation (1.1) (Liss and Slater, 1974), commonly written as equation 1.7 (Wanninkhof et al., 2013).

Equation 1.7

$$F = \mathcal{K}(\Delta pCO_2)$$

Where ΔpCO_2 is the difference between atmospheric and seawater pCO_2. The direction of subtraction (i.e. air-sea or sea-air) will only change the final sign of the flux, and must be carefully stated. In this work, we treat ΔpCO_2 as sea pCO_2 –air pCO_2. $\mathcal{K}$ is the combination of the gas transfer coefficient and the solubility coefficient ($k \cdot k_0^*$).

The solubility of CO_2, is strongly dependent on temperature and salinity, described by the solubility coefficient (k_0), experimentally determined by equation 1.8, in mol L^{-1} atm^{-1} (Weiss, 1974).

Equation 1.8

$$\ln(k_0) = A_1 + A_2\left(\frac{100}{T}\right) + A_3 \cdot \ln\left(\frac{T}{100}\right) + S\left(B_1 + B_2\left(\frac{T}{100}\right) + B_3\left(\frac{T}{100}\right)^2\right)$$

Where the A's and B's denote constants, T is absolute temperature (K) and S is practical salinity.

The gas transfer coefficient is equivalent to the molecular diffusivity in water divided by the thickness of the concentration gradient, with units of velocity (cm hr^{-1}) - also referred to as the piston velocity, and gas transfer velocity. The gas transfer velocity for air-water was determined to be significantly larger than the gas transfer velocity for water-air so can be ignored in these estimations (Liss and Slater, 1974). There are several parameterisations of this coefficient based on its relationship with wind speed. Wanninkhof (2014) recently reviewed these parameterisations in detail.

Briefly, the gas transfer velocity can be estimated from the molecular diffusivity (D, m^2 s^{-1}) of CO_2, the kinematic viscosity of seawater (μ, m^2 s^{-1}) and the atmospheric wind speed at a height of 10 m (u_{10}, m s^{-2}). The Schmidt number is equivalent to μ/D leading to the following equation:

Equation 1.9

$$k = 0.251 \cdot (u_{10})^2 \cdot \left(\frac{Sc}{660}\right)^{-\frac{1}{2}}$$

The coefficient has units of (cm hr^{-1})(m s^{-1})^2, and was recently updated to 0.251 in Wanninkhof (2014) to account for improvements in wind speed and bomb ^{14}C estimates. The Schmidt number is strongly temperature-dependent and can be estimated from (Jähne et al., 1987):

$$Sc = 2116.8 + At + Bt^2 + Ct^3 + dt^4$$

Where A-d are constant coefficients, listed both in Jähne et al. (1987) and Wanninkhof (2014) and t is temperature in °C.

Previous parameterisations (Liss and Merlivat, 1986, Wanninkhof, 1992, Nightingale et al., 2000) determined different relationships with wind speed. Liss and Merlivat (1986) determined three linear relationships based on three categories of wind speed 0-3.6 m s^{-1}, 3.6 – 13 m s^{-1} and >13 m s^{-1}, however the linear nature underestimates k at high wind speeds. Wanninkhof (1992) produced two equations of the same form as equation 1.9, but determined for short term instantaneous winds and longer term (>1 year) averaged winds. The more recent update to this (Wanninkhof, 2014) is applicable to either wind speed range with uncertainty estimates of ± 20 % for global applications.

1.2.3 Determining the ocean carbonate system

Of the six key variables of the carbonate system (pH, $[CO_3^{2-}]$, $[HCO_3^-]$, DIC, TA, pCO_2), four are commonly measured -pH, pCO_2, DIC and TA. From these four, only two are required to calculate other original six parameters, alongside *in situ* temperature, salinity and nutrient metadata (Zeebe and Wolf-Gladrow, 2005, Dickson, 2010). The calculation of pH or pCO_2 from the DIC and TA combination provides the highest uncertainty (Millero, 2007), due to the current uncertainties in the determination of k_2 and uncertainties of the measurements themselves, Table 1.1.

Table 1.1 Estimated errors from calculated parameters of the carbonate system, when considering different input combinations. Taken from Millero (2007), where the assumed precision is the precision in measurement technique from the Millero paper for each variable, Spectro =spectrophotometric, Pot= potentiometric, Coul= coulometric, IR = Infrared spectrometric.

	pH	**TA ($\mu mol\ kg^{-1}$)**	**DIC ($\mu mol\ kg^{-1}$)**	**fCO_2 (μatm)**
Assumed precision	± 0.0004 Spectro	± 1 Pot	± 1 Coul	± 0.5 IR
pH-TA			±3.8	±2.1
pH-DIC		±2.7		±1.8
pH-fCO_2		±21	±18	
fCO_2-DIC	±0.0025	±3.4		
fCO_2-TA	±0.0026		±3.2	
TA-DIC	±0.0062			±5.7

Inconsistencies of up to 30 % in determining pCO_2 were observed when using different combinations of variables from overdetermined samples (Hoppe et al., 2012). There is currently no widely-accepted explanation for these errors, however potential reasons for this include uncertainties in the analytical measurements and equilibrium constants, and the presence of organic matter that is not taken into account during the determination of TA (Byrne, 2014). This organic matter contributes to organic alkalinity, where organic acid base pairs affect the buffering capacity of the waters without contributing towards DIC. The organic alkalinity has a greater effect in river and lake systems (Köhler et al., 2000) where more of the buffering capacity comes from the organic acid-base pairs.

The best pairing overall (as per Table 1.1) is DIC and pH, particularly for wide ranging use in both natural seawaters and ocean acidification experiments (Dickson, 2010) due to the lack of interference with other acid-base measurements. pCO_2 in combination with DIC and TA also gives lower errors than using either the two temperature-conservative variables (DIC and TA) or pH and pCO_2 together. To obtain the best accuracy it is advisable to measure

rather than calculate variables of interest, as opposed to relying on calculation, and where possible measure multiple parameters to verify results (Ribas-Ribas et al., 2014).

1.2.4 pH definitions

pH is related to the concentration of protons in a solution according to Equation 1.10.

Equation 1.10

$$\mathrm{pH} = -\log[\mathrm{H}^+]$$

The logarithmic term means a ten-fold increase in the concentration of hydrogen ions causes a change of one pH unit. This definition deals with the absolute concentration of H^+, which requires the addition of activity coefficients (γ). The activity coefficient accounts for the interaction of protons with other ions and solvents, which might indirectly increase or decrease the acidity of the solution through the change in chemical potential of the proton. The coefficient is dependent on temperature, salinity and pressure changes. The use of the activity of hydrogen ions (a_{H+}, unmeasurable effective concentrations in solution) provides a more accurate definition, and negates the need for activity coefficients. The National Institute for Standards and Technology (NIST) provides standard buffer solutions that have been given defined pH values according to $-\log a_{H+}$.

Equation 1.11

$$\mathrm{pH_{NIST}} \approx \mathrm{pH_a} = -\log \mathrm{a_{H^+}}$$

This relationship was determined at a lower ionic strength (~0.1) than seawater (~0.7). This creates problems when calibrating glass pH electrodes due to the changing liquid junction potentials when increasing ionic strength. In seawater, the activity of single hydrogen ions are not the only contributor to acidity – HSO_4^- and HF also contribute (Hansson, 1973, Dickson, 1984). This led to additional pH scales being used to determine the pH of seawater (Zeebe and Wolf-Gladrow, 2005).

Equation 1.12

$$\mathrm{pH_{SWS}} = -\log([\mathrm{H}^+]_\mathrm{F} + [\mathrm{HSO}_4^-] + [\mathrm{HF}]) = -\log[\mathrm{H}^+]_\mathrm{SWS}$$

The seawater scale (Equation 1.12) was introduced to include both HSO_4^- and HF, alongside the free hydrogen ions. The much larger concentrations of hydrogen sulphate compared to the hydrogen fluoride in seawater combined with the poor constraints on the HSO_4^- dissociation constant means that the total scale (Equation 1.13) is more widely used (Hansson, 1973).

Equation 1.13

$$pH_T = -\log([H^+]_F + [HSO_4^-]) = -\log[H^+]_T$$

Bates and Culberson made measurements in seawater diluted to varying salinities creating the free scale (Equation 1.14) where no dissociation constants are required, save for free protons (Bates and Culberson, 1977).

Equation 1.14

$$pH_F = -\log[H^+]_F$$

This scale appears the simplest and is the closest to the original relationship (Equation 1.10). However, the "free" hydrogen ions include hydrated molecules, requiring knowledge of the rate constants for these other forms of hydrogen also present in seawater.

It is important to note which scale the pH measurements are recorded in to ensure accurate comparisons between datasets. In this thesis, pH is referenced to the total scale due to the use of varying pH tris buffers characterised by (Pratt, 2014), and for ease of comparison between the pH certified reference material (CRM) provided by Dickson (Dickson, 1993). The total scale is used for both for measurements and calculation of pH, as indicated by either pH_T or pH_{tot}.

1.3 Measurement platforms

In order to improve our understanding of the effects from the increasing atmospheric pCO_2 and quantify changes on longer temporal and wider spatial scales, increasing numbers of measurements are desirable. Manual sampling on ships provides limited temporal coverage and has a high cost per data point (Johnson et al., 2009). To counteract this, novel platforms have been developed to allow deployment of sensors *in situ,* with increasing temporal and spatial resolution in the data and lower costs, and chemical sensor development is therefore focused towards such *in situ* deployments. These platforms can be split into two categories: mobile platforms such as Argo floats and gliders, and static platforms such as moorings and buoys.

1.4 Techniques to determine pH in seawater

The most widely recognised and accurate measurement of pH is made using the hydrogen gas electrode, also known as a Harned Cell. Solutions that have been analysed using this are generally considered primary standards (Buck et al., 2002). Due to impracticalities with field use of the Harned Cell, potentiometric measurements using glass electrodes calibrated with

standards (such as Dickson tris buffer pH CRMs) traceable to the Harned cell are commonly used. When analysing samples with higher salinities, the increased ionic strength causes impedance with the liquid junction potential and results in pH drift compared to measurement of the same pH at lower ionic strength (Kadis and Leito, 2010). Recently work has attempted to remove liquid junctions from classic electrodes in order to reduce this resistance and improve the quality of the measurement (Tishchenko et al., 2011).

Ion selective field effect transistors (ISFET) are a major advance in potentiometric pH measurements in seawater. They have been successfully tested and commercialised (Martz et al., 2010), allowing analysis of up to ca. 20 samples per minute (Satlantic, 2014) with a precision of 0.005 pH (Le Bris and Birot, 1997). The sensors require long conditioning periods (1.5 months) to minimise drift when deployed in situ in the ocean (Martz et al., 2010) and each sensor requires a full individual calibration at varying temperature and salinity prior to deployment (Bresnahan et al., 2014).

Spectrophotometric determination of pH is suited to seawater measurements, as indicator pK_a variation due to ionic strength changes can be accurately determined and corrected. Precision values for spectrophotometric range from 4 mpH (McElligott et al., 1998) to 0.7 mpH (Seidel et al., 2008, Aßmann et al., 2011) with several reports of precision near 1 mpH (Bellerby et al., 2002, Friis et al., 2004, Liu et al., 2006, Nakano et al., 2006, Rérolle et al., 2013). Miniaturisation of the instrumentation with reduced power requirements, allows for longer deployment periods (Rérolle et al., 2013). Spectrophotometric methods require sample filtration as bubbles and particulate matter can lead to poor quality measurements (DeGrandpre et al., 1995), with this being particularly important in miniaturised systems due to the smaller channel diameters. Immobilisation of the pH indicator into a solid porous matrix provides a promising alternative to wet spectrophotometry, discussed further in section 1.6 and Chapter 2.

1.5 Techniques to determine pCO_2 in seawater

Several techniques can be used to determine seawater pCO_2 *in situ*. These are reviewed in greater detail in Chapter 3, with the most well-known techniques briefly summarised here.

The original method for measurements of pCO_2 in seawater was developed by J.W. Severinghaus based on a pH electrode alongside a bicarbonate buffer solution (Severinghaus and Bradley, 1958). These have changed very little over time, with many of the same limitations as the electrodes measuring pH (Taillefert et al., 2000, Zosel et al., 2011) and are not widely used *in situ*.

There are several gas-based methods that require equilibration to convert the seawater dissolved CO_2 into gas phase CO_2. Gas chromatography is a well-established laboratory method to determine pCO_2. The pCO_2 is equilibrated into the gas phase, and subsequently reduced using a nickel/palladium catalyst to methane with subsequent analysis using a flame ionising detector (Goyet et al., 1991, Wanninkhof and Knox, 1996). This method has several advantages: a lack of interference from water vapour, small sample volumes, and a linear response over a large range of concentrations. However is not suitable for *in situ* development due to the use of the flame ionising detector and reference gases.

Non-dispersive infrared spectrometry is widely used to measure both the *in situ* atmospheric pCO_2 and seawater pCO_2 and this is demonstrated by the number of available commercial sensors listed by the International Ocean Carbon Coordination Project (IOCCP, (Martz, 2014)). The technique exploits the characteristic vibration of gaseous CO_2 upon absorption of infrared radiation (4.3 μm), and has been deployed *in situ* in a number of locations.

The spectrophotometric pH technique has also been adapted to measure seawater pCO_2. It is based on the colorimetric measurement of an indicator solution that changes colour in response to pH changes. The indicator solution is pumped into a gas permeable tube, where it equilibrates with seawater and dissolved CO_2, subsequently the solution absorption is measured at wavelengths that correspond to the absorbance frequencies of the acidic and conjugate base forms of the indicator and a reference wavelength that is independent (DeGrandpre et al., 1995, Lu et al., 2008). This method has been deployed *in situ* on moorings but more work is required before deployment on more dynamic platforms. Similar to pH sensors, immobilised sensor spots employed as an optode are a step towards a promising new technology with advantages from both the spectrophotometric method and the electrochemical methods (Hakonen and Hulth, 2008). This technique as applied to pCO_2 measurement is detailed more in section 1.6, and Chapters 3 and 4.

1.6 Immobilised sensor spots

These are briefly introduced here and discussed in more detail throughout Chapters 2 and 3.

Based on the recent success of oxygen optodes for oceanic measurements (Tengberg et al., 2006), there has been much interest in immobilising fluorescent molecules for use in analysing pH and pCO_2 in the ocean. The method immobilises analyte-sensitive fluorescent indicators in a permeable membrane. The sensitive compounds include 1-hydroxy-3,6,8-pyrenetrisulfonic acid (HPTS) (Oter et al., 2006, Zhu et al., 2006, Chu and Lo, 2008) and bromocresol purple (Nakano et al., 2006, Nakano and Yoshida, 2011). The compounds are immobilised into membrane matrices such as ethyl cellulose, hydrogels and sol-gels. Both the

membrane and the immobilisation technique influence the fluorescence response by altering the pK_a of indicators. Immobilisation within hydrophilic membrane such as cellulose results in smaller pK_a changes compared to more hydrophobic membranes such as polyurethane hydrogels (Boniello et al., 2012). Charged matrices can affect the sensitivity and pK_a of indicators. Potential crosslinking within the matrix can change the pore size altering the effectiveness of the spot (Tian et al., 2013), which is particularly important in distinguishing between ions and gas molecules.

There are several interrogation techniques: fluorescence intensity, fluorescent resonance energy transfer (FRET) (Neurauter et al., 1999) and the ratiometric dual lifetime referencing (DLR) (Burke et al., 2006). Fluorescence intensity measurements are highly variable, affected significantly by ambient light, solution turbidity and LED fluctuations (Klimant et al., 2001). To combat this variability, FRET and DLR both use a reference dye in addition to the pCO_2/pH sensitive dye. This provides a baseline to eliminate factors that will affect the fluorescence of both dyes such as LED fluctuations and background light.

With FRET analysis, the fluorescence is from a donor chromophore, for example the Ru(II) complex, and transfers energy to a pH dependant absorber (for example thymol blue) that has good absorption spectra overlap with the Ru(II) fluorescence. At increasing pCO_2 the pH dependant absorber becomes protonated and the overlap diminishes giving the Ru(II) a longer fluorescence lifetime. The lifetime can be measured through a change in the phase angle of the modulation frequency signal (Von Bültzingslöwen et al., 2003). The use of FRET allows the integration with existing dissolved oxygen sensor technology reducing the development costs (Neurauter et al., 1999). The sensor has rapid response times of 24 s for 99 % of the final value with tuneable sensitivity and limited drift after 2 months storage (<10 %). However, this method has lower signal to noise ratios and a susceptibility to measurement signal drift compared to the dual luminophore referencing techniques. FRET methods using ruthenium complexes also show a cross-sensitivity toward oxygen due to the use of a ruthenium compound as a luminescence donor (Von Bültzingslöwen et al., 2003).

The ratiometric dual lifetime referencing uses an analyte sensitive fluorophore with a short lifetime, immobilised alongside an analyte inert fluorophore with a long lifetime. These are excited by similar wavelengths and emit over a similar range (Schäferling and Duerkop, 2008). The ratio between the two can then be correlated to the analyte concentration. There are two methods for analysis, frequency and time based analysis. Frequency domain dual lifetime referencing (*f*-DLR) uses the phase angle shift caused by the ratio of analyte sensitive dye's and analyte insensitive dye's fluorescence intensities. The overall phase shift can be

directly related to the analyte concentration, if the modulation frequency of the excitation light is adjusted to match the analyte inert fluorophore (shown Figure 1.3a).

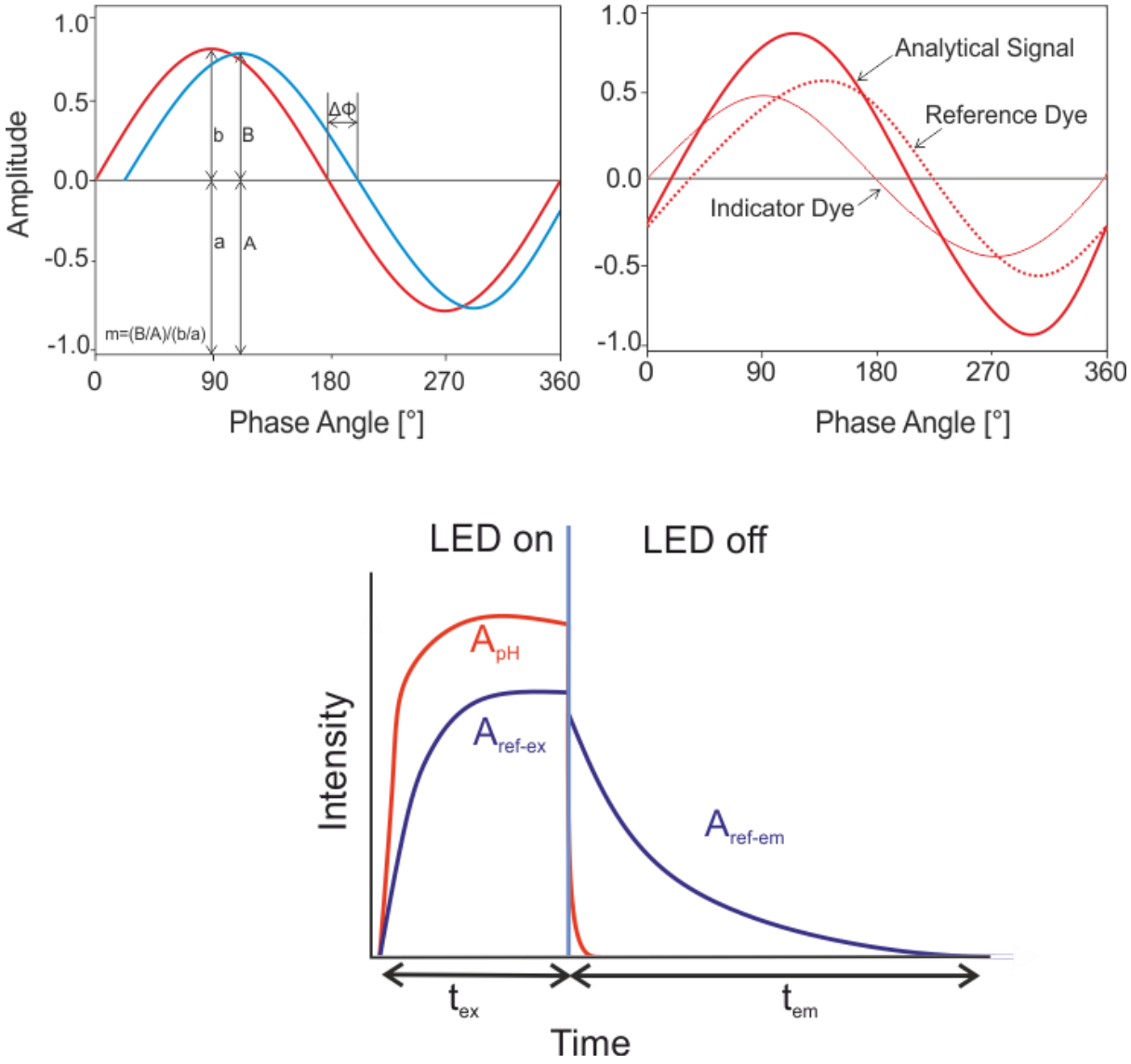

Figure 1.3 a) Graphical representation of the *f*-DLR signal broken down into it constituent parts in the right hand image. The left hand image shows the imagined shift with a theoretical pH change with *f*-DLR analysis, image reproduced from Klimant et al. (2001). b) Graphical representation of t-DLR signal with the two windows and the signal broken down into its constituent parts, adapted from Schröder et al. (2005).

Alternately, the time domain dual lifetime referencing (t-DLR) takes the intensity ratio at two "windows" in time. One – while the LED is on – is termed t_{ex}, and the other – while the LED is off – is termed t_{em}. The emission while the LED is on is dominated by the fluorescence from the analyte sensitive fluorophore (A_{pH}) with the short fluorescent lifetime, comparatively the emission while the LED is off is dominated by the fluorescence from the analyte insensitive fluorophore ($A_{ref\text{-}ex}$) with a longer fluorescence lifetime as shown in Figure 1.3b.

Both *f*-DLR and t-DLR show similar advantages compared to the intensity-only measurements. The choice to use t-DLR over *f*-DLR can be attributed to *f*-DLR's requirement

for expensive equipment, image amplifiers and the need to continuously excite the foil, prolonging the excitation time of the foil and causing a perceived enhancement of the spot bleaching rate (Liebsch et al., 2001).

The sensor spots used in this work require no external indicator solutions, are small in size (7mm diameter) and have low maintenance requirements. Light sensitivity needs to be taken into consideration when the sensor is used in the surface ocean; bleaching of the sensors by the ambient light and backscatter of light from other objects can cause false readouts. Biofouling and false readouts from other acidic gases (such as H_2S) is also a problem.

1.6.1 PreSens spots

Both pH and pCO_2 sensitive spots were obtained from PreSens (Germany). With the pCO_2 spots, CO_2 molecules diffuse across a gas-permeable membrane to an internal buffer solution, altering the pH, and causing the fluorescence of the pH sensitive indicator dye to change. With the spots for pH measurements, protons diffuse across a membrane (for example, made of ethyl cellulose) and cause decreased fluorescence of the pH sensitive indicator dye.

Both pCO_2 and pH Presens spots are designed for the use of DLR, and contain an immobilised pH-insensitive reference that fluoresces at similar wavelengths to the pH sensitive dye, but with a longer decay lifetime. The similarity in operation of the pCO_2 and pH spots allows the interchanging of the spots with the same electrical hardware. The sensor spots are both excited by blue light and emit in the red light range.

1.7 Overarching aims of the thesis

The main aim of this thesis was to determine the suitability of sensor spots for use in measuring carbonate system parameters in an open ocean environment. pH and pCO_2 are both key variables of the carbonate system and as such are important to monitor in order to evaluate the anthropogenic CO_2 impact on the oceans. This main aim was broken down into the following project aims:

1. Characterisation of the sensors response to pH/pCO_2 at varying temperatures and salinities in a lab setting
2. Evaluate the ability of the sensors to cope in a real world setting (e.g. dock deployment or underway system at sea)
3. Interpret sensor data from deployments to evaluate suitability for ocean measurements

To achieve this, commercial pH and pCO_2 spots were obtained and characterised for use under seawater conditions in controlled laboratory environments. The pH and pCO_2 spots were deployed as autonomous underway (surface ocean) analysis systems on cruises in the Southern Ocean and the North Atlantic respectively. These environments are strong sinks for atmospheric carbon dioxide (Takahashi et al., 2009). Therefore, they are important regions to assess the ability of the spot to determine impacts from anthropogenic CO_2 influx to the oceans.

1.8 Breakdown of Ph.D. Thesis

Chapter 2 describes the analytical approach applied to pH measurements using the PreSens pH sensor spots in association with SensOptics hardware. The applicability of the pH sensors to the marine system, specifically the surface open ocean, is assessed. The temperature and salinity dependences of the spot were determined and an algorithm generated to determine the pH from the fluorescent ratio. The measurement ranges, response time and lifetime estimations are discussed. Precision and accuracy were determined from the repeat measurement of tris buffered artificial seawater Certified Reference Material (CRM; obtained from A.G. Dickson, Scripps Institution of Oceanography, USA) and DIC and TA CRMs (also from A.G. Dickson). The pH sensor was tested on deployment in the challenging Southern Ocean environment in the austral summer, and results from that expedition are presented. This chapter also lays out the method development.

Chapter 3 critically reviews the current methods available for pCO_2 determination in the surface ocean. pCO_2 is a dynamic and constantly changing variable with complex interactions between the ocean and atmosphere. New platforms have been developed to extend the available data temporally and spatially. Therefore, it is not only the type of sensor that is used, but also the desired type of platform and location, that plays a factor in sensor development.

Chapter 4 describes the in-lab characterisation of pCO_2 sensor spots for use in seawater. The pCO_2 sensor system was subject to similar temperature and salinity tests as the pH system. A method developed by Sosna et al. (2007) for oxygen experiments was adapted and used to change the pCO_2. We also investigated the effects of chlorophyll, determined the lifetime of the sensors, and evaluated their response time and precision.

Chapter 5 contains the results of the initial pCO_2 sensor deployment for underway surface ocean measurements in the Labrador Sea, North Atlantic and Irminger Basins on the RAGNARoCC cruise in summer 2014. Underway DIC was collected using the Apollo LICOR DIC system, and discrete bottle samples. The success of the deployment allowed the optode pCO_2 to be used to calculate air-sea flux, and along with nutrients and metadata also collected on the cruise, to determine the regional controls on pCO_2 observed.

A summary of this work is contained in Chapter 6 with all the salient points, along with suggestions to improve the optode, and to further develop the pH and pCO_2 optode systems for *in situ* measurements.

Chapter 2:

Characterisation and deployment of an immobilised pH sensor spot towards surface ocean pH measurements

*This chapter has been published as Clarke, J. S., Achterberg, E. P., Rérolle, V. M. C., Bey, S. A. K., Floquet, C. F. A., Mowlem, M. C., (2015). "Characterisation and deployment of an immobilised pH sensor spot towards surface ocean pH measurements." Analytica Chimica Acta **897** : 69-80*

Abstract

The oceans are a major sink for anthropogenic atmospheric carbon dioxide, with subsequent changes to the marine carbonate system and wide ranging effects on flora and fauna. It is crucial to develop analytical systems that allow us to follow the increase in oceanic pCO_2 and corresponding reduction in pH. Miniaturised sensor systems using immobilised fluorescence spots are attractive for this purpose because of their simple design and low power requirements, and are being increasingly used for oceanic oxygen measurements.

A detailed method is presented to investigate the use of immobilised fluorescence spots to determine pH in ocean waters across the pH range 7.6 – 8.2. I characterised temperature (- 0.046 pH / °C from 5-25 °C) and salinity dependences (-0.01 pH /psu over 5-35), and performed a preliminary investigation into the influences of chlorophyll on the pH measurement. The apparent pK_a of the sensor spots was 6.93 at 20 °C. The sensor achieved a precision of 0.0074 pH units, and observed a drift of 0.06 pH units during a test deployment in the Southern Ocean as an underway surface ocean sensor, which was corrected for using certified reference materials. The temperature and salinity dependences were accounted for with the algorithm, $R = (0.00034 - 0.17 \cdot pH + 0.15 \cdot S^2 + 0.0067 \cdot T - 0.0084 \cdot S) \cdot 1.075$. A lab based drift experiment showed a drift of only 0.00014 R over 3 days (ca. 0.0004 pH, at 25 °C, salinity 35) was observed. This chapter provides a first step towards a pH optode system suitable for autonomous *in situ* deployment. The use of a short duration low power illumination (LED current 0.2 mA, 5 µs illumination time) improved the lifetime and precision of the spot. Further improvements are suggested including regular application of certified reference materials for drift correction, recalibration with a spectrophotometric pH system

and the development of novel fluorescence spots with improved performance and apparent pK_a values closer to the pH of surface ocean waters.

2.1 Introduction

During the period 2002-2011, global average atmospheric carbon dioxide (CO_2) concentrations increased by ~2.0 ppm per year; the highest rate of increase since monitoring began in the 1950s (Ciais et al., 2013). Atmospheric CO_2 concentrations are expected to continue to rise, with the ocean absorbing ca. 24 % of the anthropogenically emitted CO_2 (Canadell et al., 2007, Le Quéré et al., 2009). The currently increasing atmospheric CO_2 is causing a surface ocean pH decrease of ~0.002 pH units per year (Bindoff et al., 2007, Dore et al., 2009, Byrne et al., 2010), and a long-term pH decrease from pre-industrial times pH of 8.25 to today's pH of 8.10 (Jacobson, 2005). The decrease in surface ocean pH has been observed through long term time series stations in both the North Atlantic and North Pacific Oceans (Bindoff et al., 2007). Under the IPCC business-as-usual CO_2 emission scenario (IS92a) (IPCC, 2001), Caldeira and Wicket have predicted further surface ocean decreases of up to 0.8 pH units by the year 2300 (Caldeira and Wickett, 2005). To monitor ocean pH and determine potential effects, *in situ* pH sensors are desirable. In this chapter, I present an optode pH sensor based on fluorescent lifetime detection, for high resolution autonomous monitoring of surface ocean waters. The pH sensor was deployed as an autonomous shipboard system for surface water measurements in the Southern Ocean. This marks a first step towards an *in situ* sensor. The Southern Ocean is an important sink for CO_2 (Sabine et al., 2004) due to low water temperatures and deep water formation, and is likely to suffer detrimental ecosystem effects as a result of ocean acidification (Bednaršek et al., 2012). It is an ideal location to assess the suitability of pH spots for open ocean measurements. The research cruise was undertaken as part of the United Kingdom ocean acidification (UKOA) programme that investigated the effects of pCO_2 gradients in surface waters on biogeochemical processes, calcification and ecosystem functioning. Dissolved inorganic carbon (DIC) and total alkalinity (TA) samples were collected, providing multiple opportunities for sensor validation.

2.1.1 pH Sensors for Oceanic Waters

Optodes consist of a pH sensitive compound immobilised in a support matrix and are typically placed at the end of a waveguide or fibre optic cable, which provides a channel for the excitation and emission light to travel (Wolfbeis, 1997). pH optodes are not unique to environmental sensing; oxygen optodes have been characterised and deployed for water column measurements on CTD (conductivity, temperature & depth) rosette frames and Argo profiling floats (Körtzinger and Schimanski, 2004). However, pH optodes have so far only been deployed *in situ* in sediments yielding a precision of 0.0057 pH (Larsen et al., 2011). The motivation for characterisation of an optode pH sensor for deployment in open ocean waters

using fluorescent lifetime detection was based on the perceived advantages of this approach over other technologies, as recently reviewed in detail by Rérolle et al. (2012).

Other widely used techniques for pH measurements in seawater include potentiometric and spectrophotometric approaches (Rérolle et al., 2012). Potentiometric pH systems are highly portable, with a measurement rate of 1 Hz (Dickson, 1993), a precision of 0.003 pH units in the laboratory (Byrne et al., 1988) and a shipboard accuracy of 0.01 pH (Idronaut, 1995). However, prolonged measurements in high ionic strength solutions lead to inexact determination of the liquid junction and reference potentials of glass electrodes (Dickson, 1993) resulting in measurement drift (0.05 pH $month^{-1}$) (Idronaut, 1995) and significant systematic errors (Kadis and Leito, 2010). Electrode drift can be tackled by regular recalibration using spectrophotometric measurements (monthly for individual electrode reference potential, and daily for electrode intercept potentials) (Easley and Byrne, 2012) or calibration with seawater based buffers (Tan et al., 2010). With seawater solution calibrations, pH electrodes have been successfully deployed on research cruises in estuarine and coastal environments with a precision of ca. 0.004 pH (Borges and Frankignoulle, 1999, Frankignoulle and Borges, 2001), and *in situ* in highly dynamic hydrothermal vent environments with a precision of ± 0.06 pH (Le Bris et al., 2001).

Recently developed ion selective field effect transistors (ISFET) are a major advance in potentiometric pH measurements, and have been successfully tested in seawater (Martz et al., 2010) allowing analysis of up ca. 20 samples per minute (Satlantic, 2014) with a precision of 0.005 pH (Le Bris and Birot, 1997). The sensors are known to drift between 0.03-0.05 pH upon initial deployment, though the exact magnitude of the drift will depend on the ISFET materials and packaging (Khanna, 2013). Long conditioning periods (1.5 months) prior to calibration can reduce this drift (Martz et al., 2010) and each sensor requires a full individual calibration prior to deployment (Bresnahan et al., 2014).

Spectrophotometry is particularly well suited to seawater pH measurements and has been widely implemented *in situ* (Rérolle et al., 2012); recent examples include the SAMI-pH instrument (Martz et al., 2003) and a high precision microfluidic system (Rérolle et al., 2013). Spectrophotometric pH measurements have improved since their initial deployments in seawater, with precisions reported as low as 0.0007 pH (Seidel et al., 2008, Aßmann et al., 2011) and several systems achieving a precision of ca. 0.001 pH unit (Bellerby et al., 2002, Friis et al., 2004, Liu et al., 2006, Nakano et al., 2006, Wang et al., 2015). The use of wet chemistry spectrophotometry requires indicator storage, as well as valves and pumps to propel sample and indicator solutions through the system. The reagents may have limited lifetimes (~1 year) and specific storage requirements (e.g. exclusion of UV), while bubbles and particles introduced in the fluidic system can interfere with the quality of the pH

measurement (DeGrandpre et al., 1995). Despite these potential issues, spectrophotometric SAMI-pH has been successfully deployed *in situ* for more than 2 years (Harris et al., 2013) and a microfluidic system with measurement frequencies of 0.5 Hz (Liu et al., 2006) has been demonstrated.

2.1.2 Sensing Spots

The pH sensing spots contain a pH-sensitive fluorescent dye (indicator) immobilised in a gas impermeable membrane attached to a support matrix. The practical measurement range is within ±1.5 pH unit of the pK_a value of the indicator (Wencel et al., 2014), where the pK_a is the isoelectric point at which the concentration of the acidic form of the indicator equals the basic form. The sensor spot's indicator pK_a can be altered with different immobilisation approaches, such as the type of membrane and support matrix used (Wolfbeis, 1997). Immobilisation in more hydrophilic membranes such as cellulose results in smaller pK_a changes compared to more hydrophobic membranes such as polyurethane hydrogels (Boniello et al., 2012). Crosslinking within the membrane may change the pore size, while charges in the membrane can affect both the sensitivity and pK_a (Tian et al., 2013). The immobilisation technique also needs to be considered, ionic associations between the membrane and the pH indicator 8-hydroxypyrene-1,3,6-trisulfonic Acid (HPTS), for example, increases the apparent pK_a of HPTS, whereas the use of more covalent interactions lowers the apparent pK_a (Hakonen and Hulth, 2008). For applications in surface ocean samples, the pK_a of the immobilised indicator should be close to pH 7.7 to cover the oceanic pH range. The majority of immobilised pH indicators are based on fluorescein (Stich et al., 2010) and pyranine derivatives such as HPTS, due to their stability upon immobilisation, and a free pK_a of 7.3 which allows for measurements between pH 6 and 9 (Hakonen and Hulth, 2008).

The pH of the sample solution determines the fluorescence emission of the pH indicator; the protonated and deprotonated forms of the indicator dye fluoresce at different wavelengths. Methods based on the measurements of fluorescence intensity alone have several inherent problems, such as sensitivity to light source fluctuations, background light and solution turbidity (Szmacinski and Lakowicz, 1994, Klimant et al., 2001). The additional immobilisation of a pH-insensitive fluorescent reference dye alongside the indicator dye allows measurement by dual lifetime referencing (DLR) or intensity ratiometric methods, thereby reducing the problems from intensity only measurements (Klimant et al., 2001, Liebsch et al., 2001). Intensity ratiometric methods utilise the intensity ratio between the indicator and reference dye emissions, requiring that the reference dye has similar optical properties to the indicator (Wencel et al., 2014). For DLR, the reference dye must be pH-insensitive, have similar or

overlapping excitation and emission frequencies to the pH indicator dye, and a longer luminescent decay time.

There are two main DLR techniques: frequency-domain (*f*-DLR) and time-domain (t-DLR)(Liebsch et al., 2000). The *f*-DLR technique continuously illuminates the spot with amplitude modulated light, and uses the phase-angle between the excitation and the dye fluorescence (Bradrick and Churchich, 2000) to determine pH. The t-DLR technique takes a ratio of two "windows" of measurement (Klimant et al., 2001): one during the excitation of the spot with the light source and one during the fluorescence decay (Liebsch et al., 2001). The t-DLR is a well-established methodology (Klimant et al., 2001) which gives an instant visual response to pH changes. Both *f*-DLR and t-DLR techniques are not affected by light intensity fluctuations, optical alignment changes, and luminophore concentration (Klimant et al., 2001). In this thesis, I apply the t-DLR method to the sensing spots.

The pH sensor spots provide reproducible results (Hakonen and Hulth, 2010) without the need for moving components, fragile electrodes or wet chemical reagents. The sensing spots are small (7 mm diameter) and require limited maintenance. Accuracy is improved by regular measurements of a certified reference material (CRM) to determine potential drift (see Materials & Method Section). The spots can be used directly with no sub-sampling, and the technique has a comparable measurement time (5-200 s; see Table 1) to some *in situ* spectrophotometric methods (ca. 60 s(Aßmann et al., 2011)- 180 s (Seidel et al., 2008)). The response times are diffusion controlled, and are proportional to the thickness of the membranes used (1-20 µm). Recent work with immobilised pH sensors in marine sediments has demonstrated a less favourable precision (from repeated measurements of CRMs) compared with spectrophotometric measurements; average of 0.02 pH (Schröder et al., 2005) to 0.001 pH (Rérolle et al., 2013), respectively, discussed further below.

The indicator molecule bleaches in ambient light and thereby becomes less sensitive for pH measurements, eventually requiring replacement of the spot. If the reference dye and the pH indicator bleach at different rates then drift will be observed, affecting the accuracy of the pH measurements. Sensing spots have successfully been deployed in marine sediments (Table 1) (Schröder et al., 2005, Zhu et al., 2005, Hakonen and Hulth, 2010, Larsen et al., 2011). Due to light sensitivity, applications to surface seawaters are lacking despite the potential use of the indicators over the oceanic pH range. Advances in oxygen optode technologies (Körtzinger and Schimanski, 2004) indicate the suitability of optodes for surface water pH measurements. In this work, I have characterised the pH sensor-spot technique for seawater application and report here the first open ocean application. I first investigate temperature and salinity dependences of the pH optode, and then constrain the response time and provide an initial estimate for the longevity of the spot. I further discuss a test deployment in the Southern Ocean,

and subsequently evaluate our system with respect to potential applications in coastal or open ocean environments.

Table 2.1 Details of reported spot-based pH optodes where, DHFA= 2', 7'-dihexyl-5(6)-N-octadecyl-carboxamidofluorescein, DHFAE = 2', 7'-dihexyl-5(6)-N-octadecyl-carboxamidofluorescein ethyl ester, DHPDS = Disodium 6, 8-dihydroxy-1, 3-pyrenedisulfonate, HPTS = 8-hydroxypyrene-1, 3, 6-trisulfonic Acid, DSLR = digital single-lens reflex camera and CTAB = cetrimonium bromide. R=fluorescence ratio.

Reference	**pH Precision**	**Response Times**	**Specifics**	**Range (pH)**	**Deployment & *Longevity***
Schröder et al. (2005) & Stahl et al. (2006)	0.02	<200 s	DHFA and DHFAE with polyurethane hydrogel membrane and polyethylene terephthalate for support, and a charge-coupled device camera for analysis	7.2-9.2	4 days in marine sediments *1 week at 1 min measurement intervals*
Hakonen and Hulth (2008) & (2010)	0.0057	5 s	DHPDS with polyester spot and cellulose acetate membrane, analysis using a spectrofluorometer.	6-9	Marine sediments samples *160,000 measurements/month*
Zhu et al. (2005)	~0.2 (precision in the ratio between 2 measured wavelengths)	<2 min	HPTS covalently linked onto a poly(vinyl alcohol) membrane backed with a polyester sheet and analysis using a DSLR camera	5.5-8.6	2 months in marine sediments and overlying water *Not Specified*
Wencel et al. (2009)	0.02	12 s	HPTS ion-paired with cetrimonium bromide (CTAB) in a sol-gel membrane, analysis using a spectrofluorometer with xenon lamp	5-8	None specified *1h illumination decreases R by 1%*
Larsen et al. (2011)	0.02	60 s	HPTS and macrolex Yellow with polyurethane hydrogel membrane and polyester support, analysis using a DSLR	6-9	Marine sediments *>7200 measurements*
Current work	0.0074	50 s at 25 °C	PreSens spot using SensOptics electronics and a photomultiplier tube (PMT)	7-8.2 seawater	Surface seawater *>254 measurements over 3 days*

2.2 Materials & Methods

2.2.1 Reference Materials for pH measurements

A glass electrode (ROSS Ultra® combination pH electrode with epoxy body) with a benchtop pH meter (Thermo Scientific Orion 3*) was used for reference potentiometric pH determinations. The glass pH electrode used internal temperature compensation derived from the Nernst equation (Barron et al., (2006)). National Institute of Standards and Technology (NIST) pH buffers (pH 4, 6, 7, 10; Sigma-Aldrich) and Certified Reference Material (CRM) tris (2-Amino-2-hydroxymethyl-propane-1,3-diol) buffer in artificial seawater (Batch 10, pH_{tot} 8.0924, salinity 35, 25 °C) from Prof. A. Dickson at Scripps Institute of Oceanography (USA) were used to calibrate the pH glass electrode for low and high salinity measurements, respectively. A lab-on-a-chip microfluidic spectrophotometric pH sensor with thymol blue as indicator (final concentration 2 mmol L^{-1}, precision of 0.001 pH), was used as a reference for the higher salinity pH analyses. The thymol blue extinction coefficients were determined in the laboratory (e1 = 0.0072, e2 = 2.3277, e3 = 0.1794) and the indicator's dissociation constant (pK_2 = 8.5293) was taken from Zhang and Byrne (1996). The reader is referred to Rérolle et al. (2013) for further detail on the instrument and analytical approach. The temperature of the samples during laboratory measurements was controlled using a water bath (Fluke Hart Scientific 7012, ±0.0007 °C). All pH values reported in this chapter are on the total pH scale. Temperature of the solutions was checked prior to measurement with an ATP DT-612 dual input K-type thermometer (±0.1 °C).

2.2.2 pH Buffer Solutions

The pH optode sensor was characterised at different pH values, salinities and temperatures. Non-equimolar tris pH buffers were prepared in artificial seawater according to Pratt, (2014). For this purpose 1 mol kg^{-1} magnesium chloride ($MgCl_2$) and calcium chloride ($CaCl_2$) solutions were calibrated using gravimetric Mohr titrations (Vogel, 1989). Hydrochloric acid (HCl, 1 mol kg^{-1}) was calibrated using a gravimetric borax titration (Mellon and Morris, 1925). Other salts (sodium chloride, sodium sulfate, tris, and potassium chloride) were dried at 110 °C for 1 h prior to weighing. Deionised water (MilliQ, Millipore, >18.2 MΩ cm^{-1}) was used to prepare and dilute all solutions. All chemicals used in the preparation of artificial seawater were of analytical grade from Sigma-Aldrich. Stock buffer solutions (50 ml) over a pH range of 7.0 – 8.3 were made by combining tris salt (0.08 mol $kg(H_2O)^{-1}$), hydrochloric acid and small amounts of sodium chloride with deionised water. The pH was altered by adjusting the ratio of acidic to basic tris (HCl to tris salt), keeping the concentration of tris constant (0.08 mol $kg(H_2O)^{-1}$) and varying the HCl concentration. The small amount of sodium chloride in

the stock buffer was varied to account for the changing ionic strength contribution from the HCl. These 50 ml buffer solutions were then made up to the desired salinity with 25 ml of stock artificial seawater, in turn made up from sodium chloride, sodium sulfate, magnesium chloride, calcium chloride and potassium chloride.

To study the temperature dependence of the sensor over the temperature range of 5-25 °C, an array of 8 tris buffers at pH ranging from 7 to 8.3 was prepared at a fixed ionic strength of 0.7 M. The pK_a of tris has a strong temperature dependence (0.03 pH $°C^{-1}$) (Sigma-Aldrich). The pH range of the buffer was therefore selected to obtain the desired pH range of 7.6 – 8.3 over the temperature range of the experiment.

To study the salinity dependence of the optodes, an array of 7 tris buffers with pH values ranging from 7.8- 8.2 with salinities of 5, 25 and 35 were prepared, following the method of Pratt, (2014). 200 mL batches of lower salinity (5 and 25) artificial stock seawater without HCl and tris were prepared by dilution of concentrated artificial seawater (142 ml and 16 ml of the salinity 35 seawater made up to 200 ml in deionised water). The stock buffer solutions were made for salinity 35 seawater regardless of the final salinity desired for the buffer solution. The 25 ml of stock seawater were added to the buffer solutions to make up the analysis solutions. The ratio between the salts was kept constant, and only the ratio of salt to water was varied to provide the different salinities.

2.2.3 pH optode hardware

A 5 mm diameter blue light emitting LED (470 nm, Farnell) with excitation filters (SemRock single bandpass filter 475 nm and SemRock short pass edge filter 532 nm) was used at low intensity (0.2 mA, 0.72 mWatts) to excite the reference and indicator dyes within the immobilised sensor spot for periods of 5 µs, thus minimizing bleaching. The blue excitation light was reflected off a dichroic beamsplitter (SemRock single edge BrightLine, 560 nm) through a fibre optic cable (600 µm diameter multimode optical fibres, Thorlabs, 3.8 mm diameter tubing, 1 m length) to the pH sensitive spot. The fluorescence signal of the excited fluorophores subsequently decayed, with the emission of red light (630 nm). The red light passed through the dichroic beam splitter, and three emission filters (SemRock single bandpass filter 609 nm, SemRock short pass edge filter 785 nm and SemRock long-pass edge filter 568 nm) before entering the detector. With the low level of light involved, a photon multiplier tube (PMT; Hamamatsu) was used. The detection system used a field-programmable gate array (Xilinx Spartan-3 XC3S400-5PQ208C FPGA) to control the PMT and LED.

Custom-made electronics (Sensoptics Ltd[1], SGS 42000) were used with dedicated software (Sensoptics Photon Counter V1.2) to record the fluorescence decay curve. A diagram of the hardware setup is shown in Figure 2.1.

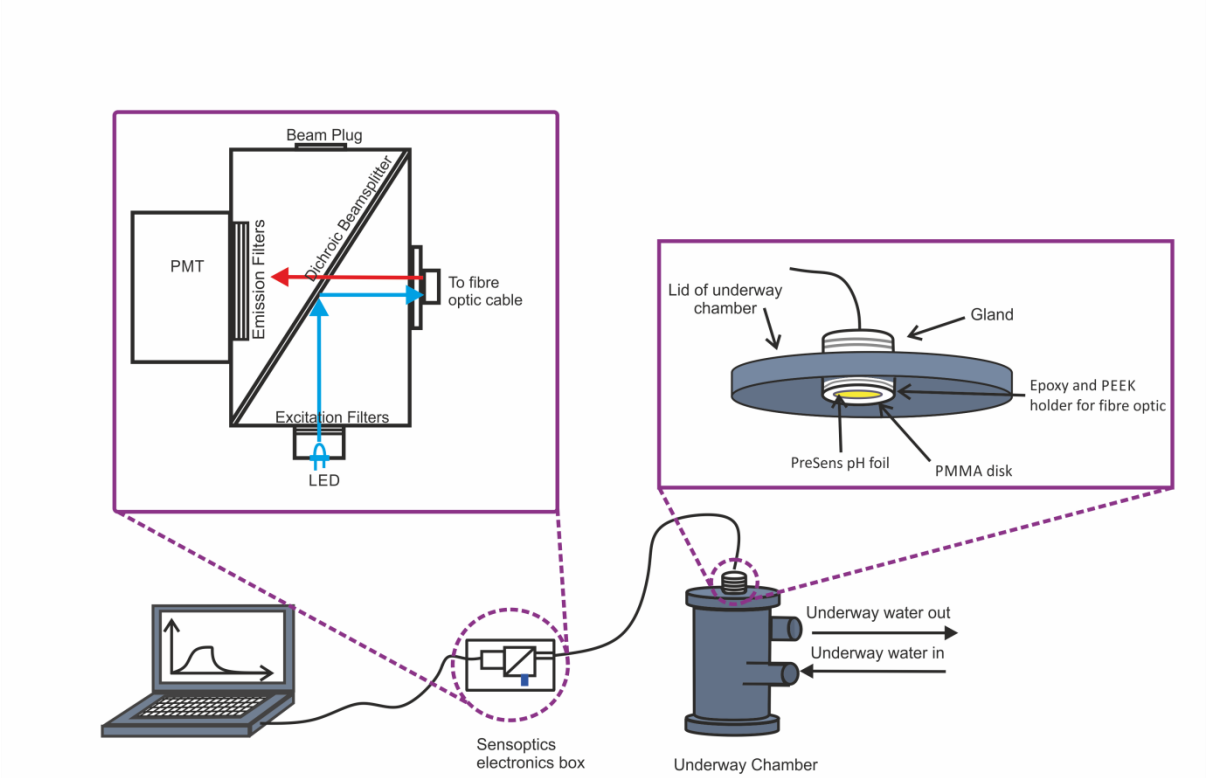

Figure 2.1 Schematic of the sensor for use as a shipboard autonomous underway system

The sensor spot (PreSens, non-invasive pH spot, SP-HP5-D7) was glued to a clear poly (methyl methacrylate) (PMMA) disc using silicone rubber glue (RS Silicone rubber glue, 692-542). Tests showed a negligible autofluorescence effect from the PMMA and glue. The set-up was left to dry for 2-3 days in the dark before being fastened using epoxy glue (Intertronic, OPT500149) to a polyether ether ketone (PEEK) head attached to the fibre optic cable (600 µm diameter multimode optical fibre, Thorlabs, 3.8 mm diameter tubing, 1 m length). The fibre optic cable was wrapped using a rubber coating to minimise light loss and ambient light penetration, and connected directly to the PMT at the distal fibre end. The PEEK head with sensor attached was stored in artificial seawater (at the specific salinity under investigation) to soak for at least half a day prior to measurements, as recommended by Stahl and co-workers (Stahl et al., 2006). Preconditioning allowed the sensor to adjust to the salinity/ionic strength of the measurement solution, and prevented leaching of indicator and reference dyes during measurements which would result in signal reduction (Stahl et al., 2006). This also allows any chemicals from the glues and epoxy to leach prior to measurement and characterisation. To minimise photo bleaching of the indicators by ambient

light, the sensor was covered with thick, dark, 'blackout' material and the laboratory work was performed in a dark room. Field measurements were undertaken with the pH optode positioned in a custom-made dark chamber, Figure 2.1.

2.2.4 Analytical protocol for pH measurements

pH indicators are weak acids and bases and hence have a capacity to respond to changes in solution pH through proton exchange. In high pH solutions, the indicator donates protons and takes its basic form, and in low pH solutions, the indicator accepts protons and takes its acidic form. The different forms of the indicator fluoresce differently allowing the pH of the solution to be determined.

To produce a single pH data point, the light source (blue light emitting diode (LED)) was pulsed using a square wave mode, with the LED on for 5 µs (t_{ex}) and the LED off for 20.5 µs (t_{em}). The LED light excited the pH indicator causing the dye molecules to fluoresce. When the LED was off the fluorescence gradually decayed. The LED pulse was recorded in 100 ns bins for 20.5 µs. This was repeated 19608 times, and averaged to give a fluorescent decay profile every 0.5 s. Higher precision and an improved signal to noise ratio were achieved by recording each sample for 200 s and integration of the profiles at 10 s intervals.

With the LED on, the emission (t_{ex}) is a combination of fluorescence from the pH sensitive (A_{pH}) and reference fluorophores ($A_{ref\text{-}ex}$), shown in Figure 2 with blue and red lines respectively. The variation in fluorescence recorded in the first 5 µs is from the indicator dye, and is related to the pH of the solution. It is assumed that the integration of the fluorescence intensity when the LED is off, (t_{em}) is entirely derived from the decay of the pH-insensitive reference dye emission ($A_{ref\text{-}em}$) due to the shorter decay lifetime of the pH sensitive fluorophore. The intensity of the first 5 µs of the profile (excitation period where the LED is on) is summed for each profile and referred to as t_{ex}. The intensity of the last 20.5 µs (emission period when the LED is off) was summed and is referred to as t_{em}. The ratio of t_{ex} over t_{em} (R, equation 2.1) is converted to pH, equation 2.2, which includes terms (a-g) for temperature and salinity dependence (see section 2.3.6).

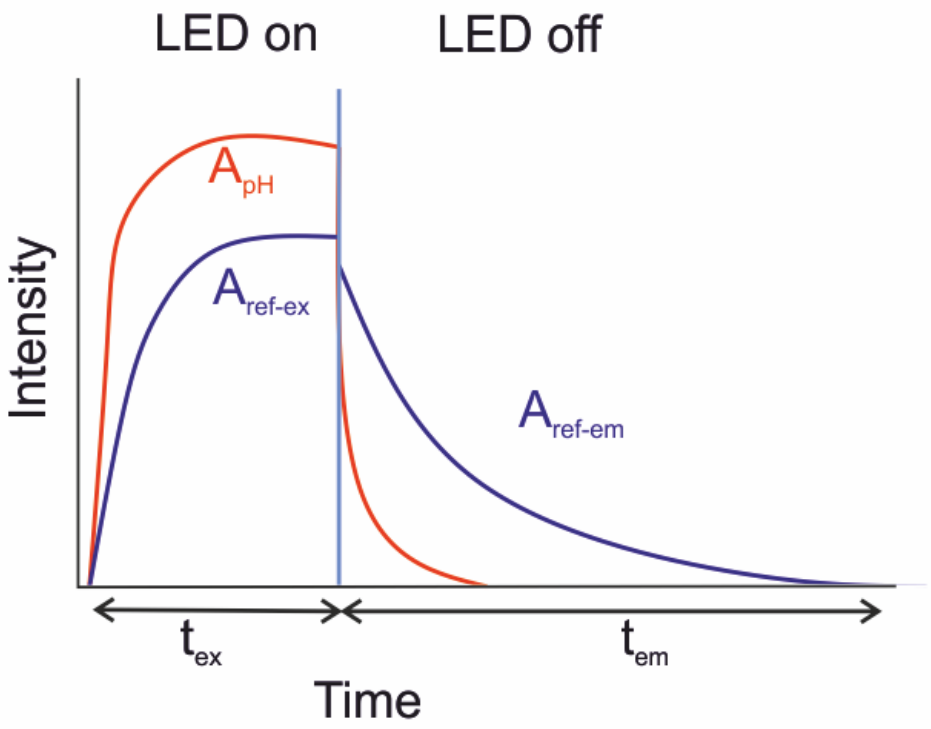

Figure 2.2 Fluorescence intensity change with time as a result of switching on and off LED light source. Signal is used to obtain the time domain-Dual Lifetime Referencing ratio (R) from the integration of the emission intensity over two windows: t_{ex}/t_{em}. The LED on emission (t_{ex}) can be broken down into the emission of the excited pH sensitive dye (A_{pH}, red line) and the excited pH insensitive dye ($A_{ref\text{-}ex}$, purple line). The LED off emission (t_{em}) is assumed to consist solely of the pH insensitive dye ($A_{ref\text{-}em}$).The reference fluorescence ($A_{ref\text{-}ex}$ and $A_{ref\text{-}em}$) has a long lifetime and is independent of pH, while the fluorescent intensity of the pH sensitive dye varies with pH and has a short lifetime (A_{pH}). Curve adapted from Schröder et al. (2005).

Equation 2.1

$$R = \frac{t_{ex}}{t_{em}} = \frac{A_{pH} + A_{ref-ex}}{A_{ref-em}}$$

Equation 2.2

$$R = (a + (b \cdot pH) + (c \cdot S^2) + (e \cdot T) - (f \cdot S)) \cdot g$$

The apparent pK_a (here onwards denoted as pK_a') of the indicator, is the pK_a where concentrations are used without the relevant activity coefficients to correct for the non-ideality of real solutions. The apparent pK_a therefore displays not only temperature dependence, but also dependence on factors that affect the activity coefficients, such as ionic strength (Valeur, 2002). Without detailed knowledge of the indicator, the relevant activity coefficients could not be used when determining the pK_a and therefore pK_a' was used in this study.

To determine the pK_a' of the pH indicator, and therefore the measurement range of the sensor, the optode was immersed in tris / 2-aminopyridine buffer solutions with a salinity of 5 prepared according to section 2.2.2, with pH values ranging from pH 9 to 5. The pK_a' was

determined using equations 2.3 (Derinkuyu et al., 2007) and 2.4 (Goncalves et al., 2008), according to the method of Salgado and Vargas-Hernández (2014) (see Figure 2.3). The term A in Figure 2.3 is the fluorescence intensity caused by a specific solution pH, A_{Basic} is the maximum fluorescence output at pH 9, corresponding to the conjugate base form of the indicator (A^-), and A_{Acidic} is the minimum fluorescence output at pH 5, corresponding to the acidic form (HA). The total indicator concentration at basic pH and maximum fluorescence is proportional to (A_{Basic} - A_{Acidic}). The concentration of the basic form of the indicator [A^-] at any pH is proportional to (A - A_{Acidic}). The concentration of acid form [HA] at any pH is proportional to (A_{Basic} - A_{Acidic}) – (A - A_{Acidic}) = (A_{Basic} - A). The ratio of the abundance of acidic and basic forms of the indicator is equal to one when pK_a' = pH as indicated by equation 2.4 (Henderson-Hasselbalch equation). The pKa' of the indicator can be obtained through linear regression of –log (A_{Basic} - A)/ (A - A_{Acidic}) against the pH of each solution, with the y-intercept divided by the gradient yielding pKa'.

Equation 2.3

$$\left[\mathrm{HA}\right]/_{\left[\mathrm{A}^-\right]} = \left(\mathrm{A_{Basic}} - \mathrm{A}\right)/_{\left(\mathrm{A} - \mathrm{A_{Acidic}}\right)}$$

Equation 2.4

$$\mathrm{pH} = \mathrm{pK_a} + \log\left(\left[\mathrm{A}^-\right]/_{\left[\mathrm{HA}\right]}\right)$$

To investigate the effects of temperature variations on pH measurement, the set of tris pH buffers (as in section 2.2.2) at salinity 35 was equilibrated in the water bath for a period of 15 min followed by pH measurements using both the reference glass electrode (as detailed in section 2.2.1) and the sensing spot. The buffers remained in the water bath during the measurements. The temperatures used for the calibration procedure were 5, 10, 15 and 25 °C. Temperatures of the samples were verified with an ATP DT-612 thermometer (± 0.1 °C). Each sample was measured three times and the results averaged (see Figure 2.4). If the pH as recorded by the reference electrode over the three repeats deviated more than 0.003 pH units, the samples were not averaged and the samples outside the deviation limit (0.003 pH) were treated as separate samples. This deviation limit (±0.003 pH) is equivalent to the temperature induced pH change in the tris buffer from the uncertainty in the thermometer measurement (± 0.1 °C).

To investigate the effects of salinity on the pH spot, the set of buffer solutions prepared at different salinities (as in section 2.2.2) were equilibrated in the water bath at 25 °C for a period of 15 min followed by pH measurements using both the reference glass electrode (as detailed in section 2.2.1) and the sensing spot. Each sample was measured three times and averaged (see Figure 2.5).

Samples of salinity 35 were also measured with the spectrophotometric pH system (section 2.2.1). The temperature was maintained at 25 °C, with the samples incubated for 15 min prior to measurement.

To study the response time of the sensor, repeat alternating measurements were made of two tris buffered seawater solutions (salinity 35) with pH values of 7.2 and 8.5 at 25 °C. These pH values are at the limits of the intended measurement range. The measurements were recorded for a period of 200 s before the optode was rinsed with deionised water and transferred into the next solution; this process was repeated 25 times. The time required for the optode to reach 97% of its final stable R (t_{97}) from first being placed in the solution is quoted as the response time, similar to the method of Tengberg and co-workers (Tengberg et al., 2006). Precision of the pH optode measurements was determined from analysis of the pH CRM tris buffer and a CRM for Total Alkalinity (TA)/Dissolved Inorganic Carbon (DIC) (Prof. A. Dickson, Scripps) at 25 °C (Dickson et al., 2007).

In order to determine the lifetime of the spot, a new spot (glued to PMMA disc and left to precondition for 2 days prior to use) was attached to the optode. It was then illuminated continuously for one hour with the LED at 0.72 mWatt (0.2 mA, normal excitation level). A 200 s measurement was taken before and after the continuous illumination to assess the change in the response. This was performed in a waterbath at 25 °C, in artificial (salinity 35) seawater. The sample was not changed between measurements and continuous illumination. The continuous excitation of the spot for one hour amounted to 720 x 10^6 LED cycles. In case of a typical pH measurement, the spot is only excited for one fifth of the total measurement and the hour-long continuous illumination was hence equivalent to 7200 decay profiles, 367 measurements of 50 s (response time) or 92 measurements assuming a 200 s measurement time.

An additional test was performed with the optode recording 200s measurements with the short illuminations. The spot was set to run for 3 days in buffered artificial seawater in a sealed container to maintain constant pH at 8.1. The spot response was recorded for 200 s every 15 min, for 254 measurements.

An investigation into the effect of chlorophyll-a on measured R was undertaken using *Emiliania huxleyi* (obtained from the Roscoff culture collection (RCC), strain number RCC1228). The *E. huxleyi* was cultured at 16 °C, under 100 µE light and diluted to specific chlorophyll-a concentrations (0.13, 0.68, 1.02, 2.05, 3.42 and 6.84 µg L^{-1}) with salinity 35 seawater. The pH of the seawater was measured with the glass electrode prior to measurement with the optode. Measurement of the solutions was performed in the dark, and at 25°C in a water bath for both the electrode and the optode. The pH was not constant during

the characterisation and the effect on R was removed by normalising the ratio (R) to a pH of 8.09 using the following equation,

$$R_n = \frac{R \cdot 8.09}{pH_{soln}}$$

where pH_{soln} is the pH of the solutions determined by electrode, and R is the measured ratio and R_n is the normalised ratio.

2.2.5 Cruise Deployment Details

The sensor was deployed aboard the R.R.S. *James Clark Ross* in the Southern Ocean in the period January-February 2013 (cruise JR274) as part of the UKOA Programme (http://www.surfaceoa.org.uk). Over the period January 22 to 26, 2013, pH measurements were undertaken along a diagonal transect north of South Georgia (54-49 °S, 38-40 °W). The pH sensor was placed in the ship's main laboratory connected to the continuous underway seawater supply, which had an intake at ca. 7 m depth, and measurements were conducted without filtration. Temperature and salinity measurements in the underway seawater supply were conducted using a thermosalinograph (SeaBird Electronics, Inc, SBE 45 thermosalinograph fluorometer) fitted in the preparation laboratory. Samples for DIC and TA were collected at hourly intervals along this transect. Measurements of pH_{tot} from the DIC/TA CRMs were undertaken at the halfway of each spot deployment on the cruise; two spots were used across the cruise. The spot was changed on 23/01/13.

pH was calculated from certified values of DIC and TA using CO_2SYS in Matlab v2.1 (Pierrot et al., 2006) with carbon dissociation constants from Roy et al. (1993), sulphate dissociation constants from Dickson (1990) and borate dissociation constants from Lee et al. (2010). The calculated pH from the DIC and TA CRM measurements was compared to the sensor-measured pH and any drift from the certified value was corrected using the ratio between the measured and the calculated value. This calculation has an estimated error of ± 0.0062, which is comparable to the current precision of the pH optode.

2.3 Results and Discussion

2.3.1 pH Sensor Spot Characterisation

To determine the pK_a' of the pH indicator, the optode was immersed in buffer solutions ranging from pH 9 to pH 5. This produced a sigmoidal-shaped fluorescent ratio (R) response (Figure 2.3) from the varying fluorescence as the immobilised indicator transitioned from the basic form to the acidic form. The signal flattened at the acidic and basic ends of the sigmoid due to the fulfilment of the proton donation and acceptance capacity of the molecules.

The value of R increased with increasing pH, indicating that the basic form of the indicator fluoresced more intensely compared with the acidic form. The most sensitive region for pH observations is where there is the highest change in R per change in pH. This occurs in middle of the sigmoidal shaped fit and demonstrates the viability of the sensor for seawater measurements (average surface ocean pH range ~7.9 - 8.2) (Jacobson, 2005). A sigmoidal shaped response upon pH variations has also been reported for other pH optode systems with immobilised indicators (Liebsch et al., 2000, Hulth et al., 2002, Schröder et al., 2005, Goncalves et al., 2008, Capel-Cuevas et al., 2010).

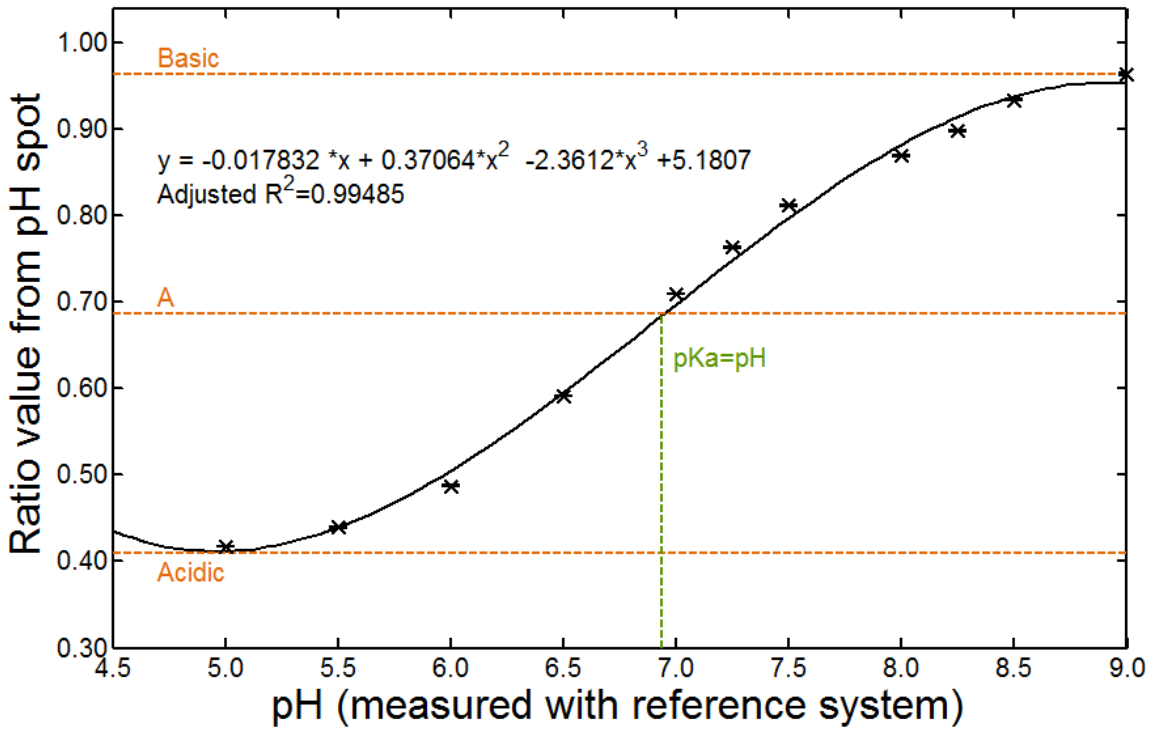

Figure 2.3 Sigmoidal shaped fluorescence ratio response from measurements of salinity 5 buffer (tris and 2-aminopyridine) solutions. pH meausured with a glass pH electrode. The horizontal orange dotted lines relate to the values in equation 2, and the vertical dotted green line is the equivalence point where pH=pKa'.

The obtained pK_a' value was 6.93 at 20 °C, as determined using the approach detailed in section 2.2.4, and denoted by the green dotted line in Figure 2.3. Immobilisation of the fluorescent compound in the sensor spot caused the pK_a' to be lower than pK_a' of the free-form of HPTS (7.3) (Hulth et al., 2002), and similar to the immobilised values reported by Hakonen and Hulth (2008). This pK_a' is lower than the pH of seawater, but the measurement range is considered to be between ± 1.5 pH units of pK_a', and hence covers the typical surface ocean pH range. Nevertheless, precision and accuracy may deteriorate at the edges of this range, i.e. near pH ca. 5.4 and 8.4. Temperature and salinity effects on the pK_a' of free (non-immobilised) pH indicator have been evaluated by other workers (Stumm and Morgan, 1996, Atkins and de Paula, 2006) and pH calibrations with immobilised sensors have been reported, although none specifically for open ocean use. This study's novel application of the optode and immobilised sensor requires characterisation at temperatures and salinities relevant to these environments.

2.3.2 Temperature Dependence

The temperature of artificial seawater with tris pH buffer was varied between 5 °C and 25 °C in order to quantify the temperature effect on the fluorescent indicator response. An increase in R was observed when comparing solutions with the same pH analysed at increasing temperatures (Figure 2.4). The overall temperature dependence was determined from the gradient of the linear regression, -0.046 pH $°C^{-1}$ over the temperature range of 5-25 °C.

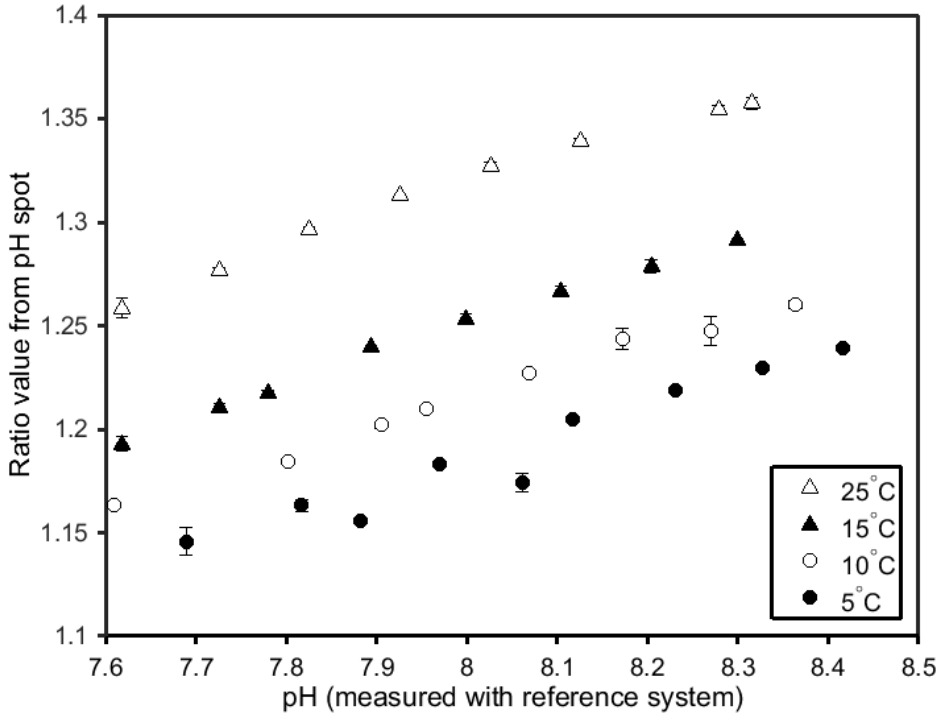

Figure 2.4 Response of the pH spot to temperature variations. Samples of tris buffered artificial seawater were analysed at temperatures between 5 °C and 25 °C. Reference pH was determined using a glass pH electrode calibrated with tris buffered CRM. Where error bars cannot be seen, they are smaller than the size of the marker.

This increase in R with temperature can be attributed to a decreased quantum yield at higher temperatures for both fluorophores from increased internal and external conversions of the fluorescence energy in addition to the temperature influence on the pK_a' of the indicator (Schröder et al., 2005). The decreased quantum yield has a minor effect on the pH sensitive fluorophore due to the short decay time but due to the longer lifetime of the pH insensitive dye, a larger effect is seen when integrating the t_{ex} time window.

The observed temperature dependence of the pH spot is similar to that reported for an immobilised sensor spot by Schröder et al. (2005), but smaller than reported by Kirkbright et al. (1984). The temperature dependence requires the accurate recording of temperature and a correction of the final pH readings. Hakonen et al. (2013) calibrated at two temperatures 25 °C and 15 °C, and extrapolated with a linear correlation to extend the system for use at lower temperatures, and found an error in pH of 0.01 pH units as a result of sharp temperature gradients. Schröder et al. (2005) found pH errors of ca. 0.03 pH $°C^{-1}$, and did not correct for temperature variations smaller than 5 °C. An alternative approach to avoid the complications of temperature corrections is to analyse pH in samples at a constant temperature (Zhu et al., 2005, Wencel et al., 2009, Larsen et al., 2011). With the ultimate aim to deploy our pH optodes *in situ*, the latter two approaches (measure at a constant temperature and apply no correction for deviations less than 5 °C) were deemed unsuitable. The temperature was included in the algorithm to convert R to *in situ* pH, with measurements

over a wider range of temperatures compared to Hakonen et al. (2013) to better characterise the dependence, with the ultimate aim to correct for temperature-induced variations (section 2.3.6).

2.3.3 Salinity Dependence

Solutions of artificial seawater (S=35) with tris pH buffer were diluted to salinities (5 and 25, see section 2.2.2) and analysed at a constant temperature of 25 °C (Figure 2.5). There was a significant difference between salinity 5 and both salinities 25 and 35 (student t-test t=-2.765 *n*=11, *two-tailed p*=0.0184 and t=12.875, *n*=12, *two-tailed p*=2.2x10^{-8} respectively). The value of R increased with salinity with an overall dependence of -0.01 pH psu^{-1}, similar to the dependence reported by Schröder et al. (2005) and pH-salinity error of 0.008 pH reported by Hakonen et al. (2013).

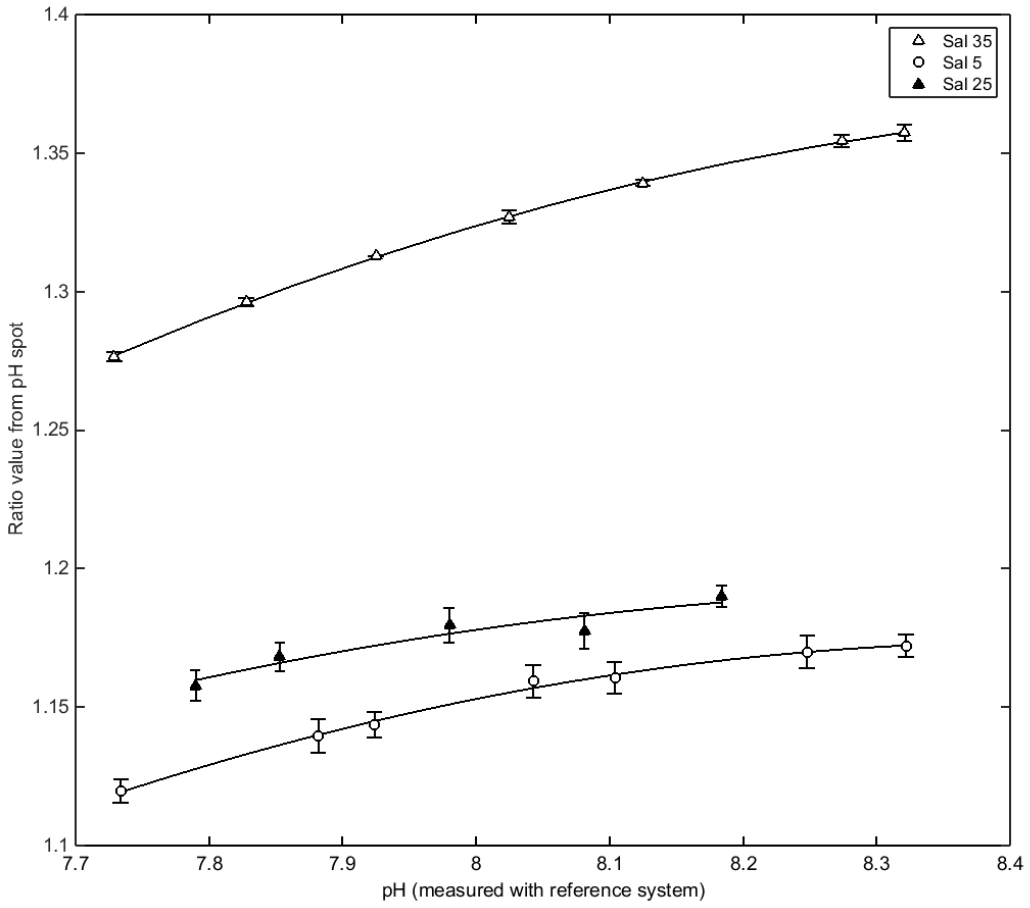

Figure 2.5 Response of the sensor spot to varying salinity of the solution from 5 – 35 over a range of pH values measured with the reference electrode. Reference pH was determined using a glass electrode calibrated with tris buffered CRM for high salinity samples and NIST buffer solutions for very low salinity samples.

The increase in R with salinity is due to changes to the indicator pK_a' caused by surface-solution interactions between the spot and the surrounding buffer solution (Janata, 1987). Theoretical considerations (Debye-Huckel) indicate that an ionic strength increase is

accompanied by an apparent pK_a' decrease (Stumm and Morgan, 1996, Hulth et al., 2002), and consequently for a constant pH there is an increasing concentration of the conjugate base form of the indicator. This causes an increase in R with salinity (Figure 2.5). The lack of a significant difference between the lower salinity solutions (5 and 25) indicates the presence of a secondary process. The ionic strength within the microenvironment of the spot is not just a consequence of the ionic strength of the external solution; charged molecules in the membrane and surrounding the indicator dye, will affect the pK_a' and thereby influence R. The pH at the surface of the optode (pH_{surf}) will be different to that of the bulk sample solution (pH_{bulk}), and is controlled by the surface potential (ψ) which is determined by the ionic species present at the interface between the optode surface and the bulk solution (Janata, 1987). The charges in the membrane allow the surface potential to be unaffected by variations in the ionic strength of the sample solutions. This process thereby stabilises the observed pH_{surf}. However, at full seawater salinity (ca. 35), the sample ionic strength is greater than the apparent ionic strength at the surface. Therefore, the bulk ionic strength will influence the surface potential and causes the apparent indicator pK_a' to decrease and the R to shift to higher values (Janata, 1987).

Typical seawater salinities (35) cause a much larger change to R compared to brackish and estuarine salinities (e.g. 5-25). This indicates that the foil could be used without salinity correction in low salinity environments. Schröder et al. (2005) did not compensate for the salinity effects on the optode response as the changes observed were within the desired accuracy (0.02 pH units), while Hakonen et al. (2013) corrected for salinity deviations using log linear transformations. In order to obtain high quality surface ocean pH measurements for monitoring the changes to the oceanic carbonate system, the shift in R as a result of salinity / high ionic strength is included in the pH determinations (section 2.3.6).

2.3.4 Chlorophyll influence

Fluorescent compounds present in seawater can potentially influence the sensor response by increasing the fluorescence counts in the t_{em} portion of the fluorescence decay curve. An investigation into chlorophyll-a interference was undertaken, involving pH analyses of solutions with increasing concentrations of chlorophyll-a from the coccolithophore, *Emiliania huxleyi*. The pH of the solutions was not controlled and normalisation was performed (see methods section) to determine if there was an influence from the increasing chlorophyll. A decrease in R_n (up to 0.15 units, ca. 0.9 pH units) was observed at enhanced chlorophyll concentrations (between 2.05 µg L^{-1} and 6.5 µg L^{-1}). These concentrations are significantly higher than generally observed in the open ocean (ca. 0.1-1 µg L^{-1} www.earthobservatory.nasa.gov), but may be encountered in coastal waters. At lower

chlorophyll concentrations (0-1 µg L^{-1}), the response showed a smaller increase in R_n (up to 0.05 units, ca. 0.3 pH units). The complex sensor response to chlorophyll fluorescence did not allow this to be included in a dependency algorithm (see e.g. equation 2.5 below). Elimination of chlorophyll fluorescence is therefore deemed more appropriate and this could be undertaken by manufacturing a blackout layer on the surface of the optode, although this would increase the response time of the sensor, or by removal of phytoplankton cells through on-line filtration of seawater prior to analysis. Obviously, in waters below the sun-lit layer in the ocean, where there are no phytoplankton, this chlorophyll interference is not relevant.

2.3.5 Metrology

Results from the response time experiment are presented Figure 2.6. The upper line of measurements represents pH 8.5 (ratio ~ 1.13) and the lower line represents pH 7.2 (ratio ~ 0.73). The points in-between represent the equilibration of the spot in the solution. The time required for the optode to reach 97 % of its final stable R (t_{97}) was 50 s. This is comparable to results from similar sensors in marine sediments (Table 2.1 (Zhu et al., 2005, Hakonen and Hulth, 2010, Larsen et al., 2011); 5 to 200 s). The standard deviation of the ratio from the mean pH for each solution had an mean value of 0.003 (n=18), equivalent to 0.03 pH units (Figure 2.6)

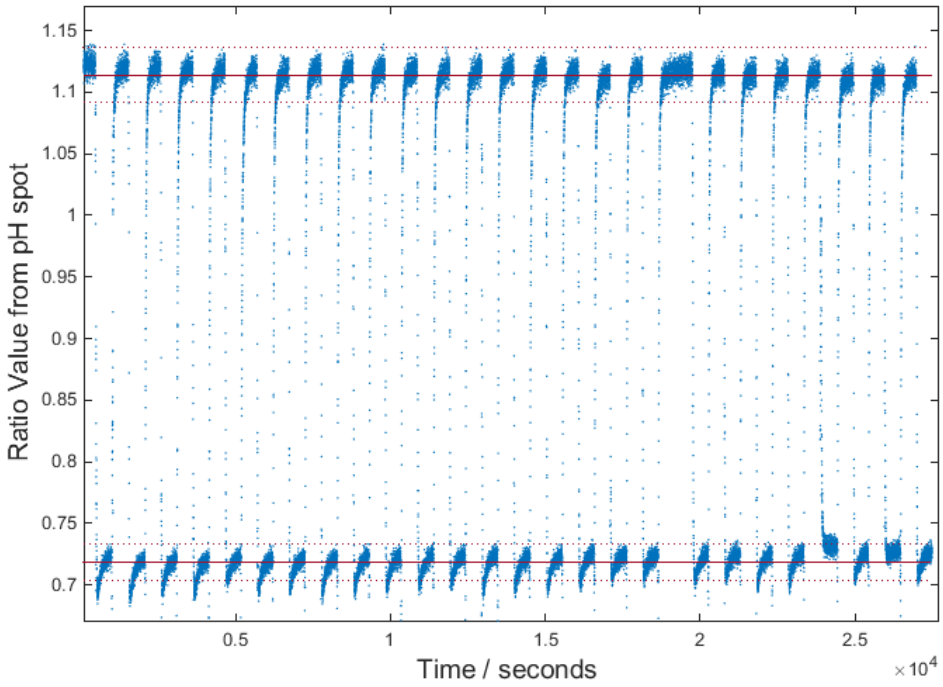

Figure 2.6 Results of repeatability experiment. The sensor was repeatedly switched between seawater solutions of pH 7.2 and 8.5. The upper line of measurements represents pH 8.5 (ratio ~ 1.13) and the lower line (ratio ~ 0.73) pH 7.2. The points in-between are the equilibration of the spot in the solution. The straight red line shows the ratio mean for the two pH solutions, and the dotted lines show 98 % of the mean (final value).

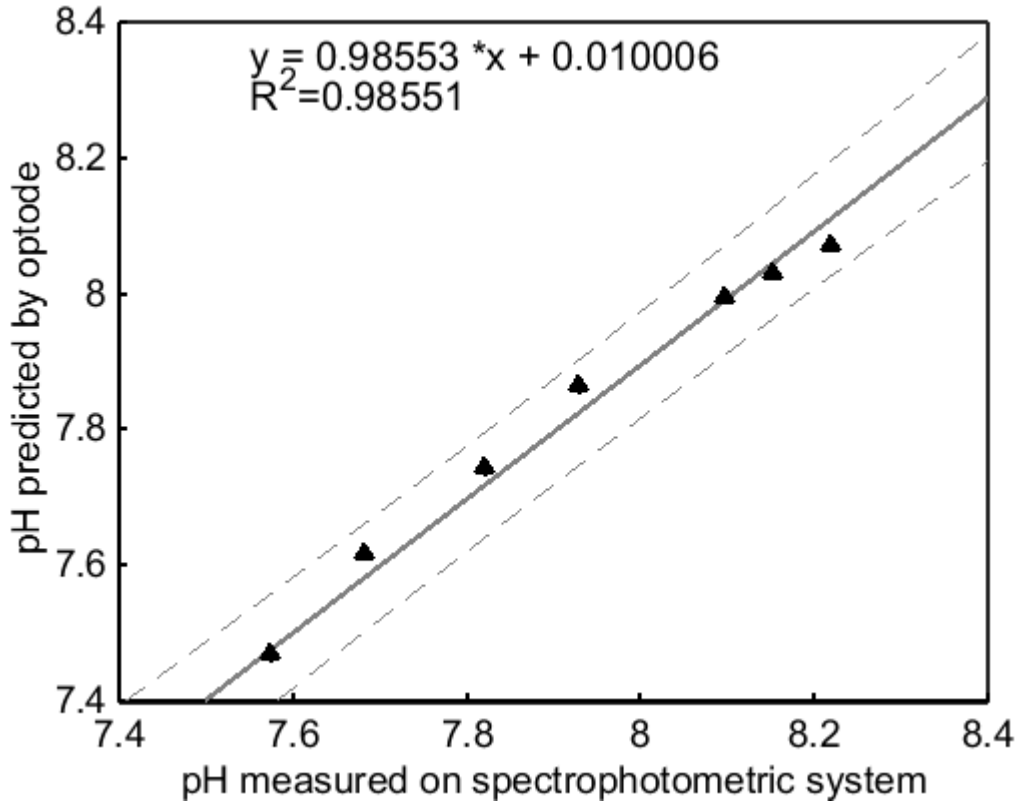

Figure 2.7 Comparison of the pH determined by the pH optode sensor against the measured spectrophotometric sensor values. Error bars are shown for both x and y measurements, based on the standard deviation of the repeat measurements (n=3) - x error bars are obscured by the size of the marker. The dotted lines represent the 95 % confidence limits.

Comparison between measurements of tris buffers with the spectrophotometric system and the optode before temperature and salinity correction showed a good agreement (Figure 2.7), with no statistically significant difference (student pairwise t- test, t=0.737, df =14, two-tailed P-value 0.473). The optode sensor algorithm (equation 2.2) yielded pH values that were 0.103 ± 0.03 pH units higher in the range 7.5 – 8.3 compared to the spectrophotometric sensor. Consequently, a final calibration step of involving a CRM is still required for the optode spot.

An experiment with continuous illumination of the spot was undertaken to give an indication of the number of measurements a single spot could make before bleaching of the indicator dye significantly affects the quality of the determination of R. A change in the ratio of <1 % was observed from measurements before and after the continuous illumination for 1 h, similar to what is reported by other workers (Larsen et al., 2011). This indicates that the foil is stable for a minimum of 92 continuous measurements of 200 s. These estimates are the lowest limits of the lifetime of this spot due to the constant illumination, which is not the normal use of the spot.

The sensor drift was evaluated over three days with consecutive 200 s measurements (Figure 2.8). The standard deviation (σ) across the 254 measurements over the three days was 0.0013 R (ca. 0.016 pH, at 25 °C, salinity 35); with a small downward drift of 0.000014 R (ca. 0.0004 pH, at 25 °C, salinity 35). This drift was smaller than the standard deviation across all the measurements. However, the measurements showed smaller variability in R over a 3-day period (σ =0.0013) with the shorter illumination cycles compared to the variability in R after the continuous illumination experiment (1 hour, σ = 0.01). This indicates that the shorter illumination times are advantageous in prolonging sensor spot use. Furthermore, according to other workers, the calibration of sensor spots is retained during dark storage for periods of months (Zhu et al., 2005, Wencel et al., 2009).

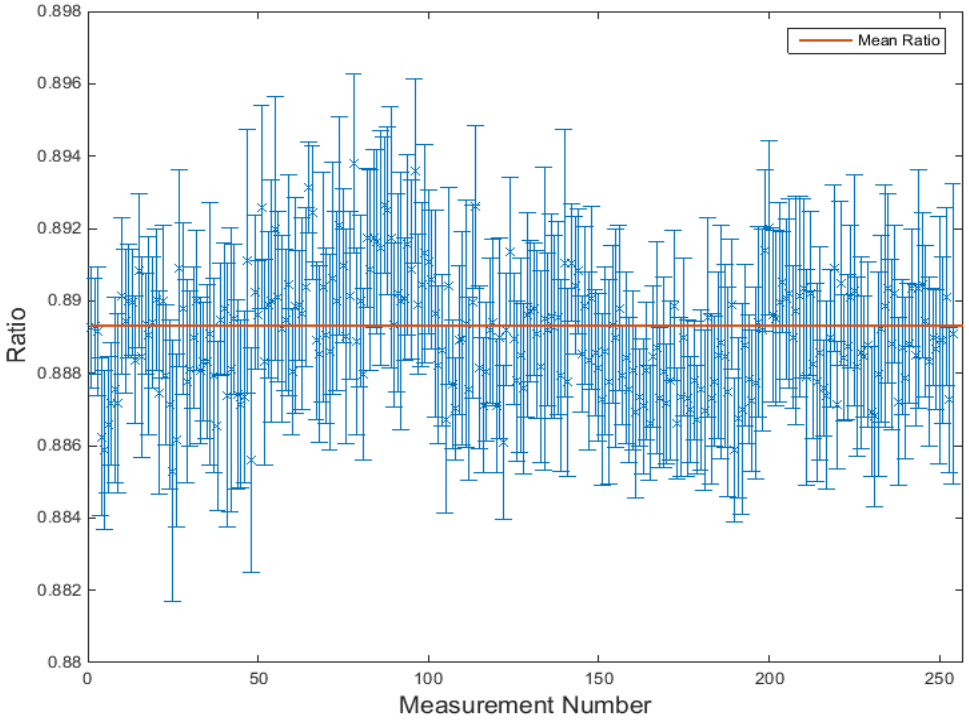

Figure 2.8 *Drift over 3 days with one measurement every 15 minutes in a sealed container, pH 8.1 salinity 35.*

2.3.6 Multi- linear regression for fluorescent signal conversion to pH

In order to convert the fluorescent signals obtained by the optode sensor to pH, a stepwise multi-linear regression was performed on data from the temperature and salinity investigations (n=120). The regression yielded equation 2.2, where T is temperature in °C and S is salinity, and R is the ratio as determined from the optode output with the coefficients specified below.

Equation 2.2

$$R = (0.00034 - 0.17 \cdot pH + 0.15 \cdot S^2 + 0.0067 \cdot T - 0.0084 \cdot S) \cdot 1.075$$

The equation was derived for the pH range 7.6-8.3, a temperature range of 5-25 °C, and a salinity range of 5-35. It has an adjusted r^2 of 0.973 (n=120), a standard error of pH is 0.005. The temperature and salinity data were obtained using a single spot. Differences between spots may occur during manufacturing process, which might create an offset when used with the above equation, but should not affect the temperature and salinity dependence determined here. To account for these offsets, CRM measurements should be used. As the chemistry of the commercial optode spots is assumed stable and repeatable, the temperature and salinity dependence calibration need only be performed for one spot (as in this study) and can then applied to others.

A future re-calibration**,** using a spectrophotometric system, would allow for improved accuracy in the characterisation of the temperature and salinity dependence due to the greater precision of the spectrophotometric system compared with the potentiometric pH measurements. This approach will be similar to the use of a correction coefficient by Yang et al. (2014), who applied this to broadband spectrometer measurements, thereby relating the data back to a narrowband calibration. This is postulated to improve the accuracy and precision of the sensor spot.

2.3.7 Cruise Data

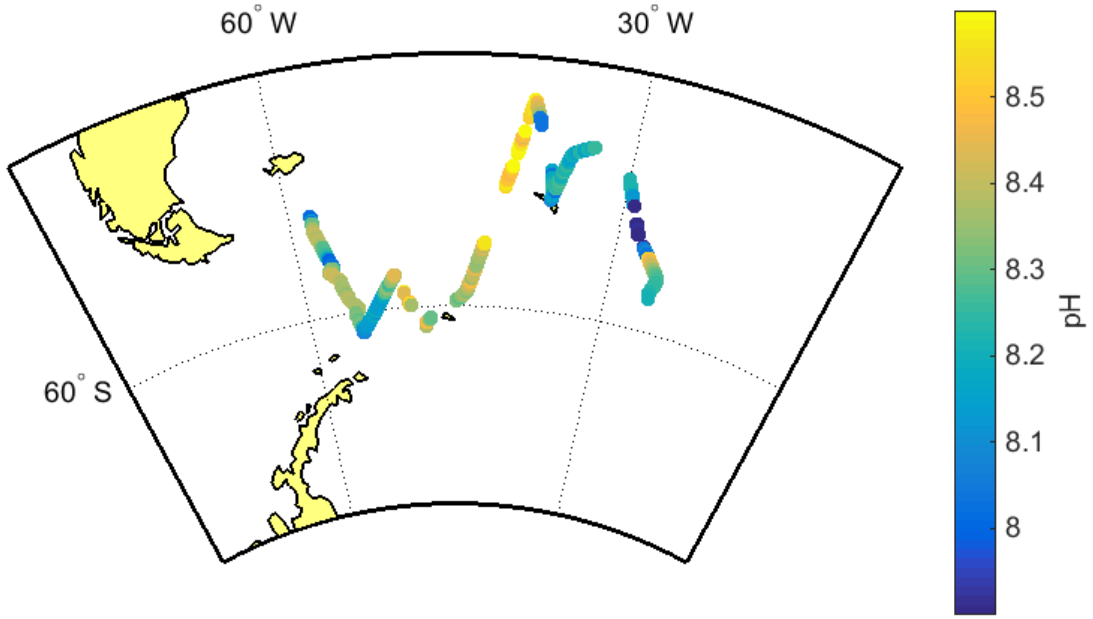

Figure 2.9 Plot of underway pH determined with the optode sensor plotted along the cruise track.

Over 3000 data points were collected on a research cruise in the Southern Ocean, involving the use of two spots (~1500 data points each). The first spot was replaced during the cruise due to concerns of light exposure and consequent photobleaching during maintenance of another system coupled to the same underway seawater supply. Certified reference material was analysed at the halfway point of the run of each spot to correct for manufacturing offsets and drift as discussed above. The total drift of the spots measurements over the course of the cruise was 0.06 pH units before applying a linear correction over time using the CRM measurement. This drift exceeds the error in the calculated pH (± 0.0062) from the CRM values. The shipboard precision (0.0074 pH, n=10) was comparable to ISFET sensors (Le Bris and Birot, 1997). The underway observations by the sensor of surface ocean pH_{tot} across the Southern Ocean transect were in the range pH 7.90-8.39, which is a larger range to that reported by Bellerby (pH 8.04-8.28 *in situ*) (Bellerby et al., 1995). These observations demonstrate the range of environments visited during our cruise, which included regions with high primary productivity and consequently enhanced CO_2 uptake and enhanced pH values (e.g. pH 8.3-8.4 north of South Georgia, ca. 52ºN, 38ºW, see Figure 2.9). The enhanced chlorophyll-a concentrations encountered in the Southern Ocean (maximum observed ca. 11.2 µg L^1), may have resulted in a decrease in R, and in future on-line filtration prior to pH analysis should preferably be undertaken. The intense blooms are less common in other open ocean regions, due to a lack of macronutrients to support enhanced phytoplankton growth.

2.4 Current limitations and future directions

The pH spots provided continuous underway data in a challenging ocean region for which there is a lack on carbonate chemistry data. The operation of the sensor was simple, with no difficulties encountered. The precision of the spot in its current configuration is 0.0074 pH (n=10), and comparable to ISFET sensors but inferior to spectrophotometric pH systems. A limitation of the optode sensor is the observed drift in response over periods of weeks at sea. The precision and drift issues are likely caused by the low apparent pK_a' of the indicator (6.93 at 20 °C) in relation to the intended open ocean seawater range of pH 7.8-8.3, and the increased chlorophyll concentrations. To overcome these issues it is advisable to investigate alternative indicator dyes with higher apparent pK_a values and potentially greater stability. Schröder et al. (2005) investigated two potential immobilised indicators, which were carboxyfluorescein derivatives, that showed similarities to the temperature and salinity dependence observed in this study, but had pK_a' values (8.16 and 8.57) more suited to seawater measurements. Efforts to develop improved pH spots for ocean measurements are currently undertaken in academic-industry collaborations as part of international research projects (e.g. SenseOcean and Atlantos, European Union Funded), and novel pH optodes will emerge over the coming years. Furthermore, the use of a spectrophotometric sensor in the calibration procedure will improve the precision on the reference pH measurements, and thereby moving the precision of the optode closer to that of spectrophotometric systems.

Further developments with our optode should focus on the use of spectrophotometric system (instead of pH glass electrode) in calibrations to reduce the pH error in the optode algorithm, and more detailed investigations into the chlorophyll dependence of R at low chlorophyll concentrations. Increased use of CRM materials will both correct for and remove drift in the system, although use of an indicator with pK_a' values closer to seawater pH may largely eliminate this.

Future optode deployments (with this spot or others) should utilise a high performance temperature sensor alongside the optode to provide a more realistic determination of measurement temperature for the conversion from R to pH. The use of the filters, dichroic beam splitter and PMT were for more specialised laboratory experiments, and these were used to investigate the effectiveness of the t-DLR technique and allow lower intensity excitation levels. However, for future deployments, the use of a photodiode as a detection system and a reduced number of filters should be investigated in order to simplify the system and allow more widespread applications, as with the oxygen optodes.

2.5 Conclusion

This work has evaluated an optode pH sensor for measurement of ocean pH. I investigated temperature and salinity dependences, metrology and the longevity of a commercially available pH sensor spot across the pH range 7.6-8.2. The lifetime of the spot was improved with the use of low optical power for excitation and repeated short illumination times, while the response time of the spot was found to be 50 s. The temperature dependence (-0.046 pH $°C^{-1}$ from 5-25 °C) and salinity dependence (-0.01 pH psu^{-1} over salinity 5-35) were accounted for using a calibration algorithm. This simplicity is an advantage compared to the individual calibrations required for ISFET and glass pH electrodes. The algorithm was tested through deployment as an underway sensor in the Southern Ocean, which displayed strong pH, chlorophyll and temperature gradients. A precision of 0.0074 pH was observed at sea, but the optode demonstrated drift of 0.06 pH over the period of the cruise (4 weeks), which was corrected for using CRM measurement. In a lab based experiment I found a drift of only 0.00014 R over 3 days (ca. 0.0004 pH, at 25 °C, salinity 35), suggesting with further improvements to the deployment system drift may not be a significant issue. To improve the precision and limit any potential drift, I suggest further investigation into alternative pH indicators with more suitable pK_a values for surface ocean measurements. With regular CRM calibrations, the spot characterised in this study is suitable for coastal deployments where pH precision requirements are lower. Optode technology is still in its infancy, and this study demonstrates its potential, with ongoing developments in spot technology delivering pH sensors over the coming years for oceanic deployments. The now widespread use of oxygen optodes demonstrates the potential of this technology.

Chapter 3:

Developments in marine pCO_2 measurement technology

This chapter has been prepared for submission to Trends in Analytical Chemistry.

Abstract

The ocean is currently a major sink for anthropogenic carbon dioxide (CO_2) causing pronounced changes to the marine carbonate system, with increasing pCO_2 and dissolved inorganic carbon concentrations and decreasing pH and carbonate ion concentrations. The CO_2 uptake lowers the buffer capacity of the ocean and consequently reduces the ability for future CO_2 uptake. To monitor the ocean's uptake of CO_2, identify regions of enhanced carbonate system change, and observe the effectiveness of CO_2 emission mitigation strategies, high quality pCO_2 measurements with good temporal and spatial coverage are required. There are currently several instruments available to measure pCO_2, but many are unsuitable for autonomous deployments on *in situ* platforms such as moorings and Argo floats. We here assess currently available technology on their suitability as *in situ* pCO_2 systems, with a focus on optode developments as a future sensor solution.

Optodes have been shown to be a flexible sensing technology for oxygen, suitable for *in situ* use with many successful oceanic deployments. A pCO_2 optode was calibrated over the range 280 -480 µatm using time domain dual lifetime referencing as detection technology, recording a laboratory precision of 0.8 µatm (n=10), and a response time (τ_{90}) of 165 s.

3.1 Introduction

Land-use changes and the combined effects of cement production and fossil fuel burning form the principal sources of anthropogenic carbon dioxide (CO_2) to the atmosphere, responsible for emissions of 1 ± 0.5 PgC yr^{-1} and 8.3 ± 0.4 PgC yr^{-1} respectively, over the period 2002-2011 (Le Quéré et al. 2013). Atmospheric CO_2 concentrations are expected to continue to increase, with a concentration of 800 ppm projected by the end of the 21st century (Doney et al. 2009). Less than half of the annual CO_2 emissions remain in the atmosphere; a quarter end up in the ocean, with the remainder absorbed by terrestrial systems and remaining in the atmosphere (Le Quéré et al. 2009). The ocean is thus a major sink in the global carbon cycle.

The movement of carbon dioxide across the air-sea interface is described by equation Equation 3.1, and the solubility coefficient K_0. The concentration of $CO_{2\,(aq)}$ can be found using Henry's law, where the concentration of a gas in a liquid is directly proportional to the partial pressure of the gas above the liquid. Once the CO_2 transfers across the air-sea interface, it dissolves and reacts to form bicarbonate ions (currently 86.5 %), carbonate ions (currently 13 %) and a small amount of carbonic acid with a similarly small amount remaining as gaseous CO_2 (currently combined 0.5 %), Equation 3.1 & 3.2 (Zeebe and Wolf-Gladrow 2005). Due to the small amount of carbonic acid, the carbonate equilibria can be simplified to equation 3.2, with K_1 and K_2 the equilibrium constants of carbonic acid. These are dependent on temperature, salinity and pressure and are used when describing the carbonate system (section 3.3.2).

Equation 3.1 Thermodynamic equilibrium between gaseous and aqueous form of carbon dioxide described by the solubility coefficient K_0.

$$CO_{2\,(g)} \overset{K_0}{\rightleftharpoons} CO_{2\,(aq)}$$

Equation 3.2 Carbonate equilibria in seawater between CO_2, bicarbonate ions and carbonate ions described by the equilibrium constants K_1 and K_2.

$$CO_{2\,(aq)} + H_2O \overset{K_1}{\rightleftharpoons} HCO_3^- + H^+ \overset{K_2}{\rightleftharpoons} CO_3^{2-} + 2H^+$$

A consequence of the increasing atmospheric CO_2 concentrations from 280 µatm in pre-industrial times to 400 µatm today, is a surface ocean pH decrease from pH 8.25 to pH of ca. 8.1 (Jacobson 2005); with an average rate of decrease of 0.002 pH units per year (Bindoff et al. 2007, Dore et al. 2009). Model projections with various emission scenarios reported by the

Intergovernmental Panel on Climate Change (IPCC), where final atmospheric pCO_2 varies between 650-970 ppm, predict a further pH decrease between 0.3-0.5 pH units (Caldeira and Wickett 2005). The proton release from the CO_2 absorbed by the ocean is partially mitigated by the buffering effect of dissolved bicarbonate and carbonate ions, but this buffer capacity will decrease as the anthropogenic carbon dioxide uptake by the ocean continues (Thomas et al. 2007, Bates et al. 2012). The effects from increasing seawater CO_2 range from changing ocean chemistry to biology, and are yet to be fully understood (Doney et al. 2009). Climate mitigation strategies are being proposed to reverse the current trend of increasing atmospheric CO_2. One such strategy - ocean carbon capture and storage (CCS) - pumps excess CO_2 into sub-seafloor reservoirs. This approach mitigates the atmospheric CO_2 effects, but new technologies are required to monitor potential seafloor CO_2 leaks and subsequent seawater pCO_2 increases. Sensors are also necessary to quantify CO_2 concentrations for any type of emissions trading scheme and to guide mitigation / remediation actions. To fully understand the effects of increasing CO_2 and monitor potential mitigation strategies, high quality, autonomous carbonate chemistry sensors are a crucial tools.

3.2 Carbonate Variables

The ocean carbonate system can be defined by six parameters- Total Dissolved Inorganic Carbon (DIC), Total Alkalinity (TA), pCO_2, pH, and the concentrations of bicarbonate and carbonate ions (Marion et al. 2011). Of the six carbonate system variables, four are readily measurable: DIC, TA, pCO_2 and pH, and knowledge of two variables along with temperature, pressure and nutrient data can be used to calculate the others. The recommended combinations apply pCO_2 with either DIC or TA.

3.3 Measurement Platforms

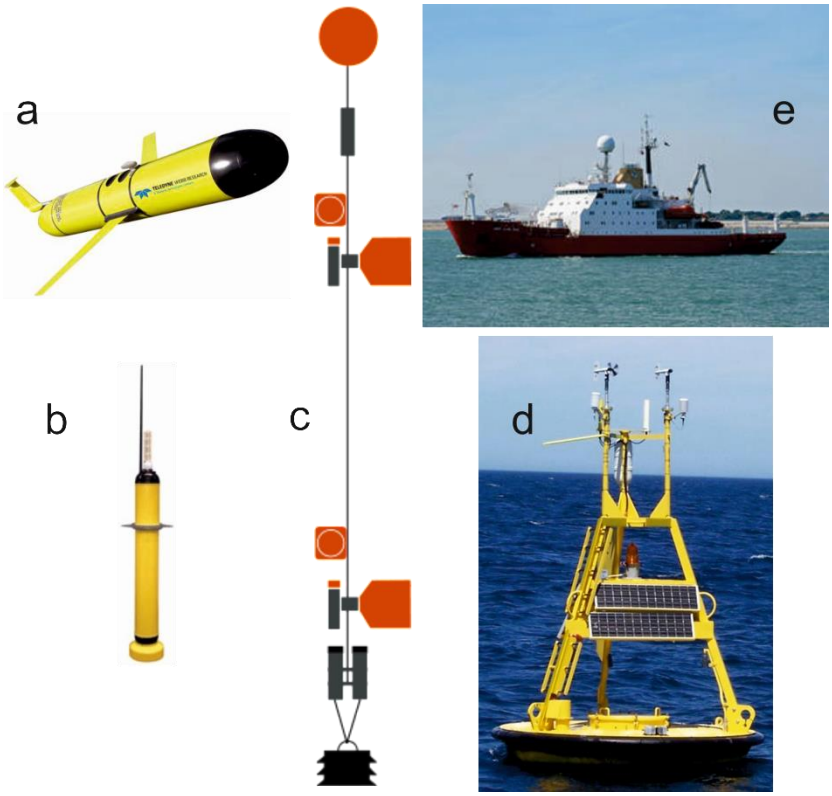

Figure 3.1 Platforms available to deploy sensors in the ocean. The dynamic *in situ* platforms include a) underwater Slocum glider, image from Teledyne (http://www.webbresearch.com/newscenter/011413.aspx) and b) Generic Argo float, image from ARGOinfo website (http://www.jcommops.org/argo) and e) British research vessel R.R.S. James Clark Ross, image from the National Oceanography Centre (http://noc.ac.uk/). The static platforms include c) Moorings secured to the seabed, schematic reproduced under the creative commons attribution-share alike 3.0 unported licence d) and buoys- National Oceanic and Atmospheric Administration (NOAA) weather buoy shown, image from http://www.nist.gov/tpo/tech_transfer-080613.cfm, Courtesy of NOAA.

To monitor global climate change resulting from the increasing CO_2 concentrations, increasing quantities of data are required. Research ships (Fig 3.1e) allow sensor deployment with few constraints on size, power or autonomy. However, ships are expensive to operate, and provide limited temporal and spatial coverage. To overcome these limitations, new platforms allowing autonomous *in situ* measurements with greater coverage are becoming available (Fig 3.1). Mobile platforms such as Argo floats (Fig 3.1b) and underwater gliders (Fig 3.1a), allow increased spatial coverage, require minimal operator input with regular and autonomous transmission of data. Moorings (Fig 3.1c) and buoys (Fig 3.1d) are static platforms, providing temporal coverage at one location, with the potential for near real-time transmission of data.

Chemical sensors must be developed with the ability to undertake measurements on these platforms, and improve both the quantity and quality of data available. Desirable characteristics for *in situ* chemical sensors include low cost, ease of integration, and limited

calibration requirements (Byrne 2014). More specifically, the mobile platforms require fast response times and an ability to cope with a wide range of temperatures and salinities, whereas the static platforms need greater longevity with measurements over limited temperature and salinity ranges (Byrne et al. 2010). A detailed review by Johnson and co-workers (Johnson et al. 2009) covered the state of the art of global biogeochemical sensors for deployment on Argo floats and gliders in 2009. Since the review, pH, pCO_2 and DIC sensors have progressed, and the first pH sensors have recently been successfully deployed on Argo floats (Dalit 2014).

This paper deals with the current state of technology for the measurement of seawater pCO_2. We compare and contrast the existing technology, investigate the deployment methods for current generation of sensors and provide an insight into future developments of *in situ* marine pCO_2 measurements, with a focus on recent developments in optode technology. A summary of some of the commercially available and commonly used sensors and their metrology is provided in Table 3.1.

Table 3.1 - A selection of commonly used, ocean pCO_2 sensors. Where Prec =precision, NDIR = non dispersive infrared spectroscopy, CRDS = cavity ring down spectroscopy, GC = gas chromatography, SPM = spectrophotometric, ISFET-pCO_2 = ion-selective field effect transistors to measure pCO_2, Ø is the diameter where a cylindrical housing is used, τ_{63} = time taken for the signal to reach 63 % of its final value (τ_{90} is the time for a 90 % response, and so on), and res refers to the sensor resolution.

Model	Type	Prec	Accuracy	Response Time	Drift	Dimension/ Weight	Range
HYDROC CO_2 (Contros Systems & Solutions 2015)	NDIR	(res) <1 µatm	1 %	τ_{63}= 6 s	Automated zeroing	89 Ø x 414 h mm 4.5 kg	200-1000 µatm
CO_2 – ProCV(Pro Oceanus 2015)	NDIR	(Res) 0.01 ppm	2 ppm	τ_{63}= 2.5 min	Automated zeroing	11.5 Ø x 33 h cm 2 kg	0-600 µatm
Seaology pCO_2 monitoring (Battelle 2011)	NDIR	1 ppm	<2 ppm	20 min	~	~	100-600 µatm
AS-P2 pCO_2 (Apollo SciTech inc 2010)	NDIR	1 ppm	~	2 min	~	~	100-4000 µatm
Kimoto CO_2 - 09	NDIR	1 ppm	~	~	~	400 x 400 x 350 mm 15 kg	0-2000 ppm
G2401 CRDS (Picarro Inc. 2015)	CRDS	< 50 ppb		5 min	500 ppb/ month	43 x 17.78 x 44.87 cm 25 kg	0-1000 µatm
SAMI-CO_2 (Sunburst Sensors LLC)	SPM	< 1 µatm	3 µatm	5 min	< 1 µatm/6 months	15.2 Ø x 55 cm 7.6 kg	150-700 µatm
Bakker et al. (1997) & Dickson et al. 2007)	GC	0.7 µatm	~	19 min	<2 %	~	250-2000 µatm (at 20 °C)
Shitashima et al. (2008)	ISFET-pCO_2	~	~	<60 s	~	~	~

3.4 Gas-Based Methods

The use of gas-based methods to measure dissolved CO_2 requires the CO_2 be transferred to the gas phase prior to measurement. To achieve this, the seawater is equilibrated with a carrier gas- such as nitrogen or air - in an equilibration chamber, before the equilibrated gas streams move to the detector. These equilibration chambers are common across gas-based measurements of seawater pCO_2. To measure atmospheric CO_2 the equilibration process is not required, the air can be used directly, although drying is common with marine air to remove water vapour distortion. The equilibrator design will influence the response time through the water-gas exchange efficiency. The original equilibrators, "bubbler type", "shower type" and the "laminar flow" equilibrators are used for techniques with detection using gas chromatography (GC), non-dispersive IR (NDIR) and cavity ring down spectroscopy (CRDS).

The "bubbler type" involves bubbling the carrier gas through the sample to extract the carbon dioxide (Goyet et al. 1991). The "shower type" equilibrator disperses seawater sample droplets through a shower head and into a gas flowing perpendicular to the droplet path (Weiss 1981, Inoue 1998); finally the "laminar flow" equilibrator refers to the continuous circulation of seawater in a counter-current flow to the carrier gas to extract the carbon dioxide (Poisson et al. 1993).

More recent variations designed for use with the NDIR include percolated bed equilibrator chambers (Cooper et al. 1998, Schuster and Watson 2007) and membrane equilibration (Saito et al. 1995, Fietzek et al. 2014, Jiang et al. 2014). The percolated bed design involves a showerhead chamber filled with marbles to increase surface area and reduce equilibration time. The membrane method does not require a built in-equilibrator chamber, allowing instead the CO_2 from seawater to diffuse across a semipermeable membrane with a silicone layer to the internally circulated gas stream (Fietzek et al. 2014, Contros Systems & Solutions 2015). The membrane approach is more compact compared to the other equilibrator methods detailed and more suited for *in situ* systems. An equilibration period of 5 min to 10 min depending on equilibrator type is required prior to CO_2 measurement.

3.4.1 Gas Chromatography based pCO_2 measurements

Gas chromatography (GC) is a widely used method in chemistry laboratories and has been adapted for analysis of seawater samples. The systems were pioneered for pCO_2 measurements on ships by Weiss during the 1970's (Weiss et al. 1992) and were widely used as part of the World Ocean Circulation Experiment and Joint Global Ocean Flux Study (Goyet et al. 1991). Measurements are undertaken in the gas phase, requiring the use of an equilibration chamber to extract CO_2 into an internal carrier gas stream. The CO_2 is then reduced to methane using a nickel/palladium catalyst before being transferred to a flame ionising detector (Goyet et al. 1991, Wanninkhof and Knox 1996). The CO_2 concentration is related to the integrated peak area, with a linear response over the range 250-2000 µatm (Dickson et al. 2007).

The GC technique can be used for analysis of both atmospheric samples and water samples, allowing calculation of air-sea pCO_2 fluxes. The approach uses small air sample volumes (1 ml (Weiss 1981)), has a linear response over a wide range of CO_2 concentrations (250-2000 µatm (Dickson et al. 2007)), and produces high quality shipboard data with a precision < 0.25 % (Schuster et al. 2009). The gas stream does not require drying nor prior composition knowledge due to a lack of cross-sensitivity in the system. However, GC requires stable temperatures, a flame and pressurised gas to dry and transfer sample through the system with an expensive catalyst for analysis as well as larger sample sizes (200—500 ml (Takahashi et al. 1993)). For these reasons, the GC analysis of CO_2 has not been developed further as an *in situ* system.

3.4.2 NDIR Spectrometry pCO_2 systems

Non-dispersive infrared (NDIR) spectrometry uses the characteristic vibration of gaseous CO_2 upon absorption of infrared radiation at 4.3 µm. Seawater samples are equilibrated into a gas stream; the gas is then dried (to remove water distortion in the resulting peak) and flows through the spectrometer for measurement. Regular calibrations with certified reference gases are required to correct for spectrometer drift, and an automatic zero-point must be carried out daily. However, when deployed *in situ*, the use of certified gases is no longer an option. Marine air can be used as an additional reference between calibrations to account for spectrophotometer drift (Fiedler et al. 2013).

NDIR can measure over a wide range of concentrations (0-3000 µatm, (Frankignoulle and Borges 2001)) but with a non-linear response. It is a widely used detector for ocean pCO_2 measurements with increasing numbers of commercial *in situ* systems, with varying response times, precisions and concentration ranges (Contros Systems & Solutions 2015, Pro Oceanus

2015) as illustrated in Table 3.1. The systems have been deployed on buoys and moorings, and on commercial ships (termed ships of opportunity) with limited scientific interaction (Schuster and Watson 2007). The latter deployments have provided high quality and high resolution (1 data point per 20 min (Cooper et al. 1998)) data along commercial shipping routes increasing our understanding of pCO_2 variability in regions such as the North Atlantic (Lüger et al. 2004, Schuster and Watson 2007) and Pacific Oceans (Jiang et al. 2014). The limited maintenance opportunities for these systems on commercial ships has stimulated the development of autonomous *in situ* pCO_2 systems. Fietzek and co-workers have developed procedures to reduce drift in *in situ* systems without requirement for human interaction or certified gases (Fietzek et al. 2014). Soda lime is, for example, used to remove CO_2 from the seawater-equilibrated air, thereby providing a blank measurement while deployed *in situ* without access to marine air. This helps counteract the drift and improve the quality of the data.

Further experiments to determine the long-term stability of NDIR deployments on mooring and buoys are underway (Fietzek and Körtzinger 2009). Deployment on mobile platforms such as Argo floats and gliders is limited due to the gas equilibration requirements influencing the response time (Fiedler et al. 2013). To counteract this, the profilers potentially could be programmed to move more slowly to allow for slower responding sensors (Byrne et al. 2010). The drift of the spectrometers is a further issue that limits the use of these systems on mobile platforms, with still limited quantification of the pressure effect on the spectrometer reading (Fiedler et al. 2013). While the calibration and zeroing procedures proposed by Fietzek are a step towards NDIR systems that are truly *in situ*, with no requirements for certified gases during deployment, the requirement for continual blank measurements combined with the gas equilibration time means that these systems may soon be abandoned in favour of dissolved phase measurements with fewer calibration requirements. At the current time, these systems are the most technologically advanced for *in situ* measurements.

3.4.3 Cavity Ring-Down Spectroscopy for pCO_2 measurements

Cavity ring down spectroscopy (CRDS) utilises the absorption of CO_2 excited at a specific frequency using a laser. The laser-derived light is directed into a cavity lined with mirrors to reflect the light back and forth, creating a long effective path length with increasing light intensity. Once a pre-set intensity is reached in the cavity, the laser is switched off and the intensity of the light is measured over time with a photodiode. A small number of photons will be lost upon each reflection cycle at the gap in the mirrors where the laser light enters. The decay is measured in the time domain, with increasing concentrations of CO_2 decreasing the decay time of the light due to the increasing absorption by the CO_2 (Friedrichs et al. 2010). The technique can be used to measure fCO_2 and corresponding isotopes ($^{12}CO_2$, $^{13}CO_2$), carbon monoxide, methane and water vapour concentrations for full characterisation of the ocean carbon cycle (Picarro Inc. 2015). Isotopes are used to help quantify anthropogenic invasion of CO_2 into the ocean and currently there are no other *in situ* measurement systems available for such isotope analyses.

Reference gases must be measured for 3 hours at least once per day (Becker et al. 2012) to correct for baseline drifts in the measurement with an additional proposed switching between sample and reference gas every 2 min. A correction is required to account for the varying oxygen and methane concentrations in the equilibration gas, due to cross-sensitivity in the measurement. CRDS is a technique only recently applied to seawater CO_2 analysis, and has been tested on research cruises in the Atlantic Ocean continuous measurements of pumped surface seawater. Early applications have shown an accuracy of 0.5 ppmv and a response time (τ_{90}) of 400 s (Becker et al. 2012).

CRDS was previously used for monitoring of gas concentrations and isotopic composition in the atmosphere and soils, and further developments for use on monitoring platforms such as buoys are expected. The technique allows measurements of both atmospheric and seawater CO_2 concentrations with an improved signal to noise ratio and no requirement for drying of the gas prior to measurement (Becker et al. 2012). Excellent stability of 0.15 ‰, with no re-calibration over a period of a year has been reported, a marked advantage compared to the NDIR techniques (Friedrichs et al. 2010). However, the CRDS systems still have many similar disadvantages as NDIR; they are bulky with a requirement for reference gases and equilibrators, currently based on the showerhead design. The matrix of carrier gases must also be known prior to measurement due to methane and oxygen cross sensitivity making autonomous measurements of marine samples increasingly complex. This system is still in its infancy with respect to seawater pCO_2 measurements, but the range of available measurable variables, including isotopes, makes this system attractive for further development towards *in situ* deployment.

3.5 Electrochemical pCO_2 systems

Electrochemical measurements of pCO_2 were introduced by Severinghaus in 1958, with a teflon membrane enclosing sodium bicarbonate buffer solution surrounding a pH electrode (Severinghaus and Bradley 1958). The pH electrode voltage is monitored relative to reference electrode. Any voltage change between the two is proportional to the pH change in the buffer solution, and can be related back to pCO_2 (Equation 3.1 and Equation 3.2). Most recent developments have focused on the type and thickness of membrane used and the pH electrode design (Zosel et al. 2011).

The systems are able to detect low CO_2 levels, with detection limits lower than 3 µM (Taillefert et al. 2000). Response times are controlled by the combination of diffusion distance and reaction time with the bicarbonate buffer, with times ranging from 60 s (Shitashima et al. 2008) to 2 min (Zhao and Cai 1997). Some electrodes have reported longer response times (ca. 4 min) at low pCO_2 concentrations (Zhao and Cai 1997, Ishiji et al. 2001). Addition of enzyme carbonic anhydrase to the membrane (Zhao and Cai 1997, Shin et al. 2000) decreases the response time, but has only been proven to be stable at low temperatures for a month (Zhao and Cai 1997), and other studies indicate that the enzyme may denature over longer sensor deployments (Tabacco et al. 1999).

The limitations of the electrochemical measurement are mostly derived from the use of the pH electrode: the standard potential of the internal and external reference electrodes is sensitive to temperature and pressure changes (Taillefert et al. 2000, Zosel et al. 2011), and there is susceptibility to electromagnetic interferences (Rérolle et al. 2012). Furthermore, the presence of colloids and polyelectrolyic media can interact with the double layer of the electrode (suspension effects), leading to liquid junction potential drifts with the migration of highly charged seawater ions (Taillefert et al. 2000). The electrodes display strong temperature sensitivity and require regular (weekly – monthly) calibrations if in constant use (Zosel et al. 2011). For these reasons, despite their small size and low power consumption, there are few commercially developed electrode-based systems for oceanography.

3.5.1 ISFET-pCO_2

A more recent electrochemical-based system applies an Ion Selective Field Effect Transistor (ISFET) pH sensor with a buffer solution and a silicone gas permeable membrane to measure pCO_2. A pCO_2 induced pH change in the buffer solution causes a change in the charge on the surface of the ISFET, and an alteration in the strength of the electric field of the internal transistor. The voltage of the transistor relative to the reference electrode is then proportional to the original pH change and thus the CO_2 concentration. It has shown promising initial results with a response time of less than 60 s whilst deployed on an autonomous unmanned vehicle (AUV), but has yet to be fully calibrated to determine pCO_2 directly from the voltage change (Shitashima et al. 2008).

The implementation of pCO_2 measurements using the ISFET-pH with a gas-permeable membrane and a buffer solutions leads to the same challenges as observed for its direct pH measurements. One such limitation of the pH ISFET is a pressure dependent output caused by the pressure dependence of the liquid junction potentials and a clear hysteresis, and the sensors are not recommended for use at depth (Martz et al. 2010, Bresnahan et al. 2014). Intense research efforts are underway to address these issues, with the pH-ISFET recently redesigned to operate at depths up to 2000 m (Jannasch et al. 2014). The pCO_2-ISFET will require careful calibration to fully relate the observed voltages to pCO_2 concentrations before its suitability to in situ deployment options can be more fully evaluated in comparison to other systems.

3.6 Wet-Chemical Spectrophotometric pCO_2 systems

Wet-chemical CO_2 sensors employ colorimetric pH indicators. The indicator is pumped through a CO_2 permeable tube (such as silicone or Teflon) where it equilibrates with the seawater which is on the other side of the tube wall, before moving to the measurement cell where the absorbance of the solution is measured at three wavelengths (absorbance of the acidic and conjugate base forms of the indicator and an independent reference wavelength). Blank, seawater only solutions are used to flush the system periodically to help prevent biofouling and correct for any light intensity fluctuations that influence the measurement precision and accuracy (Moore et al. 2011).

Several systems have been designed for *in situ* use. SAMI-pCO_2 is a commercial system based on bromothymol blue as indicator pH dye with silicone rubber tubing (DeGrandpre 1993, DeGrandpre et al. 1995), a precision of < 1 µatm and a proven capability for 10000 consecutive measurements (Sunburst Sensors LLC). A similar design based on the indicator bromothymol blue but with Teflon AF™ tubing has shown laboratory stability of 1-2 % over a

month, and a precision of 0.4 % (Lu et al. 2008). A system based on the use of thymol blue with a silicone membrane showed a resolution of ± 1 µatm and a deployment drift of 5 µatm over 6 months when deployed on a moored buoys (Hood and Merlivat 2001). A prototype microfluidic system has recently been developed using the pH indicator 8-Hyrdroxypyrene-1,3,6-Trisulfonic Acid (HPTS)(Ge et al. 2014).

Like several CO_2 sensors, the diffusion of the CO_2 into the sensor is the major contributor to the response time; this is influenced by the type and thickness of the membrane, the temperature as well as the volume of the indicator used for equilibration. For spectrophotometric sensors, response time varies from minutes (DeGrandpre et al. 1995, Lu et al. 2008) up to an hour (Lefevre et al. 1993). The response time of the microfluidic system varies with CO_2 concentration from 1 min at 214 µatm to 3.8 min at 493 µatm (Ge et al. 2014).

The maximum deployment time is currently determined by the battery lifetime, 6 months with 0.5 hr^{-1} resolution for the SAMI-pCO_2 (DeGrandpre et al. 1999). The sensor with bromothymol blue and a Teflon membrane (Lu et al. (2008)) showed drift (> 1-2 %) after 30 days of deployment, speculated to be from light source instability, membrane deterioration and biofouling effects during deployment. Bubbles in the system can also hinder or distort the measurements, particularly in microfluidic systems (Rérolle et al. 2013). The systems have been successfully deployed on moorings (DeGrandpre et al. 1995) and langrian buoys that float with surface currents (Hood and Merlivat 2001). In order to deploy these systems on mobile platforms such as Argo floats and gliders, the response time and physical sensor size needs to be reduced. Microfluidic sensors have smaller reagent requirements (Rérolle et al. 2013) and demonstrated faster pCO_2 response times (1 min), and further development may see them being more widely used on mobile platforms.

3.7 Optodes for pCO_2 measurements

Optodes for CO_2 measurements consist of an analyte-sensitive indicator immobilised in a gas-permeable membrane attached to a fibre optic cable. Light is directed down the fibre optic cable, exciting the indicator, which emits photons subsequently measured with a photodetector. The photodetector can be located either, opposite the chemical spot in a flow-through system or alongside the light source. Response times are controlled by diffusion across the membrane, similar to the spectrophotometric and electrochemical pCO_2 methods.

pCO_2 optodes currently allow measurement of CO_2 in the dissolved phase. They are small and rugged with simple electronics and a lack any wet chemicals and hence have no waste production. As there is no CO_2 consumption, they allow repeated analysis of small sample volumes. The pCO_2 optodes have yet to be commercialised for ocean measurement and are

undergoing initial testing (Table 3.2). The pCO_2 optodes can be deployed directly in seawater with no wet chemicals or gas equilibration prior to measurements, which is a significant advantage compared to the gas based and spectrophotometric CO_2 methods.

3.7.1 Spot Composition

The three main components of optodes are the support, the membrane, and the indicator (Figure 3.2). The supports generally consist of inert strong compounds such as polyethylene terephthalate (Weigl and Wolfbeis 1995).

There may also be an optically isolating layer to limit potential interaction of the light produced by the LED (Light Emitting Diode) with the sample solution, and potential signal loss due to scattering, thereby improving the signal to noise ratio. A suitable material for optical isolation is Teflon AF™, due to its low refractive index and high gas permeability with no water uptake. Silicone rubber may also be used for optical isolation due to its excellent adhesion, chemical inertness and high gas permeability. The optical isolation layer slows the sensor response time by increasing the diffusion distance, and depending on the polymers used to make the gas permeable membrane (specifically with hydrogel membranes), indicator dye and buffer may be absorbed by a silicone optical isolation layer and resulting in non-reproducible results (Neurauter et al. 2000).

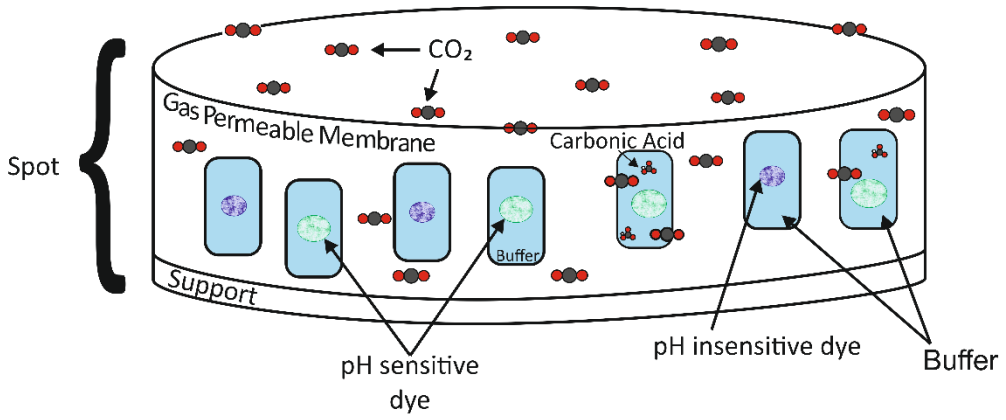

Figure 3.2 Generalised pCO_2 spot composition. The gas permeable membrane is in contact with the solution. The CO_2 molecules diffuse across the membrane and interact with the buffer solutions (denoted by the blue rectangles) and form carbonic acid which in turn interacts with the pH sensitive dye (the green circles) causing a change in the fluorescence signal. The pH insensitive dye is not influenced by the carbonic acid and provides a constant background fluorescence signal. The support is made of a strong, transparent inert compound and is attached to the fibre optic cable.

3.7.1.1 Membrane

The primary consideration with membrane selection is gas permeability followed by non-fluorescent behaviour. Further requirements include mechanical strength and hydrophobicity, with consequently few materials being suitable. Cellulose, sol-gels, and hydrogel membranes fit these requirements.

Ethyl cellulose is a widely used polymer membrane due its stability over the basic pH range and robustness with high permeability towards CO_2 (Neurauter et al. 1999). Cellulose membranes suffer from some ion penetration and require an additional silicone membrane layer between the sample and the spot to prevent this. However, this can have a second purpose as an optical insulation layer (Weigl and Wolfbeis 1995). Hydrogels (such as polyurethane hydrogels (Stahl et al. 2006, Borisov et al. 2011)) use covalent coupling with the indicator as opposed to the ionic interaction of ethyl cellulose, which can lead to increased leaching of indicator dye into sample solution causing irreproducible results. Silica sol-gels have similar features to hydrogels, but use encapsulated silica to form the membrane as opposed to linked polymers used in hydrogels. Both the curing time and starting polymers or silica used to form the hydrogels and sol-gels must be carefully chosen to select the correct pore size and interaction method with the indicator. If the sol-gels and hydrogels are left to cure for too long then the pores will be accessible only for ions such as sulfate, which can interact with the indicators and buffers causing erroneous responses.

3.7.1.2 Indicators

There has been much interest in developing fluorescent molecules for pCO_2 sensors. The use of pH indicators requires the additional presence of a buffer. The response time for optodes is diffusion controlled and increases on the addition of the pH buffer. However, pH indicators are still in common use amongst pCO_2 optodes due to the range of previously determined, suitable pH indicators for the marine pH range. Molecules in use include the pH indicators 1-hydroxy-3,6,8-pyrenetrisulfonic acid (HPTS)(Oter et al. 2006, Zhu et al. 2006, Chu and Lo 2008), bromocresol purple (Nakano and Yoshida 2011) and the diazo dye Sudan III (Von Bültzingslöwen et al. 2003). A recent study proposed the use of pH indicator diketo-pyrrolo-pyrolle (DPP), a chromophore with a high quantum yield over both protonated and deprotonated forms (Schutting et al. 2014). Desirable characteristics for the indicator include stability upon immobilisation, an analytical detection range suitable for CO_2 concentrations in seawater (determined by the indicator isoelectric point upon immobilisation), and a low bleaching rate.

An anion stabiliser is often immobilised alongside the indicator, creating an ion-pair which helps to reduce ion leaching (Muller and Hauser 1996). The stabiliser can also be used as the

immobilised buffer to induce a pH change. Quaternary ammonium hydroxides are the most common molecule type used for this purpose such as tetraoctylammonium (TOA), which when equilibrated with CO_2 gas is a lipophilic hydrogen carbonate buffer. HPTS –TOA is the most widely used pH-ion pair combination in pCO_2 sensing (Neurauter et al. 2000, Ertekin et al. 2003, Oter et al. 2008) due to the high sensitivity of HPTS to pCO_2 with high photostability (under illumination at 460 nm (Offenbacher et al. 1986)), and an excellent quantum yield (near 100 %, (Schröder 2006)). TOA-hydroxide (TOAOH) has also been used with Sudan III (Von Bültzingslöwen et al. 2003). From here on, the analyte-sensitive indicator refers to the combination of pH indicator with a buffer molecule as opposed to a directly CO_2 sensitive molecule.

3.7.1.3 Hardware

The electronic components required for optode operation consist of a light source, optical waveguide, wavelength filters and a photodetector (Figure 3.3). The main variations between optode systems come from selection of the light source and photodetectors. Excitation filters refine the excitation light for the analyte sensitive chemicals, and emission filters exclude unwanted wavelengths from the sample or ambient environment to improve the signal to noise ratio. These are both dependent on the type of light source and photodetector selected, as well as the required wavelength of the indicator.

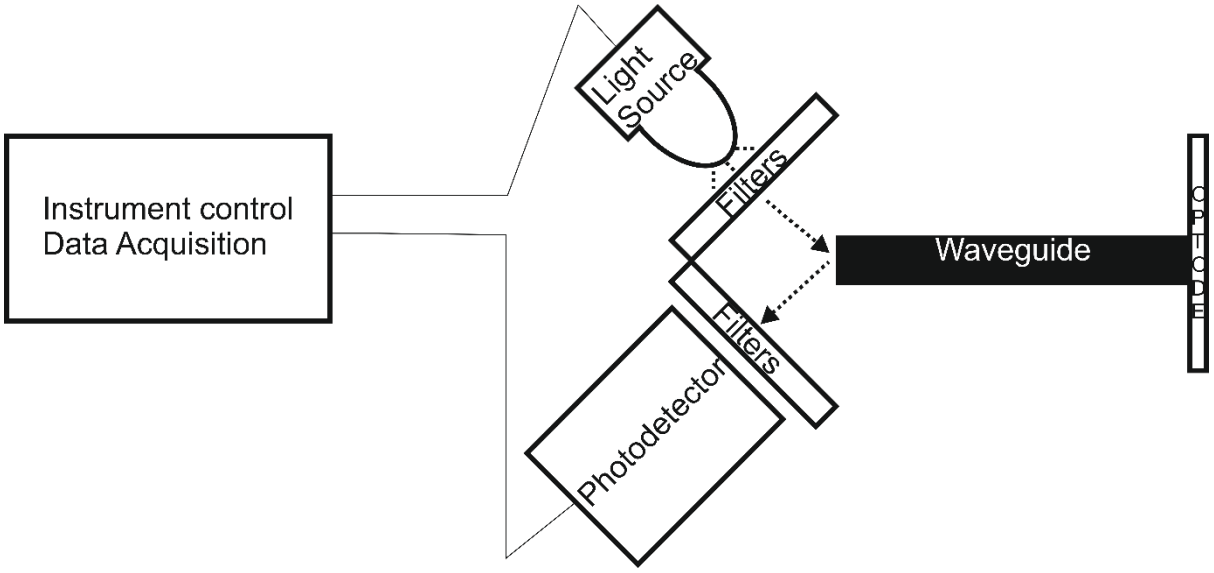

Figure 3.3 Schematic of optode setup.

3.7.2 Light Source

The light source must be able to provide a stable illumination with low power consumption. LED's and laser diodes (LD) are the most commonly applied sources due to their reliability, variety and small size. Laser diodes are less common due to their requirements for higher and more stable power sources (Taib and Narayanaswamy 1995). Light emitting diodes are produced at a variety of different wavelengths and at different sizes. The LEDs are small with low power requirements making them ideal for in situ systems. They also have a full width at half maximum (FWHM) of ca. 25 nm, allowing use without wavelength-discriminators such as filters (Hauser et al. 1995).

3.7.3 Photodetector

The photoemission from the optode spot is quantified with a photodetector, which should have a high sensitivity with a fast response to variations in intensity (Kuswandi et al. 2001). There is a range of suitable detectors from small photodiodes to the larger photon multiplier tubes (PMT). Typically, photodiodes work well when there is a strong light signal, but are not as sensitive towards photon counting and show large noise levels (Knoll 2010). PMTs show a good signal to noise ratio due to the amplification of the photon signal and are able to detect weak intensity light. Charged coupled devices (CCD) linked to cameras can be used to create a planar image of the pCO_2 concentration across the surface of the foil. This simple set-up allows for better imaging of the pCO_2 surface around the spot with fast shutter speeds. However, they require high quality lenses making the systems bulkier compared to photodiodes. Photodiodes are cheaper and smaller, compared to CCDs and PMTs making them attractive for *in situ* pCO_2 optodes.

3.7.4 Analysis methods

There are three main techniques for signal detection in optode systems; fluorescence intensity, fluorescent resonance energy transfer (FRET)(Neurauter et al. 1999) and dual luminophore referencing (DLR)(Burke et al. 2006), with the ratiometric DLR further subdivided between frequency and time domain approaches (*f*-DLR and *t*-DLR respectively).

3.7.4.1 Fluorescence Intensity

Fluorescence intensity measurements simply record, upon excitation, the total fluorescence response from the pCO_2 sensitive indicator dye at a specific wavelength. This approach suffers from interferences due to fluorophore photo bleaching and leaching, sample turbidity resulting in absorption and scattering along the optical path, and excitation light source fluctuations. These intensity only measurements are largely obsolete with the development and application of fluorescence reference molecules (see below) which eliminate these interferences (Klimant et al. 2001).

3.7.4.2 FRET

With FRET analysis, a CO_2 insensitive donor complex luminesces upon excitation with light and transfers energy to a colorimetric pH dependant absorber that has a good absorption spectrum overlap with the fluorescence emission spectrum of the CO_2 insensitive donor complex. At increasing CO_2 (and therefore decreasing pH), the pH dependent absorber becomes protonated and the overlap diminishes giving the CO_2 insensitive donor complex a longer fluorescence lifetime. The lifetime can be measured through a change in the phase angle of a single modulation frequency signal (Von Bültzingslöwen et al. 2003).

The use of FRET allows integration with existing oxygen sensor technology, thereby reducing the development costs (Neurauter et al. 1999). A sensor applying the FRET analysis (row 2, Table 3.2) has rapid response times of 24 s for 99 % of the final value (τ_{99}) with tuneable sensitivity and a limited drift after 2 months storage (<10 %). The FRET applied pCO_2 optodes however show a cross-sensitivity toward oxygen due to the use of a ruthenium compound as the luminescence donor. This method has lower signal to noise ratios, but a susceptibility to measurement signal drift compared to the dual luminophore referencing techniques.

3.7.4.3 *f*-DLR

The *f*-DLR technique uses the change in the phase angle caused by a change in the ratio of the fluorescence signal amplitude of the indicator and reference molecules. The reference fluorophore provides a background fluorescence signal that is not affected by changes in pCO_2; the major change in the phase angle comes from the change in the pCO_2 sensitive indicator fluorescence. The DLR technique requires the two molecules to fluoresce with different lifetimes- a reference dye with a long lifetime (microseconds) and an indicator molecule with a short lifetime (nanoseconds)(Klimant et al. 2001). Frequency domain DLR measurements are applied to individual point measurements as opposed to surface imaging where expensive imaging intensifiers are required (Morgan et al. 1991).

Recent work (Atamanchuk et al. 2014) has shown the suitability of commercially available optode spots (PreSens GmbH) for *f*-DLR based pCO_2 analysis in seawater. The setup achieved a precision of ±2 µatm over a CO_2 range of 200-1000 µatm and a response time (τ_{63}) of 88 s at 20°C. The system is simple plug and play, but irreversibly poisoned by the presence hydrogen sulphide. The system has been successfully deployed in benthic environments as part of carbon capture and storage experiments, in aqua-culturing fisheries and in a dynamic fjord environment, thereby demonstrating the versatility of the optodes and the analysis technique.

3.7.4.4 t-DLR

The DLR approach can also be used in the time domain (*t*-DLR). Both reference and indicator molecules are excited with the same wavelength and the intensity through two 'time windows' is integrated. One window is during the molecular excitation where the response is controlled by the strong fluorescence from the pCO_2 sensitive dye; the other window is during the fluorescence decay where the response is mostly attributed to the pCO_2 insensitive long lifetime dye. The ratio of these integrations can be directly related to the ambient pCO_2 concentration. This method has similar disadvantages to the *f*-DLR technique, such as drift from the indicator and references photobleaching at different rates, and, but the use of time windows allows shorter excitation times of the spot, and therefore increased spot longevity.

Table 3.2 Optodes deployed in marine environments with analysis technique, precision, response time and the desired deployment environment. Where HPTS = 8-hydroxypyrene-1, 3, 6-trisulfonic Acid, TOA = tetraoctyl-ammonium, TOA-OH = tetraoctyl ammonium hydroxide, f-DLR = frequency domain dual lifetime referencing, *t*-DLR = time domain dual lifetime referencing, FRET= fluorescence resonance energy transfer.

Study	Indicator and support	Analysis	Precision	Response time	Deployment
Schroeder et al. (2007)	HPTS, TOA(HCO_3) in ethyl cellulose membrane	*t*-DLR	~	~	Aquatic systems/sediments
Zhu et al. (2006)	HPTS, TOA and TOA-OH in ethyl cellulose membrane	*f*-DLR		<2 min	Marine sediments
Nakano and Yoshida (2011) and Nakano et al. (2006)	Bromocresol purple and sodium hydroxide		5 µatm	<5 min	Ocean water column
Neurauter et al. (2000)	HPTS-TOA in cellulose membrane	FRET	60 ppb	<1 min	Marine

3.8 Optode pCO_2 for ocean monitoring

A pCO_2 sensor system aimed at biotechnological research applications (PreSens GmbH) has been characterised and tested in an oceanographic setting. The spot was illuminated with a blue LED at low power to minimise power requirements (1.8 Watts for the whole system) and foil bleaching, with pCO_2 determination using the *t*-DLR technique. The time taken to achieve 90 % of the final value (τ_{90}) was determined as 160 s at 25 °C, and a laboratory precision of 0.8 µatm (n=10 Dickson certified dissolved inorganic carbon and total alkalinity reference material, batch 144, 20 °C) was observed.

An initial calibration over 290-450 µatm at 25°C and seawater salinity (35) was performed using a gas calibration rig adapted from oxygen measurements (Sosna et al. 2007). The gas calibration rig consists of two 2 L glass containers, joined by a glass "bridge", with one container connected to a pump at its base. Both containers were filled with seawater, and one was saturated with CO_2 by bubbling with CO_2 gas. The other chamber (connected to the pump) had CO_2 removed by bubbling with nitrogen, termed "degassing". The bridge was used to connect the two after the bubbling had ceased and the "degassed" low CO_2 chamber was

sealed with the optode tip in contact with the solution with care taken to ensure there was no air in the chamber at the time of sealing. The pCO_2 was varied by removing small volumes (~1.2 g at salinity 35, 20 °C) of "degassed" pCO_2 seawater solution (~250 µatm). This then pulled saturated seawater (~1000 µatm) across the bridge into the degassed solution. This was then left to stir for two minutes and homogenise the "degassed" solution prior to measurement by the optode. This method allowed smaller pCO_2 changes (~1.3 ppm per pump) to be measured by the optode compared to direct bubbling or manual manipulation techniques.

The pCO_2 optode underwent preliminary deployment as a shipboard system over a period of 6 weeks, from the Labrador Sea across the North Atlantic to the Iceland Basin. The optode was placed in a custom-made dark chamber and water was sampled from the ship's continuous underway seawater supply, which was positioned at ca. 6 m depth. The pCO_2 optode system was deployed alongside a NDIR based dissolved inorganic carbon (DIC) analyser (Apollo SciTech inc 2010), for validation. This shipboard deployment allowed rigorous testing of the spot deployment lifetime, and drift in a variety of oceanographic environments while maintaining the experimental laboratory set-up. The test deployment produced a high-resolution data set, with one measurement every 6 min. To account for and quantify any potential drift (1.7 µatm over the 5 week cruise), certified reference materials for total alkalinity (TA) and DIC, obtained from Prof. A. Dickson (Scripps, USA), were measured every 24 h. This daily measurement allowed a long-term shipboard precision of 9.5 µatm (n=64) to be derived. The observed pCO_2 ranged from ~100 µatm in the Labrador Sea up to ~450 µatm where sea ice was present close to Greenland. The North Atlantic Irminger current regions was ca. 400 ppm. The lowest concentrations were observed in regions influenced by polar currents where sea-ice recently retreated. The loss of sea ice led to phytoplankton blooms causing the low CO_2 levels observed.

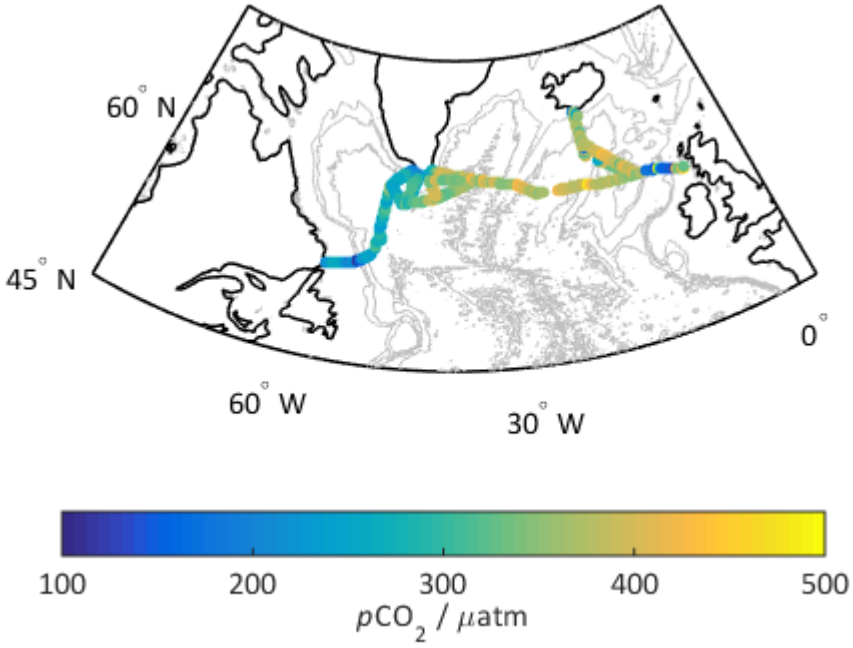

Figure 3.4 Shipboard deployment of a pCO_2 optode spot using the t-DLR analysis technique over a period of 7 weeks, with initial pCO_2 concentration denoted by the coloured points overlaid on the cruise track.

3.9 Summary and Future Directions

pCO_2 sensors with NDIR detection are currently the most developed technology for *in situ* deployment in ocean waters, but suffer from spectrometer drift and the CO_2 needs to equilibrated into the gas phase prior to measurement. NDIR pCO_2 sensors have been deployed on moorings and buoys, but further work is required to improve the response time (up to 20 min (Battelle 2011)) and minimise the need for frequent gas calibrations before deployment on mobile platforms. The wet-chemical spectrophotometric techniques show rapid response times in the case of the microfluidic systems, with slower responses for the larger volume systems but both have the advantage of being virtually calibration free. The pCO_2- ISFET shows promising initial results but further calibration, and laboratory testing is required before a more robust evaluation and comparison can be provided. The pCO_2 optode systems show comparable response times to the spectrophotometric and NDIR systems, with no requirement for gas equilibrium or wet chemical storage. The pCO_2 optode system applying *f*-DLR analysis has demonstrated the versatility of deployment ranging from seafloor CCS to aquaculture activity monitoring (Atamanchuk et al. 2014).

The work presented here, indicates the suitability for pCO_2 optode deployment in open oceans, opening up future development towards placement on mobile platforms. Further developments to pCO_2 optodes should involve the development of calibrations using atmospheric pCO_2 as well as seawater pCO_2. The measurement of both atmospheric and

marine gases has proved a success with oxygen optodes, and calibrations with atmospheric CO_2 would be the next step towards using pCO_2 optodes to quantify the CO_2 air-sea flux quantification. Optode spot design has also is progressing towards multiple analyte determinations with combinations such as pCO_2 /O_2 /pH, and/or temperature within a single sensing spot (Schroeder et al. 2007). This will be a significant advantage on platforms such as Argo floats and gliders where space and weight are limited. However, optodes are still in primary development phases, for example more work is required to fully quantify any pressure changes for when they are deployed on mobile platforms, and further investigation into ways to reduce the response time by limiting the thickness of membranes and optical isolation layers, and investigating pCO_2 indicators opposed to the use of pH indicators with a buffer. There is a need for more *in situ* testing over longer periods before they can be considered as technologically advanced as the NDIR technique.

Chapter 4:

Characterisation of a pCO_2 sensor spot

Abstract

The ocean is a major sink for anthropogenically produced CO_2, causing a myriad of changes to ocean chemistry. To monitor these changes and provide a chemical background for biological and biogeochemical studies, precise pCO_2 sensors are required. Optodes have the potential to measure *in situ* CO_2 concentrations without the need for wet chemicals or bulky gas equilibration chambers, common amongst other pCO_2 systems.

The optode sensing spot was illuminated with low intensity light (0.2 mA, 0.72 mWatt), and the time-domain dual lifetime referencing analysis method used to maximise spot lifetime and reduce overall power consumption of the instrument (1.8 Watt). A gas calibration rig, previously applied to dissolved oxygen calibrations, was used for pCO_2 calibration over a range of 280 – 1000 µatm. A response time to reach 90 % of the final value (t_{90}) of 165 s at 25°C was determined with a temperature dependence of -39 µatm $°C^{-1}$, and a chlorophyll dependence of 1.66 µatm $(µg/L)^{-1}$. Shipboard precision over a 6 week deployment was 9.5 µatm. Further work is required to optimise the gas calibration rig for CO_2 calibrations, and determine the full influence of different fluorescent compounds in seawater on the optode response.

4.1 Introduction

Atmospheric emissions of carbon dioxide (CO_2) due to fossil fuel combustion and cement production totalled ca. 330 Pg C in the period between 1850 and 2006 (Canadell et al., 2007), while land use changes contributed a further 158 Pg C. The increase in atmospheric CO_2 concentrations is mirrored in the ocean, with an increase of ca. 1.3 Pg C year $^{-1}$, between 1960 and 2011 (Le Quéré et al., 2013). The increasing anthropogenic CO_2 uptake by the ocean has caused changes to biogeochemical processes with potentially detrimental impacts on ecosystems (Doney et al., 2009). To understand these potential impacts and quantify changes to the marine carbonate system, it is important to collect CO_2 data with high spatial and temporal resolution, making autonomous *in situ* sensors desirable. The ideal characteristics for *in situ* chemical sensors include a small size with low power consumption, good precision and the possibility for high frequency measurements (Byrne, 2014). The desired precision for autonomous seawater pCO_2 sensors is 2 µatm (Pierrot et al., 2009), to enable regional air-sea CO_2 fluxes to be constrained within 0.2 Pg C yr^{-1}. There are several *in situ* pCO_2 systems available with a precision of 1 µatm measuring for the surface seawater pCO_2 range of 0-1000 µatm (Sunburst Sensors LLC, Battelle, 2011, Contros Systems & Solutions, 2015) but these require either gas equilibration or mechanical components to move wet chemicals through the analytical systems, making deployment more complex.

Optode based sensors employ fluorescent indicators immobilised in a membrane, termed sensor spot, attached to an optical waveguide such as a fibre optic cable. Optodes measure pCO_2 in the solution using fluorescent techniques without subsampling or consumption of CO_2. Measurements based on only the indicator fluorescence intensity are generally avoided due to drift caused by light intensity fluctuations, and solution turbidity (Klimant et al., 2001). To reduce these adverse influences, a reference dye is immobilised alongside the indicator dye, allowing ratiometric analysis. The immobilised reference dye must have similar excitation and emission wavelengths to the pCO_2 indicator while its fluorescence output must be insensitive to pCO_2 changes, and the fluorescence decay time must be longer than that of the indicator. There are 3 main detection and analysis methods: time domain-dual lifetime referencing (*t*-DLR), frequency domain- dual lifetime referencing (*f*-DLR)(Burke et al., 2006), and fluorescence resonance energy transfer (FRET)(Neurauter et al., 1999). These are detailed further in Chapter 3.

Photobleaching is a limiting factor with the use of any fluorescence based sensor, causing irreversible changes to the fluorophore such that it no longer fluoresces on excitation, ultimately causing increased measurement drift and imprecision over time until a response is no longer detectable. The length of excitation time is directly proportional to photobleaching

of the indicator and reference dyes (Borisov et al., 2011). The t-DLR method allows short LED pulses, reducing the overall irradiation time of the spot and prolonging the spot longevity.

The sensor spots used in this study, and throughout this thesis, were originally designed for use in physiological solutions so a thorough characterisation was required to determine their suitability for marine measurements. Atamanchuk (2013) applied the *f*-DLR method over a wide pCO_2 range (0-10,000 µatm), and produced an eighth by third degree polynomial to convert the fluorescent response to pCO_2 (Atamanchuk et al., 2014), proving that the sensors were capable of seawater measurements.

In this chapter, the *t*-DLR method was applied to the PreSens pCO_2 sensor spots to limit the potential for photobleaching of the spot. The calibration was simplified by focusing on a smaller pCO_2 range from 280 - 1000 µatm, commonly found in seawater. A gas calibration rig allowed for small incremental pCO_2 increases (~1.5 µatm), and varied temperatures (5, 10, 20 °C) and salinities (20, 30, 35), with results evaluated in context of previous studies. An investigation into the effects of chlorophyll concentration on sensor response was undertaken and results from a preliminary deployment of the optode as an underway shipboard system alongside an Apollo DIC infrared sensor are presented.

4.2 pCO_2 sensor spot

The pCO_2 spots were obtained from PreSens GmbH (www.presens.de). The sensor spot consists of a gas permeable, ion-impermeable membrane, secured to a support structure, and containing a pH sensitive dye, a reference dye and a buffer (Atamanchuk et al., 2014). Nevertheless, the exact composition of the pCO_2 spots is unknown.

The choice of membrane, buffer and indicator will influence the range and sensitivity of the sensor spot. Membranes must be gas permeable and ion impermeable making them more hydrophobic than pH sensor membranes. They must also have a pore size that is sufficiently large for CO_2 molecules to diffuse through to the indicators. Despite the need for a buffer molecule to convert pCO_2 change to pH, pH indicators are commonly used in pCO_2 sensor spots due to their well characterised response in seawater; for example, 8-hydroxpyrene-1, 3, 6-trisulfonic acid (HPTS) is used due to its stability on immobilisation and strong fluorescent response (Schulman et al., 1995, Wencel et al., 2009, Wencel et al., 2014). Ideally, the pK_a' should be close to pH 7.8 with a measurement range that spans the seawater pH range, ca. 7.6 - 8.4. However, the polar nature of the pH indicators (being weak acids) makes them less suited to being immobilised in the more hydrophobic gas permeable membranes. Buffer molecules can be used to stabilise the indictors in the membrane, by immobilisation alongside the indicator as a buffer-indicator ion-pair. Tetraoctyl ammonium (TOA) exposed

to CO_2 prior to immobilisation is commonly used as both as a buffer and an indicator stabiliser.

The change in protonation state of the immobilised pH indicator will cause a change, upon excitation, in the intensity of the emitted fluorescence, controlled by the buffer molecule. The interactions between the immobilised buffer and indicator have been well described previously by Mills et al. (1992) and Chu and Lo (2008) and briefly here. The buffer-indicator ion pair can be considered as equation 4.1.

Equation 4.1

$$QOH + HD \rightleftharpoons \{Q^+D^- \cdot xH_2O\}$$

Where QOH is the buffer molecule and HD is the pH indicator of interest. They interact with dissolved pCO_2 as per equation 4.2, with the pH indicator protonation occurring only upon the dissolution of CO_2 to HCO_3^-.

Equation 4.2

$$\{Q^+D^- \cdot (x-1)H_2O \cdot H_2CO_3\} \rightleftharpoons \{Q^+HCO_3^- \cdot (x-1)H_2O \cdot HD\}$$

The change in pH indicator fluorescence can be related back to the pCO_2 of the solution. The same light emission and excitation data analysis (*t*-DLR) as applied to pH spots (Chapter 2) is utilised.

To produce a single pCO_2 data point, the light source (blue light emitting diode (LED)) was pulsed on for 5 µs (t_{ex}) and off for 20.5 µs (t_{em}). The LED light excites the pH indicator causing the dye molecules to fluoresce. When the LED was turned off, the fluorescence signal decayed. The LED pulsing is repeated, and averaged to give a fluorescent decay profile every 0.5 s.

With the LED on, the emission (t_{ex}) is a combination of fluorescence from the pH sensitive (A_{pH}) and reference fluorophores ($A_{ref\text{-}ex}$). We assumed that the integration of the fluorescence intensity when the LED is off, (t_{em}) is entirely derived from the decay of the pH-inert reference dye emission ($A_{ref\text{-}em}$) due to the shorter decay lifetime of the pH sensitive fluorophore. The ratio of intensity integrated t_{ex} to intensity integrated t_{em} (R, Equation 4.3) relates to the solution pCO_2 through the calibration discussed herein. Improved precision and signal to noise ratio were achieved by measuring each sample for 200 s and integrating the fluorescence decay profiles over 10 s intervals.

$$R = \frac{t_{ex}}{t_{em}} = \frac{A_{pH} + A_{ref-ex}}{A_{ref-em}}$$

Equation 4.3 Conversion of optode fluorescence to R, which is correlated to pCO_2

4.3 Methods

4.3.1 Hardware

The same hardware as used for the pH sensor spot was applied to the pCO_2 spot, detailed briefly here. A blue LED (5 mm diameter, λ 470 nm, Farnell) with excitation filters (SemRock single bandpass filter 475 nm and SemRock short pass edge filter 532 nm) was pulsed at a low intensity (0.2 mA, 0.72 mWatt) to excite the reference and indicator dyes within the immobilised sensor spot. The blue light is channelled through a fibre optic cable (600 μm diameter multimode optical fibres, Thorlabs, 3.8 mm diameter, 2 m length) to the sensor spot. The fluorescence decay (red light λ 630 nm) travels back through the fibre optic cable to a dichroic beamsplitter (SemRock single edge BrightLine, 560 nm), used to separate the blue excitation light from the returning emission. The red light passes through the dichroic beamsplitter (while blue light is reflecting), three emission filters (SemRock single bandpass filter 609 nm, SemRock short pass edge filter 785 nm and SemRock long-pass edge filter 568 nm) to a photon multiplier tube (PMT; Hamamatsu). The PMT and LED are controlled by a field-programmable gate array (FPGA, Xilinx Spartan-3 XC3S400-5PQ208C FPGA).

Sensoptics Ltd[1] assembled the custom-made electronics (Sensoptics, SGS 42000) and developed the software used to record the fluorescence decay curve (Sensoptics Photon Counter V1.2).

4.3.2 Artificial Seawater Solutions

Artificial seawater solutions were made up according to Kester et al. (1967). This seawater was selected due to the inclusion of boric acid, which is known to influence CO_2 dissolution through the activity coefficients of the carbonate equilibrium constants k_1 and k_2 (Chapter 1). Salts were obtained from Sigma Aldrich (analytical grade); while CO_2 / N_2 gas (1000 ppm) was obtained from BOC. N_2 gas was used directly from the National Oceanography Centre's building supply. Deionised water (MilliQ, Millipore, > 18.2 MΩ cm^{-1}) was used to prepare and subsequently dilute all solutions.

[1] Sensoptics is now a wholly owned subsidiary of Optasense (A QinetiQ company) www.optasense.com

Magnesium chloride ($MgCl_2$, 1 mol kg^{-1}) and calcium chloride ($CaCl_2$, 1 mol kg^{-1}) solutions were calibrated using gravimetric Mohr titrations (Vogel, 1989). Where required, calcium chloride was substituted for strontium chloride. Sodium chloride, potassium chloride, sodium sulfate, and potassium bromide were all dried at 110°C for 1 hour prior to weighing. The other salts (boric acid, sodium bicarbonate and sodium fluoride) were weighed directly into solution.

Sodium chloride solutions were made up with concentrations of 35 g kg^{-1}, 25 g kg^{-1}, 15 g kg^{-1}, and 5 g kg^{-1} to obtain salinities of 35, 25, 15, and 5. Dissolved inorganic carbon (DIC) and total alkalinity (TA) Certified Reference Material (CRM) seawater (batch 144) from Prof. A. Dickson at Scripps Institute of Oceanography (USA) was used to verify the pCO_2 optode precision.

4.3.3 Methods to alter levels of pCO_2

4.3.3.1 Sosna Rig

The Sosna et al. (2007) gas calibration methodology, originally developed for dissolved oxygen microelectrode calibration, was applied to the calibration of the CO_2 optode. Figure 4.1 shows a schematic of the laboratory glassware setup used.

Initially a 2 L seawater solution (chamber B) was saturated with CO_2 by bubbling CO_2 /N_2 gas that was humidified in chamber A. Simultaneously, a 2 L solution of seawater was degassed with nitrogen (chamber C, inlet F). Two “top-Up” solutions of equal salinity as in the 2 L chambers were equilibrated to the same temperature and gassed / degassed alongside the rig. Samples of the saturated chamber and the degassed chamber were collected to verify the pCO_2 levels.

Once degassing was complete, the inlet labelled F was sealed. Valve E was then opened and the bridge between chamber C and B filled with degassed solution, and the bridge between chambers C and B checked to ensure there were no bubbles. Chamber C was then topped up with more degassed seawater from the “top-up” solution, and the optode slotted into place ensuring, again, there were no bubbles (in the chamber or in the bridge). Chamber B was topped up with further gassed seawater from the “top-up” solution. One pump cycle was then run to ensure there were no bubbles or air entering the measurement cell. Chamber B was left open to the atmosphere, unsealed with a lid resting on top to limit gas exchange.

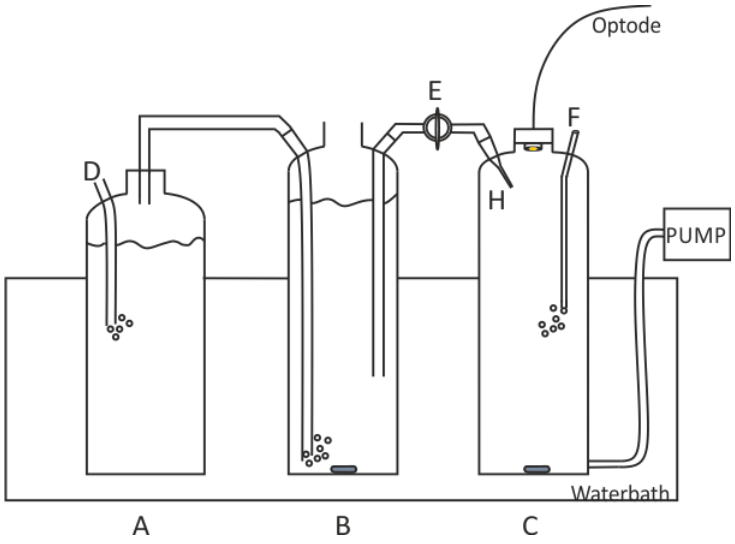

Figure 4.1 Schematic of the Sosna calibration rig. A: 1.5 L Gas humidifier, B: 2L saturated solution, C: 2L sample solution, D: CO_2 gas tube to CO_2 /N_2 gas cylinder, E: Bridge with valve, F: nitrogen gas inlet, H: Saturated solution inlet capillary. Figure adapted from Sosna et al. (2007).

A calibration curve was generated by sequentially adding small amounts of solution B to solution C (1.2 g, 2 s pump time). Each pump pulled a small amount of solution C out of the chamber, which was replaced with the same amount of solution B (saturated solution). After each pump action, the solution was stirred for 3 minutes to allow solution homogeneity before the optode measurements began.

The concentration of carbon dioxide at each step was calculated using Equation 4.4.

$$c_i = c_{i-1} + \frac{c_{sat} V_{ex}}{V_{tot}} - \frac{c_{i-1} V_{ex}}{V_{tot}}$$

Equation 4.4 The equation to determine the CO_2 concentration from Sosna et al. (2007). c_i concentration of solution C after the ith addition of CO_2 saturated solution, V_{ex} weight injected/removed with each pump, V_{tot} total weight of chamber C (2 L ~2 Kg), c_{sat} concentration of CO_2 in saturated solution (B).

In order to rely on Equation 4.4 to determine the value of CO_2 in chamber C, the V_{ex} must be small such that none of the CO_2 added from the saturated solution is removed during the pumping. The sensitivity of the pCO_2 optode was determined by incrementally increasing the pumping time (pumping amount) until a change was detected by the optode, ensuring the pumping time was below the maximum V_{ex} (pump time of 5 seconds, weight at salinity 35 of 3.21 g). The optode was able to detect changes at a 2 s pump time, equivalent to 1.2 g of seawater and 1.3 µatm. Any bubbles found in the bridge or chamber C, will change the solution volume and may cause dissolved CO_2 to diffuse into the air bubble, thereby changing the pCO_2^{SW} concentration in chamber C. Therefore, when a bubble was observed at the end of the calibration run (or at any point during) the results were discarded. All work using the

sosna gas-calibration rig was carried out in a dark room in order to minimise optode spot dye photobleaching from excess ambient light, due to the clear glass of the calibration rig.

At the end of each experiment, sample aliquots were taken to verify the final pCO_2. The pCO_2 was calculated from pH measured with a glass electrode and DIC measured using an Apollo SciTech DIC analyser. The software programme CO_2SYS (Matlab v2.1) was used to determine pCO_2 with carbon dissociation constants from Mehrbach et al. (1973), refitted by Dickson and Millero (1987), the sulphate dissociation constants from Dickson (1990) and boron-chlorinity ratio from Lee et al. (2010). The error in calculated pCO_2 from pH and DIC is ± 1.8 µatm (Millero, 2007).

4.3.3.2 Manual manipulation

The manual manipulation of seawater to pre-determined pCO_2 levels was based on the calibrations of Muller and Hauser (1996) and Burke et al. (2006). Kester's artificial seawater, 1 M sodium bicarbonate solution with 35 g of sodium chloride and 1 M hydrochloric acid with 35 g sodium chloride were made up. The seawater was degassed to a set pH (8.296) in order to obtain an initial pCO_2 of ca. 300 ppm.

The oa function in the seacarb library was used in R 3.04 (Lavigne et al., 2011), to determine the quantities of sodium bicarbonate and hydrochloric acid to add to the artificial seawater to induce a specific pCO_2 level. The pH was determined on the total scale, the carbonate dissociation constants were from Mehrbach et al. (1973), the sulfate dissociation constant from Dickson (1990), the fluoride dissociation constant from Dickson and Riley (1979 in (DOE, 1994)) and finally the boron-chlorinity ratio from Lee et al. (2010). The solutions were subsampled and DIC measured to confirm the pCO_2, as for the gas calibration rig.

4.3.4 Equipment and Additional Reference material

A glass electrode (Orion VersaStar with a Fischer FB68801 Semi-micro pH electrode) was used to determine the pH of calibration samples, and DIC was measured using an Apollo SciTech AS-C3 DIC analyser.

The reference bench top glass electrode used internal temperature compensation derived from the Nernst equation, when determining pH. Certified Reference Material (CRM) tris (2-Amino-2-hydroxymethyl-propane-1,3-diol) pH buffer in artificial seawater (Batch 10, pH_{tot} 8.0924, salinity 35, 25 °C) from Prof. A. Dickson at Scripps Institute of Oceanography (USA) were used for calibration of the electrode. All pH values reported in this chapter are on the total pH scale.

The Apollo DIC analyser acidifies the samples with 1 M phosphoric acid, converting all the dissolved inorganic carbon to gaseous CO_2 which is subsequently measured using a LICOR infrared spectrometer (Apollo SciTech inc, 2010). The samples were analysed in batches to reduce the required instrument time. DIC and TA CRMs (batches 138, 141, 142 and 144) were used for calibration at the start of analysis and every 8 subsequent samples to correct for the IR spectrometer drift.

4.3.5 Salinity and Temperature variations

Salinity of the solutions was determined with a conductivity probe (Orion VersaStar with an Orion DuraProbe 013005MD conductivity cell, ± 0.01 ppt) prior to measurement. The probe multiplies the cell constant (distance between the electrodes in the probe) multiplied by the measured conductance, and compares the product to a previously measured conductivity standard to determine salinity. Sodium chloride solutions and artificial seawater with the same salinities were left to equilibrate, for 3 days, to ambient lab CO_2 levels prior to measurement. Lower salinity artificial seawater (salinity 5, 15, 25, and 30) were made by diluting the Kester artificial seawater, keeping the ratio of salts the same, and only altering the ratio of salt to water.

Temperature variations were achieved by changing the temperature of the waterbath in which the sosna rig was placed, and allowing one to two hours for solution equilibration prior to gassing or degassing and measurement. The temperature during the measurements was maintained with the water bath (Grant TX150 ST26, ± 0.01 °C). Temperature of the solutions was checked prior to measurement with an ATP DT-612 dual input K-type thermometer (± 0.1 °C). Carbon dioxide has a temperature dependence of $\delta \ln(fCO_2) / \delta T = 4$ % $°C^{-1}$ (Millero, 1995), for a 0.1 °C change a CO_2 change of 0.12 ppm will be observed (below the current instrument precision).

4.3.6 Chlorophyll Interference with the pCO_2 measurement

The coccolithophore *Emiliania Huxleyi* was cultured by Lucie Munns and Rosie Sheward, in artificial seawater at 16 °C, under 100 µE light. The culture was then diluted with artificial seawater to 100 ml chlorophyll concentrations of 0.1, 1, 2, 2.5, 5, 10 µg L^{-1}. Samples were stored (ca. 2 hours) in the dark between dilution and measurement. The pH and salinity of each sample was measured at 20 °C, and pCO_2 (as above) bubbled through each sample in the dark until a constant pH (8.022) was reached immediately prior to measurement.

4.3.7 Metrology

The response time of the pCO_2 spot is diffusion controlled. The response time was determined by measuring the pCO_2 of the water (~280 ppm) with the optode for 3 minutes before injecting the solution with high concentration (~800 ppm) pCO_2 seawater and measuring for a further 3 minutes. This was performed at 25 °C.

The spot was subjected to a bleaching experiment to determine if exposure to higher intensities of blue light would influence the measurement quality or cause photo bleaching (Zhu et al., 2006). The spot was subjected initially with light of the LED powered with 0.2 mA as normal, for 200 seconds. The spot was then illuminated with the LED at 2 mA (10 times the normal intensity) for 2 hours continuously (no LED pulses). The spots response was then re-measured with the LED powered at 0.2 mA for 200 s, to asses for any sensor response changes or drift.

In order to assess the drift of the optode, it was left over a period of three days in artificial seawater in a sealed gas calibration rig measuring every 5 minutes. This provided a number of measurements (494) from which to assess the drift and precision of the sensor. The drift was further assessed through the weekly measurement of DIC/TA CRMS (Batches 135 and 136, at 20 °C) from Prof. A. Dickson (Scripps Institute of Oceanography, USA) on a 6-week long cruise across the North Atlantic where the optode was used to autonomously measure underway seawater every 6 minutes.

Short- term precision was calculated as the standard deviation of 10 repeats of DIC and TA certified seawater (Batch 144). Long-term precision was calculated from the pooled standard deviations ($\sqrt{\sum SS / \sum D_f}$, where SS is the sum of squares for individual CRM and D_f is degrees of freedom for individual CRM measurement) of DIC/TA CRMs (Batches 135 and 136, at 20 °C) measured throughout the cruise.

4.4 Results and Discussion

4.4.1 Calibration

The PreSens pCO_2 sensor spots are designed for the concentration range of 1 % - 25 % pCO_2, which is significantly wider than found in the surface ocean (ca. 300 – 500 ppm). Previous calibrations with *f*-DLR looked at a similarly wide range (0-10,000 µatm) (Atamanchuk et al., 2014). To determine the suitability of the *t*-DLR method with the lower pCO_2 range, an initial calibration was undertaken to determine the expected response from the optode. The pCO_2 of artificial seawater sample was altered by injecting 1 M sodium bicarbonate into freshly made seawater solutions followed by 1 M hydrochloric acid at room temperature (ca. 20 °C). The pCO_2 was varied from 300 ppm to just above 550 ppm shown in Figure 4.2. The initial calibration produced a linear fit, with a gradient of -0.0009 R/ppm and an R^2 of 0.94.

This initial calibration was expanded upon using the gas calibration rig to produce a calibration with smaller pCO_2 changes, Figure 4.3. The experiment time was greater due to the smaller increments andwas performed in a water bath at 20 °C. A straight line fit (as the initial calibration) showed a poorer fit (R^2 = 0.83) with the more detailed calibration, fitting to a second order polynomial (R^2 = 0.91).

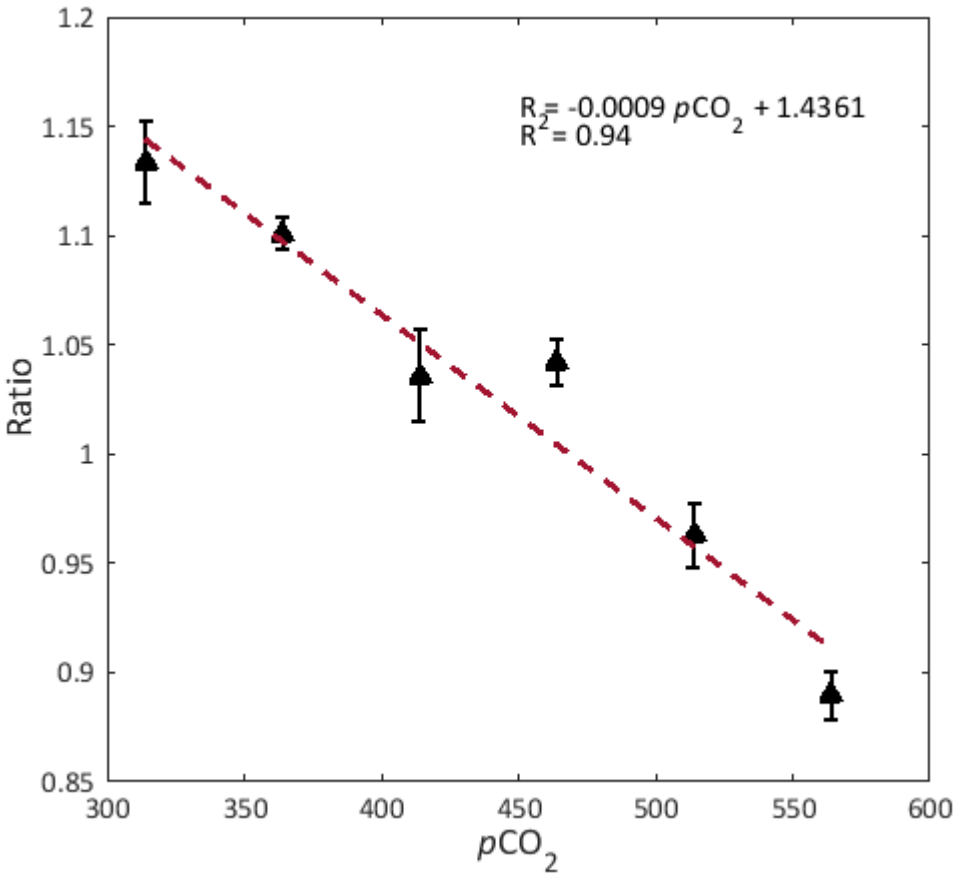

Figure 4.2 Manual manipulation of pCO_2 in artificial seawater (Kester et al., 1967) against optode output, R (equation 4.3) at room temperature. The error bars are the standard deviation of the repeated measurements (n=3) of the solution.

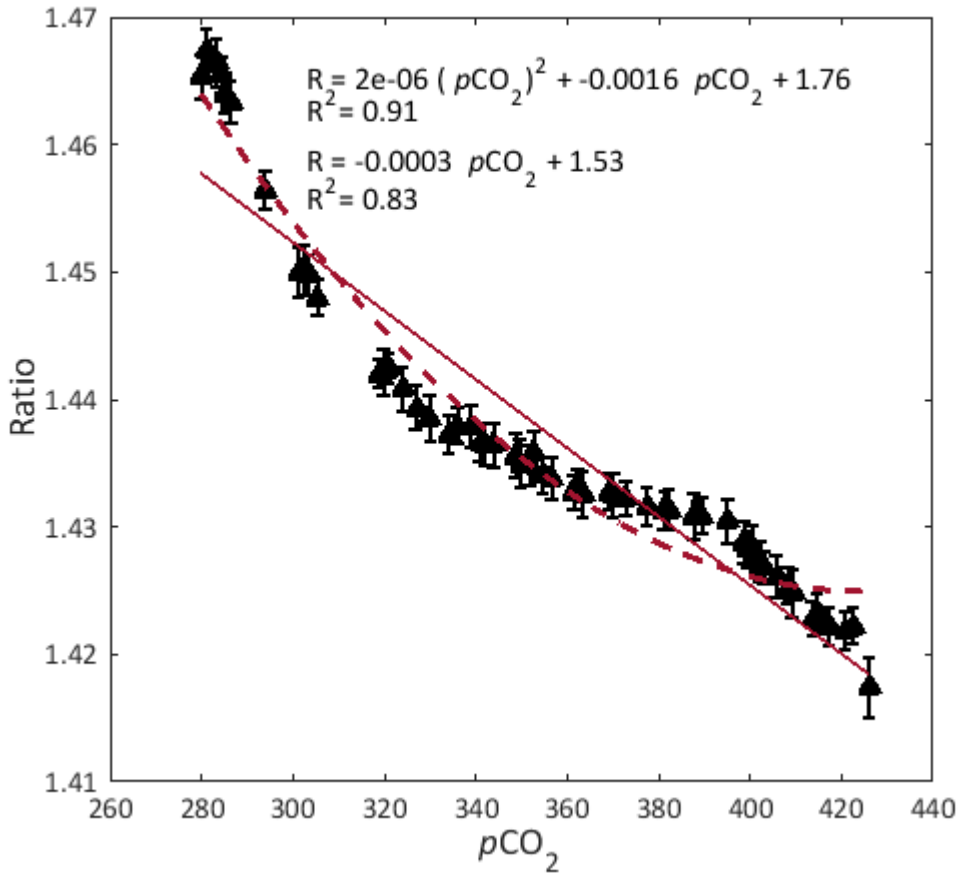

Figure 4.3 Initial calibration run with the sosna rig in artificial seawater over a pCO_2 range of 280-420 µatm at 20 °C. The error bars are the standard deviation in R (equation 4.3) for each incremental measurement. The dotted red line is the second order polynomial best fit with the equation and R^2 in the top right corner of the figure, the straight red line is a linear fit, with the equation below the polynomial equation.

The negative gradient shown by both calibrations is a result of the use of the pH indicator and is common across pCO_2 optodes (Ertekin et al., 2003). At higher pCO_2 levels, protons are released, which alter the protonation state of pH indicator and consequently the fluorescence output. The fluorescence of the pH indicator is increased at more basic pH (Liebsch et al., 2000, Schröder et al., 2005) corresponding to lower pCO_2 values. The gradient and range of R shown in both figures is small due to the small pH range across the desired pCO_2 range (< 0.2 pH across the range 280 – 420 ppm) and the measured range of pCO_2 at the lower end of the quoted spot sensitivity. The large error bars in the initial calibration are due to the poor precision from the manual manipulation procedure, while the difference in the Ratio range between Figure 4.2 and Figure 4.3 is likely related to the use of differing spot batches.

Neurauter et al. (2000) found that the ratio of the buffer molecule concentration to indicator concentration will alter the range and sensitivity, with enhanced concentrations of tetraoctyl ammonium hydroxide (TOAOH) producing more linear fits and therefore a higher sensitivity. However, at high TOAOH concentrations the increase in sensitivity is limited (Zhu et al.,

2006). The linear fit in figure 4.2 points towards the higher concentrations of TOAOH in the spot, explaining the wide measurement range of the spot. The polynomial fits the data better but extrapolation does not allow for the wider range of pCO_2 values as reported previously (Atamanchuk et al., 2014). This initial calibration curve, at 20°C provided a starting point to expand with temperature and salinity variations.

4.4.2 Temperature Variations

To determine the temperature effect on R (equation 4.3), the Sosna rig calibration was repeated at 3 different temperatures, 5°C, 10°C, with the salinity of the artificial seawater kept at 35. The second order polynomial best fits (red dashed line) in figure 4.4 have the general form of equation 4.5, and the coefficients are specified in table 4. 1. The linear fits (grey dash-dot line, figure 4.4) are shown for comparison with the coefficients in table 4.2.

Equation 4.5

$$\text{Ratio} = A \cdot (pCO_2)^2 + B \cdot pCO_2 + C$$

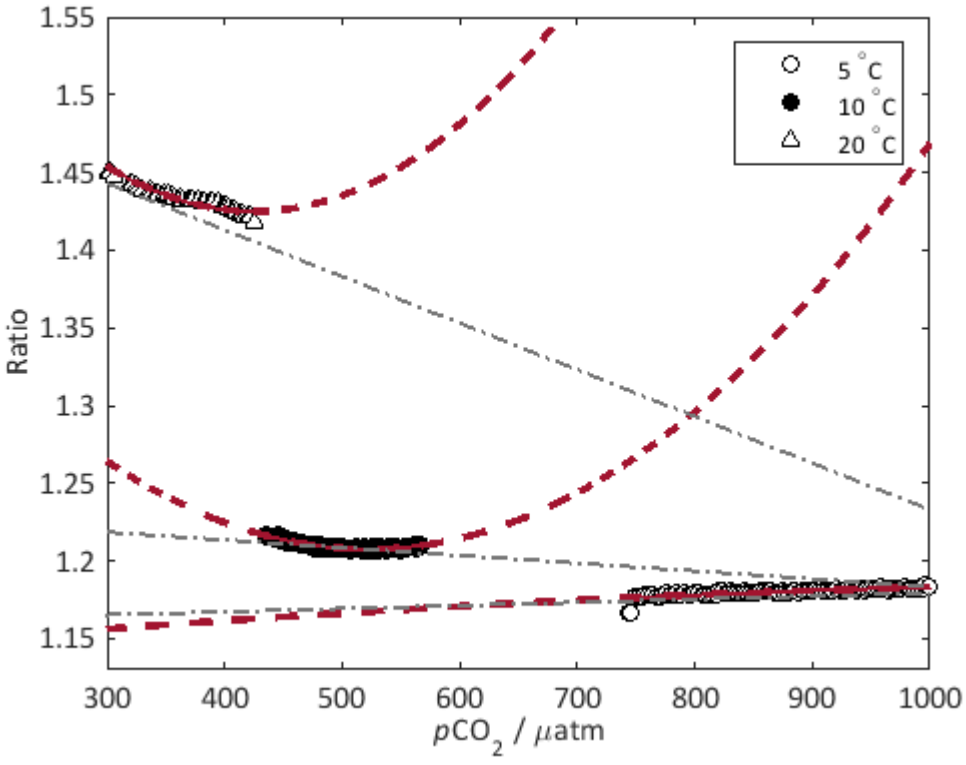

Figure 4.4 Optode temperature variations measured in Kester artificial seawater at salinity of 35. Open triangles indicate 20 °C, closed circles indicate 10 °C and open circles 5 °C. The solid red lines show the fitted data (table 4.1), and the dashed red lines indicate the extrapolation of each, to allow comparison between temperatures. The grey dash-dot lines are the linear regressions at each temperature listed in table 4.2.

Table 4.1 Coefficients of the polynomial temperature fits in figure 4.4 according to equation 4.5.

Temperature	A	B	C	R^2
20°C	2×10^{-6}	-0.0016	1.76	0.91
10°C	1.15×10^{-6}	-0.0012	1.52	0.92
5°C	-2.46×10^{-8}	7.07×10^{-5}	1.14	0.81

Table 4.2 Coefficients of the linear fits in figure 4.4

Temperature	A	C	R^2
20°C	-2.69×10^{-4}	1.533	0.83
10°C	-4.74×10^{-5}	1.2336	0.54
5°C	2.37×10^{-5}	1.1594	0.8

Temperature dependence is common amongst these sensor spots (Mills et al., 1992, Borisov et al., 2011, Atamanchuk et al., 2014). The temperature dependence is primarily caused by the apparent indicator dissociation constant (pK_a'). As the temperature increases the pK_a' increases causing the measurement range of the pH indicator to shift to more basic pH. As the indicator range becomes more basic, the spot becomes less sensitive over the lower pCO_2 range (Borisov et al., 2011). The pK_a' of the buffer will also increase with temperature, and enhances the sensitivity loss through the flattening of the gradient (Mills et al., 1992). This is flattening of the gradients is seen in both polynomial fit and the linear fit to the data (tables 4.1 and 4.2 respectively) with the gradient positive at 5 °C. By inclusion of temperature in her calibration Atamanchuk et al. (2014) successfully compensated for the dependence, indicated the necessity of temperature inclusion in the calibration algorithm. However, the significant loss of sensitivity at 5 °C indicates that these spots require further investigation into alternative pH indicator-buffer combinations, with lower pK_a' to improve sensitivity at the low temperatures, and allow application of the spots *in situ* in colder environments.

4.4.3 Salinity Variations

In her doctoral thesis, Atamanchuk (2013) applied multivariate experiments with artificial seawater ranging from 5 psu to 35 psu and observed no salinity influence, but a salinity drift of 200-250 µatm in sodium chloride solutions. For the purpose of this study, it is imperative that the cause of this difference is understood.

It is known that preconditioning the spot is an essential preparation prior to deployment in seawater conditions. The ionic strength of the solution will influence the activity of the water molecules and the fugacity of the CO_2 molecules through the extended Debye-Hückel limiting law, equation 4.7. The counter charge of the ionic atmosphere surrounding each ion or molecule in seawater arises from the competitive influences of thermal motion and coulombic interactions. This ionic atmosphere, made up of other ions in solution, increases with increasing ionic strength, lowering the activity coefficient (γ), and so the activity, which

in turn lowers the chemical potential (Equation 4.6) compared to an ideal solution of the molecule.

Equation 4.6 The chemical potential of any ion or gas in solution, μ_i is related to the activity, a_i through the chemical potential under standard conditions μ_i^{Θ} , the gas constant R and the temperature of the solution. The activity may be substituted for fugacity, f_i when referring to gases.

$$\mu_i = \mu_i^{\Theta} + RTln\, a_i$$

Equation 4.7 The extended Debye-Hückel limiting law, where γ is the activity coefficient, z is the charge of the salt or gas, I is the ionic strength of the solution and A, B and C are constants.

$$\log \gamma_{\pm} = -\frac{A|z_+ z_-|I^{1/2}}{1 + BI^{1/2}} + CI$$

Osmotic pressure will also influence any potential salinity response through the membrane. If the ionic strength differs inside and outside the membrane the osmotic pressure may force water vapour to diffuse across the membrane causing sensor response drift (Ge et al., 2014). Sodium chloride and seawater have different osmotic coefficients (0.926 (Hamer and Wu, 1972) and 0.9 (Sharqawy et al., 2012) respectively). An experiment was undertaken to determine if there was a significant difference between sodium chloride and artificial seawater on the response of the spot with changing salinity/ionic strength. The sodium chloride solutions and Kester artificial seawater were equilibrated over several days to ambient laboratory pCO_2 levels prior to measurement and the spot was preconditioned in seawater. The results are shown Figure 4.5.

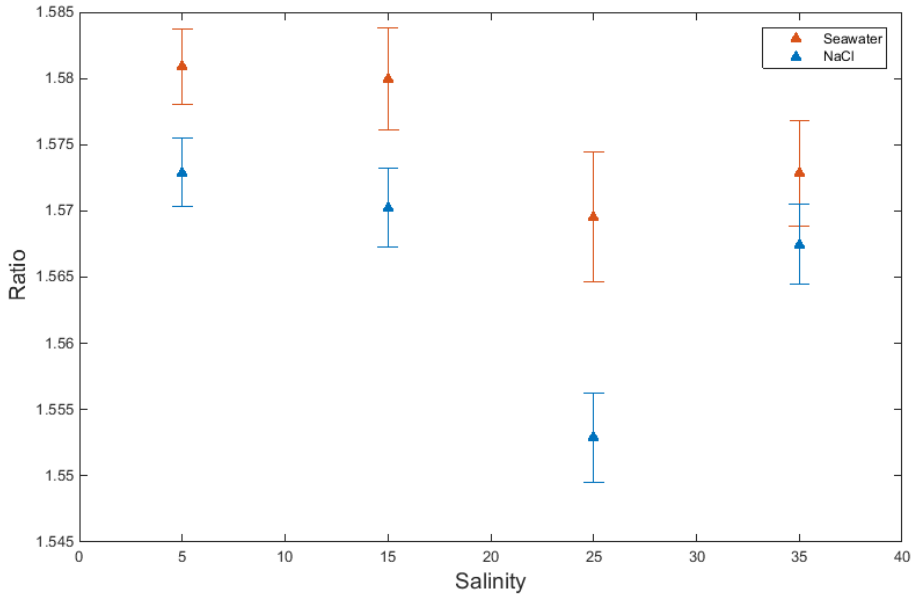

Figure 4.5 The response of the pCO_2 optode to solutions of NaCl, blue triangles, and Kester's artificial seawater, orange triangles at varying salinity (5, 15, 25, 35) left to equilibrate over several weeks to ambient laboratory pCO_2 prior to measurement. The measurement was undertaken at 20 °C.

There is an apparent decrease in the ratio from seawater solutions to sodium chloride at the same salinity, however the difference across all the salinities of 0.00994 was found statistically not significant (t = 1.893, n = 6.0, one tailed p value = 0.0536). However, a 0.005 variation at salinity 35 in the ratio corresponds to a difference of approximately 20 µatm at 20 °C (applying the linear fit). The optical isolation layer should restrict the movement of ions across the membrane, limiting any effects from salinity (Stangelmayer et al., 1998), however the difference observed in figure 4.5 may be significant over the small CO_2 range used in this study.

This difference has been attributed to the preconditioning of the spot prior to measurement. The spots used in this section, were preconditioned in seawater and show an offset between sodium chloride and seawater solutions of the same salinity. Previous studies as shown above stipulate that the indicator-buffer ion pair should be considered to be hydrated (equations 4.1 and 4.2, (Mills et al., 1992)) from the immobilisation process. The pre-conditioning may allow the spot to equilibrate the osmotic pressure by losing and gaining the water molecules (H_2O) around the ion-pair.

4.4.4 Combined temperature and salinity variations

Due to the temperature term in equation 4.6, it was hypothesised that any potential ionic strength influence may be enhanced with increasing temperatures due to increasing chemical potentials. In order to determine if there were any additional combined effects from temperature and salinity variations with *t*-DLR, the gas calibration procedure was repeated over three temperatures of 5, 10 and 20 °C with artificial seawater at salinities 20 and 30 (Figure 4.6).

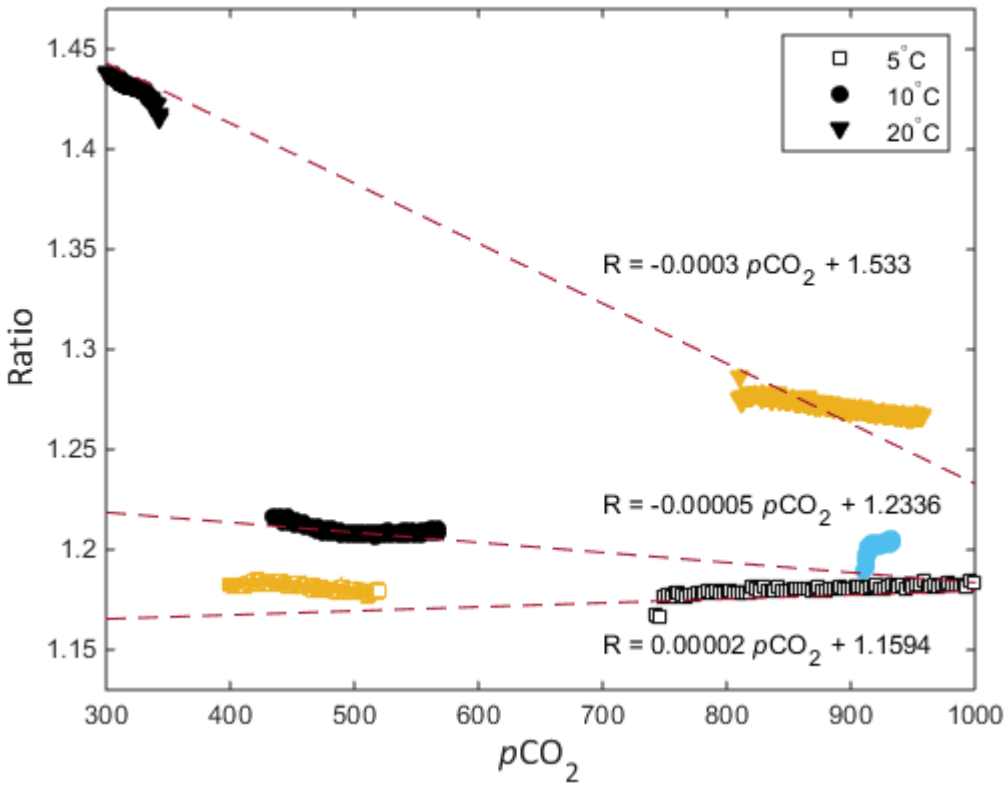

Figure 4.6 Plot of salinity calibrations at different temperatures at different pCO_2 levels. The yellow data points corresponds to salinity 20, the blue data points to salinity 30 and black to salinity 35. The data point shapes correspond to the temperature, with the open squares being 5 °C, the filled circles 10 °C, the filled triangles 20 °C. The dotted red lines correspond to the linear temperature regressions from the previous calibration experiments.

The regression lines from the temperature experiments plotted in Figure 4.6 indicate that the primary effect on the spot output fluorescence is from pCO_2 and temperature. The deviations from the linear regressions from the different salinities may be indicative of the drift experienced by Atamanchuk (2013), which we attribute to the preconditioning step creating differences in osmotic pressures between the spot and the solution- the spots in this temperature-salinity study was preconditioned in salinity 35 Kester seawater. Loss of water molecules during osmotic equilibration, may also be tied to a loss of TOA, reducing the sensitivity of the spot accounting for the flatter gradients of the lower salinity solutions (Mills et al., 1992).

The salinity is not included in the calibration due to the protective nature of the optical isolation layer, combined with the limited effect as illustrated in figure 4.6.

4.4.5 Multi-linear Regression

A stepwise multi linear regression was performed using the pCO_2, and temperature data, to produce a simple linear calibration.

$$R = a \cdot CO_2 + b \cdot T + c$$

Equation 4.9 General form of the algorithm, where R is the fluorescent optode output calculated from equation 4.3, T is temperature, CO_2 is pCO_2 of the solution. The coefficients are listed in table 4.3.

The intercept, denoted with c, takes the value of 0.028. The coefficients (a, b and the intercept) are listed with their standard errors in Table 4.1. The root mean square error of the model is 0.04, with an R^2 of 0.913 (degrees of freedom = 1219). This is an improvement upon the initial calibration due to the inclusion of the temperature term, which has a strong influence through the acidity constants and activity coefficients.

Table 4.3 Coefficients and their standard error for the pCO_2 conversion of spot fluorescence output to pCO_2 equation 4.9.

Coefficient	Value	Standard Error
a	0.0022	± 7.334 x 10^{-6}
b	-0.023	± 0.00031
c	0.028	± 0.00025

4.4.6 Chlorophyll

PreSens note on their website, that the output of the spot might be influenced by high concentrations of fluorescent materials in the sample being measured. Therefore, if chlorophyll concentrations in the natural seawater under investigation are enhanced (for example, during phytoplankton blooms) there may be some fluorescence penetration through the optical isolation layer. To this end, pCO_2 measurements with the spot were undertaken using solutions containing increasing abundances of the coccolithophore *E. Huxleyi*. The solutions were bubbled to a set pH (pH 8.022 at 20 °C) immediately prior to measurements to limit the effect of respiration from the coccolithophores during storage. The experiments were all performed in the dark in a waterbath, inserting the optode directly into the sample solutions.

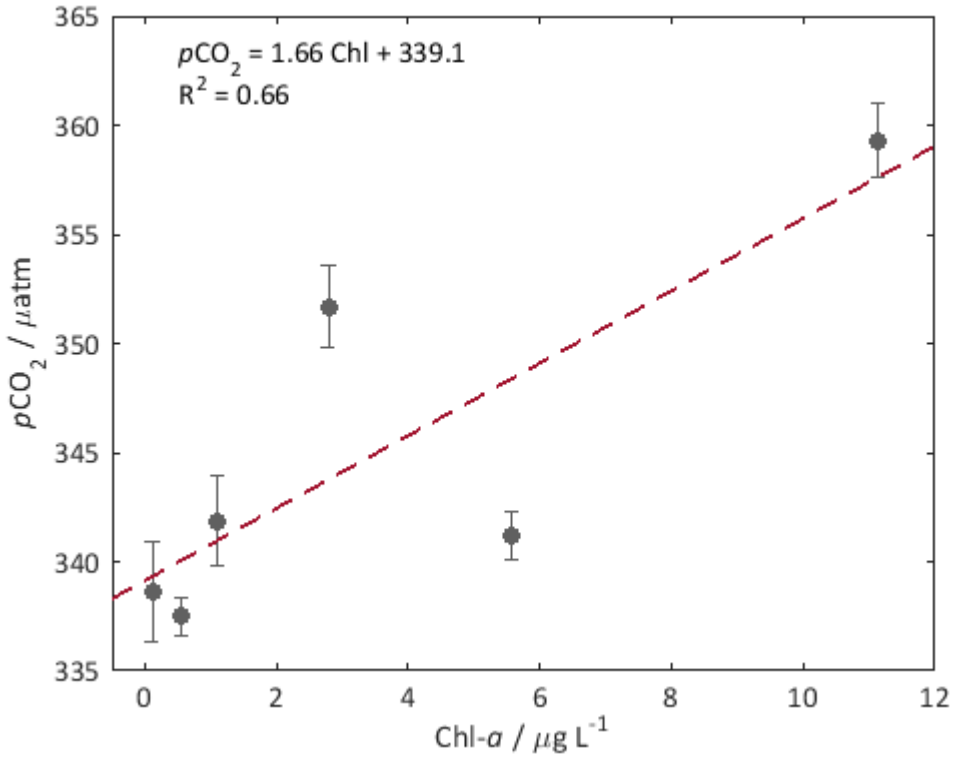

Figure 4.7 Chlorophyll influence on the pCO_2 calculated from the sensor fluorescence output (determined from the MLR in section 4.4.5). The error bars are the standard deviation over 4 repeat sample measurements. The dashed line is a linear regression with an R^2=0.81. The error bars are the standard deviation in the ratio over four 200 s measurements.

The ratio response for the increasing chlorophyll concentrations indicated a linear increase (Figure 4.7, 1.66 µatm/ µg L^{-1}), but with large error bars particularly at low concentrations of chlorophyll. The results suggest that at low concentrations (< 1 µg L^{-1}) such as normally found in the open ocean (Yoder et al., 1993) the optode is unaffected by presence and variations of chlorophyll concentrations in the surface ocean. The large error bars are attributed to the respiration of *E. Hux*leyi under the low light conditions employed during the experiment. However, this study was undertaken with only one species and no coloured organic matter in the seawater. To further test this hypothesis, more work should be done incorporating coloured dissolved organic matter and multiple species within the artificial seawater sample. It is recommended for deployments in high chlorophyll regions, that water be filtered prior to measurement.

4.4.7 Drift

The pCO_2 sensor spot was subjected to one measurement every 5 minutes over 3 days, amounting to 494 measurements. The drift was <1 % once the spot reached equilibrium with the solution at measurement number of ca. 100. Figure 4.8 displays the results with the mean (denoted μ_x) and the 2-sigma deviation (denoted $2\sigma_x$). The residuals (Figure 4.9, mean-$data_{obs}$) show no significant pattern.

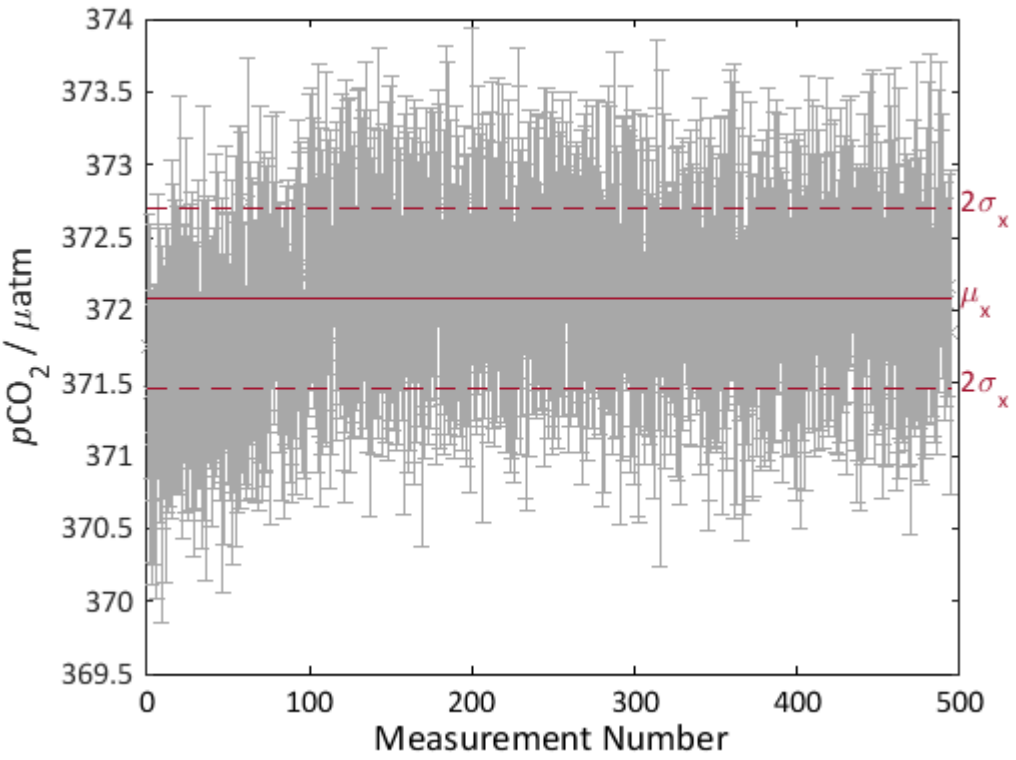

Figure 4.8 The stability of the spot of the course 3 days (494 measurements). The mean of the data points is denoted μ_x and the mean ± two times the standard deviation of the mean ($2\sigma_x$). The errorbars are the standard deviations in the ratio of each measurement converted to pCO_2, with a mode of 0.002.

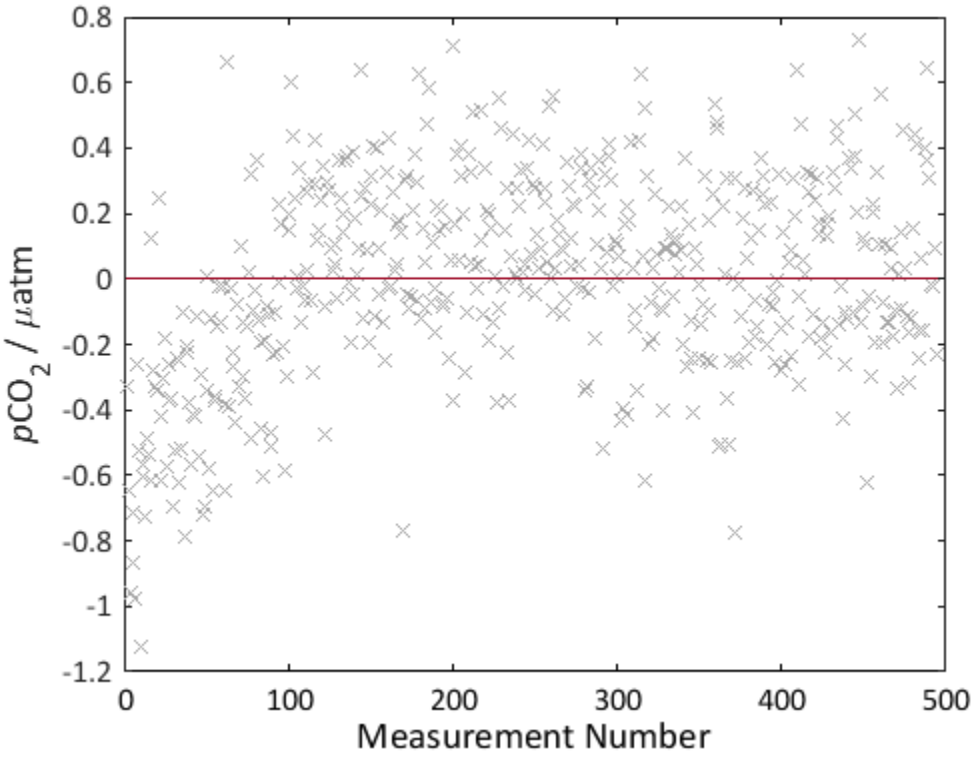

Figure 4.9 The residuals from the stability test are equivalent to the datapoint subtracted from the mean ratio. The residuals show no clear pattern, save for a slight increase in the first 100 measurements (which is seen in the ratio in figure 4.9). The mean is denoted is by the solid red line at zero.

The deviation from the mean is well within the 2σ limits and the residuals (Figure 4.9) show no obvious patterns, indicating the spot shows no evidence of bleaching even after three days of measurement and 450 200 s measurements. The standard error in the mean was 0.0014 µatm (R = 1.1719 x 10^{-6}). The optode appeared to require a significant number of measurement before a stable response was reached (ca. 100). This was attributed to the shorter preconditioning time of this spot (half a day) compared to the normal 2 day preconditioning time.

A bleaching test was undertaken to see if the deviation was consistent after illumination at levels ten times higher than the regular LED strength in order to assess the potential number of measurements the spot could be exposed to in a short time. It was expected that if indicator dye bleaching occurred then the standard deviation in the post-bleaching experiment would be greatly increased. The spot was continuously illuminated for two hours at 2 mA. This is equivalent to 1.44 x 10^{9} LED illuminations, and the results are shown through the residuals in Figure 4.10.

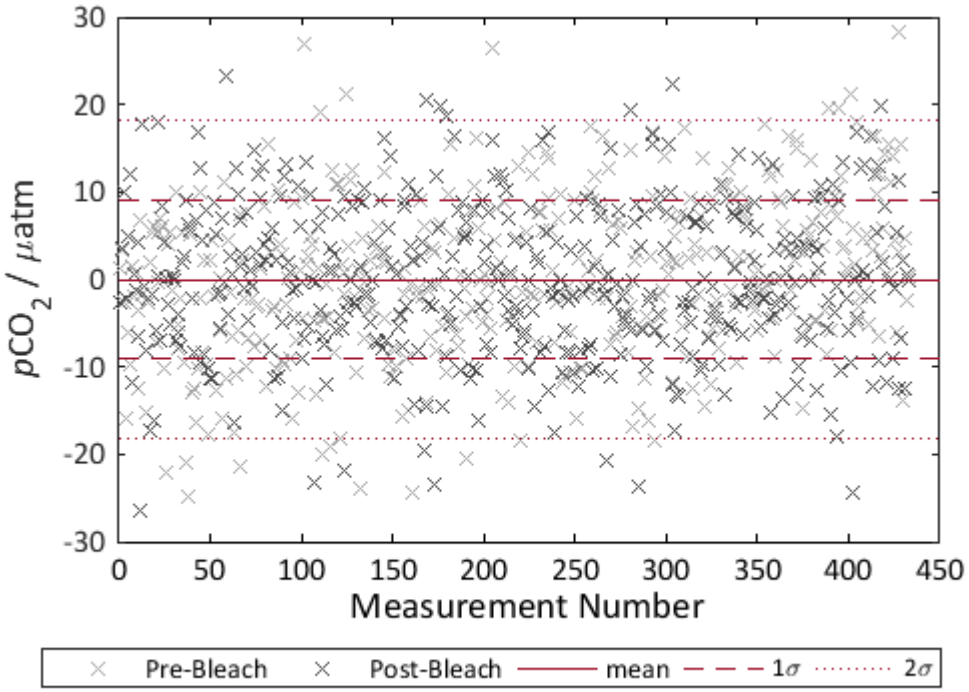

Figure 4.10 The residuals for each of the post-bleach and pre-bleach measurements with the light grey crosses representing the pre-bleach measurement and the dark grey the post-bleach measurement. The mean, 1σ and 2σ were calculated for the pre-bleach measurements and plotted here with red dashed and dotted line respectively.

There was no obvious difference in the residuals before and after enhanced illumination, and there was no distinct pattern or offset between the measurements. The standard deviation pre-bleach was 9 µatm compared to 8.8 µatm after, and the standard error of the mean was 0.02 µatm. To determine the number of equivalent 200 s measurements the bleaching experiment corresponds to, the following equation can be used.

$$\text{No of measurements} = \left(10 \cdot \left(\frac{I_{bleach}}{t_{ex}}\right)\right) \Bigg/ \left(\frac{200\ s}{t_{ex} + t_{em}}\right)$$

Equation 4.10 Equation to determine the equivalent number of measurements from the bleaching experiment.

where I_{bleach} is the amount of time the spot was "bleached"- 7200 s, t_{ex} is the time of the LED pulse (LED on) in the square waveform- 5 µs, $t_{ex} + t_{em}$ is the total time for the square waveform (LED on + LED off) 25.5 µs, and 200 s is the time for a single normal measurement. The theoretical number of measurements of 200 s duration that the spot could undergo according to this study was calculated to be 18,360 measurements.

To further, this testing the spot was deployed as an autonomous underway sensor with drift being continuously monitored using CRMs. The spot lasted for ca. 6000 measurements (over a period of 4 weeks). The optode measurements from ca. weekly CRM measurements

(batches 135 and 136) are shown in Figure 4.11. The optode results were significantly different from the CRM value in the second half of the cruise that corresponded to a potential hardware issue, discussed further in chapter 5. The shift may also be indicative of the photobleaching of the indicator or the reference dye at differing rates which is a known problem when applying DLR methods (Wencel et al., 2014).

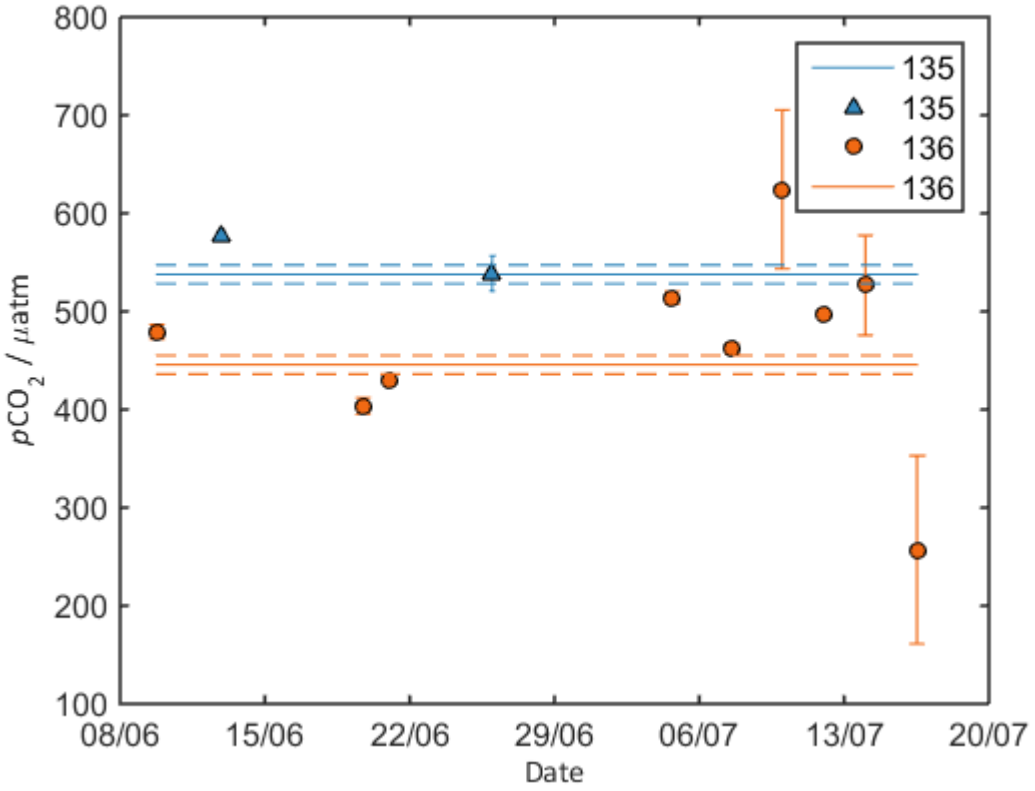

Figure 4.11 Measurements of CRM by the optode pCO_2 and the CRM calculated pCO_2 value. The CRMs were measured ca. once per week. The dashed lines indicate the precision of the optode (± 9.5 µatm).

4.4.8 Metrology

Response time is defined as the time for the ratio value to reach 95 % of the final stable response (τ_{95}). A response time (τ_{95}) of 165 s at 25 °C was found compared to a response time (τ_{63}) of 88 s at 20 °C reported by Atamanchuk et al. (2014). This response time was determined over a much smaller pCO_2 range (280-800 µatm) compared to the previously reported observations (5000-50000 µatm) and is quoted to a higher percentage of the final value. These response times are significantly slower than other pCO_2 optode sensors (Oter et al., 2006, Chu and Lo, 2008, Borisov et al., 2011), which is assumed to be due to the presence of an optical isolation layer. The response times are diffusion controlled so the extra optical isolation layer will increase the response time.

Precision was determined by the repeated measurement of Dickson CRMs in a water bath at 20 °C (Figure 4.12). The short-term precision was calculated as the standard deviation over 10 samples- 0.8 µatm. A longer-term precision (standard pooled deviation) from the cruise was found to be 9.5 µatm. The standard deviation over the three-day stability experiment in the laboratory was found to be 0.31 µatm, which was more consistent with the short-term precision evaluation. This laboratory precision is significantly better than the desired 2 µatm precision, and is similar to 1 µatm Lefevre et al. (1993) and 1.7 µatm from Ge et al. (2014). However, the deployment precision requires further investigation.

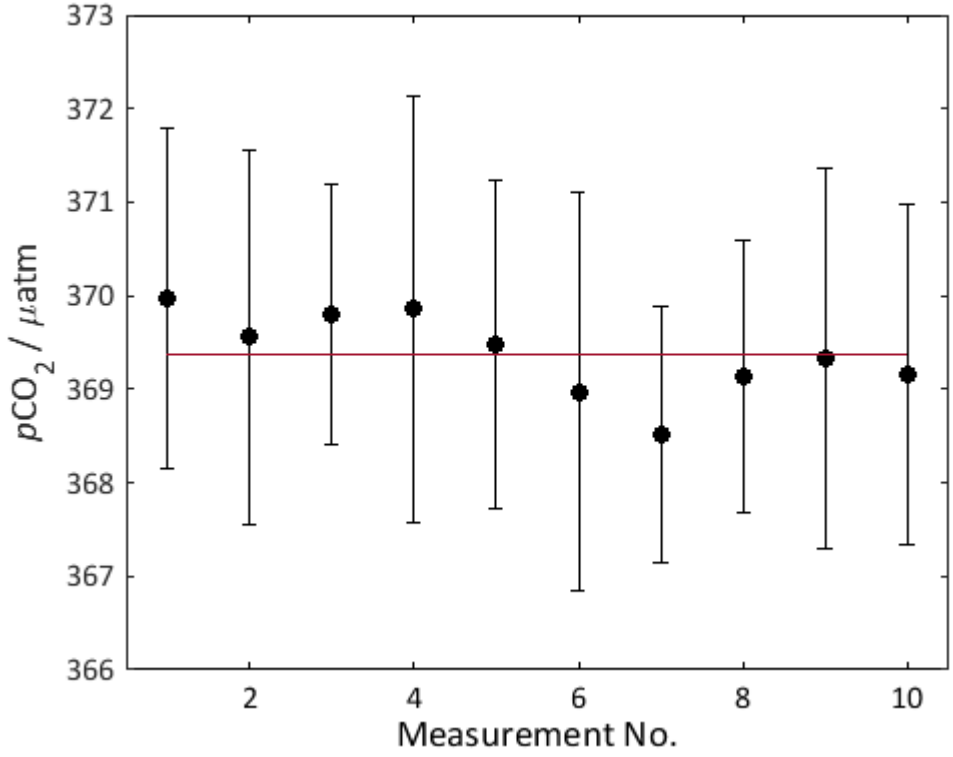

Figure 4.12 10 repeat Dickson DIC/TA CRM measurements in a water bath at 20°C. Each point was a measurement of the CRM for 200 s. The red line is mean value of the optode measurements, and the error bars are the standard deviation in the optode response converted to µatm.

4.5 Limitations and Future work

The major limitation of this work is the lack of a standard pCO_2 range across the calibrations with varying temperature and salinity, due to the pCO_2 of the seawater being determined by collected samples, analysed at a later date. This could be avoided and the calibration improved by amending the gas calibration rig to fit a secondary CO_2 sensor to determine (at the least) the saturation and degassing levels prior to starting the calibration. The oxygen method uses a secondary sensor, which measures O_2 continuously alongside the oxygen microelectrode (Andrew Morris, *pers comm*), which would further improve the accuracy of the method.

Oter et al. (2006) applied the pH indicator HPTS to measure gaseous CO_2 and demonstrated the potential of optodes to measure in the gas phase as well as the dissolved phase. Future work incorporating a gas calibration alongside the seawater calibration would allow for *in situ* drift correction as applied with oxygen optodes on ARGO floats (Bushinsky and Emerson, 2013). This may require the use of a pCO_2 specific indicator, rather than a pH indicator with a buffer solution, so further investigation towards pCO_2 indicators would be advantageous. A pCO_2 indicator may also act to reduce the response time and improve sensitivity at the lower pCO_2 range.

Finally, the salinity drift observed previously was postulated to be from changing osmotic pressure, this requires longer-term investigation.

4.6 Conclusions

The salinity results in this chapter confirm the initial findings of Atamanchuk (2013) however attempts have been made to further improve the understanding of the PreSens spot response, to allow interpretation from any deviations in future deployments. We found comparable response times but overall the sensor spot shows much slower response time when compared to other sensor spots. The lifetime experiments indicate the successful implementation of t-DLR to prolong sensor lifetime compared to the *f*-DLR method, along with the shorter excitation time and optical isolation layer. We performed a calibration using the sosna rig adapted for use with CO_2, valid over the range 280-1000 µatm, with a linear regression to convert from spot output to pCO_2. This is significantly simpler than the 8^{th} degree polynomial previously proposed (Atamanchuk et al., 2014). The spot has a proven working life of at least ca. one month as an autonomous underway sensor collecting ca. 3000 measurements at six minute resolution, and a predicted 18000 measurements based on bleaching experiments. The spot precision was significantly better than the 2 µatm, at 0.81 µatm. The shipboard precision was 9 µatm, likely due to contamination of the sample tubing. The work could be further enhanced by improving the gas calibration rig to allow multiple pCO_2 sensors to measure simultaneously, and with further knowledge of the pCO_2 spot chemical constituents. Future work should focus on measurements in both gas and aqueous phases to allow *in situ* drift corrections to data.

Chapter 5:

Surface water pCO_2 variability in the high latitude North Atlantic

Abstract

Atmospheric anthropogenic carbon dioxide (CO_2) emissions are resulting in increased seawater CO_2 concentrations, with potentially important consequences for biogeochemical processes and marine ecosystems. To understand the chemical and biological responses in regions sensitive to the increasing CO_2 levels, it is important to accurately constrain the carbonate system to obtain improved mechanistic process understanding and model parametrisation in order to better inform model simulations and projections. *In situ* autonomous sensors are key for achieving the required high spatial and temporal data resolution of carbonate chemistry variables, as they can be deployed on spatially dynamic platforms such as gliders and drifters or on static mooring systems.

A prototype pCO_2 optode was deployed as an autonomous underway system on board a research vessel during a cruise in the sub-polar North Atlantic. The pCO_2 optode was used alongside an infrared dissolved inorganic carbon (DIC) sensor, with additional collection of discrete bottled samples. The cruise covered three distinct biogeographical regions: Arctic, sub-Arctic and North Atlantic drift, as well as four transects from the open ocean towards the coast of Greenland. The high-resolution pCO_2 data is compared to underway DIC and discretely collected DIC and total alkalinity (TA) samples, with the optode showing good agreement with the discrete samples. The optode pCO_2 data is used to evaluate the influence of sampling rate and interpolation methods on air-sea CO_2 flux calculations, showing that the sampling rate makes no significant difference to the overall flux calculation, while the interpolation method does influence the results. Finally, surface water-pCO_2 measurements are regressed with the underway data to compare the different controls on pCO_2 over the sub-polar North Atlantic, with the warmer, more saline Atlantic waters showing greater control from biological processes (photosynthesis and respiration) and CO_2 solubility, while the Labrador Sea has a stronger dependence on the underlying water mass properties. Further work is required to apply *in situ* wind speed to our pCO_2 flux calculations and to determine the cause of the observed offset of the underway DIC measurements.

5.1 Introduction

Atmospheric carbon dioxide (CO_2) concentrations have been increasing since monitoring began in the 1950's (Keeling, 1986). Increased seawater pCO_2 has implications for seawater biogeochemistry including a reduction in ocean pH and calcium carbonate mineral saturation state (Ω). The high-latitude ocean regions have been shown to be more affected by enhanced atmospheric CO_2 concentrations due to their lower buffering capacity and reduced seawater temperatures (Sabine et al., 2004), with evidence of pronounced seasonal acidification and undersaturation in some polar regions (Orr et al., 2005).

The global oceans are on average close to equilibrium with atmospheric CO_2 concentrations (Takahashi et al., 2009) when considering a sufficiently long period of time (e.g. over a year), but there are temporal and regional differences in oceanic CO_2 saturation which determine whether any given area acts as a CO_2 sink or source. The high latitude North Atlantic is a significant regional sink for CO_2, both storing anthropogenic CO_2 and acting as a CO_2 conduit to the rest of the world's oceans (Álvarez et al., 2003, Schuster et al., 2009), particularly in summer months (Lefèvre et al., 2004, Takahashi et al., 2009). This is supported by data from the Bermuda Atlantic Time- series Study (BATS), which suggests that the North Atlantic mode waters formed at high latitudes have higher anthropogenic CO_2 levels than those at lower latitudes (Gruber et al., 2002).

Air-sea CO_2 flux calculated from cruise data is generally obtained from interpolated pCO_2 measurements, with climatological wind speeds and spectrometric or chromatographically determined atmospheric pCO_2 concentrations (Takahashi et al., 2009). Due to the sparse nature of the data, fluxes are evaluated over long periods and/or wide spatial scales (Schuster and Watson, 2007, Schuster et al., 2009, Takahashi et al., 2009). Data at higher temporal resolution is required to allow a more robust statistical evaluations of CO_2 fluxes over shorter time scales (Wanninkhof et al., 2013) and better constrain the mechanisms that drive the air sea fluxes (Schuster et al., 2013). This is of particular relevance to the North Atlantic sub-polar gyre, which forms an important CO_2 sink with sparse measurements (Corbière et al., 2007). *In situ* autonomous pCO_2 sensors are therefore highly beneficial to further constrain estimates of pCO_2 fluxes over longer times and smaller spatial scales (Watson et al., 2009), allowing improved spatial coverage over this large region.

There are currently several infrared spectrometer based instruments deployed as shipboard systems in the North Atlantic on voluntary ships of observation (Schuster et al., 2009). These instruments provide excellent high quality data, but require regular maintenance, are complex and as shipboard instruments cannot provide the increasing quantities of data required over wider spatial scales; therefore *in situ* pCO_2 sensors are desirable. Chapter 3

reviews the currently available analytical systems and *in situ* sensors for pCO_2, and in this chapter, a preliminary deployment of a t-DLR pCO_2 optode as an underway surface water sensor is presented. The optode based pCO_2 sensor has potential to be an *in situ* system due to the simple hardware and lack of moveable parts or wet chemicals; the sensor has a lab precision of 0.8 µatm (Chapter 4). With further calibration it may also be possible to measure atmospheric pCO_2 as with oxygen optodes (Bushinsky and Emerson, 2013), this would significantly enhance the spatial coverage of pCO_2 flux measurements.

The North Atlantic sub-polar seasonally stratified (SP-SS) gyre, as defined by McKinley et al. (2011), has surface water influences from the sub-tropical, sub-polar and polar regions (Metzl et al., 2010). The waters in the SP-SS gyre are sourced from the North Atlantic Current (NAC) and surface water overflows from Greenland and Labrador seas. The surface water composition varies spatially within the gyre, controlled by the physical circulation and water mass mixing. Doney et al. (2009) suggested that carbonate chemistry in the seasonal ice edge zones, such as coastal Greenland and Canada in this study, is determined primarily by the gas exchange coefficient (defined in Chapter 1), while along the sub-arctic Extended Ellett Line repeat transect it is controlled by physical circulation modulation, and in the central North Atlantic drift region by biological processes and thermal solubility. The large spatial scale of the discrete DIC and TA data collected combined with the high-resolution underway pCO_2 data set allows us to examine regional differences in the controls on carbonate chemistry.

Autonomous high-resolution underway data for pCO_2 (1 measurement per 6 minutes) and dissolved inorganic carbon (DIC, 1 measurement per 3 minutes) were collected, alongside discrete seawater samples from the ship's underway surface water supply and CTD casts. This far exceeds the spatial sampling scheme recommended by Lenton et al. (2009) to determine basin wide air-sea fluxes, and provides an opportunity to evaluate the influence of sampling scale and data interpolation methods on air-sea CO_2 flux calculations, while giving a snapshot into the carbonate chemistry at the transition between the spring and summer season.

5.2 Methods

5.2.1 Cruise

The data for this chapter were collected over the period 7/06/2014 to 18/07/2014 aboard the RRS *James Clark Ross* (cruise JR302), as a part of the RAGNARoCC (Radiatively Active Gases from the North Atlantic Region and Climate Change) and OSNAP (Overturning in the Sub-polar North Atlantic Program) cruise programmes. This trans-Atlantic cruise (Figure 5.1) crossed the Labrador Sea (LS) and then tracked around the coast of Greenland with several

transects inshore before crossing the Irminger Basin (IrB) to the Iceland Basin (IcB). Surface water samples and underway measurements were obtained from the ship's underway seawater supply, with an intake at the hull at ca. 6 m depth. Where water column data are shown, they were discretely sampled water from rosette casts (CTD) along the cruise route. Discrete samples were analysed both on the ship and at the National Oceanography Centre, Southampton. This chapter focuses on the processes in the surface water, and all data presented here were sampled in the top 100 m of the water column.

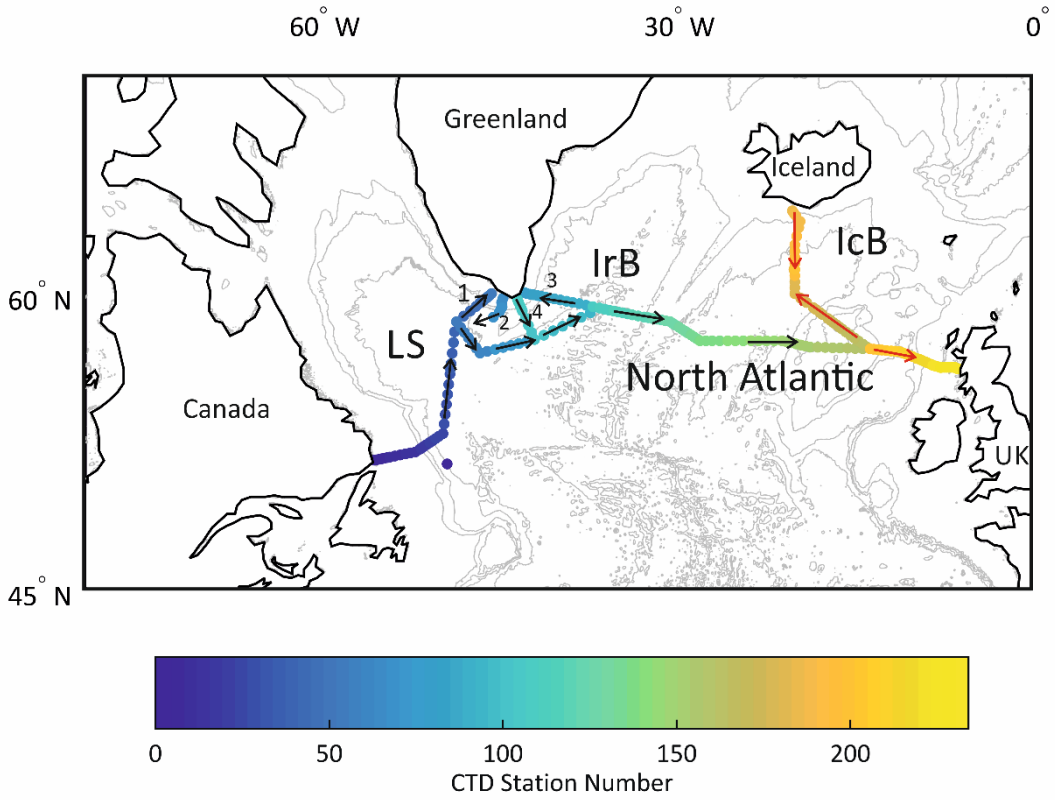

Figure 5.1 Cruise route with arrows indicating the direction travelled, with the colour of the dots indicating the CTD station number. The red arrows indicate the Extended Ellet Line segment of the cruise. The numbers around the Greenland coast indicate the sampling order of transects towards the Greenland coast. LS = Labrador Sea, IrB = Irminger Basin, IcB = Iceland Basin.

5.2.1.1 Continuous underway measurements

Continuous temperature, conductivity and chlorophyll-*a* fluorescence were obtained using a shipboard thermosalinograph (TSG, SeaBird Electronics, Inc. SBE 45) connected to the underway supply.

Discrete salinity samples were collected and analysed using an AutoSal salinometer (Guildline) by the physical oceanographers on the ship (Penny Holliday, Brian King and Damien Desbruyéres), and used to calibrate the TSG and CTD conductivity sensors (by Brian King and Penny Holliday).

Mixed layer depth was determined as the depth where potential density differs from the surface density by 0.03 kg m^{-3} as per de Boyer Montégut et al. (2004).

5.2.1.1.1 pCO_2 optode

A pCO_2 optode based on a fluorescent pH indicator, immobilised alongside a buffer and a reference fluorophore in a gas permeable membrane (Chapter 4), was deployed as an autonomous underway system. The optode measured at a rate of 0.0028 Hz (one measurement every 6 minutes), with the fluorescent output evaluated using time domain Dual Lifetime Referencing (*t*-DLR), as detailed in Chapter 4. It was operated continuously, stopped only near sea ice due to cessation of underway water intake, and for measurements of certified reference materials (CRMs) to determine the potential drift of the optode. Seawater was transferred from the underway supply to a custom-built 15 ml chamber using a solenoid pump controlled by LabView software. The optode was suspended in a 20 °C water bath (Grant TX150-ST26, ± 0.01 °C) due to the temperature dependence of the sensor spot not being fully constrained at the time of the cruise. The uncertainty in the water bath temperature (± 0.01 °C) led to a ± 0.0917 µatm uncertainty in pCO_2, smaller than the best short-term laboratory precision of 0.8 µatm (Chapter 4), and therefore the water bath induced temperature uncertainty was negligible. It was assumed that the measurement temperature remained at 20 °C for the duration of the cruise, so a temperature-independent conversion from R (optode fluorescent output, chapter 2 & 4) to pCO_2 was applied with a linear relationship as determined in Chapter 4 (figure 4.3), and Equation 5.1 (see below). The data were converted to pCO_2 using Equation 5.1, and subsequently corrected to *in situ* temperature using version 1.1 of the CO_2SYS software for MATLAB® (Van Heuven et al., 2011).

$$pCO_2 = \frac{R - 1.542}{-0.0003}$$

Equation 5.1 Conversion from R to pCO_2, determined from calibration, where R is the optode output.

5.2.1.1.2 DIC measurements

Underway DIC measurements were made with an Apollo SciTech inc (2010) DIC Analyzer AS-C3 with a LiCOR 7000 spectrometer, sampling 0.75 ml every 3 minutes from the underway seawater supply using tygon tubing. CO_2-free Nitrogen gas (ca. 302 ml min^{-1}, purchased from BOC) was used as the carrier gas, and dried with a scrubber (magnesium perchlorate and glass wool, changed every 3 days) prior to entering the instrument. The instrument used phosphoric acid (10 % v/v) to acidify the samples in order to release CO_2 gas which was subsequently analysed using the LiCOR 7000; the acid was diluted from concentrated stock ca. every 2 days as required. CRMs were analysed ca. every 30 samples or while stationary on

a CTD deployment station using tygon tubing from the same reel as the instrument used to sample from the underway supply. During the analysis of CRMs, seawater was allowed to continue flowing through the seawater sample tube to prevent bubbles entering the system upon reconnection.

The spectrometer was calibrated with increasing volumes (0.5, 0.75 and 1 ml) of CRM, and a linear regression was used to correlate peak area to the carbon content of each sample. The spectrometer was re-calibrated every 12 hours to limit the drift. Final underway DIC data was density-corrected with the underway temperature and salinity measurements, using the equation from Millero and Poisson (1981).

5.2.1.2 Discrete Sampling

Discrete seawater samples were collected from the underway supply 3 times per day and from all CTD casts. Seawater was collected according to the Guide for Best Practices (Dickson et al., 2007), in 250 ml borosilicate glass bottles that were filled and then allowed to overflow with sample until a full bottle volume had been replaced. Each sample was poisoned with 50 µL of saturated mercuric chloride solution and a 2.5 ml air headspace introduced. These were then sealed with Apiezon L silicone grease, taped shut and stored in a dark and cool environment until analysis. Analysis of DIC and total alkalinity (TA) samples was performed aboard the ship by Claudia Fry, Becky Garley, Eithne Tynan and Alex Griffiths, and any remaining samples measured at the National Oceanography Centre, Southampton by Alex Griffiths. All samples were measured on a VINDTA 3c. DIC was measured coulometrically, and TA measured with a potentiometric titration (Mintrop, 2004). Correction of the DIC was using the ratio of density-corrected certified values to the measured CRM values using a correction factor (C*f*),

$$Cf = \rho \frac{\mathrm{DIC}^{\mathrm{cert}}}{\mathrm{DIC}^{\mathrm{meas}}}$$

Equation 5.2

where ρ is the CRM density calculated from the certified salinity and the temperature of measurement (25 °C), $\mathrm{DIC}^{\mathrm{cert}}$ is the certified DIC value and $\mathrm{DIC}^{\mathrm{meas}}$ is the measured DIC value. The correction factor was then multiplied by bottle samples which had been density corrected using the measurement temperature (25 °C) and *in situ* salinity.

The TA was corrected using the CRM acid molality with the use of Matthew Humphrey's calkulate functions (Matlab® v0.1.2,Humphreys (2015)).

The manually-collected depth cast and underway samples were analysed on the VINDTA with a DIC precision of ± 3.1 µmol kg^{-1} and a TA precision of ± 4.1 µmol kg^{-1}.

5.2.2 Nutrient and Oxygen data

Discrete inorganic nutrient and oxygen samples were collected on CTD casts and analysed on the ship by Sinhue Torres-Valdes, Mark Stinchcombe, Carolyn Graves and Hannah Donald.

The inorganic nutrients (silicate, phosphate, nitrate plus nitrite, nitrite) were collected in 15 ml plastic centrifuge tubes and stored at ca. 4 °C until a minimum of 40 samples had been collected. Samples were analysed using a 7-channel Seal Analytical AA3 autoanalyser with 2-10 CTD stations per run. The instrument was calibrated prior to each run according to Seal Analytical Protocols. Generally, this consisted of 5 standards in artificial seawater, baseline checks and drift checks, with additional certified reference materials from Hansell's Lab, University of Florida, USA and The General Environmental Technos co.,Ltd., (KANSO).

Dissolved oxygen (DO) was sampled directly into pre-calibrated glass flasks using Tygon® tubing and fixed with manganese chloride and sodium hydroxide/sodium iodide solutions. These were thoroughly mixed and left for 30-40 min in the dark before being re-shaken to improve the reaction efficiency and left again for a further 30-40 min. The DO was determined by Winkler titration using a potentiometric Ω-Metrohm titration unit (916 Ti-Touch with electronic burettes) according to Dickson (1994) and Holley and Hydes (1994), with reagents prepared prior to the cruise following Dickson (1994).

5.2.3 Calculation of carbonate parameters

DIC and TA samples were used to calculate pCO_2 using CO_2SYS (Matlab v1.1, Van Heuven et al. (2011)). We used the carbonic acid dissociation constants of Mehrbach et al. (1973) refitted by Dickson and Millero (1987), the boric acid dissociation constant of Dickson (1990), the bisulfate ion acidity constant of Dickson (1990), and the boron-to-chlorinity ratio of Lee et al. (2010), and pH is reported on the total pH scale (Chapter 1).

A TA-salinity relationship was determined using an ordinary least squares regression from the underway bottled samples across the whole cruise and applied to the underway continuous salinity measurements to predict TA.

$$TA = 48.13 \cdot S + 0.0504 \cdot S^2 + 550.96$$

Equation 5.3 The TA salinity relationship derived across the whole cruise, where TA is total alkalinity, and underway S is salinity. RMSE = 28.9 μmol kg^{-1}.

DIC was calculated from measured pCO_2 and predicted TA (Equation 5.3) using the same dissociation constants listed above.

5.2.4 Satellite Data

8-Day composites of MODIS-A satellite chlorophyll-*a* concentrations were downloaded from NASA Earth Observation site (http://neo.sci.gsfc.nasa.gov/view.php?datasetId=MY1DMW_CHLORA&date=2015-04-01) and cropped with the image composite explorer to the study region. These are shown in Appendix A.1. Sea-ice data was downloaded from the National Snow and Ice Data Centre (https://nsidc.org/data/) and analysed using code provided by Matthew P. Humphreys. Bathymetry data was downloaded from the National Oceanic and Atmospheric Administration's National Centers for Environmental Information (http://www.ngdc.noaa.gov/mgg/global/global.html).

5.2.5 Statistical Analysis

The data were filtered with the latitude and longitude boundaries for each region (Sub-Arctic (SARCT, 58-66 °N, 24-10 °W), Arctic (ARCT, 50-70 °N, 60-10 °W), and North Atlantic Drift (NADR, 44-58 °N, 42-10 °W)) according to Lefèvre et al. (2004). Longhurst et al. (1995) who originally defined the regions based on the chlorophyll response to the underlying vertical transport of nutrients with characteristic seasonal cycles. The boundaries when used in model scenarios (as designed) should be varied to account for seasonal and annual changes. We used the same boundaries as specified in Lefèvre et al. (2004) and assume they are constant throughout our cruise period as it was completed in a single season.

Kruskal-Wallis One-Way Analysis of Variance (ANOVA) was carried out in SigmaPlot with T, S, pCO_2, Chlorophyll-a to determine if the regions were statistically significantly different ($p < 0.001$). Pairwise multiple comparison procedures (Holm-Sidak Method) were performed to isolate the variables that are significantly different in each region (T, S, pCO_2, Chlorophyll-a). Finally, stepwise multiple linear regressions were performed in SigmaPlot with variables in each region to determine the controls on the observed pCO_2 and air-sea pCO_2 fluxes across the different regions.

5.2.6 Flux Calculations

The pCO_2 fluxes were calculated according to Wanninkhof (2014), and the general formula in equation 5.4.

$$F = \mathcal{K}(C_w - C_a)$$

Equation 5.4 General flux calculation, where F is the flux (mass area^{-1} time^{-1}), $\mathcal{K}$ is the gas transfer velocity (length time^{-1}) and C_w and C_a are the concentrations of the gas of interest in the liquid and air in contact with the liquid (mass volume^{-1}).

Converting from concentration to partial pressure requires the inclusion of the gas specific solubility coefficient, K_0, leading to equation 5.5 and 5.6

$$F = k \cdot K_0(\Delta pCO_2)$$

Equation 5.5 pCO_2 flux calculation, where F is flux (mol m^{-2} yr^{-1}), k is gas transfer velocity (m yr^{-1}), K_0 is the solubility coefficient (mol kg-soln $^{-1}atm^{-1}$), and $\Delta pCO2$ is the air-sea disequilibrium according to equation 5.10 in (atm).

$$\Delta pCO_2 = pCO_2^{sw} - pCO_2^{atm}$$

Equation 5.6 Air-sea pCO_2 disequilibrium, where pCO_2^{sw} is the seawater pCO_2 from the optode, pCO_2^{atm} is the atmospheric pCO_2 set to 398.79 µatm.

K_0 was calculated according to Weiss (1974), using the observed temperature and salinity. The gas transfer velocity (k, equation 5.7) is the rate of gas transfer between the air and ocean and can be parameterised using the instantaneous wind speed and the ratio of the viscosity of water to the molecular mass diffusion rate of a gas into the water (the Schmidt number, equation 5.8).

$$k = 0.251\ {u_{10}}^2(Sc/660)^{-0.5}$$

Equation 5.7 Gas transfer velocity as a function of 10 m wind speed (u_{10}) in m s^{-1}, and Sc is the Schmidt number calculated from equation 5.11.

The Schmidt number (Sc) is calculated using the observed temperature according to Wanninkhof (2014), equation 5.8.

$$Sc = 2116.8 + At + Bt^2 + Ct^3 + dt^4$$

Equation 5.8 Calculation of the Schmidt constant from temperature measurements, where t is temperature (°C), A =-136.25, B = 4.74, C = -0.093 and d=0.00076.

Underway temperature and salinity were used to calculate the Schmidt number according to equation 5.8 and solubility coefficient K_0 according to Weiss (1974), and compared to results obtained using the mean temperature and salinity. These two different values, termed k^{UW} and k^{const}, respectively, were used to calculate the fluxes across the cruise route.

The pCO_2^{atm} was set to 398.79 µatm based on Mauna Loa June monthly average at the time of the cruise. For wind speed an average value at 10 m of 5 m s^{-1} based on Thomas et al. (2005) was used. Both wind speed and atmospheric pCO_2 were kept constant due to a lack of available data to, and as such the focus of this chapter on the variability based on sampling rates rather than the absolute values. The wind speed will be a significant source of error in the final flux calculations, due to the squared wind speed term in equation 5.7. A brief comparison was performed of sampling rates between 5 m s^{-1} and 10 m s^{-1} to give an indication of whether sampling rate was more influential at lower wind speeds.

The pCO_2 optode data was resampled every 10 points (hourly sampling), 20 points (2 hourly sampling), 5 points (30 minute sampling) and every alternate point (12 minute sampling) and interpolated to the original resolution. The residuals were calculated by subtracting the interpolated data from the original data. All interpolations were performed with the Matlab 2014b interp1 function applying linear, PCHIP (a shape preserving piecewise cubic interpolation) and spline methods.

The fluxes were calculated across each region (NADR, SARCT, and ARCT) for the different sampling rates and their means and standard deviations compared to the mean and standard deviation for the whole cruise.

5.3 Results and Discussion

5.3.1 Observed Hydrography

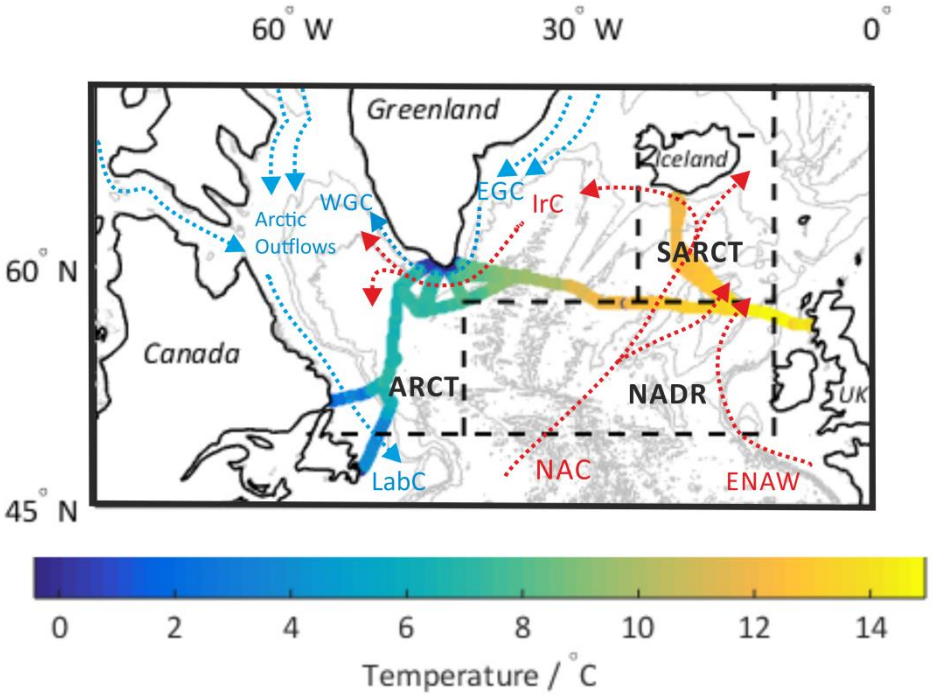

Figure 5.2 The temperature along the cruise route overlaid with the major currents acting in each region and the 3 biogeographical regions as defined by Lefèvre et al. (2004) divided by the black dashed lines. Red dotted arrows indicate warmer saltier currents, while blue dotted arrows represent the colder polar current. EGC = East Greenland Current, IrC = Irminger Current, NAC = North Atlantic Current, LabC = Labrador Current, ARCT = Arctic region, SARCT= Sub Arctic Region, NADR = North Atlantic Drift Region, ENAW = Eastern North Atlantic Water also called North Atlantic Water (NAW) in (Hansen and Østerhus, 2000) and WGC =West Greenland Current.

The cruise crossed several different water masses (Figure 5.2), which can be traced using alkalinity-salinity relationships (Figure 5.3) and nitrate: phosphate ratios (Figure 5.4).

Atlantic and Pacific source water ratios from Jones et al. (2008) are indicated in figure 5.4 with the red and dashed blue line, respectively. The increase in phosphate relative to nitrate of the Pacific line is attributed to nitrogen loss processes such as denitrification (Jones et al., 1998). The currents in the subpolar North Atlantic flow north and westward in an anti-clockwise manner (McCartney and Talley, 1984), while the cruise progressed in an easterly direction.

Low temperatures (< 5°C) and low salinities (ca. 32) were observed at the start of the cruise and corresponded to the Labrador Current, which has the Pacific water influence from the Arctic inflow through the Canadian archipelago. This is demonstrated by the nitrate : phosphate deviation from the Atlantic source line (dark blue/purple points, Figure 5.4) and the similarity of the T-S plot (Figure 5.5, station 10) to the warm Polar Surface Water as reported in Sutherland and Pickart (2008). The Pacific waters are combined with Siberian river runoff and sea ice melt from the East and West Greenland Currents, assumed to have the same nitrate-phosphate ratio as Atlantic water and causing Labrador Sea data to fall between the Pacific to the Atlantic source lines (Jones et al., 2008, Sutherland et al., 2009) and the T-S line of station 10 to be similar to station 51 in figure 5.5.

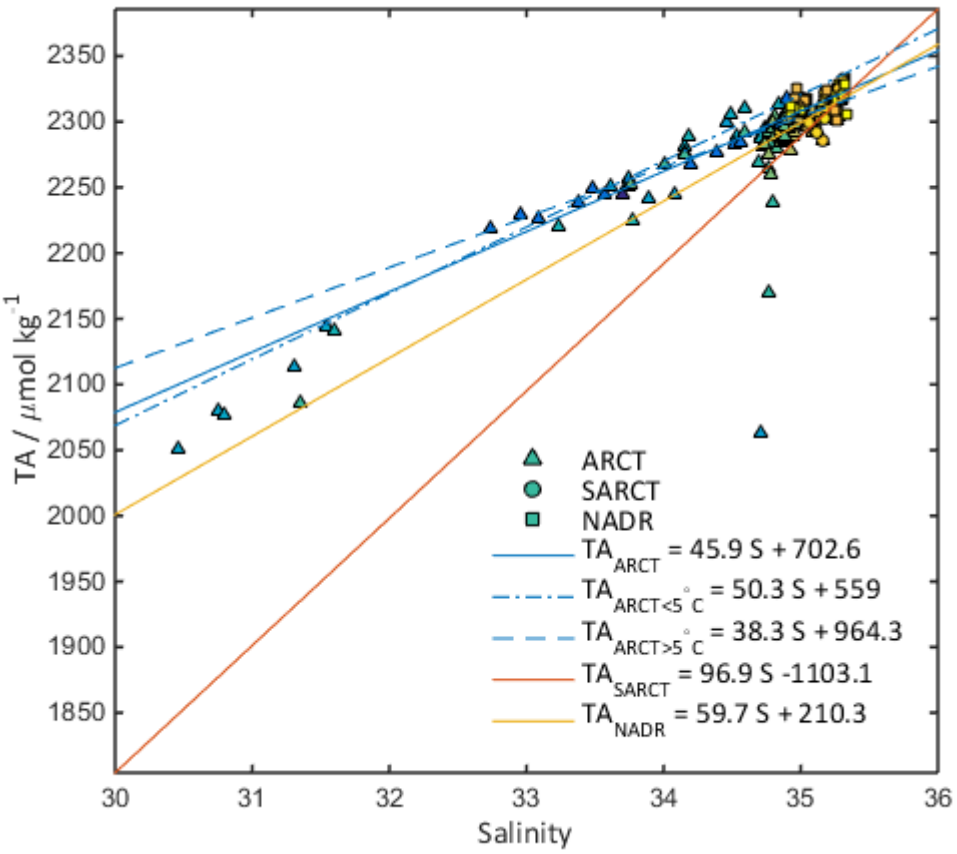

Figure 5.3 The TA plotted against salinity. The relationships are categorised by the biogeographical region where the data was collected and subdivided by temperature in the case of the ARCT. The zero-salinity end members (TA_0) can be identified from the intercept of each of the linear regressions. ARCT = Arctic region, SARCT = sub-arctic region, NADR =North Atlantic drift region. The two relationships for the ARCT region arise from the different water mass influences – the polar East Greenland current arctic outflows (T<5 °C) and the warmer Irminger current (T>5 °C). The colour of the spots is indicative of the sampling date, with darker blue at the start of the cruise and yellow at the end.

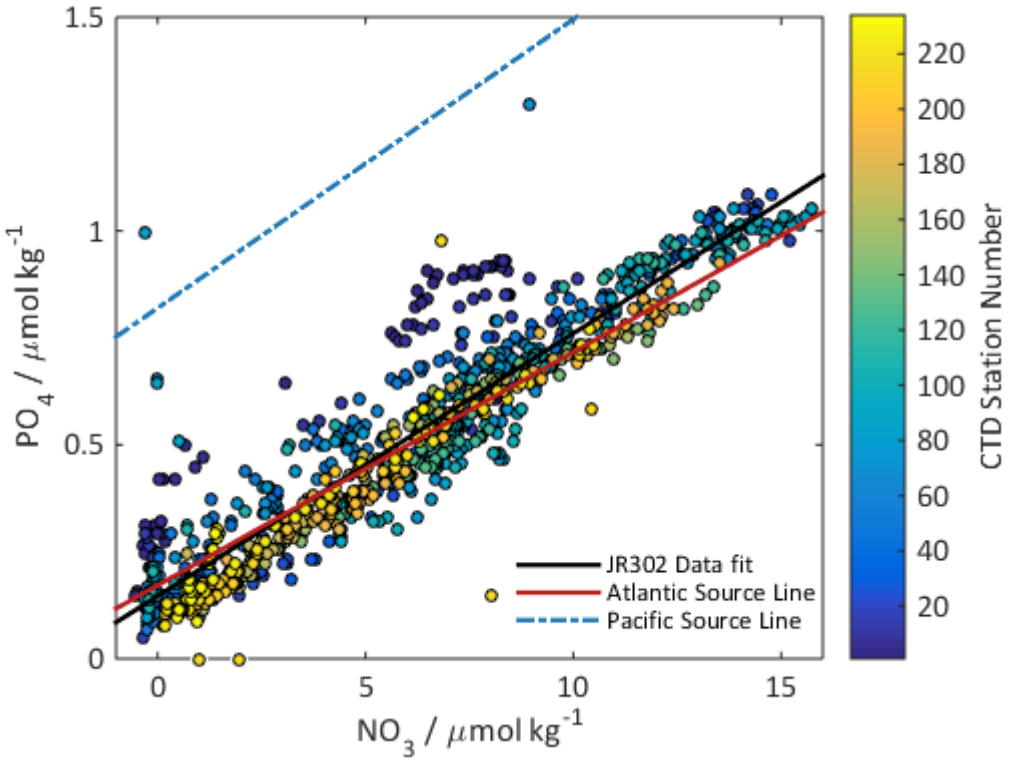

Figure 5.4 Nutrient tracers used to determine the source waters across the cruise track. The Atlantic (orange solid) and Pacific (blue dash dot) source lines are from Jones et al. (2008). The data is separated by CTD station numbers with low stations corresponding to rosette casts towards the start of the cruise in the Labrador Sea. The mixing line for the cruise is regressed from the surface 100 m of the phosphate and nitrate data, shown in black.

The Labrador Sea had lower salinity (32) and temperature (ca. 0 °C) than the rest of the sub-polar gyre, due to the Labrador Current (LabC) bringing the polar waters south from the Canadian Archipelago and the East Greenland current bringing water from the Greenland-Iceland-Norwegian Seas. The central Labrador Sea has a weak circulation relative to the edges (Lazier et al., 2002), which primarily consists of sub-polar mode water formed in the Iceland Basin, mixed with cooler polar waters in the Irminger basin and around the coast of Greenland (McCartney and Talley, 1984).

The East Greenland Current (EGC) and the East Greenland Coastal Current bring colder fresher water around the coast of Greenland into the LS (Sutherland et al., 2009). The EGC is characterised by low temperatures (ca 4-5°C), low salinity (34) and the presence of sea ice closer to the coast in the East Greenland Coastal current (Figure 5.9) (Holliday et al., 2007). The stations in this regions exhibited two conservative mixing regimes with different zero-salinity endmembers, Figure 5.3.

The zero-salinity endmember for the samples with temperatures >5 °C, $TA_{s=0}$ = 964 µmol kg^{-1}, indicates an influence of Arctic river waters, which feature TA in the range 800 - 1100 µmol kg^{-1} (Yamamoto-Kawai, 2005, Cooper et al., 2008, Jones et al., 2008). The

endmember for the samples with temperatures <5 °C, $TA_{s=0}$ = 559 μmol kg^{-1} indicates mixing with sea ice meltwater (50 – 600 μmol kg^{-1}, Rysgaard et al. (2009)); sea- ice was present around Greenland and Canada during May along the cruise track, although it retreated through June and July (Figure 5.9). Ice was encountered close to the Greenland coast with an ocean coverage fraction of ca. 0.1-0.2 (Figure 5.9b) close to the coast, decreasing to ≤ 0.1 further off shore. These two TA endmembers are indicative of Arctic water from the (ca. 0 °C, salinity 30, blue dotted dashed line) mixed with the warmer Arctic water of the EGC (Holliday et al., 2007).

The EGC has a weaker Pacific influence than the LabC waters due to the increased dilution from Siberian river waters and sea ice as it travelled south from the Bering Strait and around the Greenland Coast (Azetsu-Scott et al., 2010). This is observed with the N: P ratio for stations 40-80, located around the Greenland Coast being offset from the Atlantic line in figure 5.4, but not as strongly as stations 1-20 in the LabC.

The EGC followed the Greenland coast, and transferred cold polar waters around to the Labrador Sea, allowing the ice to persist for longer than the central LS or the IrB, which are influenced by the warmer North Atlantic Current waters. The EGC has enhanced chlorophyll-*a* concentrations in summer due to higher nutrient concentrations (Holliday et al., 2006), and the increased light availability due to sea ice retreat. This was observed across the Labrador Sea (Figure 5.7). The three ARCT triangles at salinity 34.8 in the TA-S plot (Figure 5.3) are likely caused by the high biological activity in this region.

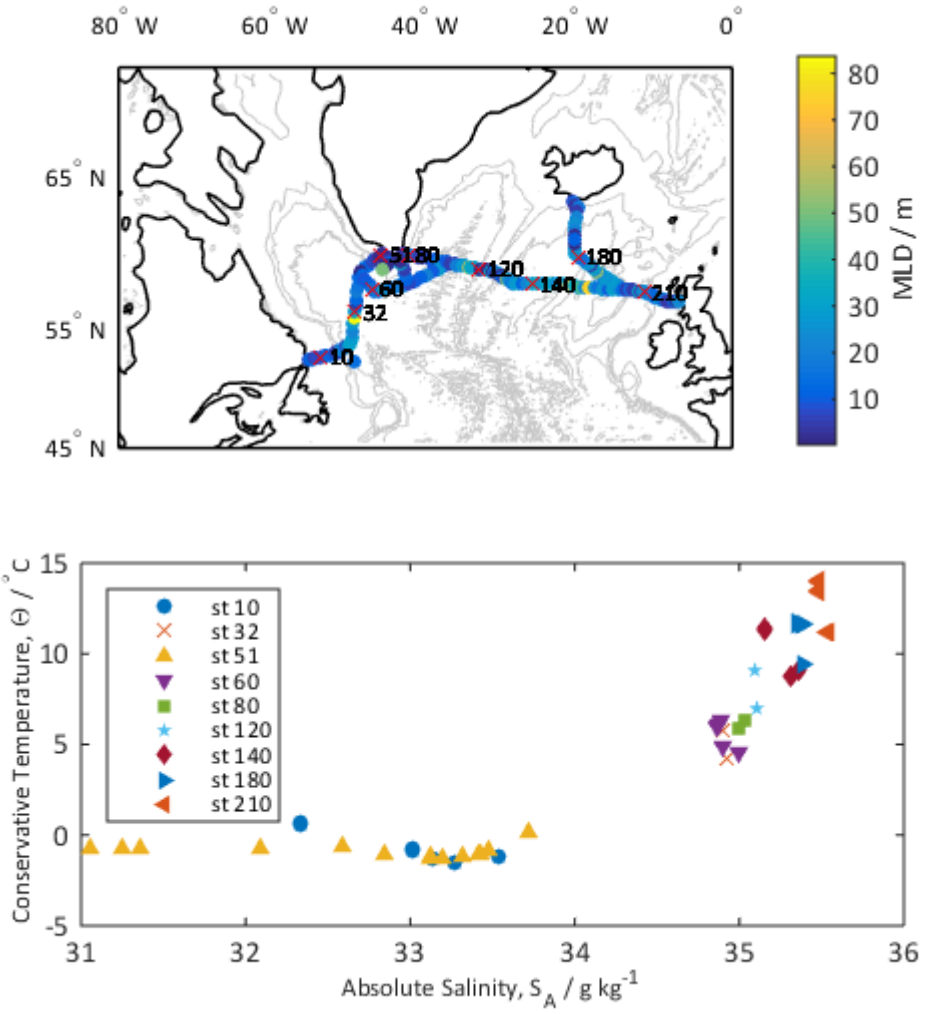

Figure 5.5 a. mixed layer depth (MLD) along the cruise track, with station numbers displayed. b. Temperature – salinity plot for top 100 m at selected stations. Stations 51 and 10 are clearly different to the other stations by the presence of cold polar waters and sea ice.

The Irminger Current (temperature 6-9 °C and salinity 34.9-35.1, Holliday et al. (2007)) consists of a branch of the North Atlantic Current (NAC) mixed with polar waters from the winter mixed layer in the Iceland Basin. This circulates in the Irminger Sea and mixes with the outer edge of the EGC (McCartney and Talley, 1982) forming Irminger Sea Water with temperatures of 4-5 °C and Salinity 34-35 (Sutherland and Pickart, 2008). This can be observed in the increased temperature and salinity values along Greenland transects GL1, GL2, GL 4 and GL3 in figure 5.7. The Atlantic-influenced waters (Figure 5.5b) are identified from T-S plots, consistent with Atlantic plots at 55°N by Emery and Dewar (1982). The increasing influence from the polar waters on the Irminger-East Greenland Current can be seen in the T-S plots (figure 5.5a and 5.5b, Appendix A.2) moving from station 120, 80 to 60, and finally 32 in the central Labrador Sea with salinity remaining constant with temperature decreasing. The NADR region TA-S regression line (Figure 5.3) shows a TA_0 endmember of 210.3 µmol kg^{-1}, consistent with calcification in this region, supported by an observed slight

increased chlorophyll (6th July, Figure 5.7, Appendix A.1). However the salinity range in the section is smaller than observed in the ARCT region, and the sample size is smaller contributing to a larger overall error on the endmember calculation from an R^2 of 0.4.

The cruise covered the Extended Ellett Line (EEL) which includes the Iceland Basin. We observe the highest salinities and temperatures in the southern most stations of the EEL. The NAC splits either side of the Rockall trough; the southern side mixes with Eastern North Atlantic water from the Bay of Biscay (Pollard et al., 1996) and continues northwards to form a principle component of the Norwegian Atlantic Current, while the rest continues north before splitting again at in the Iceland basin in east and north westerly directions (Hansen and Østerhus, 2000). The water found across the surface of the EEL is from these two North Atlantic waters, with the Eastern North Atlantic waters exhibiting slightly higher temperatures and salinities (station 210, Figure 5.5b,(Jiang et al., 2013)) than waters transported by the NAC (station 180, figure 5.5b). The SARCT TA-S regression line displays a negative endmember (-1103.1, Figure 5.3), most likely caused by the small salinity range over a small sample size causing large errors in the regression with an R^2 of 0.42.

5.3.2 Carbonate Chemistry Variability

The central LS showed homogeneity in the TA down to 200 m (Figure 5.6b, ca. 2280 - 2310 µmol kg^{-1}) consistent with the 2295 µmol kg^{-1} reported by Azetsu-Scott et al. (2010). The DIC (figure 5.6c, ca. 2090-2015 µmol kg^{-1}) across the central region is similar to early summer values of 2125 µmol kg^{-1} reported by DeGrandpre et al. (2006) and 2080 µmol kg^{-1} in June by Körtzinger et al. (2008). The large decrease in pCO_2 (to ca. 100 µatm, figure 5.7) is attributed to biological production, with a similar response observed DeGrandpre et al. (2006). This is supported by a corresponding increase in chlorophyll (2.5 µg L^{-1}, Figure 5.7) and high DO (Figure 5.8, stations 0-45), and enhanced chlorophyll across the central LS (Appendix A.1, and Figure 5.7) compared to the rest of the cruise track. At the time of the cruise, biological production formed the primary control on pCO_2 variations in the central LS due to favourable phytoplankton growth conditions with increasing temperatures, a shoaling mixed layer depth and nutrient availability from winter convection (Körtzinger et al., 2008).

The coastal edges of the Labrador Sea showed increased stratification from the polar influenced waters (LS, Figure 5.6b & 5.6c). LS has a clearly-defined water mass in the centre of the section with higher TA, indicating the presence of warmer Atlantic waters from the Irminger current flowing adjacent to the polar coastal currents.

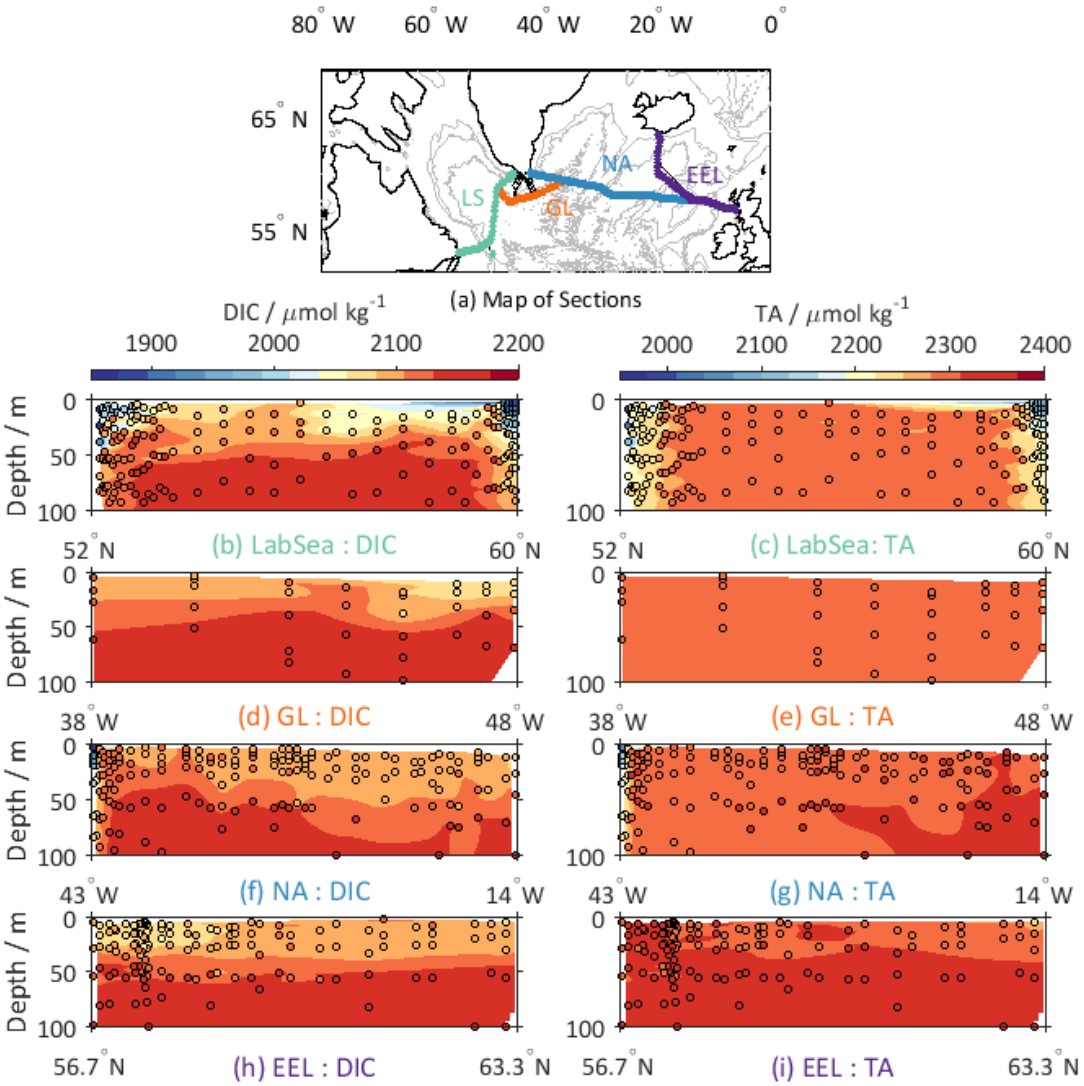

Figure 5.6 Water Column TA and DIC sections along the cruise track. (a) Map of the sections where LS = Labrador Sea, GL = Greenland Edge, NA= North Atlantic, EEL = Extended Ellett Line, green – Labrador Sea from Canada to Greenland plotted in (b) and (c) against latitude, orange – the edge of Greenland plotted in (d) and (e) against longitude, blue- the North Atlantic plotted in (f) and (g) against longitude, and purple- the Extended Ellett Line plotted in (h) and (i) against latitude.

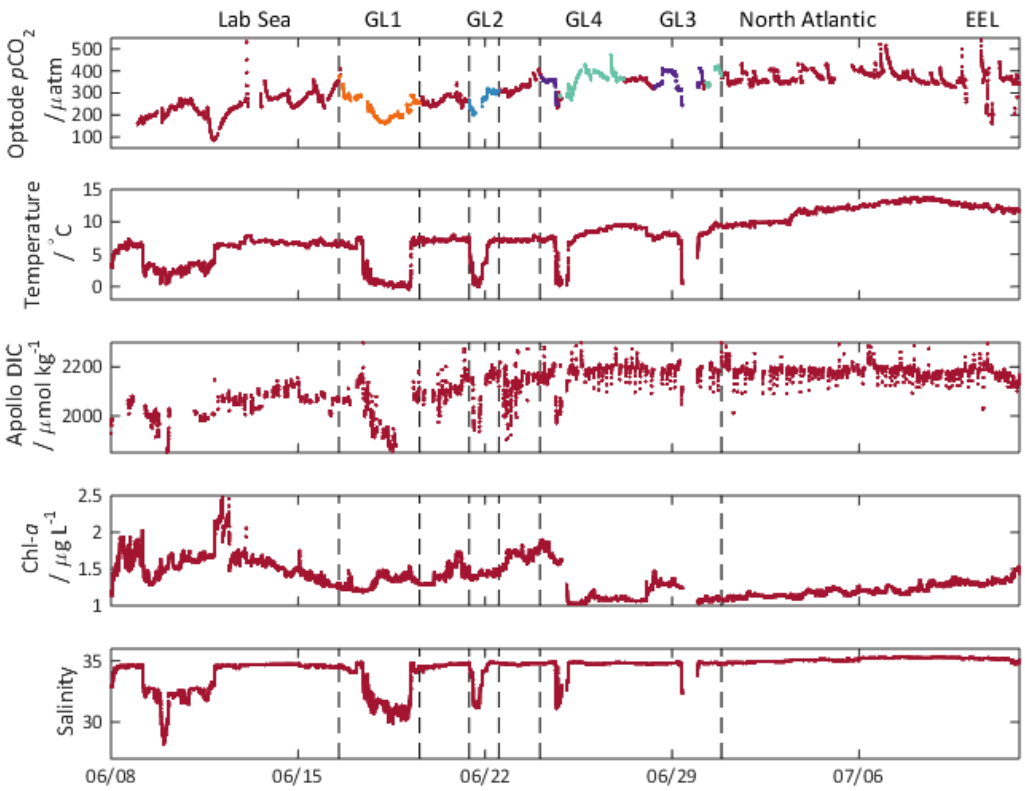

Figure 5.7 Plots of the measured variables from the underway supply along the cruise track. The different coloured pCO_2 indicate data collected on the sections towards Greenland labelled at the top (GL1-4) and corresponding to the same sections as shown in figure 5.10. Lab Sea= Labrador Sea, and EEL = Extended Ellett line, North Atlantic= Irminger Basin and AR1/E line

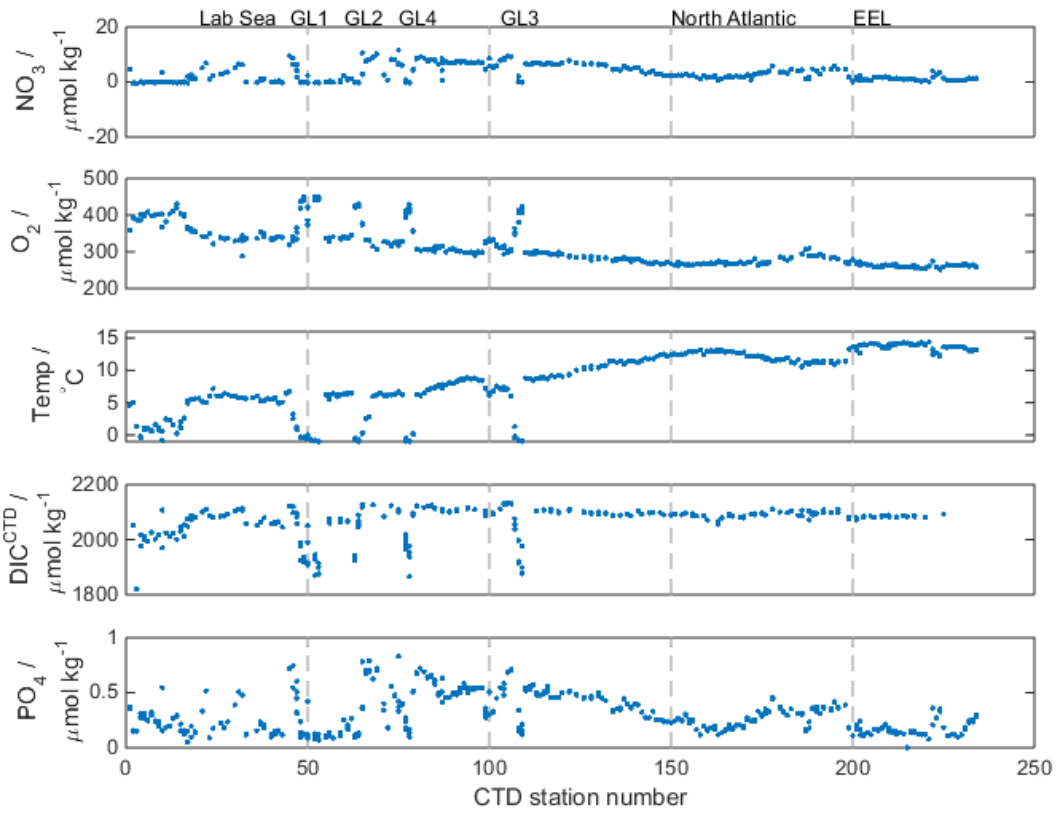

Figure 5.8 Subplots of variables sampled in the top 20 m of the CTD casts. NO_3 =nitrate, O_2 = Dissolved Oxygen concentration from bottle CTD samples, DIC^{CTD} = bottled DIC samples measured on the VINDTA, PO_4 =phosphate. CTD station numbers increase eastward along the cruise, and each minimum in temperature corresponds to the most inland point on the transects to the Greenland coast (GL1-4).

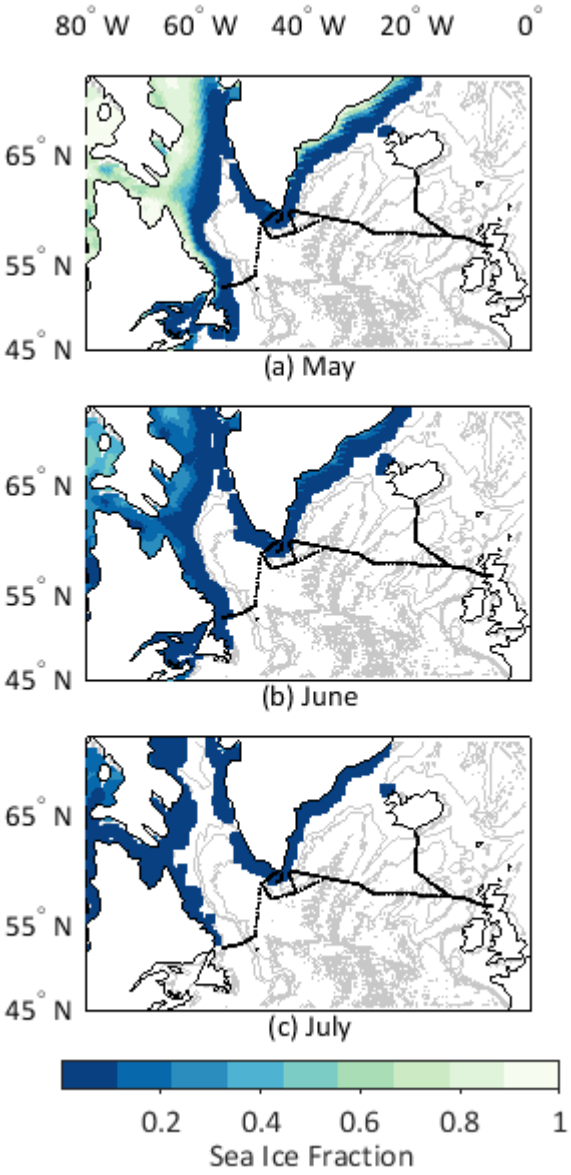

Figure 5.9 The 2014 sea-ice fraction in the North Atlantic averaged per month, for (a) May, (b) June and (c) July. The data were obtained from http://nsidc.org/data/ on [16/05/15]. Cruise track is shown in black. The cruise passed into the ice ca. 17th June. July is shown for comparison. The darkest blue shows ice fractions greater than zero, but less than or equal to 0.1. The ice fraction increases with decreasing colour, where zero ice cover is shown in white (except for land regions).

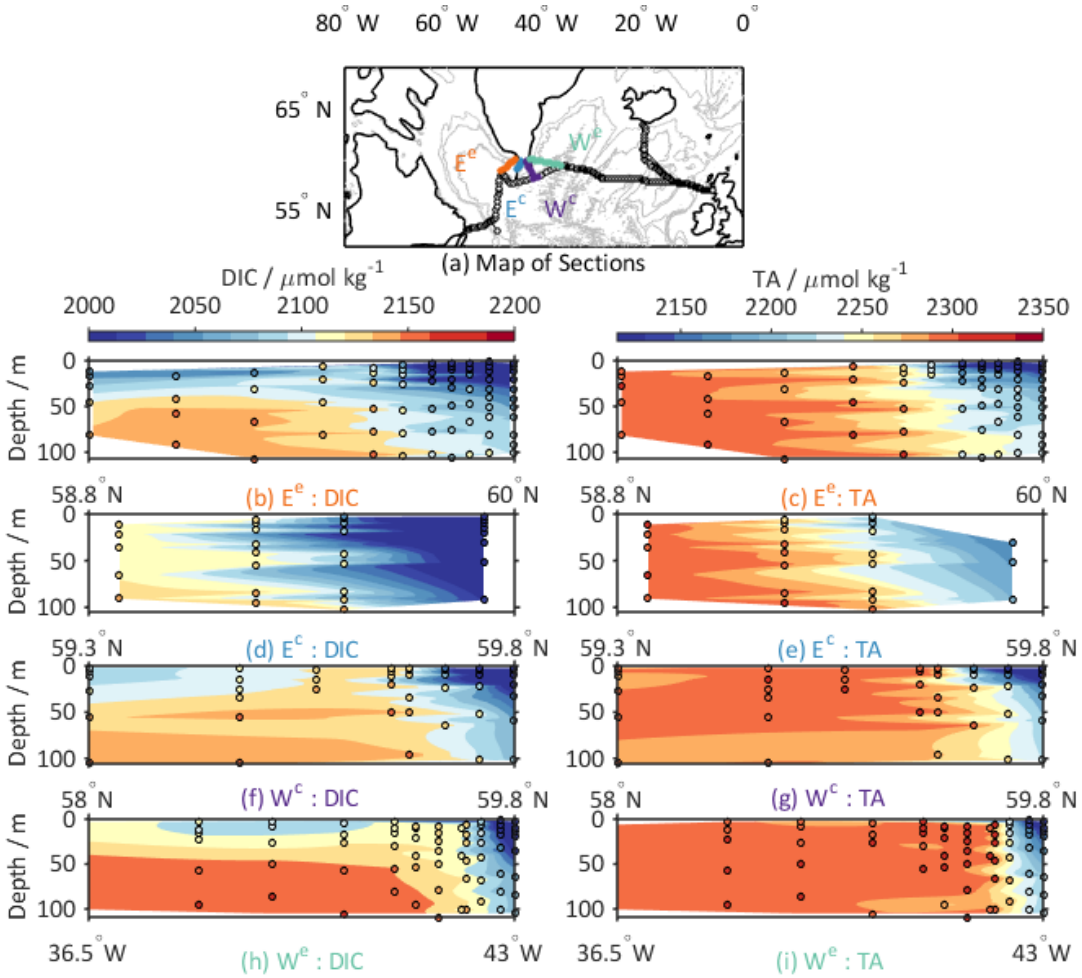

Figure 5.10 The top 100 m water column TA and DIC along each transect into the Greenland coast, moving closer to the coast from left to right. (a) Map of the sections. The water column data is plotted in order of increasing longitude. Eastern Edge (E^e)- Orange –plotted in (b) and (c), Central East (E^c)-Blue –plotted in (d) and (e), Central West (W^c) - Purple- plotted in (f) and (g), and Western Edge (W^e)- Green- plotted in (h) and (i).

The lowest TA and DIC concentrations observed during the cruise (2000 and 1850 μmol kg^{-1} respectively) were observed, close to the coast of Greenland (Figure 5.10 Section E^c). The low DIC and TA emanated from the surface and propagated south and downwards through the water column suggesting they were due to melting sea ice or glacial river water, consistent with the TA endmembers for this region as discussed in section 5.3.1. The low-DIC waters come from previously ice-covered areas (Figure 5.9), where the sea ice retreat has led to phytoplankton blooms due to the increased light availability (Appendix A.1 for satellite chlorophyll images, week of 2nd June to 9th June) combined with enhanced nutrient concentrations of up to 10 μmol kg^{-1} nitrate and 1 μmol kg^{-1} phosphate (Figure 5.7). Closer to the southern tip of Greenland (59.8°N) the influence of photosynthesis is evidenced by the increased O_2 and low DIC values (Figure 5.8). We thus attribute the initial decrease observed in the pCO_2 to a phytoplankton bloom consistent with the enhanced chlorophyll concentrations in figure 5.8.

The North Atlantic region, along the WOCE A1/E and AR7E lines showed constant TA (ca. 2100 μmol kg^{-1}, Figure 5.6f, NA) consistent with NAC water (highest temperature and salinity of the regions (Stoll et al., 1996)) advecting north and northeast as the Irminger current. DIC values (2100-2150 μmol kg^{-1}, Figure 5.6g, NA) west of the mid-Atlantic Ridge along the WOCE A1/E transect are similar to previous measurements by Thomas and Ittekkot (2001) of 2090-2130 μmol kg^{-1}. While moving further east to the EEL the surface concentrations of DIC were nearly constant ca. 2100 μmol kg^{1}, while TA decreases from ca. 2180 to 2150 μmol kg^{-1} by 50 μmol kg^{-1}.

There were lower DIC concentrations closer to the Scottish Coast (Figure 5.6i), where the TA (Figure 5.6h) remained comparable with that observed in the North Atlantic region. This is consistent with penetration of the North Atlantic current waters bringing sub-tropical low-DIC water north (Thomas et al., 2008) into the Rockall Trough, and similar to the low DIC water found in the Bay of Biscay in early summer (Jiang et al., 2013), brought north by the ENAW.

5.3.3 Continuous underway carbonate chemistry data compared to discretely collected samples

The pCO_2 optode showed good agreement with the underway discrete DIC/TA samples when corrected to *in situ* temperatures (Figure 5.11). The pCO_2 optode displayed a wide range of CO_2 values across the LS and ARCT regions, from 100 μatm to 400 μatm. The optode displayed a drift in the weekly CRM's totalling -1.7 μatm which was primarily towards the end of the cruise (Chapter 4, Figure 4.11, weekly CRM measurements compared to certified values). The optode showed less variability across the NADR consistent with the above discussed DIC and TA (Section 5.3.2), and the hydrography (Section 5.3.1). The SARCT region (including the EEL) showed significant variability, inconsistent with the carbonate chemistry discussed previously, which is further discussed below.

There is an offset between the bottled samples and the optode in the period from from 22nd June to 6th July ranging from 15 μatm to 30 μatm. The optode showed significant and sudden variability in the pCO_2 (ranging between ca. 100 -500 μatm) from 11th July. This was during the final part of the cruise route, along the Extended Ellett Line and near the Scotland coastline. Large oscillations in the output from the spot recorded by the PMT were noted. This is not consistent with photobleaching of the indicator or the reference fluorophore, instead indicating a hardware or software issue. Despite several investigations into the electronics, the cause of these oscillations is still unclear. Both the PMT and the LED performed well when returned to the lab and tested in similar conditions. Due to this uncertainty, the optode pCO_2 data was flagged from the 12th July and not used in this

chapter's analysis from this point onward (figure 5.11). The precision calculated prior to this point was ± 9.5 µatm, based on the pooled standard deviation of repeated measurement of DIC/TA CRMs.

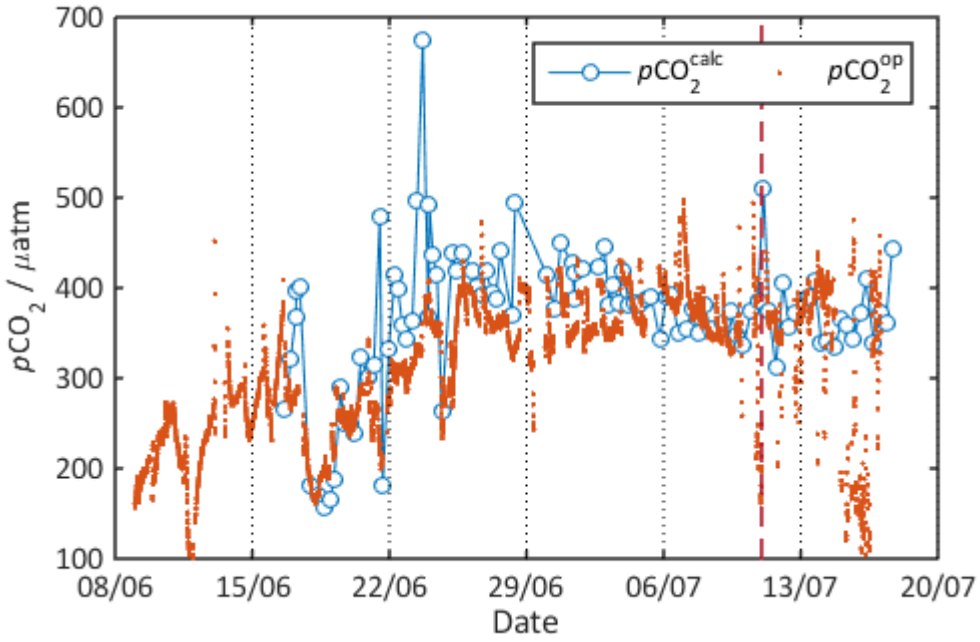

Figure 5.11 The underway optode pCO_2 (orange dots) compared to pCO_2 calculated from underway discrete DIC and TA measurements (blue open circles). The red dashed line indicates when the oscillation in the spot began (11th July).

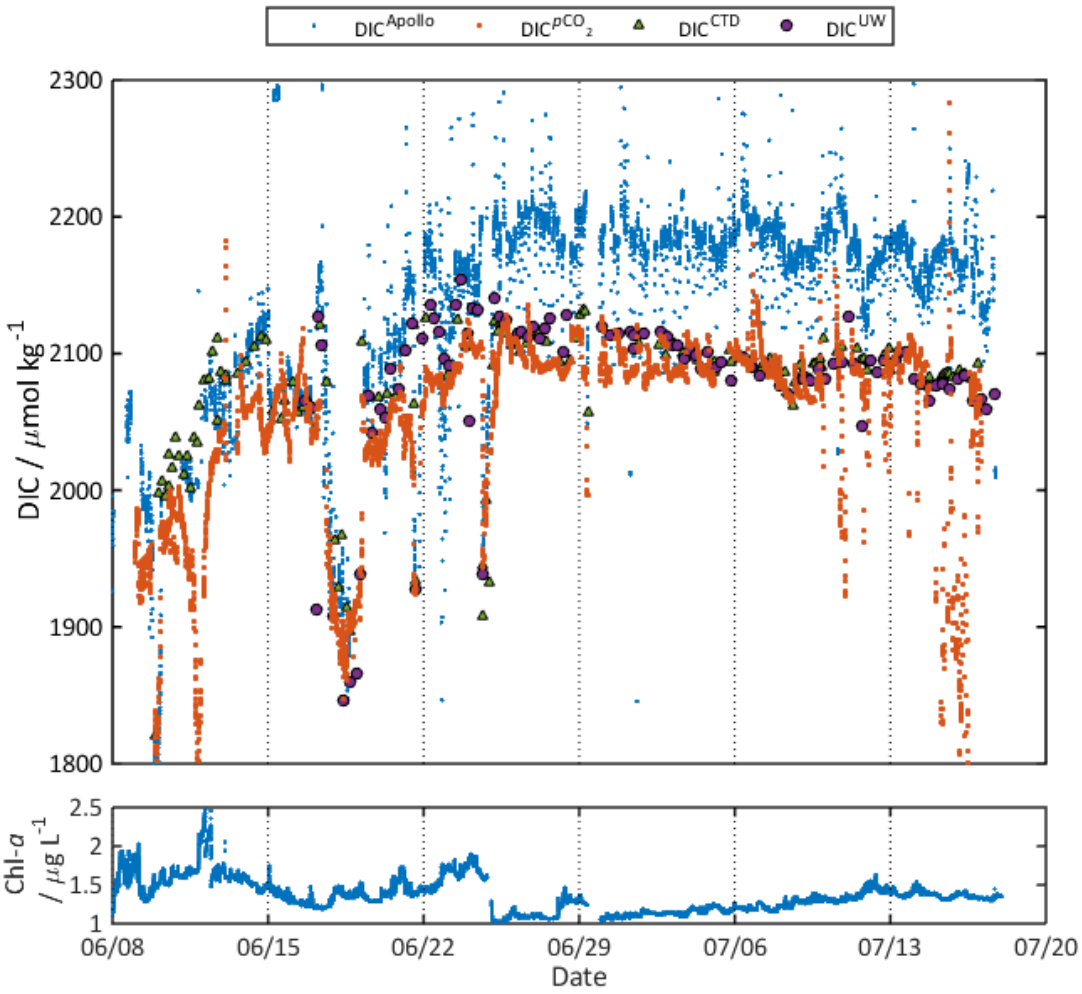

Figure 5.12 Discretely collected dissolved inorganic carbon (DIC) samples from the underway (purple circles, DIC^{UW}), and surface CTD (<20 m green triangles, DIC^{CTD}) plotted against time and alongside the underway measurements by the Apollo DIC analyser (blue dots, DIC^{APOLLO}), and the underway optode pCO_2 converted to DIC with regressed underway TA (orange dots, DIC^{pCO2}). Underway Chlorophyll-a is shown in the bottom subplot for comparison.

The underway Apollo DIC measurements showed an offset of ca. 100 µmol kg^{-1} from the discretely collected samples (from both shallow CTDs and underway samples) and DIC calculated from pCO_2 and regressed underway TA, from the 23rd June onwards, with a smaller offset from the 18th July Figure 5.12. The CRM measurements (conducted ca. every 30 measurements) showed neither drift, nor significant offset from the certified values (Appendix A.3 Figure 4.8). There was a sustained increase in chlorophyll-*a* from the start of the cruise until the 25th June (Figure 5.7). Biological contamination in the Apollo sample tubing is a potential explanation for these offsets. However the Apollo offset was fairly constant (varying up to 5 µmol kg^{-1} from the 100 µmol kg^{-1} from the mean) and the Apollo DIC data appeared to track the bottle and the optode samples, both inconsistent with the presence of biological contamination in any of the Apollo sampling tubing. The twice-daily calibrations and repeated CRM measurements (Appendix A.3, daily CRM measurements)

theoretically eliminate the influence from hardware, carrier gas, or acid changes. The Apollo conducted measurements at room temperature, and is calibrated at room temperature despite the *in situ* temperature being used for density corrections for the underway seawater. Changing the measurement temperature from *in situ* to the last recorded lab temperature changes the DIC from between 5-6 µatm, which is much too small to cause the observed 100 µmol kg^{-1} offset. Following extensive quality control of the calculations and raw data manipulation, the cause of the offset remains unclear and continues to be investigated.

5.3.4 Air-Sea Flux

The high-resolution dataset allowed the examination of the spatial variability in the air-sea flux, and the effect that the seawater pCO_2 sampling rate can have on calculated fluxes. Wind speed (5 m s^{-1}) and atmospheric pCO_2 (389.79 µatm) were kept constant while the sampling rate was varied from a maximum of once per 6 minute, to once per hour (Table 5.1), whilst the real optode data was obtained once per 6 minutes. The down-sampled data was interpolated back to the original sensor sample rate, once per 6 minutes. Given the aim of identifying any influence of the sampling rate on the air-sea CO_2 flux calculation, it was deemed necessary to simplify the calculation by removing other sources of variability where possible. The wind speed and atmospheric pCO_2 where therefore kept constant at 5 m s^{-1} and 389.79 µatm, respectively.

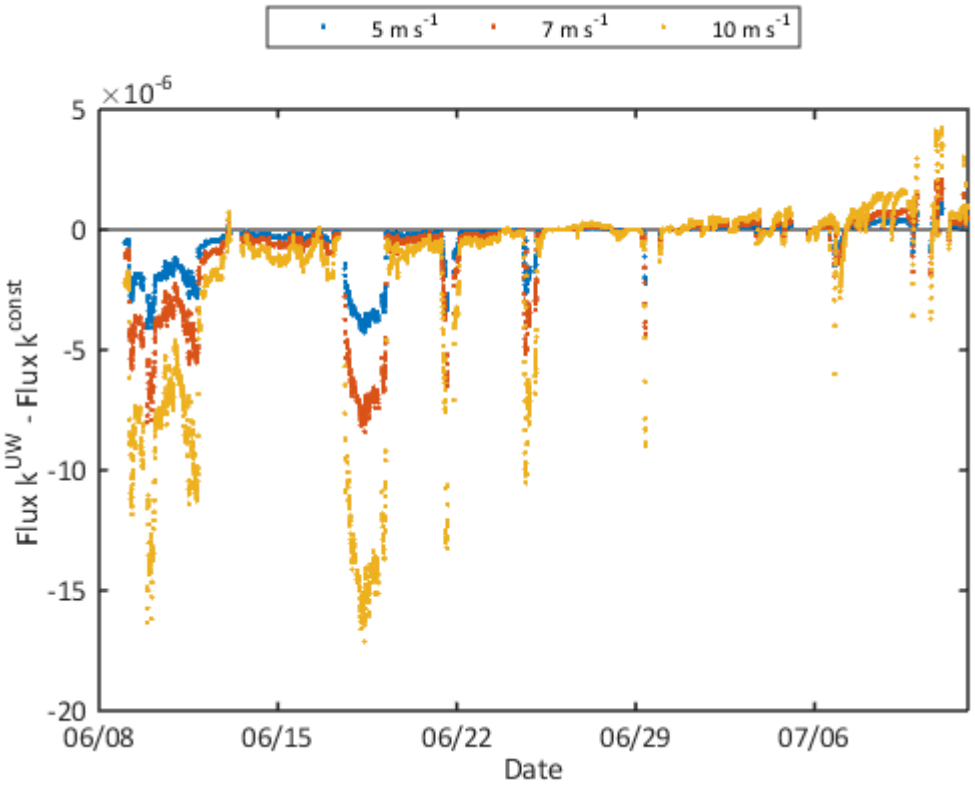

Figure 5.13 Effect of varying the ($k \cdot K_0$) on the final flux calculated along the length of the cruise where Flux k^{UW} refers the calculation using *in situ* measured temperature and salinity while Flux k^{const} refers to the use of the cruise mean temperature and salinity (8.7 °C and 34.4). The colour of the dots refers to the windspeed used in the calculations, blue dots are 5 m s^{-1}, orange dots are at 7 m s^{-1}, and yellow dots are 10 m s^{-1}.

The influence on the flux of the assumption that the gas transfer coefficient multiplied by the solubility coefficient ($k \cdot K_0$) is invariant with temperature (Etcheto and Merlivat, 1988) was investigated by comparing fluxes calculated with cruise-mean salinity and temperature values with fluxes calculated using underway temperature and salinity values. The difference between the two temperature and salinity conditions was applied for different wind speeds, in Figure 5.13. The residuals indicate that the assumption that ($k \cdot K_0$) is largely invariant with temperature is more valid at lower wind speeds (5 m s^{-1}) than at higher wind speeds. This is due to the high wind speeds reducing the surface tension of the sea-water; influencing the Schmidt number, and causing increased bubble entrainment which further changes K_0, further discussed in Wanninkhof et al. (2013). Wanninkhof (1992) advised against assuming constant temperature due to the systematic bias this caused. The strong temperature and salinity gradients observed in the LS and the Greenland coastline (Figure 5.7) correlate to large discrepancies in the calculated flux residuals in Figure 5.13, confirm that using the mean temperature and salinity are not appropriate for this study.

The interpolation of limited observations is known to impact the error of the flux calculations by up to 75 %, alongside any normalisation to a reference year, wind speed variability, surface skin temperature and the gas transfer coefficients used (Takahashi et al., 1997). The interpolation method was varied across the 12 min, 1 hour and 2 hour pCO_2 sampling rates, and one way Analysis of Variance (ANOVA) performed. The interpolation methods produced significantly different results ($p<0.005$), with the PCHIP method producing the consistently lowest standard deviation in fluxes between different sample rates. This is in contrast to Takahashi et al. (2009) who used linear interpolation to account for months and regions with no available data.

Table 5.1 Mean air-sea fluxes in mol m^{-2} calculated from interpolated values and their standard deviation. NADR = North Atlantic Drift Region, SARCT= SubArctic Region, ARCT= Arctic region

Sampling rate	**NADR / x 10^{-6}**	**SARCT / x 10^{-5}**	**ARCT / x 10^{-5}**	**Full Dataset / x 10^{-5}**
Original data (1 per 6 minutes)	-3.79 ± 8.8	-1.34± 1.4	-2.91 ± 2.0	-2.45 ± 2.2
1 per 12 minutes	-3.8 ± 8.87	-1.34 ± 1.31	-2.91 ± 2.0	-2.47 ± 2.05
1 per 30 minutes	-3.75 ± 8.50	-1.32 ± 1.34	-2.91 ± 2.0	-2.46 ± 2.05
1 per hour	-3.95 ± 7.65	-1.32 ± 1.20	-2.89 ± 2.0	-2.45 ± 2.05
1 per 2 hours	-4.66 ± 7.25	-1.37 ± 1.49	-2.92 ± 2.0	-2.49 ± 2.03

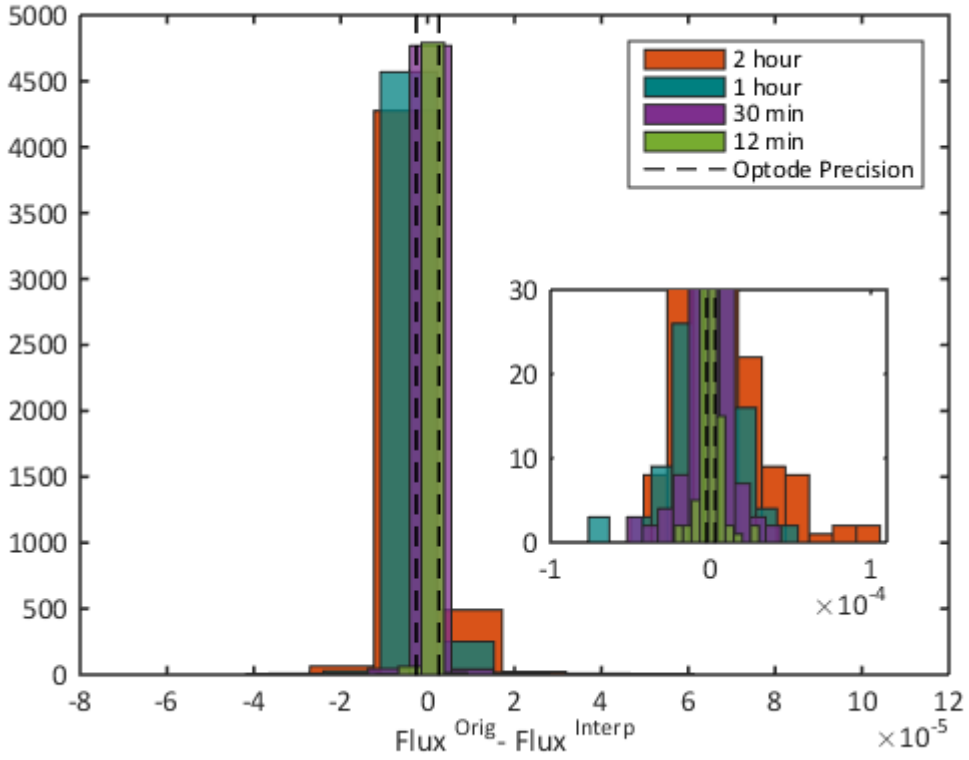

Figure 5.14 Residuals calculated for sample rates lower than the original flux calculation at a wind speed of 5 m s^{-1}. Orange is the interpolated 2 hourly samples, Dark Green is interpolated hourly samples, Purple is interpolated half hourly samples, and Light green is interpolated 12 minute samples. The dashed black line was the shipboard optode precision in the flux. The inset graph shows detail of the base of the histogram.

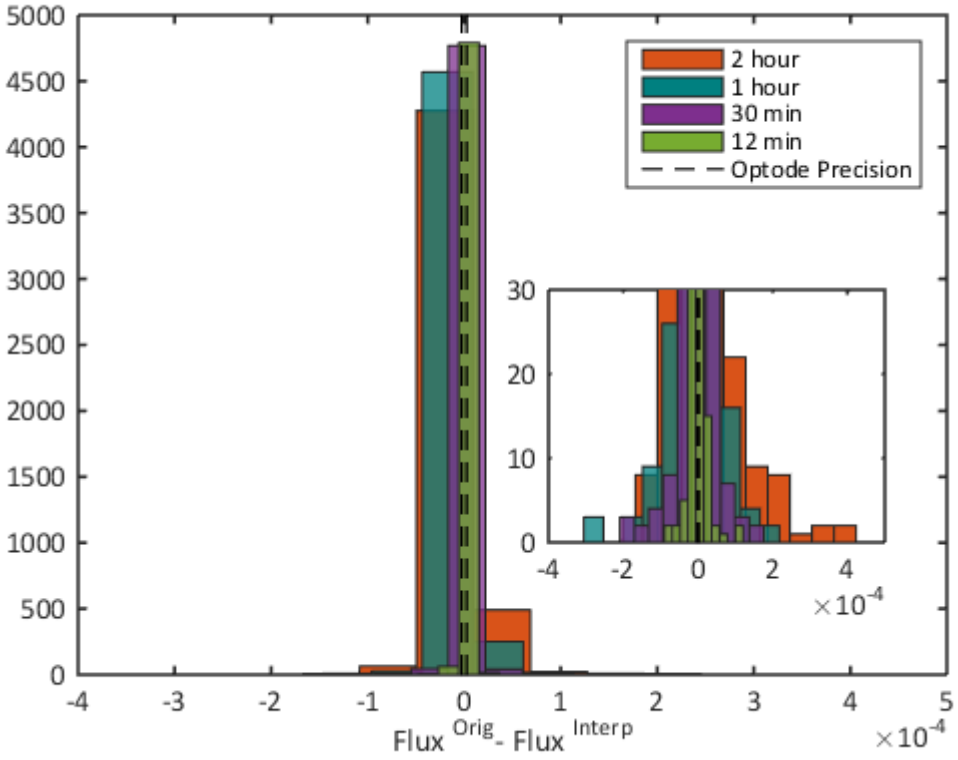

Figure 5.15 Residuals calculated for sample rates lower than the original flux calculation at a wind speed of 10 m s^{-1}. Orange is the interpolated 2 hourly samples, Dark Green is interpolated hourly samples, Purple is interpolated half hourly samples, and Light green is interpolated 12 minute samples. The dashed black line was the shipboard optode precision in the flux. The inset graph shows detail of the base of the histogram.

One way Analysis of Variance (ANOVA) was performed to determine if there was any significant differences caused by variation in sample rate. Pairwise multiple comparisons (Holm-Sidak method) showed that at different sampling rates were not significantly different ($p>0.05$, t-stat 0-1.27) across the whole cruise. The standard deviations in the fluxes were greater than the measurement across both the NADR and the SARCT (n = 571 and 460 respectively), due to the limited data in these regions compared to the ARCT (n = 3852) region. The residuals in Figure 5.14 indicate large deviations from the measured flux at hourly and 2-hourly sampling; these are primarily in regions where sharp changes in temperature and pCO_2 were observed, such as in the ARCT. Without the higher resolution data with the sharp gradients in pCO_2, these may have been considered outliers and discarded prior to interpolation, leading to incomplete spatial assessments of fluxes in these regions. The residuals at higher wind speed (10 m s^{-1}, Figure 5.15) show an increase in the deviations from the original sampled rate. This is consistent with the strong effect from wind speed on the flux calculation seen in figure 5.16. There however there is still no statistically significant difference between sampling rates, even at higher wind speeds. There is a statistically significant difference between the sample rates at 5 m s^{-1} and 10 m s^{-1} (student t-

test t= 30978739, p<0.001) at both the 6 minute sampling rate and the 2 hour sampling rate, as expected from the squared wind speed term in the calculation of k.

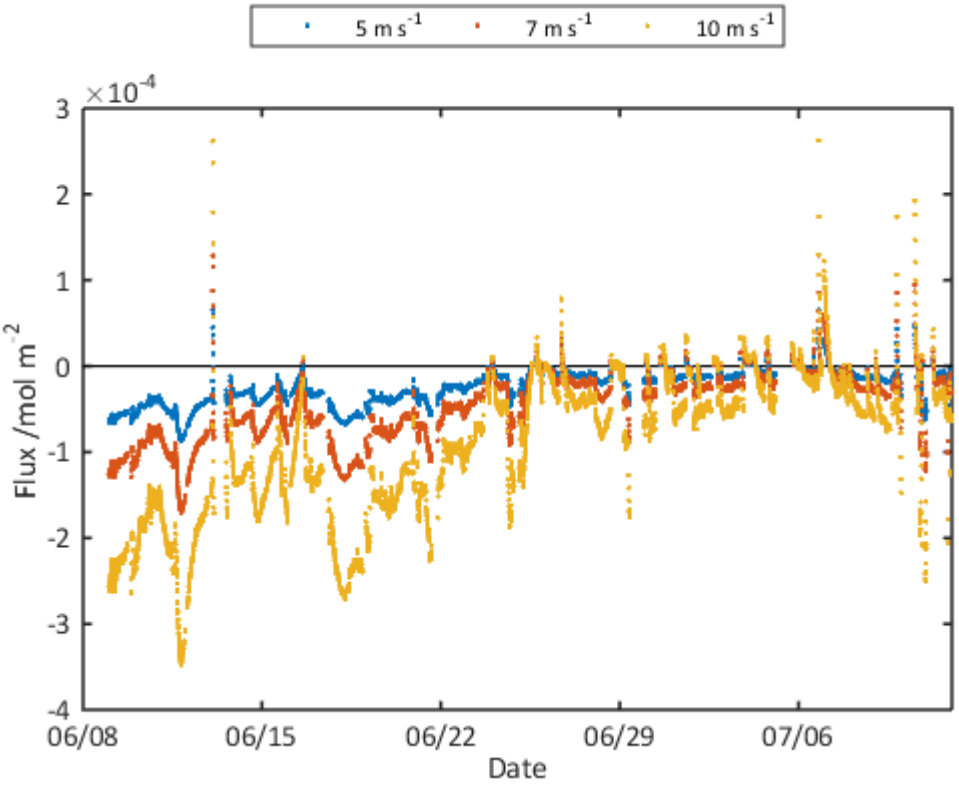

Figure 5.16 Effect of wind speed on flux calculated along the length of the cruise, blue dots are 5 m s^{-1}, orange dots are at 7 m s^{-1}, and yellow dots are 10 m s^{-1}.

The constant wind speed used in this study may have caused large underestimations of the fluxes (Figure 5.16), because of the quadratic dependence on wind speed when calculating k in equation 5.8, further evidenced from the residuals in figure 5.13 and figure 5.14. This is particularly noticeable in the LS and around the Greenland coast where low temperatures increased the solubility of the CO_2. This region is strongly controlled by the underlying water mass properties from the cool fresher waters from the EGC and LS, with recently melted sea-ice and the Labrador Sea Atlantic influenced central surface waters. This is a large source of uncertainty in our final flux calculations (up to ± 2 mol m^{-2}, Figure 5.16). Further investigations will apply climatological wind speed data obtained from satellite data to better constrain our estimates.

The total air-sea flux across the cruise (-0.12 mol m^{-2} per 35 days) indicated that the North Atlantic sub-polar gyre was a CO_2 sink, as previously observed (DeGrandpre et al., 2006, Takahashi et al., 2009). The highest cumulative fluxes (-0.112 mol m^{-2} per 3 weeks) were observed in the ARCT region, and were consistent with those measured previously in the LS during June (Körtzinger et al., 2008), and are attributed to the enhanced primary productivity

encountered particularly in areas where sea ice had recently retreated (Rysgaard et al., 2011). The NADR showed the smallest cumulative flux (-0.0022 mol m^{-2}), but of a similar magnitude to the SARCT region (-0.0062 mol m^{-2}). Along the cruise route (Figure 5.17) the flux changed direction, with the North Atlantic becoming a smaller CO_2 sink moving eastward. Due to the seasonal timing of the cruise, this may be attributed to later start of the spring primary productivity bloom moving east across the North Atlantic (Olsen et al., 2008).

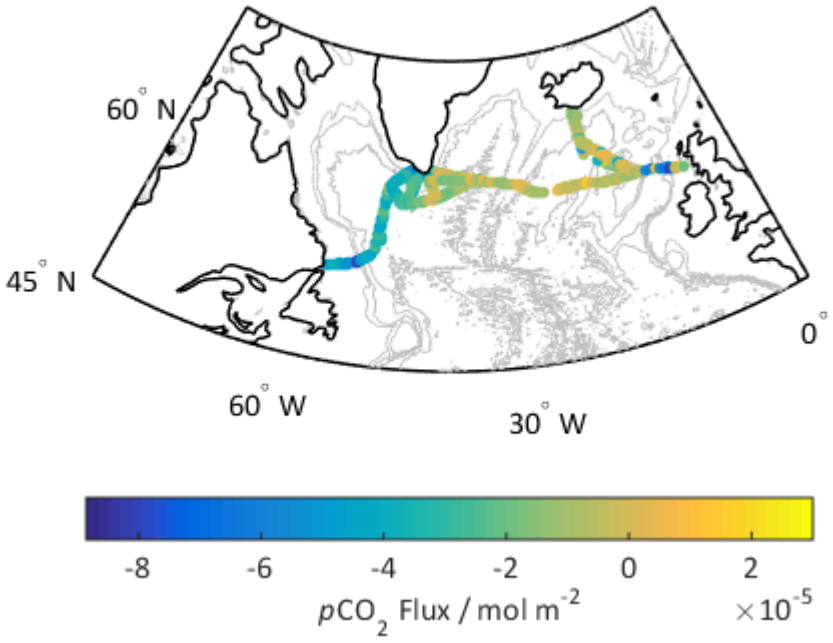

Figure 5.17 Map of pCO_2 flux along the cruise route in mol m^{-2} per 6 minutes.

5.3.5 Controls on surface pCO_2

The controls on the surface carbonate chemistry were evaluated using multilinear regression and one-way analysis of variance (ANOVA) in order to understand the mechanisms controlling the air-sea flux in the sub-polar North Atlantic, and across each of the previously defined sub-regions. The controls on surface pCO_2 were evaluated by performing stepwise regressions in SigmaPlot using (underway temperature, salinity, chlorophyll, and CTD sampled surface nitrate, phosphate, silicate and oxygen). The stepwise backward regression removed variables that exhibited collinearity, and those variables with P values > 0.058 were sequentially removed. The r^2 values indicate the percentage of pCO_2 variability the regressions explain. Due to the removal of the flagged optode data (along the EEL section), no regression could be attributed to the SARCT region due to the small sample size.

Table 5.2 Means ± standard deviations of underway measured variables for each biogeographical region. NADR = North Atlantic Drift Region, SARCT = sub-arctic region, ARCT = arctic region, T = temperature, S = salinity, Chl-a = Chlorophyll, DIC = dissolved inorganic carbon

	NADR	**SARCT**	**ARCT**	**Whole Cruise**
T / °C	12.7 ± 0.9	12.3 ± 0.5	6.6 ± 2.9	7.9 ± 3.6
S	35.2 ± 0.1	35.2 ± 0.1	34.1 ± 1.2	34.3 ± 1.2
Chl-*a*/ µg L^{-1}	1.21 ± 0.07	1.4 ± 0.08	1.4 ± 0.25	1.4 ± 0.23
Apollo DIC / µmol kg^{-1}	2188 ± 35	2172 ± 26	2115 ± 97	2133 ± 88
Optode pCO_2 / µatm	384 ± 34	348 ± 52	293 ± 72	309 ± 79

The SARCT region has the least variability across the underway samples particularly with temperature. This is attributed to the major influence of the NAC combined with the ENAW (Figure 5.2) which have similar properties with respect to nutrients, temperature and salinity, further discussed in section 5.3.1. The chlorophyll is increased compared to the NADR region and similar to the ARCT region where there was significant biological activity, however its standard deviation is small indicating sustained biological activity rather than blooms over the small sample. The satellite chlorophyll (Appendix A.1 4th – 11th July) indicates increased chlorophyll on the EEL, consistant with a small increase in the underway measured chlorophyll (1.3 to 1.5 µg L^{-1}, Figure 5.7). We expect that due to the similarity between the NADR and SARCT in the underway variables, and similar water mass influences that there would be a similar outcome from the regression.

The NADR has similar low variability in the underway variables. The same mean salinity and standard deviation as found in the SARCT regions indicates again the major influence of the North Atlantic water in this region. The temperature shows increased standard deviation compared to the SARCT however, which is attributed to the additional mixing of the North Atlantic Water in the IrB with cooler polar waters from the Denmark Strait and from the sub-polar mode water formed in the IcB. The chlorophyll-a mean was lower than the SARCT or ARCT regions, where satellite chlorophyll (Appendix A.1) and underway chlorophyll (Figure 5.7) indicate the presence of phytoplankton blooms.

The NADR regression produced an r^2 of 0.64 with independent variables of temperature, dissolved oxygen concentration and silicate concentration. These controls agree with the sub -polar controls modelled by Doney et al. (2009) from biology (oxygen and silicate) and solubility (temperature). The solubility term is primarily from the combined influence of the North Atlantic waters and the polar waters mixed in the IrB and sub-polar mode water.

Satellite chlorophyll indicates a bloom prior to the ship's arrival in this region (Appendix A.1, 26th June -3rd July), which would explain the influence of the biological terms despite the lower observed chlorophyll in this region compared to the ARCT and SARCT.

The ARCT region has large standard deviations compared to the other two regions due to the observed sharp gradients (figure 5.7). An initial stepwise regression r^2 of 0.27 with variables of chlorophyll and phosphate was produced. To improve the r^2, the ARCT region was further subdivided, using temperature to separate the polar waters from the Atlantic waters due to the significant temperature differences observed between the water masses. Measurements collected in water < 5 °C were deemed polar influenced regions, while the waters > 5 °C were deemed Atlantic influenced regions.

For the polar water influenced ARCT, the pCO_2 is correlated with salinity, silicate, phosphate and density with an r^2 of 0.52. These independent variables are attributed to two processes. The seasonal ice cover in this region increases the pCO_2 dependence on underlying water mass (from the density term) due to the lack of atmospheric interaction to drive changing pCO_2 (Doney et al., 2009). The salinity, phosphate and silicate terms are attributed to the blooms occurring where sea ice retreats, driving a change to the pCO_2 close to the Greenland coast (Section 5.3.2).

The Atlantic influence waters were correlated with phosphate, silicate and nitrate with an r^2 of 0.261- indicative of the primarily biological influence in these waters. This can be seen in the increased chlorophyll in the LS either side of the temperature minimums at the start of the cruise and around the Greenland coast (GL section on the map, Figure 5.6a and corresponding chlorophyll in Figure 5.7). Mixing with the cooler nutrient rich polar waters, may have stimulated these blooms, and made them more intense compared to the Atlantic waters in the NADR regions (chlorophyll peaks of 2-2.5 μg L^{-1} compared to 1 - 1.5 μg L^{-1} respectively, Figure 5.7).

The seasonal sea ice regions studied here fit better with the controls Doney et al. (2009) specified for the sub-polar regions, which may be due to the season the samples were collected and the retreating nature of the sea ice encountered. The simple multilinear regressions are in no way as comprehensive as the Doney et al. (2009) model equations for each region, however they provide additional evidence supporting Doney's results based on *in situ* observations.

5.4 Summary and Conclusions

The pCO_2 optode was successfully deployed over a 40-day cruise in the North Atlantic, with excellent agreement with pCO_2 calculated from TA and DIC measurements from discretely collected samples for 35 days. The precision of the optode was 9.5 µatm (excluding the last week of data). Investigation into the cause of the signal problems at the end of the cruise proved inconclusive. The underway DIC instrument deployed alongside showed a 100 µmol kg^{-1} offset from the second week into the cruise. The cause of the offset is undetermined, yet similarity in the shape of the DIC results across the cruise to the optode, CTD and underway bottle samples indicates biological contamination of the instrument is unlikely. The offset in the underway DIC sensor requires significant further investigation.

The high-resolution optode data was used to investigate the effect of sampling rate on CO_2 flux calculations. The high-resolution data was down sampled to simulate the effects of a lower sample resolution. The sampling rates (1 sample per 6 minutes – 1 sample per 2 hours) showed no significant difference in the fluxes calculated. However with wind speed being a large controlling factor of the overall flux calculation, it would be advantageous to develop sensors that can measure at a similar rate to anemometers (one sample per second) if focusing on a smaller regional scale, particularly in regions with changeable wind speeds. The calculated fluxes agreed well with previous estimates in the Labrador Sea, despite the assumption of constant wind speed in this study. This work can be developed further by using varied wind speed along with the interpolation method and different sampling rates to calculate sea-air CO_2 flux and improving the measurement time of the pCO_2 sensor to match the 1 sample per minute shipboard wind speed measurement rate (Wanninkhof, 2014).

Finally, the carbonate chemistry data collected on the cruise were used to determine the drivers of pCO_2 in the different biogeographical regions encountered on the cruise route. The North Atlantic sub-polar region showed high spatial variability in the surface waters, which was primarily attributed to the combined influences of water masses, sea ice and biology. Multiple linear regressions were performed using underway data and surface CTD sampled nutrients and oxygen in both the NADR and the ARCT regions where the majority of data were collected. Due to the strong gradients from the different water masses in the ARCT region, we subdivided this using temperature as the deciding factor. The coldest temperature regions with polar water influences indicated that the primary control on pCO_2 was the water masses while warmer waters in similar areas, but with Atlantic influences, were biologically controlled. The NADR was found to be controlled by biology and solubility.

Chapter 6:

Conclusions and Future Directions

Abstract

This chapter aims to summarise the previous chapter's findings while bringing them into context of current measurement requirements. The limitations of the current optode system are evaluated, and suggestions for future developments are made. The development and use of optodes in the wider community is evaluated for pH and pCO_2 based on the current successes of oxygen optodes.

6.1 Optodes

Oxygen optodes have undergone significant development and are becoming increasingly widely used. Recent work has demonstrated that oxygen optodes can be used to measure both aqueous and gaseous oxygen (Bushinsky and Emerson, 2013). This allows these optode sensors to use the marine air to undertake in situ calibration, thereby facilitating the removal of any calibration drifts during deployments. The optodes are also designed to work in a recess in the housing, with the additional use of a black silicone cover to protect the photosensitive chemicals of the spots (Tengberg et al., 2006). Oxygen optodes indicate the deployment potentials of this technology. Furthermore, with increasing climate concerns, the development of optode-type sensors to encompass carbonate chemistry variables such as pH and pCO_2 would be an invaluable asset. The low power requirements, small size and lack of reagents are favourable for prolonged deployment on platforms such as buoys and drifters. The characterisation of the PreSens pH and pCO_2 sensor spots allowed for a thorough an evaluation of the potential of these systems for marine measurements, applying the time domain dual lifetime referencing method.

6.2 Sensor spots

The pH sensor spot showed great potential with the seawater pH range being within the measurement range. An algorithm was used to account for the temperature and salinity dependence of the foil, and an initial deployment was undertaken in the Southern Ocean. The deployment highlighted the need for a more comprehensive evaluation including biological fouling testing. The optode also exhibited drift, which may have been a consequence of photobleaching.

The pCO_2 sensor underwent characterisation over a relatively small incremental change (280-1000 µatm) in pCO_2. The spot showed no significant salinity dependence, but strong temperature dependence was observed. A short term lab precision of 0.8 µatm demonstrates the potential precision of these optodes however the deployment precision of 9.5 µatm warrants further investigation. The spot was deployed as an underway sensor but with a water bath due to the temperature influence not being fully constrained at the time of the cruise. The spot showed good agreement with discrete underway and surface CTD DIC samples, however shows a discrepancy with the underway DIC spectrometer deployed alongside it. The results of the deployments were successfully used to identify spatial variations in the pCO_2 fluxes and controls on carbonate chemistry in the North Atlantic (Chapter 5).

While both the pCO_2 and pH spots show an excellent promise for measurements over the relevant ranges in seawaters, more work is required to characterise the temperature effects and refine the algorithms to convert the optode output.

In both cases the exact constituents of the spots are unknown due to commercial secrecy. This hinders our understanding and the development of such systems. Without this relevant knowledge, the accurate diagnosis of the underlying causes of temperature and salinity dependence, as well as potential drift, is difficult. Throughout this thesis, generalised conclusions and assumptions have been made as to spot composition- particularly with the pH spot. However, for these particular optodes to be developed further knowledge of the spot compositions will be vital. For example, the pH range of the pH spot was estimated from an initial apparent pK_a calculation. The low precision of the pH sensor compared to the spectrophotometric method could be better understood with knowledge of the indicator, as well as immobilisation technique and membrane type.

Table 6.1 Specifications as determined in this thesis for the pCO_2 and pH spots used, where Ø = diameter, λ = wavelength

	pCO_2 optode	**pH optode**
Precision	9.5 µatm (at sea) 0.8 µatm (lab)	0.01 pH
Drift	1.7 µatm	0.06 pH
Ranges examined	5 < T (°C) < 20 5 < S < 35 280 < pCO_2 (µatm) < 1000	5 < T (°C) < 25 5 < S < 35 7.6 < pH < 8.2
Light	5 mm Ø Blue LED λ470 nm	5 mm Ø Blue LED λ470 nm
Detector	PMT, Hamamatsu	PMT, Hamamatsu
Fibre Optic cable	600 µm Ø multimode optical fibres , 3.8 mm Ø diameter tubing, 1 m length	600 µm Ø multimode optical fibres , 3.8 mm Ø diameter tubing, 1 m length

The pH optode in its current state is not yet suitable for open ocean deployments due to the relatively low precision compared to other methods, along with the drift observed during the Southern Ocean deployment. However coastal and estuarine environments show much larger pH changes than the open ocean, and may be a more suitable deployment options. In addition, the pH optodes can be used for biological ocean acidification experiments, where a lower precision is appropriate.

The pCO_2 optode showed a lack of drift upon deployment, however was deployed in a waterbath on the research cruise, with filtration of the water prior to measurement. An *in situ* deployment would allow a greater insight into the reliability of the spots calibration and performance with temperature changes and potential biological interferences (high chlorophyll).

The initial aims of this project were:

1. Characterisation of the sensors response to pH/pCO_2 at varying temperatures and salinities in a lab setting
2. Evaluation of the ability of the sensors to be deployed in a real world setting (e.g. dock deployment or underway system on research cruises)
3. Interpretation sensor data from deployments to identify suitability for ocean measurements

pH and pCO_2 sensors were successfully characterised in a lab setting and deployed as shipboard sensors. During pH optode deployment, drift was observed and attributed to interference from chlorophyll. The pCO_2 optode was deployed with sample filtration and in a water bath with the aim to limit the temperature and chlorophyll fluorescence effects as observed with the pH system. This allowed the data to be used in combination with other carbonate chemistry variables obtained from the ship's underway seawater systems to describe the spatial variation in carbonate chemistry and CO_2 flux and investigate the controls in the North Atlantic Ocean.

6.3 Future developments for the system

Ultimately, significant progress in pH and pCO_2 optode development can only be made with close collaboration between research teams developing the chemistries behind the spots and the research teams calibrating, validating and deploying them as optodes. This was demonstrated in this thesis, where knowledge of the spot chemistry may have hindered calibration and deployment evaluations. With both spots, an indicator that has a more basic known pK_a upon deployment would improve the precision and sensitivity of the sensors. For the pCO_2 optode, the response time is diffusion limited, but is slower than pH optode. It would be advantageous to reduce the membrane thickness as much as possible, without limiting the fluorophore concentrations. This would be important for deployments on moving platforms such as CTD casts. Temperature effects and ionic strength issues would be better understood in both optodes with knowledge of the membrane types and respective indicators. The hypothesis that osmotic pressure may influence the pCO_2 sensor may only be confirmed with

knowledge of spot chemistry, and may explain the long term drifts observed by Atamanchuk (2013).

In order to detect the photons emitted by the sensor spots, a photon multiplier tube (PMT) was used. These are highly sensitive, allowing the excitation of the spot at low power. With the ultimate aim of optodes to be deployed as *in situ* systems it is vital we investigate the use of smaller more rugged detection methods such as photodiodes (Rérolle et al., 2012). The use of a photodiode will allow a more compact system and the potential to have the LED and the photodiode closer to the spot. This will limit potential light loss along the fibre optic cable allowing more photons to reach the photodetector and increasing the signal to noise ratio. The removal of fibre optic cables will increase the ruggedness of the system making it more suitable than the current system for *in situ* deployment.

Integration of thermistors into any final sensor packaging is essential due to the strong temperature dependence displayed by both optodes. This requires a more flexible control program, which could be achieved, using LabView software. This would facilitate troubleshooting with respect to hardware and software issues, and would allow integration between systems- for example measuring both pH and pCO_2 with one system. Finally, use of a sensor controller (such as those used in house for *in situ* nitrate and spectrophotometric pH systems) to record data would allow significantly better flexibility in deployment, particularly when monitoring benthic seawater for carbon capture storage schemes.

Laboratory calibrations over wider temperature ranges (such as below zero temperatures as encountered in the polar oceans) is required, particularly with the proposed hardware changes. Smaller incremental changes in temperature and pH/pCO_2 will hopefully also allow increased understanding of the optode deployment potential. The addition of biofouling and pressure testing would allow more deployment options. Attempts to characterise the pCO_2 optode response to atmospheric CO_2 will enable calibration *in situ* as the oxygen optodes have successfully undertaken. This would work to counteract any drift in the same way as Fietzek and Körtzinger (2009) employed a blank gas zero for a spectrometer. This would be an asset when deploying on drifters such as ARGO floats or moorings where there would be access to marine air on a regular basis.

6.4 Concluding Remarks

The development of autonomous sensors is essential to increase spatial and temporal measurements. Shipboard measurements are costly per data point and require large amounts of time and manpower. Alternately autonomous sensors may be deployed *in situ* on a variety of platforms allowing high quantities of data to be collected with lower cost per point. The platforms may be mobile allowing increased spatial resolution across the ocean water column or stationary platforms which allow temporal coverage. The data is required to determine the current state of the ocean, and with the use of model simulations, to determine the potential response of the ocean to the climate change.

While more work is required on the optodes described in this work before they are widely deployable as *in situ* systems, I believe with more work they will be a versatile sensor providing much needed data. There is also a significant scope to expand optode technology beyond pH, pCO_2 and oxygen with development of the appropriate molecular sensors.

Appendices

Appendix A

A.1 Satellite Chlorophyll Maps

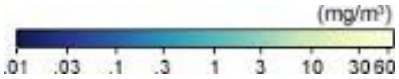

25th May – 1st June

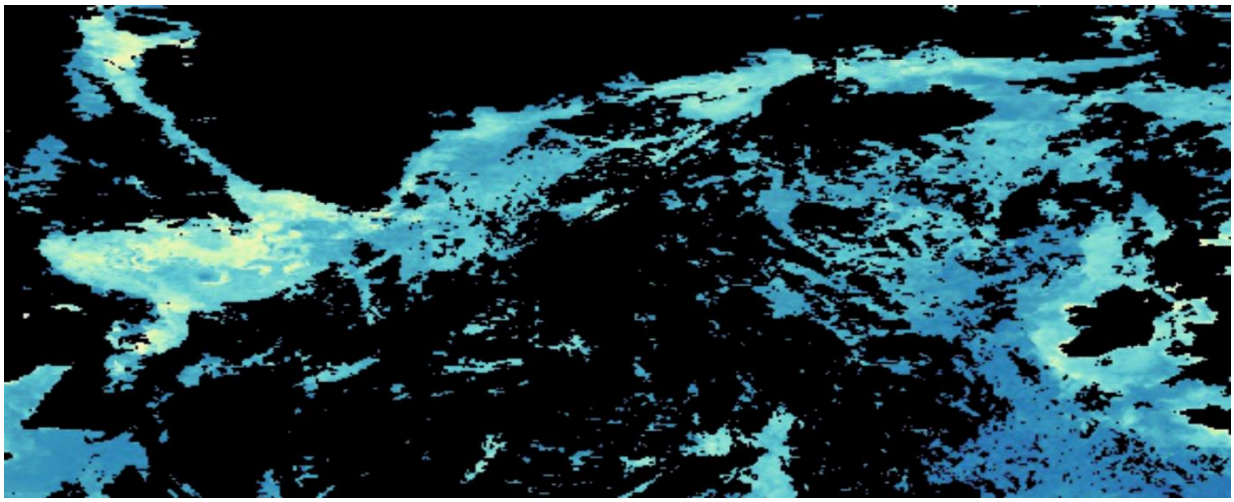

2nd June – 9th June

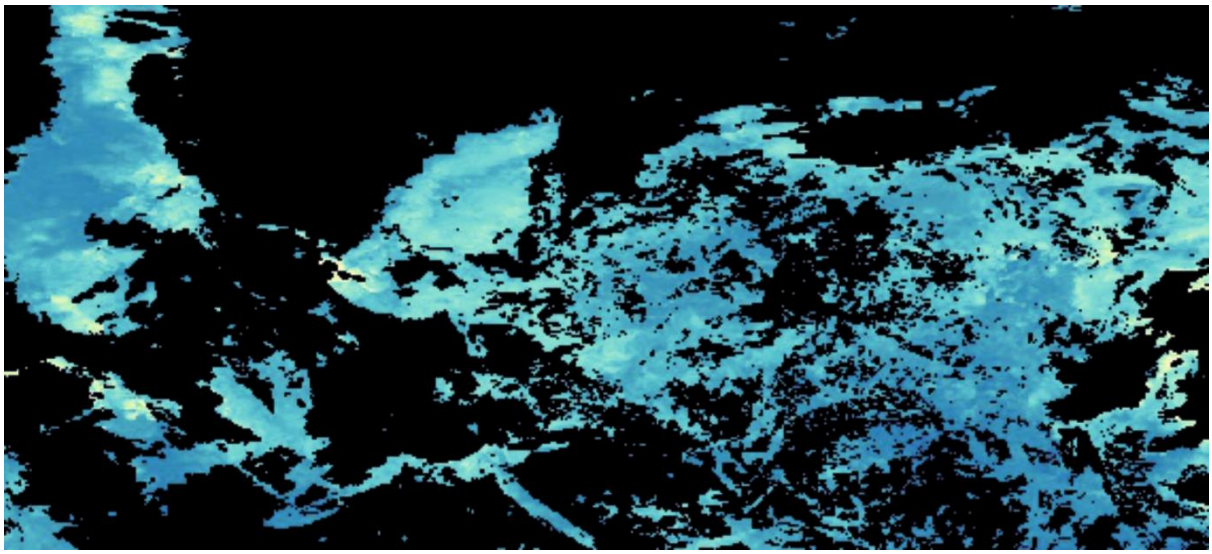

Appendix A

10th June -17th June

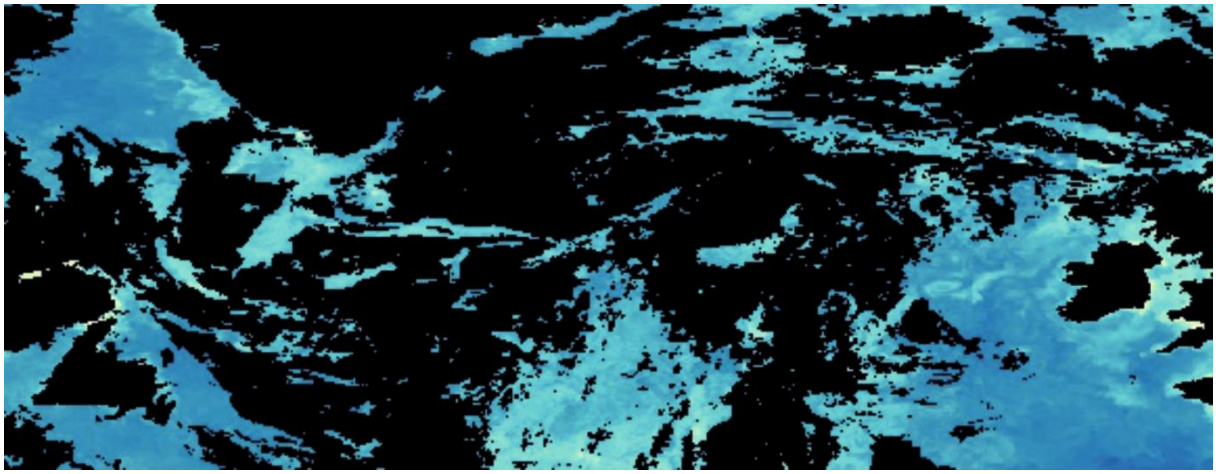

18th June – 25th June

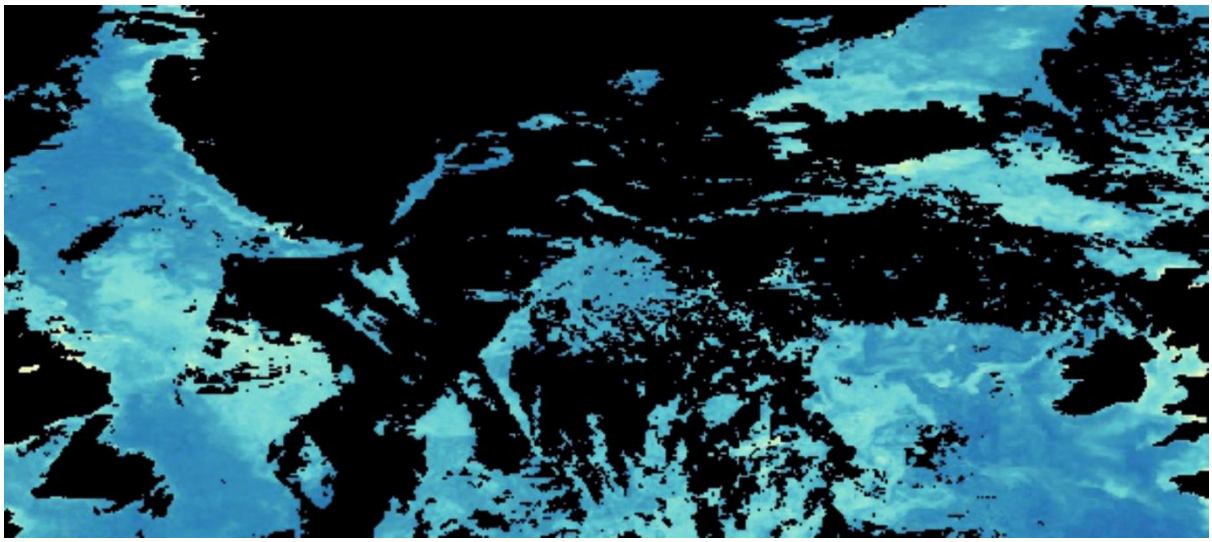

26th June – 3rd July

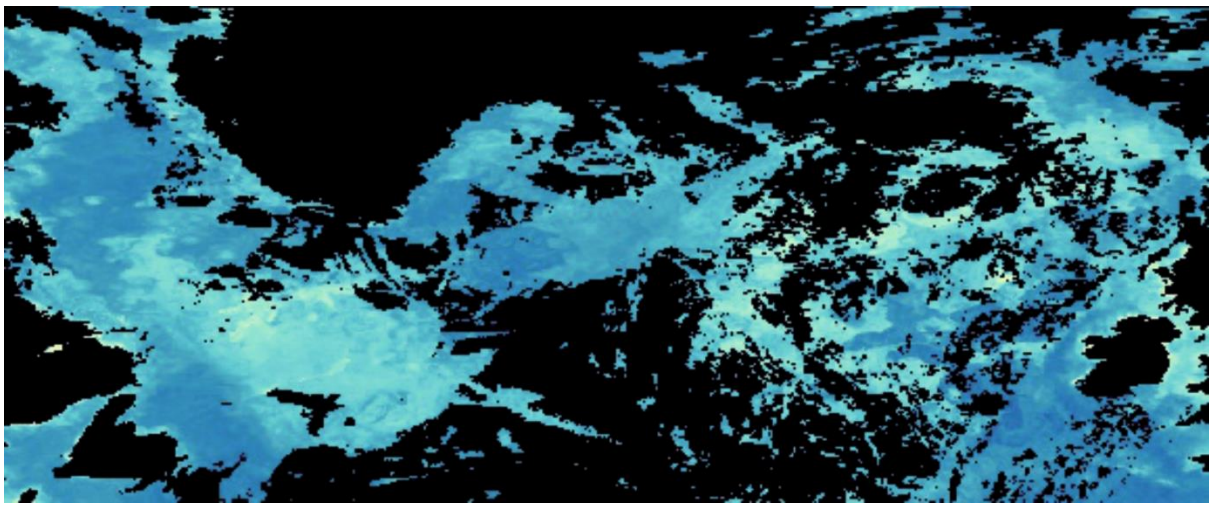

4th July -11th July

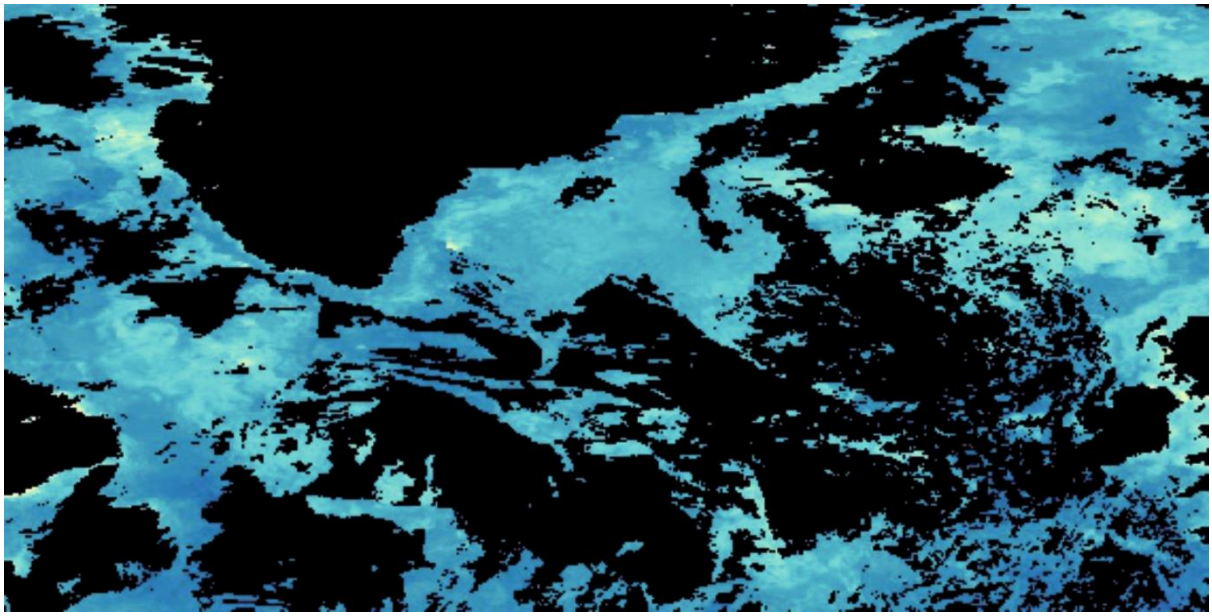

12th July – 19th July

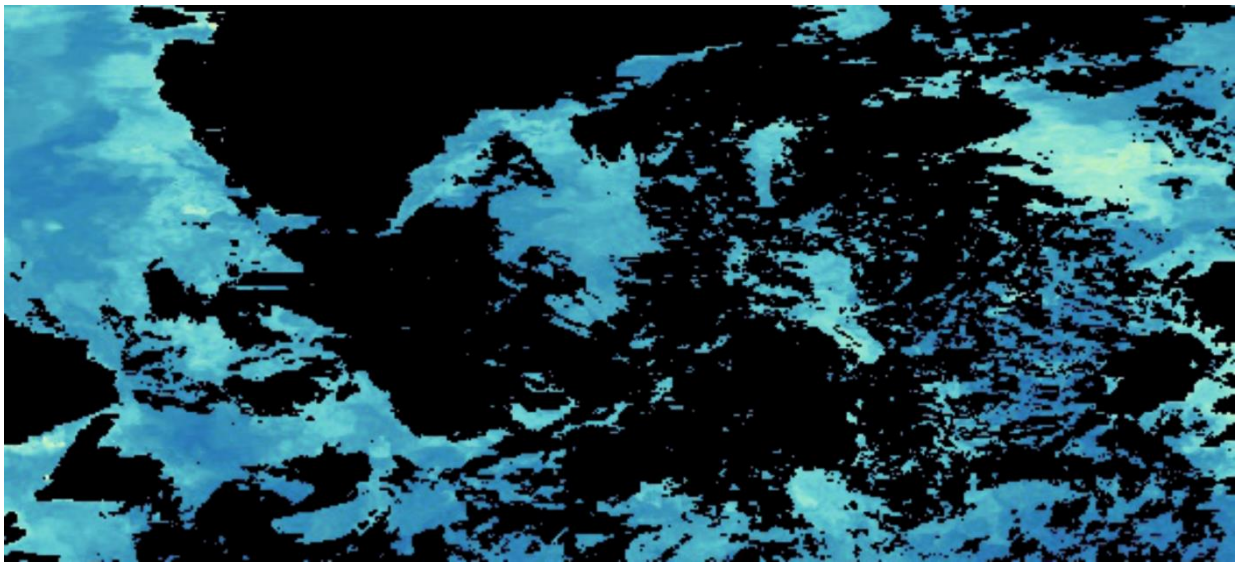

Appendix A

20th July – 27th July

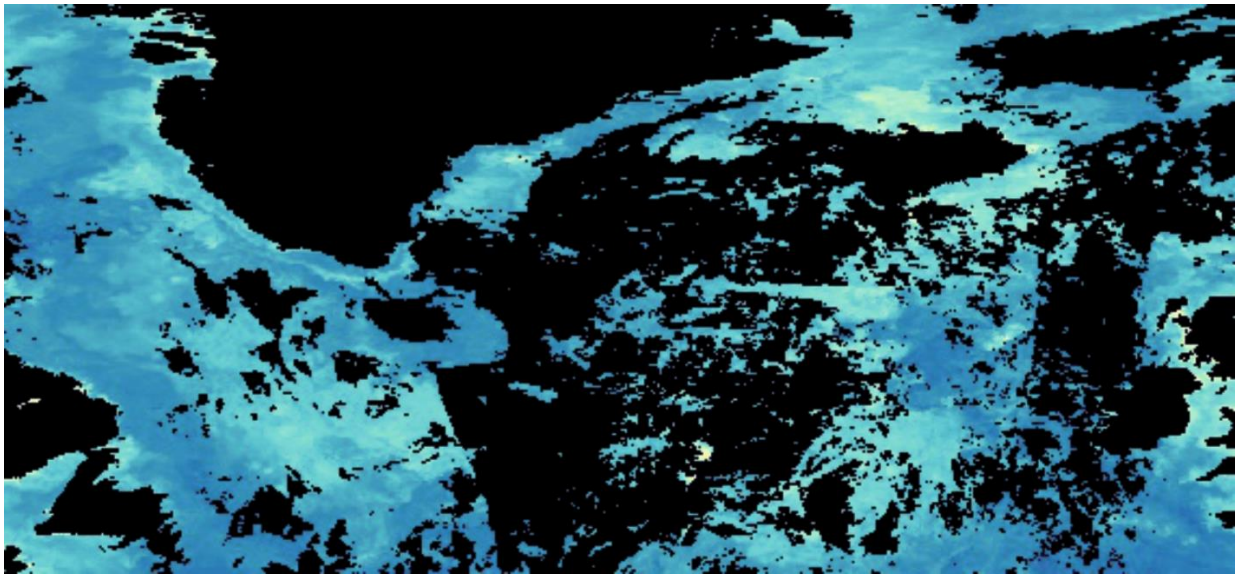

A.2 Temperature and Salinity Plots

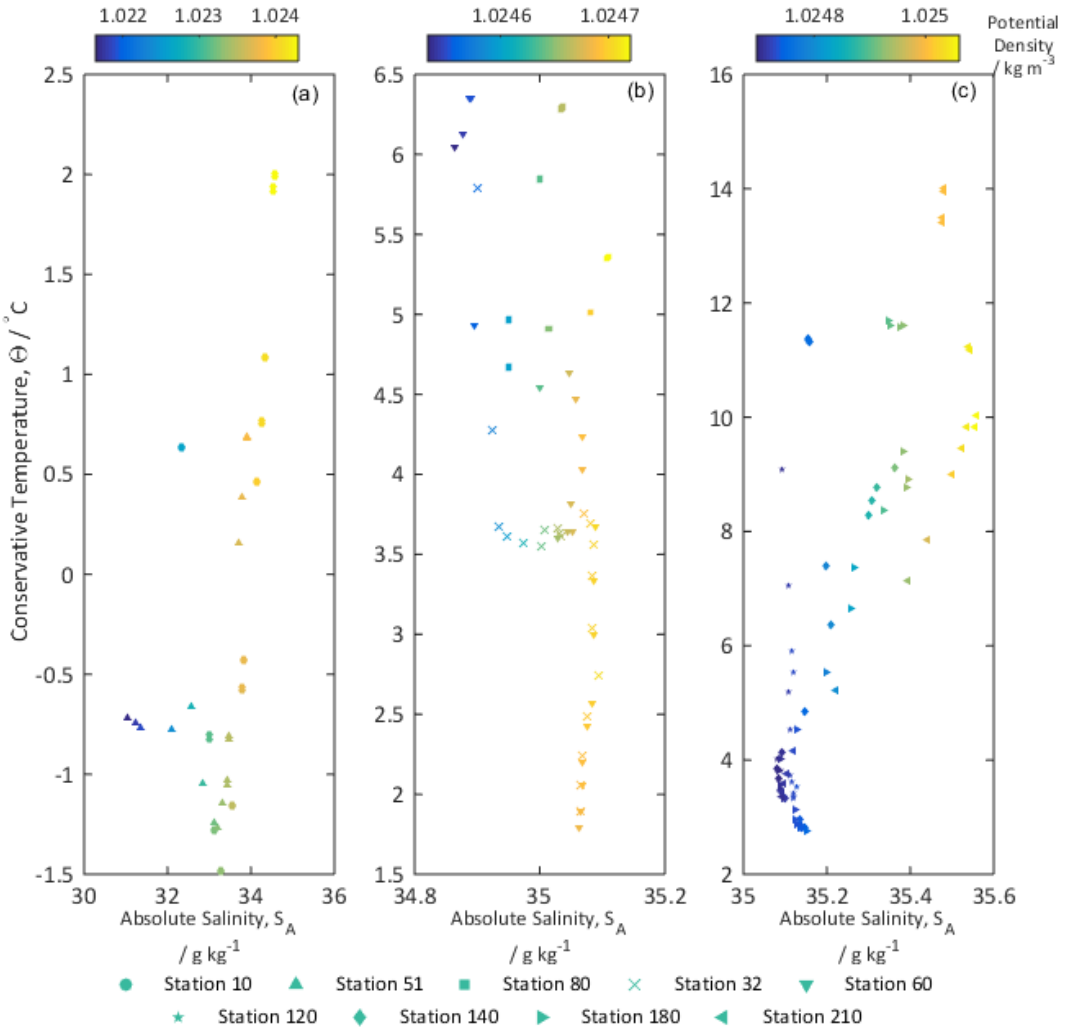

Figure A.2.1 T-S plots showing the differing water masses through the water column (a) station 10 (circles) and station 51 (triangles) from coastal Canada and Greenland respectively, (b) station 80 (squares), station 32 (crosses), and station 60 (downward triangles) correspond to Atlantic and polar waters mixed on the Greenland edge and central Labrador Sea, (c) station 120 (stars), station 140 (diamonds), station 180 (right triangle) and station 210 (left triangles) showing the Atlantic water profiles.

A.3 Underway DIC CRM measurements

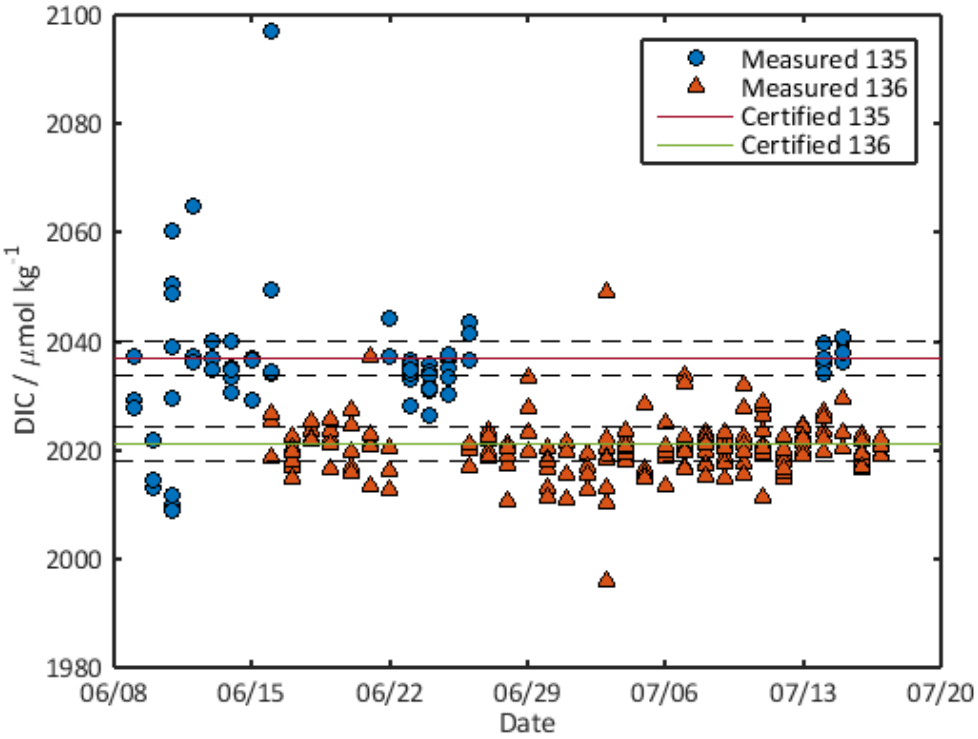

Figure A.3.1 The certified reference material measured DIC values plotted against time. Measurements of batch 136 are denoted with orange triangles, and batch 135 are the blue circles. The red and green lines are the certified values for batches 135 and 136 respectively. The black dashed lines are the certified values ± the precision of the Apollo.

List of References

Álvarez, M., A. F. Ríos, F. F. Pérez, H. L. Bryden and G. Rosón (2003). "Transports and budgets of total inorganic carbon in the subpolar and temperate North Atlantic." Global Biogeochemical Cycles **17**(1): 2-1-2-21.

Apollo SciTech inc. (2010). "The Determination of Carbon Dioxide System Parameters in Aquatic Systems." Retrieved 22/04/2014, 2014, from http://www.apolloscitech.com/index.htm.

Archer, D. (2005). "Fate of fossil fuel CO_2 in geologic time." Journal of Geophysical Research **110**: C09S05.

Archer, D., M. Eby, V. Brovkin, A. Ridgwell, L. Cao, U. Mikolajewicz, K. Caldeira, K. Matsumoto, G. Munhoven and A. Montenegro (2009). "Atmospheric lifetime of fossil fuel carbon dioxide." Annual Review of Earth and Planetary Sciences **37**: 117-134.

Aßmann, S., C. Frank and A. Körtzinger (2011). "Spectrophotometric high-precision seawater pH determination for use in underway measuring systems." Ocean Science **7**(5): 597-607.

Atamanchuk, D. (2013). Development and use of an optical pCO_2 sensor in marine studies. Ph.D. Natural Science, University of Gothenburg.

Atamanchuk, D., A. Tengberg, P. J. Thomas, J. Hovdenes, A. Apostolidis, C. Huber and P. O. J. Hall (2014). "Performance of a lifetime-based optode for measuring partial pressure of carbon dioxide in natural waters." Limnology and Oceanography: Methods **12**: 63-73.

Atkins, P. and J. de Paula (2006). Physical Chemistry, W. H. Freeman.

Azetsu-Scott, K., A. Clarke, K. Falkner, J. Hamilton, E. P. Jones, C. Lee, B. Petrie, S. Prinsenberg, M. Starr and P. Yeats (2010). "Calcium carbonate saturation states in the waters of the Canadian Arctic Archipelago and the Labrador Sea." Journal of Geophysical Research **115**(C11).

Bach, L. T., U. Riebesell, M. A. Gutowska, L. Federwisch and K. G. Schulz (2015). "A unifying concept of coccolithophore sensitivity to changing carbonate chemistry embedded in an ecological framework." Progress in Oceanography **135**(0): 125-138.

Bakker, D. C. E., H. J. W. De Baar and U. V. Bathmann (1997). "Changes of carbon dioxide in surface waters during spring in the Southern Ocean." Deep-Sea Research II **44**(1-2): 91-127.

References

Barron, J. J., C. Ashton and L. Geary (2006). The Effects of Temperature on pH Measurement. 57th Annual Meeting of the International Society of Electrochemistry,. Edinburgh, Technical Services Department, Reagecon Diagnostics Ltd, Ireland.

Bates, N. R., M. H. P. Best, K. Neely, R. Garley, A. G. Dickson and R. J. Johnson (2012). "Detecting anthropogenic carbon dioxide uptake and ocean acidification in the North Atlantic Ocean." Biogeosciences **9**(1): 989-1019.

Bates, N. R. and J. T. Mathis (2009). "The Arctic Ocean marine carbon cycle: evaluation of air-sea CO_2 exchanges, ocean acidification impacts and potential feedbacks." Biogeosciences **6**: 2433-2459.

Bates, R. G. and C. Culberson (1977). Hydrogen ions and the thermodynamic state of marine systems. The Fate of Fossil Fuel CO_2 in the Oceans. N. R. Anderson and A. Malahoff. New York, USA, Plenum Press**:** 45-61.

Battelle. (2011, 2012). "Battelle Designs Commercial Rugged Sensor System to Capture Our Oceans CO_2 Data." Retrieved 13:58 22/11/2012, 2012, from http://www.battelle.org/our-work/case-studies/battelle-designs-commercial-rugged-sensor-system-to-capture-our-oceans-co2-data.

Becker, M., N. Andersen, B. Fiedler, P. Fietzek, A. Körtzinger, T. Steinhoff and G. Friedrichs (2012). "Using cavity ringdown spectroscopy for continuous monitoring of $d^{13}C(CO_2)$ and fCO_2 in the surface ocean." Limnology and Oceanography: Methods **10**: 752-766.

Bednaršek, N., G. Tarling, D. Bakker, S. Fielding, E. Jones, H. Venables, P. Ward, A. Kuzirian, B. Lézé and R. Feely (2012). "Extensive dissolution of live pteropods in the Southern Ocean." Nature Geoscience **5**: 881-885.

Bellerby, R. G. J., D. R. Turner and J. E. Robertson (1995). "Surface pH and pCO_2 distributions in the Bellinghausen Sea, Southern Ocean, during the early Austral Summer." Deep-Sea Research II **42**(4-5): 1093-1107.

Bindoff, N. L., J. Willebrand, V. Artale, A. Cazenave, J. Gregory, S. Gulev, K. Hanawa, C. Le Quéré, S. Levitus, Y. Nojiri, C. K. Shum, L. D. Talley and A. Unnikrishnan (2007). Observations: Oceanic Climate Change and Sea Level. Contribution of Working Group I to the Fourth Assessment Report of the Intergovernmental Panel on Climate Change. S. Solomon, D. Qin, M. Manning et al. Cambridge, United Kingdom and New York, NY, USA., Cambridge University Press**:** 385-432.

Blain, S., B. Queguiner, L. Armand, S. Belviso, B. Bombled, L. Bopp, A. Bowie, C. Brunet, C. Brussaard, F. Carlotti, U. Christaki, A. Corbiere, I. Durand, F. Ebersbach, J. L. Fuda, N. Garcia, L.

Gerringa, B. Griffiths, C. Guigue, C. Guillerm, S. Jacquet, C. Jeandel, P. Laan, D. Lefevre, C. Lo Monaco, A. Malits, J. Mosseri, I. Obernosterer, Y. H. Park, M. Picheral, P. Pondaven, T. Remenyi, V. Sandroni, G. Sarthou, N. Savoye, L. Scouarnec, M. Souhaut, D. Thuiller, K. Timmermans, T. Trull, J. Uitz, P. van Beek, M. Veldhuis, D. Vincent, E. Viollier, L. Vong and T. Wagener (2007). "Effect of natural iron fertilization on carbon sequestration in the Southern Ocean." Nature **446**(7139): 1070-1074.

Boniello, C., T. Mayr, J. M. Bolivar and B. Nidetzky (2012). "Dual-lifetime referencing (DLR): a powerful method for on-line measurements of internal pH in carrier-bound immobilized biocatalysts." BMC Biotechnology **12**(11).

Borges, A. V. and M. Frankignoulle (1999). "Daily and seasonal variations of the partial pressure of CO_2 in surface seawater along Belgian and southern Dutch coastal areas." Journal of Marine Systems **19**: 251-266.

Borisov, S. M., R. Seifner and I. Klimant (2011). "A novel planar optical sensor for simultaneous monitoring of oxygen, carbon dioxide, pH and temperature." Analytical and Bioanalytical Chemistry **400**(8): 2463-2474.

Bradrick, T. D. and J. E. Churchich (2000). Time-resolved fluorescence and phosphorescence spectroscopy. Spectrophotometry and Spectrofluorimetry. M. G. Gore. Great Clarendon Street, Oxford, Oxford University Press**:** 69-97.

Bresnahan, P. J., T. R. Martz, Y. Takeshita, K. S. Johnson and M. LaShomb (2014). "Best practices for autonomous measurement of seawater pH with the Honeywell Durafet." Methods in Oceanography **9**: 44-60.

Buck, R. P., S. Rondinini, A. K. Covington, F. G. K. Baucke, C. M. A. Brett, M. F. Camões, M. J. T. Milton, T. Mussini, R. Naumann, K. W. Pratt, P. Spitzer and G. S. Wilson (2002). "Measurement of pH: Definition, Standards and Procedures." Pure and Applied Chemistry **74**(11): 2169-2200.

Burke, C. S., A. Markey, R. I. Nooney, P. Byrne and C. McDonagh (2006). "Development of an optical sensor probe for the detection of dissolved carbon dioxide." Sensors and Actuators B **119**(1): 288-294.

Bushinsky, S. M. and S. Emerson (2013). "A method for in-situ calibration of Aanderaa oxygen sensors on surface moorings." Marine Chemistry **155**(0): 22-28.

References

Byrne, R. H. (2014). "Measuring Ocean Acidification: New Technology for a New Era of Ocean Chemistry." Environmental Science & Technology **48**(10): 5352-5360.

Byrne, R. H., M. D. DeGrandpre, R. T. Short, T. R. Martz, L. Merlivat, C. McNeil, F. L. Sayles, R. Bell and P. Fietzek (2010). Sensors and Systems for in situ Observations of Marine Carbon Dioxide System Variables. OceanObs'09: Sustained Ocean Observations and Information for Society. J. Hall, D. E. Harrison and D. Stammer. Venice, Italy, ESA Publication WPP-306. **2**.

Byrne, R. H., S. Mecking, R. A. Feely and X. Liu (2010). "Direct observations of basin-wide acidification of the North Pacific Ocean." Geophysical Research Letters **37**(2): L02601.

Byrne, R. H., G. L. Robert-Baldo, S. W. Thompson and C. T. A. Chen (1988). "Seawater pH measurements: an at-sea comparison of spectrophotometric and potentiometric methods." Deep-Sea Research **35**(8): 1405-1410.

Caldeira, K. and P. B. Duffy (2000). "The role of the Southern Ocean in uptake and storage of anthropogenic carbon dioxide." Science **287**(5453): 620-622.

Caldeira, K. and M. W. Wickett (2003). "Anthropogenic carbon and ocean pH." Nature **425**: 365.

Caldeira, K. and M. W. Wickett (2005). "Ocean model predictions of chemistry changes from carbon dioxide emissions to the atmosphere and ocean." Journal of Geophysical Research **110**(C9).

Canadell, J. G., C. Le Quere, M. R. Raupach, C. B. Field, E. T. Buitenhuis, P. Ciais, T. J. Conway, N. P. Gillett, R. A. Houghton and G. Marland (2007). "Contributions to accelerating atmospheric CO_2 growth from economic activity, carbon intensity, and efficiency of natural sinks." Proceedings of the National Academy of Sciences of the United States of America **104**(47): 18866-18870.

Capel-Cuevas, S., M. P. Cuéllar, I. de Orbe-Payá, M. C. Pegalajar and L. F. Capitán-Vallvey (2010). "Full-range optical pH sensor based on imaging techniques." Analytica Chimica Acta **681**(1–2): 71-81.

Chu, C.-S. and Y.-L. Lo (2008). "Fiber-optic carbon dioxide sensor based on fluorinated xerogels doped with HPTS." Sensors and Actuators B **129**: 120-125.

Ciais, P., C. Sabine, G. Bala, L. Bopp, V. Brovkin, J. G. Canadell, A. Chhabra, R. DeFries, J. Galloway, M. Heimann, C. Jones, C. Le Quéré, R. B. Myneni, S. Piao and P. Thornton (2013). Carbon and Other Biogeochemical Cycles. Climate Change 2013: The Physical Science Basis. Contribution of Working Group 1 to the Fifth Assessment Report of the Intergovernmental

Panel on Climate Change. T. F. Stocker, D. Qin, G.-K. Plattner et al. Cambridge, United Kingdom and New York, N.Y., U.S.A., Cambridge University Press.

Contros Systems & Solutions (2015). "HydroC™ CO2 Carbon Dioxide Sensor."

Cooper, D. J., A. J. Watson and R. D. Ling (1998). "Variation of P_{CO2} along a North Atlantic shipping route (U.K. to the Caribbean): A year of automated observations." Marine Chemistry **60**: 147-164.

Cooper, L. W., J. W. McClelland, R. M. Holmes, P. A. Raymond, J. J. Gibson, C. K. Guay and B. J. Peterson (2008). "Flow-weighted values of runoff tracers (δ18O, DOC, Ba, alkalinity) from the six largest Arctic rivers." Geophysical Research Letters **35**(18).

Corbière, A., N. Metzl, G. Reverdin, C. Brunet and T. Takahashi (2007). "Interannual and decadal variability of the oceanic carbon sink in the North Atlantic subpolar gyre." Tellus B **59**(2): 168-178.

Dalit, M. (2014, 15/09/14). "Chemical sensors built at MBARI to provide unprecedented view of Southern Ocean." Retrieved 09/02/15, from http://www.mbari.org/news/homepage/2014/soccom/soccom.html.

de Boyer Montégut, C., G. Madec, A. S. Fischer, A. Lazar and D. Iudicone (2004). "Mixed layer depth over the global ocean: An examination of profile data and a profile-based climatology." Journal of Geophysical Research **109**: C12003.

De'ath, G., J. M. Lough and K. E. Fabricius (2005). "Declining Coral Calcification on the Great Barrier Reef." Science **323**: 116-119.

DeGrandpre, M. D. (1993). "Measurement of seawater pCO_2 using a renewable-reagent fiber optic sensor with colorimetric detection." Analytical Chemistry **65**(4): 331-337.

DeGrandpre, M. D., M. M. Baehr and T. R. Hammar (1999). "Calibration-Free optical chemical sensors." Analytical Chemistry **71**: 1152-1159.

DeGrandpre, M. D., T. R. Hammar, S. P. Smith and F. L. Sayles (1995). "In situ measurements of seawater pCO_2." Limnology and Oceanography **40**(5): 969-975.

DeGrandpre, M. D., A. Körtzinger, U. Send, D. W. R. Wallace and R. G. J. Bellerby (2006). "Uptake and sequestration of atmospheric CO_2 in the Labrador Sea deep convection region." Geophysical Research Letters **33**(21).

References

Derinkuyu, S., K. Ertekin, O. Oter, S. Denizalti and E. Cetinkaya (2007). "Fiber optic pH sensing with long wavelength excitable Schiff bases in the pH range of 7.0-12.0." Analytica Chimica Acta **588**(1): 42-49.

Dickson, A. G. (1981). "An exact definition of total alkalinity and a procedure for the estimation of alkalinity and total inorganic carbon from titration data." Deep-Sea Research **28A**(6): 609-623.

Dickson, A. G. (1984). "pH scales and proton-transfer reactions in saline media such as sea water." Geochimica et Cosmochimica Acta **48**(11): 2299-2308.

Dickson, A. G. (1990). "Standard potential of the reaction AgCl(s)+1/2H_2(g) = Ag(s)+HCl(aq) and the standard acidifty constant of the bisulfate ion in synthetic seawater from 273.15 K to 318.15 K." Journal of Chemical Thermodynamics **22**(2): 113-127.

Dickson, A. G. (1993). "The measurement of sea water pH." Marine Chemistry **44**(2–4): 131-142.

Dickson, A. G. (1993). "pH buffers for sea water media based on the total hydrogen ion concentration scale." Deep-Sea Research I **40**(1): 107-118.

Dickson, A. G. (1994). Determination of dissolved oxygen in seawater by Winkler titration. . WOCE operations manual. **Technical Report**.

Dickson, A. G. (2010). The carbon dioxide system in seawater: equilibrium chemistry and measurements. Guide to best practices for ocean acidification research and data reporting. U. Riebesell, V. J. Fabry, L. Hansson and J.-P. Gattuso. Luxembourg, Publications Office of the European Union.

Dickson, A. G. and F. J. Millero (1987). "A comparison of the equilibrium constants for the dissociation of carbonic acid in seawater media." Deep-Sea Research **34A**(10): 1733-1743.

Dickson, A. G., C. L. Sabine and J. R. Christian (2007). Guide to best practices for ocean CO_2 measurements. A. G. Dickson, C. L. Sabine and J. R. Christian, PICES Special Publication. **3**.

Dickson, A. G., C. L. Sabine and J. R. Christian (2007). Recommended standard operating procedure- SOP 4 : Determination of $p(CO_2)$ in air that is in equilibrium with a discrete sample of seawater. Guide to best practices for ocean CO_2 measurements. A. G. Dickson, C. L. Sabine and J. R. Christian, PICES Special Publication. **3**.

DOE (1994). Handbook of methods for the analysis of the various parameters of the carbon dioxide system in seawater. A. G. Dickson and C. Goyet. USA.

Doney, S. C., V. J. Fabry, R. A. Feely and J. A. Kleypas (2009). "Ocean acidification: the other CO_2 problem." The Annual Review of Marine Science **1**: 169-192.

Doney, S. C., I. Lima, R. A. Feely, D. M. Glover, K. Lindsay, N. Mahowald, J. K. Moore and R. Wanninkhof (2009). "Mechanisms governing interannual variability in upper-ocean inorganic carbon system and air–sea CO_2 fluxes: Physical climate and atmospheric dust." Deep-Sea Research II **56**(8–10): 640-655.

Doney, S. C., B. Tilbrook, S. Roy, N. Metzl, C. Le Quéré, M. Hood, R. A. Feely and D. Bakker (2009). "Surface-ocean CO_2 variability and vulnerability." Deep-Sea Research II **56**(8–10): 504-511.

Dore, J. E., R. Lukas, D. W. Sadler, M. J. Church and D. M. Karl (2009). "Physical and biogeochemical modulation of ocean acidification in the central North Pacific." Proceedings of the National Academy of Sciences of the United States of America **106**(30): 12235-12240.

Easley, R. A. and R. H. Byrne (2012). "Spectrophotometric Calibration of pH Electrodes in Seawater Using Purified m-Cresol Purple." Environmental Science & Technology **46**(9): 5018-5024.

Emery, W. J. and J. S. Dewar (1982). "Mean Temperature-Salinity, Salinity-Depth and Temperature-Depth Curves for the North Atlantic and the North Pacific." Progress in Oceanography **11**: 219-305.

Ertekin, K., I. Klimant, G. Neurauter and O. S. Wolfbeis (2003). "Characterization of a reservoir-type capillary optical microsensor for pCO_2 measurements." Talanta **59**: 261-267.

Etcheto, J. and L. Merlivat (1988). "Satellite determination of the carbon dioxide exchange coefficient at the ocean-atmosphere interface: A first step." Journal of Geophysical Research **93**(C12): 15669.

Fiedler, B., P. Fietzek, N. Vieira, P. Silva, H. C. Bittig and A. Körtzinger (2013). "In Situ CO_2 and O_2 Measurements on a Profiling Float." Journal of Atmospheric and Oceanic Technology **30**(1): 112-126.

Fietzek, P., B. Fiedler, T. Steinhoff and A. Körtzinger (2014). "In situ Quality Assessment of a Novel Underwater pCO_2 Sensor Based on Membrane Equilibration and NDIR Spectrometry." Journal of Atmospheric and Oceanic Technology **31**(1): 181-196.

Fietzek, P. and A. Körtzinger (2009). Optimization of a Membrane-Based NDIR Sensor for Dissolved Carbon Dioxide. OceanObs'09: Sustained Ocean Observations and Information for

Society, Venice, Italy, OceanObs'09: Sustained Ocean Observations and Information for Society.

Frankignoulle, M. and A. V. Borges (2001). "Direct and Indirect pCO_2 Measurements in a Wide Range of pCO_2 and Salinity Values (The Scheldt Estuary)." Aquatic Geochemistry **7**: 267-273.

Friedrichs, G., J. Bock, F. Temps, P. Fietzek, A. Körtzinger and D. W. R. Wallace (2010). "Toward continuous monitoring of seawater $^{13}CO_2/^{12}CO_2$ isotope ratio and pCO_2: Performance of cavity ringdown spectroscopy and gas matrix effects." Limnology and Oceanography: Methods **8**: 539-551.

Friis, K., A. Körtzinger and D. W. R. Wallace (2004). "Spectrophotometric pH measurement in the ocean: Requirements, design, and testing of an autonomous charge-coupled device detector system." Limnology and Oceanography : Methods **2**: 126-136.

Ge, X., Y. Kostov, R. Henderson, N. Selock and G. Rao (2014). "A Low-Cost Fluorescent Sensor for pCO_2 Measurements." Chemosensors **2**(2): 108-120.

Goncalves, H. M., C. D. Maule, P. A. Jorge and J. C. Esteves da Silva (2008). "Fiber optic lifetime pH sensing based on ruthenium(II) complexes with dicarboxybipyridine." Analytica Chimica Acta **626**(1): 62-70.

Goyet, C., C. Beauverger, C. Brunet and A. Poisson (1991). "Distribution of carbon dioxide partial pressure in surface waters of the Southwest Indian Ocean." Tellus B **43B**: 1-11.

Gruber, N., C. D. Keeling and N. R. Bates (2002). "Interannual Variability in the North Atlantic Ocean Carbon Sink." Science **298**: 2374-2378.

Hakonen, A., L. G. Anderson, J. Engelbrektsson, S. Hulth and B. Karlson (2013). "A potential tool for high-resolution monitoring of ocean acidification." Analytica Chimica Acta **786**: 1-7.

Hakonen, A. and S. Hulth (2008). "A high-precision ratiometric fluorosensor for pH: Implementing time-dependent non-linear calibration protocols for drift compensation." Analytica Chimica Acta **606**(1): 63-71.

Hakonen, A. and S. Hulth (2010). "A high-performance fluorosensor for pH measurements between 6 and 9." Talanta **80**(5): 1964-1969.

Hamer, W. J. and Y.-C. Wu (1972). "Osmotic Coefficients and Mean Activity Coefficients of Uni-univalent Electrolytes in Water at 25 C." Journal of Physical Chemistry Reference Data **1**(4): 1047-1100.

Hansen, B. and S. Østerhus (2000). "North Atlantic-Nordic Seas exchanges." Progress in Oceanography **45**: 109-208.

Hansen, J., D. Johnson, A. Lacis, S. Lebedeff, P. Lee, D. Rind and G. Russell (1981). "Climate Impact of Increasing Atmospheric Carbon Dioxide." Science **213**(4511): 957-966.

Hansson, I. (1973). "A new set of pH-scales and standard buffers for sea water." Deep-Sea Research **20**: 479-491.

Harris, K. E., M. D. DeGrandpre and B. Hales (2013). "Aragonite saturation state dynamics in a coastal upwelling zone." Geophysical Research Letters **40**(11): 2720-2725.

Hauser, P. C., T. W. T. Rupasinghe and N. E. Cates (1995). "A Multi-wavelength photometer based on light-emitting diodes." Talanta **42**(4).

Hoegh-Guldberg, O., P. J. Mumby, A. J. Hooten, R. S. Steneck, P. Greenfield, E. Gomez, C. D. Harvell, P. F. Sale, A. J. Edwards, K. Caldeira, N. Knowlton, C. M. Eakin, R. Iglesias-Prieto, N. Muthiga, R. H. Bradbury, A. Dubi and M. E. Hatziolos (2007). "Coral Reefs Under Rapid Climate Change and Ocean Acidification." Science **318**(5857): 1737-1742.

Holley, S. E. and D. J. Hydes (1994). Procedures for the determination of dissolved oxygen in seawater. James Rennell Centre for Ocean Circulation. **Technical Report**.

Holliday, N. P., A. Meyer, S. Bacon, S. G. Alderson and B. de Cuevas (2007). "Retroflection of part of the east Greenland current at Cape Farewell." Geophysical Research Letters **34**(7).

Holliday, N. P., J. J. Waniek, R. Davidson, D. Wilson, L. Brown, R. Sanders, R. T. Pollard and J. T. Allen (2006). "Large-scale physical controls on phytoplankton growth in the Irminger Sea Part I: Hydrographic zones, mixing and stratification." Journal of Marine Systems **59**(3–4): 201-218.

Honjo, S., S. J. Manganini, R. A. Krishfield and R. Francois (2008). "Particulate organic carbon fluxes to the ocean interior and factors controlling the biological pump: A synthesis of global sediment trap programs since 1983." Progress in Oceanography **76**(3): 217-285.

Hood, E. M. and L. Merlivat (2001). "Annual to interannual variations of fCO_2 in the northwestern Mediterranean Sea: Results from hourly measurements made by CARIOCA buoys, 1995-1997." Journal of Marine Research **59**.

Hoppe, C. J. M., G. Langer, S. D. Rokitta, D. A. Wolf-Gladrow and B. Rost (2012). "Implications of observed inconsistencies in carbonate chemistry measurements for ocean acidification studies." Biogeosciences **9**: 2401-2405.

Hulth, S., R. C. Aller, P. Engstrom and E. Selander (2002). "A pH plate fluorosensor (optode) for early diagenetic studies of marine sediments." Limnology and Oceanography **47**(1): 212-220.

Humphreys, M. P. (2015). Calkulate: seawater total alkalinity from open cell titration data using a modified Gran plot approach. National Oceanography Centre.

Idronaut. (1995). "Cylindrical, high pressure glass membrane pH electrode." Retrieved 13/11/2014, 2014, from http://www.idronaut.it/products-ph-sensors-water-quality.

Inoue, H. Y. (1998). CO_2 exchange between the atmosphere and the ocean. Dynamics and Characterization of Marine Organic Matter. N. Handa, E. Tanoue and T. Hama. Tokyo, Japan, Terra Scientific Publishing Company.

IPCC (2001). Climate Change 2001: The Scientific Basis. Contribution of Working Group I to the Third Assessment Report of the Intergovernmental Panel on Climate Change. J. T. Houghton, Y. Ding, D. J. Griggs et al. Cambridge, United Kingdom and New York, NY, USA,, Cambridge University Press**:** 881.

IPCC (2013). Summary for Policymakers. Climate Change 2013: The Physical Science Basis. Contribution of Working Group I to the Fifth Assessment Report of the Intergovernmental Panel on Climate Change. T. F. Stocker, D. Qin, G.-K. Plattner et al. Cambridge, United Kingdom and New York, NY, USA, Cambridge University Press.

Ishiji, T., D. W. Chipman, T. Takahashi and K. Takahashi (2001). "Amperometric sensor for monitoring of dissolved carbon dioxide in seawater." Sensors and Actuators B **76**: 265-269.

Jacobson, M. Z. (2005). "Studying ocean acidification with conservative, stable numerical schemes for nonequilibrium air-ocean exchange and ocean equilibrium chemistry." Journal of Geophysical Research **110**(D7).

Jähne, B., G. Heinz and W. Dietrich (1987). "Measurement of the diffusion coefficients of sparingly soluble gases in water." Journal of Geophysical Research: Oceans **92**(C10): 10767-10776.

Janata, J. (1987). "Do optical sensors really measure pH?" Analytical Chemistry **59**(9): 1351-1356.

Jannasch, H. W., K. S. Johnson, L. J. Coletti, V. Elrod and Y. Takeshita (2014). Pressure tolerant DURAFET pH sensors on APEX profiling floats. 2014 Ocean Sciences Meeting. Honolulu, Hawaii, USA.

Jiang, Z.-p., D. J. Hydes, S. E. Hartman, M. C. Hartman, J. M. Campbell, B. D. Johnson, B. Schofield, D. Turk, D. Wallace, W. J. Burt, H. Thomas, C. Cosca and R. Feely (2014). "Application and assessment of a membrane-based pCO_2 sensor under field and laboratory conditions." Limnology and Oceanography: Methods **12**: 264-280.

Jiang, Z.-P., D. J. Hydes, T. Tyrrell, S. E. Hartman, M. C. Hartman, C. Dumousseaud, X. A. Padin, I. Skjelvan and C. González-Pola (2013). "Key controls on the seasonal and interannual variations of the carbonate system and air-sea CO_2 flux in the Northeast Atlantic (Bay of Biscay)." Journal of Geophysical Research: Oceans **118**(2): 785-800.

Johnson, K., W. Berelson, E. Boss, Z. Chase, H. Claustre, S. Emerson, N. Gruber, A. Körtzinger, M. J. Perry and S. Rise (2009). "Observing Biogeochemical Cycles at Global Scales with Profiling Floats and Gliders." Oceanography **22**(3): 216-225.

Jones, E. P., L. G. Anderson, S. Jutterström and J. H. Swift (2008). "Sources and distribution of fresh water in the East Greenland Current." Progress in Oceanography **78**(1): 37-44.

Kadis, R. and I. Leito (2010). "Evaluation of the residual liquid junction potential contribution to the uncertainty in pH measurement: A case study on low ionic strength natural waters." Analytica Chimica Acta **664**(2): 129-135.

Keeling, C. (1986). Atmospheric CO2 Concentrations-Mauna Loa Observatory, Hawaii 1958-1986, Oak Ridge National Laboratory.

Kester, D. R., I. W. Duedall, D. N. Connors and R. M. Pytkowicz (1967). "Preparation of Artificial Seawater." Limnology and Oceanography **12**(1): 176-179.

Khanna, V. K. (2013). "Remedial and adaptive solutions of ISFET non-ideal behaviour." Sensor Review **33**(3): 228-237.

Khatiwala, S., T. Tanhua, S. Mikaloff Fletcher, M. Gerber, S. C. Doney, H. D. Graven, N. Gruber, G. A. McKinley, A. Murata, A. F. Ríos and C. L. Sabine (2013). "Global ocean storage of anthropogenic carbon." Biogeosciences **10**(4): 2169-2191.

Kim, H.-C. and K. Lee (2009). "Significant contribution of dissolved organic matter to seawater alkalinity." Geophysical Research Letters **36**: L20603.

Kim, H.-C., K. Lee and W. Choi (2006). "Contribution of phytoplankton and bacterial cells to the measured alkalinity of seawater." Limnology and Oceanography **51**(1): 331-338.

Kirkbright, G. F., R. Narayanaswamy and N. A. Welti (1984). "Fibre-optic pH probe based on the use of an immobilised colorimetric indicator." The Analyst **109**: 1025-1028.

Kleypas, J. A. and C. Langdon (2006). Coral reefs and changing seawater carbonate chemistry. Coral Reefs and Climate Change: Science and Management. Washington, DC, AGU. **61:** 73-110.

Klimant, I., C. Huber, G. Liebsch, G. Neurauter, A. Stangelmayer and O. S. Wolfbeis (2001). Dual Lifetime Referencing (DLR) - a New Scheme for Converting Fluorescence Intensity into a Frequency-Domain or Time-Domain Information. New trends in fluorescence spectroscopy :applpications to chemical and life science. B. Valeur and J.-c. Brochon. Germany, Springer-Verlag**:** 257-274.

Knoll, G. F. (2010). Photomultiplier Tubes and Photodiodes. Radiation Detection and Measurement. D. Matteson, J. Welter and A. Spicehandler. United States of America, Hamilton Printing Company.

Knorr, W. (2009). "Is the airborne fraction of anthropogenic CO_2 emissions increasing?" Geophysical Research Letters **36**(21).

Köhler, S., H. Laudon, A. Wilander and K. Bishop (2000). "Estimating organic acid dissociation in natural surface waters using total alkalnity and TOC." Water Research **34**(5): 1425-1434.

Körtzinger, A. and J. Schimanski (2004). "High Quality Oxygen Measurements from Profiling Floats: A Promising New Technique." Journal of Atmospheric and Oceanic Technology **22**: 302-308.

Körtzinger, A., U. Send, D. W. R. Wallace, J. Karstensen and M. DeGrandpre (2008). "Seasonal cycle of O_2 and pCO_2 in the central Labrador Sea: Atmospheric, biological, and physical implications." Global Biogeochemical Cycles **22**: GB1014.

Kuswandi, B., R. Andres and R. Narayanaswamy (2001). "Optical fibre biosensors based on immobilised enzymes." The Analyst **126**(8): 1469-1491.

Larsen, M., S. Borisov, B. Grunwald, I. Klimant and R. Glud (2011). "A simple and inexpensive high resolution color ratiometric planar optode imaging approach: application to oxygen and pH sensing." Limnology and Oceanography : Methods **9**: 348-360.

Lauvset, S. K. and N. Gruber (2014). "Long-term trends in surface ocean pH in the North Atlantic." Marine Chemistry **162**: 71-76.

Lauvset, S. K., N. Gruber, P. Landschützer, A. Olsen and J. Tjiputra (2015). "Trends and drivers in global surface ocean pH over the past 3 decades." Biogeosciences **12**(5): 1285-1298.

Lavigne, H., J.-M. Epitalon and J.-P. Gattuso (2011). seacarb: seawater carbonate chemistry with R, R package, version 3.0.4.

Lazier, J., R. Hendry, A. Clarke, I. Yashayaev and P. Rhines (2002). "Convection and restratification in the Labrador Sea, 1990–2000." Deep-Sea Research I **49**(10): 1819-1835.

Le Bris, N. and D. Birot (1997). "Automated pH-ISFET measurements under hydrostatic pressure for marine monitoring application." Analytica Chimica Acta **356**: 205-215.

Le Bris, N., P.-M. Sarradin and S. Pennec (2001). "A new deep-sea probe for in situ pH measurement in the environment of hydrothermal vent biological communities." Deep-Sea Research I **48**(8): 1941-1951.

Le Quéré, C., R. J. Andres, T. Boden, T. Conway, R. A. Houghton, J. I. House, G. Marland, G. P. Peters, G. R. van der Werf, A. Ahlström, R. M. Andrew, L. Bopp, J. G. Canadell, P. Ciais, S. C. Doney, C. Enright, P. Friedlingstein, C. Huntingford, A. K. Jain, C. Jourdain, E. Kato, R. F. Keeling, K. Klein Goldewijk, S. Levis, P. Levy, M. Lomas, B. Poulter, M. R. Raupach, J. Schwinger, S. Sitch, B. D. Stocker, N. Viovy, S. Zaehle and N. Zeng (2013). "The Global Carbon Budget 1959-2011." Earth System Science Data **5**: 165-186.

Le Quéré, C., M. R. Raupach, J. G. Canadell, G. Marland and *e. al.* (2009). "Trends in the sources and sinks of carbon dioxide." Nature Geoscience **2**: 831-836.

Lee, K., T. W. Kim, R. H. Byrne, F. J. Millero, R. A. Feely and Y. M. Liu (2010). "The universal ratio of boron to chlorinity for the North Pacific and North Atlantic oceans." Geochimica et Cosmochimica Acta **74**(6): 1801-1811.

Lefevre, N., J. P. Ciabrini, G. Michard, B. Brient, M. DuChaffaut and L. Merlivat (1993). "A new optical sensor for PCO_2 measurements in seawater." Marine Chemistry **42**: 189-198.

Lefèvre, N., A. J. Watson, A. Olsen, A. F. Ríos, F. F. Pérez and T. Johannessen (2004). "A decrease in the sink for atmospheric CO_2 in the North Atlantic." Geophysical Research Letters **31**: L07306.

Lenton, A., L. Bopp and R. J. Matear (2009). "Strategies for high-latitude northern hemisphere CO_2 sampling now and in the future." Deep-Sea Research II **56**(8–10): 523-532.

Liebsch, G., I. Klimant, B. Frank, G. Holst and O. S. Wolfbeis (2000). "Luminescence lifetime imaging of oxygen, ph and carbon dioxide distribution using optical sensors." Applied Spectroscopy **54**(4): 548-559.

Liebsch, G., I. Klimant, C. Krause and O. S. Wolfbeis (2001). "Fluorescent Imaging of pH with Optical Sensors Using Time Domain Dual Lifetime Referencing." Analytical Chemistry **73**(17): 4354-4363.

Liss, P. S. and L. Merlivat (1986). Air-sea gas exchange rates: Introduction and synthesis. The role of air-sea exchange in geochemical cycling, Springer**:** 113-127.

Liss, P. S. and P. G. Slater (1974). "Flux of Gases across the Air-Sea Interface." Nature **247**: 181-184.

Liu, X., Z. A. Wang, R. H. Byrne, E. A. Kaltenbacher and R. E. Bernstein (2006). "Spectrophotometric Measurements of pH in-Situ: Laboratory and Field Evaluations of Instrumental Performance." Environmental Science & Technology **40**(16): 5036-5044.

Longhurst, A., S. Sathyendranath, T. Platt and C. Caverhill (1995). "An estimate of global primary production in the ocean from satellite radiometer data." Journal of Plankton Research **17**(6): 1245-1271.

Lu, Z., M. Dai, K. Xu, J. Chen and Y. Liao (2008). "A high precision, fast response, and low power consumption in situ optical fiber chemical pCO2 sensor." Talanta **76**: 353-359.

Lüger, H., D. W. R. Wallace and A. Kortzinger (2004). "The pCO_2 variability in the midlatitude North Atlantic Ocean during a full annual cycle." Global Biogeochemical Cycles **18**: GB3023.

Marion, G. M., F. J. Millero, M. F. Camões, P. Spitzer, R. Feistel and C. T. A. Chen (2011). "pH of seawater." Marine Chemistry **126**(1-4): 89-96.

Martz, T. R. "Ocean Carbon Instrument and Sensor Directory." Retrieved 19/12/2014, from http://www.ioccp.org/instruments-and-sensors.

Martz, T. R., J. J. Carr, C. R. French and M. D. DeGrandpre (2003). "A Submersible Autonomous Sensor for Spectrophotometric pH Measurements of Natural Waters." Analytical Chemistry **75**(8): 1844-1850.

Martz, T. R., J. G. Connery and K. S. Johnson (2010). "Testing the Honeywell Durafet for seawater pH applications." Limnology and Oceanography: Methods **8**: 172-184.

McCartney, M. S. and L. D. Talley (1982). "The Subpolar Mode Water of the North Atlantic Ocean." Journal of Physical Oceanography **12**: 1169-1188.

McCartney, M. S. and L. D. Talley (1984). "Warm-to-Cold water Conversion in the Northern North Atlantic Ocean." Journal of Physical Oceanography **14**: 922-935.

McDougall, T. J. and P. M. Barker (2011). Getting started with TEOS-10 and the Gibbs Seawater (GSW) Oceanographic Toolbox. SCOR/IAPSO WG127**:** 28.

McElligott, S., R. H. Byrne, K. Lee, R. Wanninkhof, F. J. Millero and R. A. Feely (1998). "Discrete water column measurements of CO2 fugacity and pHT in seawater: A comparison of direct measurements and thermodynamic calculations." Marine Chemistry **60**(1–2): 63-73.

McKinley, G. A., A. R. Fay, T. Takahashi and N. Metzl (2011). "Convergence of atmospheric and North Atlantic carbon dioxide trends on multidecadal timescales." Nature Geoscience **4**: 606-610.

Mehrbach, C., C. H. Culberso, J. E. Hawley and R. M. Pytkowic (1973). "Measurement of apparent dissociation constants of carbonic acid in seawater at atmospheric pressure." Limnology and Oceanography **18**(6): 897-907.

Mellon, M. G. and V. N. Morris (1925). "Standardizing Acids and Bases with Borax." Industrial and Engineering Chemistry **17**(2): 145-146.

Metzl, N., A. Corbière, G. Reverdin, A. Lenton, T. Takahashi, A. Olsen, T. Johannessen, D. Pierrot, R. Wanninkhof, S. R. Ólafsdóttir, J. Olafsson and M. Ramonet (2010). "Recent acceleration of the sea surface fCO_2 growth rate in the North Atlantic subpolar gyre (1993-2008) revealed by winter observations." Global Biogeochemical Cycles **24**: GB4004.

Millero, F. J. (1995). "Thermodynamics of the carbon dioxide system in the oceans." Geochimica et Cosmochimica Acta **59**(4): 661-677.

Millero, F. J. (2007). "The Marine Inorganic Carbon Cycle." Chemical Reviews **107**(2): 308-341.

Millero, F. J. and A. Poisson (1981). "International one-atmosphere equation of state of seawater." Deep-Sea Research **28A**(6): 625-629.

Mills, A., Q. Chang and N. McMurray (1992). "Equilibrium Studies on Colorimetric Plastic Film Sensors for Carbon Dioxide." Analytical Chemistry **64**(13): 1383-1389.

Mintrop, L. (2004). Versatile Instrument for the Determination of Titration Alkalinity, Manual for versions5 3S and 3C, Version 2.0, MARine ANalytics and DAta (MARIANDA). Kiel, Germany**:** 45.

Moore, T. S., M. D. DeGrandpre, C. L. Sabine, R. C. Hamme, C. J. Zappa, W. R. McGillis, R. A. Feely and W. M. Drennan (2011). "Sea surface pCO_2 and O_2 in the Southern Ocean during the austral fall, 2008." Journal of Geophysical Research **116**: C00F11.

Morgan, C. G., J. G. Murray and A. C. Mitchell (1991). Frequency domain imaging using array detectors : Present status and prospects for picosecond resolution. SPIE: Future Trends in Biomedical Applications of Lasers, Berlin, Germany, SPIE.

Muller, B. and P. C. Hauser (1996). "Fluorescence optical sensor for low concentrations of dissolved carbon dioxide." The Analyst **121**(3): 339.

Muller, F. L. and B. Bleie (2008). "Estimating the organic acid contribution to coastal seawater alkalinity by potentiometric titrations in a closed cell." Analytica Chimica Acta **619**(2): 183-191.

Nakano, Y., H. Kimoto, S. Watanabe, H. Koh and Y. Watanabe (2006). "Simultaneous Vertical Measurements of *in situ* pH and CO_2 in the Sea Using Spectrophotometric Profilers." Journal of Oceanography **62**: 71-81.

Nakano, Y. and H. Yoshida (2011). Development of in situ CO_2 and pH sensor (Hybrid CO_2-pH sensor: HCS) for AUV. Underwater Technology (UT), 2011 IEEE Symposium on and 2011 Workshop on Scientific Use of Submarine Cables and Related Technologies (SSC).

Neurauter, G., I. Klimant and O. S. Wolfbeis (1999). "Microsecond lifetime-based optical carbon dioxide sensor using luminescence resonance energy transfer." Analytica Chimica Acta **382**(1-2): 67-75.

Neurauter, G., I. Klimant and O. S. Wolfbeis (2000). "Fiber-optic microsensor for high resolution pCO_2 sensing in marine environment." Fresenius Journal of Analytical Chemistry **366**: 481-487.

Nightingale, P. D., G. Malin, C. S. Law, A. J. Watson, P. S. Liss, M. I. Liddicoat, J. Boutin and R. C. Upstill-Goddard (2000). "In situ evaluation of air-sea gas exchange parameterizations using novel conservative and volatile tracers." Global Biogeochemical Cycles **14**(1): 373-387.

Offenbacher, H., O. S. Wolfbeis and E. Furlinger (1986). "Fluorescence optical sensors for continuous determination of near-neutral pH values." Sensors and Actuators **9**(1): 73-84.

Olsen, A., K. R. Brown, M. Chierici, T. Johannessen and C. Neill (2008). "Sea-surface CO_2 fugacity in the subpolar North Atlantic." Biogeosciences **5**: 535-547.

Orr, J. C., V. J. Fabry, O. Aumont, L. Bopp, S. C. Doney, R. A. Feely, A. Gnanadesikan, N. Gruber, A. Ishida, F. Joos, R. M. Key, K. Lindsay, E. Maier-Reimer, R. Matear, P. Monfray, A. Mouchet, R. G.

Najjar, G.-K. Plattner, K. B. Rodgers, C. L. Sabine, J. L. Sarmiento, R. Schlitzer, R. D. Slater, I. J. Totterdell, M.-F. Weirig, Y. Yamanaka and A. Yool (2005). "Anthropogenic ocean acidification over the twenty-first century and its impact on calcifying organisms." Nature **437**(7059): 681-686.

Oter, O., K. Ertekin and S. Derinkuyu (2008). "Ratiometric sensing of CO_2 in ionic liquid modified ethyl cellulose matrix." Talanta **76**(3): 557-563.

Oter, O., K. Ertekin, D. Topkaya and S. Alp (2006). "Emission-based optical carbon dioxide sensing with HPTS in green chemistry reagents: room-temperature ionic liquids." Analytical and Bioanalytical Chemistry **386**: 1225-1234.

Picarro Inc. (2015). "Picarro Inc." Retrieved 18/02/2015, from http://www.picarro.com/.

Pierrot, D., E. Lewis and D. W. R. Wallace (2006). MS Excel Program Developed for CO2 System Calcuations. Carbon Dioxide Information Analysis Center,Oak Ridge National Laboratory,U.S. Department of Energy,Oak Ridge, Tennessee

Pierrot, D., C. Neill, K. Sullivan, R. Castle, R. Wanninkhof, H. Lüger, T. Johannessen, A. Olsen, R. A. Feely and C. E. Cosca (2009). "Recommendations for autonomous underway pCO_2 measuring systems and data-reduction routines." Deep-Sea Research II **56**(8): 512-522.

Poisson, A., N. Metzl, C. Brunet, B. Schauer, B. Bres, D. Ruiz-Pino and F. Louanchi (1993). "Variability of Sources and Sinks of CO_2 in the Western Indian and Southern Oceans During the Year 1991." Journal of Geophysical Research **98**(C12): 22759-22778.

Pollard, R. T., M. J. Griffiths, S. A. Cunningham, J. F. Read, F. F. Pérez and A. F. Ríos (1996). "Vivaldi 1991- A study of the formation, circulation and ventilation of Eastern North Atlantic Central Water." Progress in Oceanography **37**: 167-192.

Pratt, K. W. (2014). "Measurement of pHT values of Tris buffers in artificial seawater at varying mole ratios of Tris:Tris·HCl." Marine Chemistry **162**: 89-95.

PreSens GmbH. Retrieved 22/03/2012, from http://www.presens.de/.

Pro Oceanus. (2015). "CO2-Pro." from http://www.pro-oceanus.com/co2-pro.php.

Raven, J. A. and P. G. Falkowski (1999). "Oceanic sinks for atmospheric CO_2." Plant, Cell and Environment **22**: 741-755.

References

Rérolle, V. M. C., C. F. A. Floquet, A. J. K. Harris, M. C. Mowlem, R. R. G. J. Bellerby and E. P. Achterberg (2013). "Development of a colorimetric microfluidic pH sensor for autonomous seawater measurements." Analytica Chimica Acta **786**(5): 124-131.

Rérolle, V. M. C., C. F. A. Floquet, M. C. Mowlem, D. P. Connelly, E. P. Achterberg and R. R. G. J. Bellerby (2012). "Seawater-pH measurements for ocean-acidification observations." Trends in Analytical Chemistry **40**: 146-157.

Ribas-Ribas, M., V. M. C. Rérolle, D. C. E. Bakker, V. Kitidis, G. A. Lee, I. Brown, E. P. Achterberg, N. J. Hardman-Mountford and T. Tyrrell (2014). "Intercomparison of carbonate chemistry measurements on a cruise in northwestern European shelf seas." Biogeosciences **11**(16): 4339-4355.

Roy, R. S., L. N. Roy, K. M. Vogel, C. Porter-Moore, T. Pearson, C. E. Good, F. J. Millero and D. M. Campbell (1993). "The dissociation constants of carbonic acid in seawater at salinities 5 to 45 and temperatures 0 to 45°C." Marine Chemistry **44**: 249-267.

Rysgaard, S., J. Bendtsen, B. Delille, G. S. Dieckmann, R. N. Glud, H. Kennedy, J. Mortensen, S. Papadimitriou, D. N. Thomas and J.-L. Tison (2011). "Sea ice contribution to the air-sea CO_2 exchange in the Arctic and Southern Oceans." Tellus B **63**(5): 823-830.

Rysgaard, S., J. Bendtsen, L. T. Pedersen, H. Ramløv and R. N. Glud (2009). "Increased CO_2 uptake due to sea ice growth and decay in the Nordic Seas." Journal of Geophysical Research **114**: C09011.

Sabine, C. L., R. A. Feely, N. Gruber, R. M. Key, K. Lee, J. L. Bullister, R. Wanninkhof, C. S. Wong, D. W. R. Wallace, B. Tilbrook, F. J. Millero, T.-H. Peng, A. Kozyr, T. Ono and A. F. Rios (2004). "The Oceanic Sink for Anthropogenic CO_2." Science **305**: 367-371.

Saito, H., N. Tamura, H. Kitano, A. Mito, C. Takahashi, A. Suzuki and H. Kayanne (1995). "A compact seawater pCO_2 measurement system with membrane equilibrator and nondispersive infrared gas analyzer." Deep-Sea Research I **42**(11/12): 2025-2033.

Salgado, L. E. V. and C. Vargas-Hernández (2014). "Spectrophotometric Determination of the pKa, Isosbestic Point and Equation of Absorbance vs. pH for a Universal pH Indicator." American Journal of Analytical Chemistry **05**(17): 1290-1301.

Sanders, R., P. J. Morris, A. J. Poulton, M. C. Stinchcombe, A. Charalampopoulou, M. I. Lucas and S. J. Thomalla (2010). "Does a ballast effect occur in the surface ocean?" Geophysical Research Letters **37**(8): L08602.

Sarmiento, J. L. and N. Gruber (2006). Ocean Biogeochemical Dynamics. Woodstock, Oxfordshire, Princeton University Press.

Satlantic. (2014). "SeaFET™ Ocean pH Sensor." Retrieved 13/11/2014, 2014, from http://satlantic.com/seafet.

Schäferling, M. and A. Duerkop (2008). Intrinsically Referenced Fluorimetric Sensing and Detection Schemes: Methods, Advantages and Applications. Standardization and Quality Assurance in Fluorescence Measurements I. U. Resch-Genger, Springer Berlin Heidelberg. **5:** 373-414.

Schröder, C. (2006). Luminescent planar single and dual optodes for time-resolved imaging of pH, pCO_2 and pO_2 in marine systems. PhD, Universität Regensburg.

Schröder, C., B. M. Weidgans and I. Klimant (2005). "pH Fluorosensors for use in marine systems." The Analyst **130**(6): 907-916.

Schroeder, C., G. Neurauter and I. Klimant (2007). "Luminescent dual sensor for time-resolved imaging of pCO_2 and pO_2 in aquatic systems." Microchimica Acta **158**: 205-218.

Schulman, S. G., S. Chen, F. Bai, M. J. P. Leiner, L. Weis and O. S. Wolfbeis (1995). "Dependence of the fluorescence of immobilized 1-hydroxypyyrene-3,6,8-trisulfonate on solution pH: extension of the range of applicatbility of a pH fluorosensor." Analytica Chimica Acta **304**: 165-170.

Schuster, U., A. Hannides, L. Mintrop and A. Kortzinger (2009). "Sensors and instruments for oceanic dissolved carbon measurements." Ocean Science **5**(4): 547-558.

Schuster, U., G. A. McKinley, N. Bates, F. Chevallier, S. C. Doney, A. R. Fay, M. González-Dávila, N. Gruber, S. Jones, J. Krijnen, P. Landschützer, N. Lefèvre, M. Manizza, J. Mathis, N. Metzl, A. Olsen, A. F. Rios, C. Rödenbeck, J. M. Santana-Casiano, T. Takahashi, R. Wanninkhof and A. J. Watson (2013). "An assessment of the Atlantic and Arctic sea–air CO_2 fluxes, 1990–2009." Biogeosciences **10**(1): 607-627.

Schuster, U. and A. J. Watson (2007). "A variable and decreasing sink for atmospheric CO_2 in the North Atlantic." Journal of Geophysical Research: Oceans **112**(C11).

Schuster, U., A. J. Watson, N. R. Bates, A. Corbiere, M. Gonzalez-Davila, N. Metzl, D. Pierrot and M. Santana-Casiano (2009). "Trends in North Atlantic sea-surface fCO_2 from 1990 to 2006." Deep-Sea Research II **56**(8-10): 620-629.

Schutting, S., I. Klimant, D. de Beer and S. M. Borisov (2014). "New highly fluorescent pH indicator for ratiometric RGB imaging of pCO2." Methods and Applications in Fluorescence **2**(2): 024001.

Seidel, M. P., M. D. DeGrandpre and A. G. Dickson (2008). "A sensor for in situ indicator-based measurements of seawater pH." Marine Chemistry **109**: 18-28.

Severinghaus, J. W. and A. F. Bradley (1958). "Electrodes for blood pO_2 and pCO_2 determination." Journal of Applied Physiology **13**(3): 515-520.

Sharqawy, M. H., J. H. Lienhard and S. M. Zubair (2012). "Thermophysical properties of seawater: a review of existing correlations and data." Desalination and Water Treatment **16**(1-3): 354-380.

Shin, J. H., J. S. Lee, S. H. Choi, D. K. Lee, H. Nam and G. S. Cha (2000). "A Planar pCO_2 sensor with enhanced electrochemical properties." Analytical Chemistry **72**(18): 4468-4473.

Shitashima, K., Y. Koike, M. Kyo and A. Hemmi (2008). Development of in-situ pH-pCO_2 sensor for deep-sea oceanography applications. Sensors, 2008 IEEE Lecce, IEEE**:** 1414-1417.

Siegenthaler, U. and J. Sarmiento (1993). "Atmospheric carbon dioxide and the ocean." Nature **365**(6442): 119-125.

Sigma-Aldrich Trizma base Product Information. Sigma-aldrich.com, Sigma Aldrich. **GCY/RXR 8/08**.

Solomon, S., G.-K. Plattner, R. Knutti and P. Friedlingstein (2009). "Irreversible climate change due to carbon dioxide emissions." Proceedings of the National Academy of Sciences **106**(6): 1704-1709.

Sosna, M., G. Denuault, R. W. Pascal, R. D. Prien and M. Mowlem (2007). "Development of a reliable microelectrode dissolved oxygen sensor." Sensors and Actuators B **123**(1): 344-351.

Stahl, H., A. Glud, C. R. Schroder, I. Klimant, A. Tengberg and R. N. Glud (2006). "Time-resolved pH imaging in marine sediments with a luminescent planar optode." Limnology and Oceanography: Methods **4**: 336-345.

Stangelmayer, A., I. Klimant and O. S. Wolfbeis (1998). "Optical sensors for dissolved sulfur dioxide." Fresenius Journal of Analytical Chemistry **362**: 73-76.

Stich, M. I., L. H. Fischer and O. S. Wolfbeis (2010). "Multiple fluorescent chemical sensing and imaging." Chemical Society Reviews **39**(8): 3102-3114.

Stoll, M. H. C., H. M. van Aken, H. J. W. de Baar and M. Kraak (1996). "Carbon dioxide characteristics of water masses in the northern North Atlantic Ocean." Marine Chemistry **55**(3–4): 217-232.

Stumm, W. and J. J. Morgan (1996). Aquatic Chemistry: Chemical Equilibria and Rates in Natural Water, 3rd Edition. Canada, Wiley-Interscience.

Sunburst Sensors LLC. "SAMI-CO2 Ocean CO2 Sensor." Retrieved 29/10/2014, 2014, from http://www.sunburstsensors.com/products/oceanographic-carbon-dioxide-sensor.html.

Sutherland, D. A. and R. S. Pickart (2008). "The East Greenland Coastal Current: Structure, variability, and forcing." Progress in Oceanography **78**(1): 58-77.

Sutherland, D. A., R. S. Pickart, E. Peter Jones, K. Azetsu-Scott, A. Jane Eert and J. Ólafsson (2009). "Freshwater composition of the waters off southeast Greenland and their link to the Arctic Ocean." Journal of Geophysical Research **114**(C5).

Szmacinski, H. and J. R. Lakowicz (1994). Lifetime-Based Sensing. Topics in Fluorescence Spectroscopy Volume 4: Probe Design and Chemical Sensing. J. Lakowicz. New York, Kluwer Academic Publishers. **4 Probe Design and Chemical Sensing:** 295-329.

Tabacco, M. B., M. Uttamlal, M. McAllister and D. R. Walt (1999). "An Autonomous Sensor and Telemetry System for Low-Level pCO_2 Measurements in Seawater." Analytical Chemistry **71**(1): 154-161.

Taib, M. N. and R. Narayanaswamy (1995). "Solid-state Instruments for Optical Fibre Chemical Sensors." The Analyst **120**: 1617-1625.

Taillefert, M., G. W. Luther III and D. B. Nuzzio (2000). "The Application of Electrochemical Tools for In Situ Measurements in Aquatic Systems." Electroanalysis **6**: 401-412.

Takahashi, T., R. A. Feely, R. F. Weiss, R. H. Wanninkhof, D. W. Chipman, S. C. Sutherland and T. T. Takahashi (1997). "Global air-sea flux of CO_2: an estimate based on measurement of sea-air pCO_2 difference." Proceedings of the National Academy of Sciences USA **94**: 8292-8299.

Takahashi, T., J. Olafsson, J. G. Goddard, D. W. Chipman and S. C. Sutherland (1993). "Seasonal variation of CO_2 and nutrients in the high-latitutde surface oceans- A comparative study." Global Biogeochemical Cycles **7**(4): 843-878.

Takahashi, T., S. C. Sutherland, C. Sweeney, A. Poisson, N. Metzl, B. Tilbrook, N. Bates, R. Wanninkhof, R. A. Feely and C. Sabine (2002). "Global sea–air CO_2 flux based on climatological

surface ocean pCO_2, and seasonal biological and temperature effects." Deep-Sea Research II **49**(9): 1601-1622.

Takahashi, T., S. C. Sutherland, R. Wanninkhof, C. Sweeney, R. A. Feely, D. W. Chipman, B. Hales, G. Friederich, F. Chavez, C. Sabine, A. Watson, D. C. E. Bakker, U. Schuster, N. Metzl, H. Yoshikawa-Inoue, M. Ishii, T. Midorikawa, Y. Nojiri, A. Körtzinger, T. Steinhoff, M. Hoppema, J. Olafsson, T. S. Arnarson, B. Tilbrook, T. Johannessen, A. Olsen, R. Bellerby, C. S. Wong, B. Delille, N. R. Bates and H. J. W. de Baar (2009). "Climatological mean and decadal change in surface ocean pCO_2, and net sea–air CO_2 flux over the global oceans." Deep-Sea Research II **56**(8-10): 554-577.

Tan, C.-y., B. Jin, K. Ding, W. E. Seyfried and Y. Chen (2010). "A long-term in situ calibration system for chemistry analysis of seawater." Journal of Zhejiang University SCIENCE A **11**(9): 701-708.

Thomas, B. R., E. C. Kent and V. R. Swail (2005). "Methods to homogenize wind speeds from ships and buoys." International Journal of Climatology **25**(7): 979-995.

Thomas, H. and V. Ittekkot (2001). "Determination of anthropogenic CO_2 in the North Atlantic Ocean using water mass ages and CO_2 equilibrium chemistry." Journal of Marine Systems **27**: 325-336.

Tian, Y., E. Fuller, S. Klug, F. Lee, F. Su, L. Zhang, S.-h. Chao and D. R. Meldrum (2013). "A fluorescent colorimetric pH sensor and the influences of matrices on sensing performances." Sensors and Actuators B **188**: 1-10.

Tishchenko, P. Y., D.-J. Kang, R. V. Chichkin, A. Y. Lazaryuk, C. Shing Wong and W. Keith Johnson (2011). "Application of potentiometric method using a cell without liquid junction to underway pH measurements in surface seawater." Deep-Sea Research I **58**(7): 778-786.

Valeur, B. (2002). Molecular Fluorescence: Principles and Applications. Germany, WILEY-VCH.

Van Heuven, S., D. Pierrot, J. W. B. Rae, E. Lewis and D. W. R. Wallace (2011). "CO2SYS v 1.1, MATLAB program developed for CO_2 system calculations." ORNL/CDIAC-105b. Carbon Dioxide Information Analysis Center, Oak Ridge National Laboratory, U.S. DoE, Oak Ridge, TN.

Vogel, A. I. (1989). Vogel's Textbook of Quantitative Chemical Analysis Essex, England, Longman Scientific & Technical.

Von Bültzingslöwen, C., A. K. McEvoy, C. McDonagh and B. D. MacCraith (2003). "Lifetime-based optical sensor for high-level pCO2 detection employing fluorescence resonance energy transfer." Analytica Chimica Acta **480**(2): 275-283.

Wang, Z. A., F. N. Sonnichsen, A. M. Bradley, K. A. Hoering, T. M. Lanagan, S. N. Chu, T. R. Hammar and R. Camilli (2015). "In Situ Sensor Technology for Simultaneous Spectrophotometric Measurements of Seawater Total Dissolved Inorganic Carbon and pH." Environmental Science & Technology **49**(7): 4441-4449.

Wanninkhof, R. (1992). "Relationship between wind speed and gas exchange over the ocean." Journal of Geophysical Research: Oceans **97**(C5): 7373-7382.

Wanninkhof, R. (2014). "Relationship between wind speed and gas exchange over the ocean revisited." Limnology and Oceanography: Methods **12**(6): 351-362.

Wanninkhof, R., G. H. Park, T. Takahashi, C. Sweeney, R. Feely, Y. Nojiri, N. Gruber, S. C. Doney, G. A. McKinley, A. Lenton, C. Le Quéré, C. Heinze, J. Schwinger, H. Graven and S. Khatiwala (2013). "Global ocean carbon uptake: magnitude, variability and trends." Biogeosciences **10**(3): 1983-2000.

Wanninkhof, R. H. and M. Knox (1996). "Chemical enhancement of CO_2 exchange in natural waters." Limnology and Oceanography **41**(4): 689-697.

Watson, A., C. Robinson, J. E. Robinson, P. J. l. B. Williams and M. J. R. Fasham (1991). "Spatial variability in the sink for atmospheric carbon dioxide in the North Atlantic." Nature **350**: 50-53.

Watson, A. J., U. Schuster, D. C. E. Bakker, N. R. Bates, A. Corbière, M. González-Dávila, T. Friedrich, J. Hauck, C. Heinze, T. Johannessen, A. Körtzinger, N. Metzl, J. Olafsson, A. Olsen, A. Oschlies, X. A. Padin, B. Pfeil, J. M. Santana-Casiano, T. Steinhoff, M. Telszewski, A. F. Rios, D. W. R. Wallace and R. Wanninkhof (2009). "Tracking the Variable North Atlantic Sink for Atmospheric CO_2." Science **326**: 1391-1393.

Weigl, B. H. and O. S. Wolfbeis (1995). "Sensitivity studies on optical carbon dioxide sensors based on ion pairing." Sensors and Actuators B **28**: 151-156.

Weiss, R. F. (1974). "Carbon dioxide in water and seawater: the solubility of a non-ideal gas." Marine Chemistry **2**(3): 203-215.

Weiss, R. F. (1981). "Determinations of carbon dioxide and methane by dual catalyst flame ionization chromatography and nitrous oxide by electron capture chromatography." Journal of Chromatographic Science **19**(12): 611-616.

Weiss, R. F., F. A. Van Woy and P. K. Salameh (1992). Surface Water and Atmospheric Carbon Dioxide and Nitrous Oxide Observations by Shipboard Automated Gas Chromatography: Results from Expeditions Between 1977 and 1990. R. J. Sepanski. Environmental Sciences Division Publication, Scripps Institution of Oceanography.

Wencel, D., T. Abel and C. McDonagh (2014). "Optical chemical pH sensors." Analytical Chemistry **86**(1): 15-29.

Wencel, D., B. D. MacCraith and C. McDonagh (2009). "High performance optical ratiometric sol–gel-based pH sensor." Sensors and Actuators B **139**(1): 208-213.

Wolfbeis, O. S. (1997). Chemical Sensing Using Indicator Dyes. Optical Fiber Sensors. J. Dakin and B. Culshaw. Boston-London, Artech House. **IV:** 53-107.

Wolf-Gladrow, D. A., R. E. Zeebe, C. Klaas, A. Körtzinger and A. G. Dickson (2007). "Total alkalinity: The explicit conservative expression and its application to biogeochemical processes." Marine Chemistry **106**: 287-300.

Yamamoto-Kawai, M. (2005). "Freshwater and brine behaviors in the Arctic Ocean deduced from historical data of $\delta^{18}O$ and alkalinity (1929–2002 A.D.)." Journal of Geophysical Research **110**(C10).

Yang, B., M. C. Patsavas, R. H. Byrne and J. Ma (2014). "Seawater pH measurements in the field: A DIY photometer with 0.01 unit pH accuracy." Marine Chemistry **160**(0): 75-81.

Yoder, J. A., C. R. McClain, G. C. Feldman and W. E. Esaias (1993). "Annual cycles of phytoplankton chlorophyll concentrations in the global ocean: A satellite view." Global Biogeochemical Cycles **7**(1): 181-193.

Zeebe, R. E. and D. A. Wolf-Gladrow (2005). CO_2 in Seawater: Equilibrium, Kinetics, Isotopes. Oxford, Elsevier.

Zhao, P. and W.-J. Cai (1997). "An improved Potentiometric pCO_2 microelectrode." Analytical Chemistry **69**: 5052-5058.

Zhu, Q., R. C. Aller and Y. Fan (2005). "High-Performance Planar pH Fluorosensor for Two Dimensional pH Measurements in Marine Sediment and Water." Environmental Science & Technology **39**: 8906-8911.

Zhu, Q., R. C. Aller and Y. Fan (2006). "A new ratiometric, planar fluorosensor for measuring high resolution, two-dimensional pCO_2 distributions in marine sediments." Marine Chemistry **101**(1-2): 40-53.

Zosel, J., W. Oelßner, M. Decker, G. Gerlach and U. Guth (2011). "The measurement of dissolved and gaseous carbon dioxide concentration." Measurement Science and Technology **22**(7): 072001.